Centre Énergie Matériaux Télécommunications

DEVELOPMENT AND APPLICATIONS OF A SINGLE-PIXEL IMAGING PLATFORM FOR THREE-DIMENSIONAL, REAL-TIME, ULTRAHIGH-SPEED, AND TERAHERTZ IMAGING

Par

Patrick Kilcullen

Thèse présentée pour l'obtention du grade de
Philosophiae Doctor (Ph.D.)
en sciences de l'énergie et des matériaux

Jury d'évaluation

Président du jury et examinateur interne	Luca Razzari INRS-EMT
Examinateur externe	Daniele Faccio School of Physics and Astronomy University of Glasgow
Examinateur externe	Maksim Skorobogatiy Département de Génie Physique Polytechnique Montréal
Directeur de recherche	Tsuneyuki Ozaki INRS-EMT
Codirecteur de recherche	Jinyang Liang INRS-EMT

Note: For the electronic version of this document, care has been taken to simplify navigation with hyperlinks which appear as blue highlighted text. Examples of hyperlinking include links to external websites, as well as in-text references to figures, equations, and bibliographic entries, each of which when clicked will navigate the viewer to the corresponding figure, equation, or item in the bibliography. Care has also been taken to associate digital object identifiers (DOIs) with each bibliographic reference, when available. These also appear as external hyperlinks to websites supporting each resource. For best use of hyperlinking, it is recommended that you use the 'Forwards' and 'Backwards' navigation commands likely available within your PDF viewer. This allows for a similar control of navigation as in a web browser. In addition, chapters and sections in this document have been given bookmarks which may be viewed in your PDF viewer's bookmarks pane.

ACKNOWLEDGEMENTS

Behind every project of scientific research is a story of collaboration and interpersonal enrichment that is routinely stripped away from the texts that reach the pages of journals, conference proceedings, and theses. The pages of this thesis too make the same omission, despite the fact that I have had the great privilege to live such a story over the past five years.

I would like to firstly extend my sincere thanks to Tsuneyuki Ozaki and Jinyang Liang for the excellent quality of their continued support and mentorship in supervising the completion of this thesis. Within their research groups, I have had the great pleasure of meeting and collaborating with many young and talented researchers with backgrounds across chemistry, mathematics, computer science, and physics. My thanks and gratitude especially goes to Cheng Jiang, with whom I have had the privilege of being a close collaborator during the completion of several fascinating and rewarding research projects, none of which I anticipated undertaking at the start of my studies. From the Laboratory of Applied Imaging (LACI) research group of Dr. Liang, I thank my additional colleagues Jingdan Liu, Xianglei Liu, Yingming Lai, Siqi Wang, Miao Liu, Madhu Beniwal, Miguel Marquez, and Hans Yecid Garcia Arenas. From the terahertz and laser physics research group of Dr. Ozaki, I would like to thank my colleagues Ahmed Mouhammed, Elchin Isagordov, Carlos Miguel Garcia Rosas, and Xavier Rapagnol, each of whom were of generous assistance in guiding this research within the difficult field of terahertz science.

My enthusiastic thanks also goes to professor My Ali El Khakani, together with Loick Pinchon, and Sanjit Varma, whose ongoing collaborative assistance and expertise in the fabrication of nanostructured materials has been of immense value.

Outside the context of scientific collaboration, my thanks also goes to Xin Jin, Jaibin Liu, Mostafa Shagar, Juan Carlos Abrego Martinez, and Fabiola Navarro Pardo, each whom I had the honor of befriending during those times when the lugubriousness of research called for the remedy of good company.

Towards my family and friends, to whom my life for the past five years has no doubt appeared sordid and enigmatic, my affections are here flaunted with veils of anonymity, so as to shelter the guilty and torment the innocent. My love goes to my parents, as well as Mo, and Big Bailey (soon to be *Bigger* Bailey, congratulations!), my musical co-conspirators Frisco, Erik, Lea, Shayne, Dan Beasy, Lloyd, Geoff, and ‘Pitted’, the creatures Marco and Bucky, and finally to Tony, to whom I owe the unfolding of many stories, herein omitted.

ABSTRACT

The ubiquity and maturity of multi-pixel optical sensors has enabled countless applications within science for high-speed and real-time imaging. However, these capabilities remain unavailable for imaging at many other wavelengths of scientific interest. In these cases, as an alternative to simple raster scanning, single-pixel imaging (SPI) has emerged as a fast and flexible imaging technique that makes use of coded wide-field illumination combined with a single non-imaging detector. When viewed from the perspective of overall performance, SPI systems exhibit a critical reliance on both dedicated hardware for spatial light modulation, as well as algorithms for image reconstruction. In spite these dependencies, the popularity of SPI owes much to the maturity of two separate technologies. The first is the digital micromirror device (DMD), which enables reconfigurable and non-mechanical light modulation with binary patterns at speeds up to 32 kHz. The second is the mathematical theory of compressive sensing (CS), which has enabled the development and theoretical study of many general-purpose algorithms for SPI reconstruction. Unfortunately, the limitations of both DMD technology and CS-based reconstruction algorithms have continued to enormously impact SPI, in particular leading many SPI techniques to suffer from low imaging rates and/or expensive reconstruction times, precluding applications demanding high-speed or real-time performance.

Whereas previous SPI approaches have traditionally adopted DMD-based modulation and CS-based reconstruction as separate and generic technologies, the development of jointly optimized schemes for faster modulation and reconstruction represents an important potential strategy to advance the capabilities of SPI. Following this strategy, this thesis introduces single-pixel imaging accelerated via scanning of aggregate patterns (SPI-ASAP), a new platform for high-speed and real-time capable SPI which augments conventional DMD-based SPI with off-the shelf laser scanning hardware to achieve modulation at MHz bandwidths. By identifying cyclic S-matrices as an optimal basis for the design of encoding patterns for aggregate scanning, a new reconstruction algorithm is introduced that is capable of CS, while also compatible with hardware for parallelized computing.

This thesis introduces the platform of SPI-ASAP as well as various applications of SPI in three parts. In the first part, an approach to three-dimensional single-pixel imaging is explored which extends the techniques of fringe projection profilometry while leveraging cyclic S-matrices for the design of encoding patterns. Further, through the principal of Helmholtz reciprocity, the system is shown to be capable of dual photography and scene relighting. In the second part, the SPI-ASAP platform is fully introduced, adding the elements of scanned pattern aggregation and fast compressive reconstruction to the cyclic S-matrix encoding patterns. The resulting system is used to demonstrate ultrahigh-speed imaging at framerates up to 12,000 frames-per-second (fps), modulation rates of up to 14.1 MHz, and real-time visualization of 101×103 single-pixel video at speeds up to 100 fps. Finally, in the third part, an application of the SPI-ASAP platform to terahertz (THz) emission imaging is proposed, along with the substantially completed design of a computational terahertz chemical microscope (TCM). Although construction of the proposed system is currently ongoing, a minimally intrusive and experimentally verified mechanism for the modulation of THz emission is reported, substantiating the feasibility of this design to enhance the operation of existing TCM systems.

Keywords: single-pixel imaging (SPI); compressed sensing; computational imaging; digital-micromirror device (DMD); cyclic S-matrices; three-dimensional imaging; ultrahigh-speed imaging; terahertz imaging; terahertz chemical microscopy (TCM)

RÉSUMÉ

L'omniprésence et la maturité des capteurs optiques multi-pixels ont favorisé d'innombrables applications scientifiques dans le domaine de l'imagerie à haute vitesse et en temps réel. Cependant, ces capacités ne sont pas disponibles pour l'imagerie à différentes longueurs d'onde dont la science s'intéresse. Dans ces cas, comme alternative au simple balayage de trame, l'imagerie mono-pixel (SPI de l'anglais single-pixel imaging) est apparue comme une technique d'imagerie rapide et flexible qui utilise un éclairage codé à large champ combiné à un seul détecteur non imageur. Du point de vue des performances globales, les systèmes d'imagerie mono-pixel SPI sont très dépendants à la fois du matériel dédié à la modulation spatiale de la lumière et des algorithmes de reconstruction de l'image. Malgré ces dépendances, la popularité de l'imagerie mono-pixel SPI doit beaucoup à la maturité de ces deux technologies distinctes. La première est le dispositif numérique à micromiroir (DMD de l'anglais digital micromirror device), qui permet une modulation lumineuse reconfigurable et non mécanique avec des motifs binaires à des vitesses allant jusqu'à 32 kHz. La seconde est la théorie mathématique de la détection par compression (CS pour compressive sensing) qui a permis le développement et l'étude théorique de nombreux algorithmes polyvalents pour la reconstruction d'images mono-pixeliques SPI. Malheureusement, les limites de la technologie du dispositif numérique à micromiroir DMD et celles des algorithmes de reconstruction basés sur la détection par compression CS ont continué à avoir un énorme impact sur la reconstitution de l'image mono-pixelique SPI. Ces limites ont fait subir à de nombreuses techniques SPI de faibles vitesses d'imagerie et/ou de temps de reconstruction coûteux, ce qui exclut les applications exigeant des performances à grande vitesse ou en temps réel.

Alors que les approches SPI précédentes ont traditionnellement adopté la modulation basée sur le dispositif numérique à micromiroir DMD et la reconstruction basée sur la détection par compression CS en tant que technologies séparées et génériques, le développement de schémas optimisés conjointement pour une modulation et une reconstruction plus rapide représente une stratégie potentielle et importante pour faire progresser les capacités de SPI. Suivant cette stratégie, cette thèse présente l'imagerie à mono-pixel accélérée par balayage de motifs agrégés (SPI-ASAP), une nouvelle plateforme pour SPI à haute vitesse et en temps réel qui augmente le SPI conventionnel basé sur DMD avec un matériel commercialisé de balayage laser pour obtenir une modulation à de bande passante en MHz. En identifiant les matrices circulantes du type S (cyclic S-matrix) comme une base optimale pour la conception de modèles de codage pour le balayage agrégé, un nouvel algorithme de reconstruction est introduit qui est capable de CS, tout en étant également compatible avec le matériel pour le calcul en parallèle.

Cette thèse présente la plateforme de l'imagerie à mono-pixel ultra-rapide par balayage de motifs agrégés SPI-ASAP ainsi que diverses applications de l'imagerie mono-pixel SPI en trois parties. Dans la première partie, une approche de l'imagerie tridimensionnelle à mono-pixel est explorée, qui étend les techniques de profilométrie par projection de franges tout en tirant parti des matrices circulantes du type S pour la conception de modèles de codage. De plus, grâce au principe de réciprocité de Helmholtz, le système s'avère capable d'une photographie bimode et d'un rééclairage de scène. Dans la deuxième partie, la plateforme SPI-ASAP est entièrement introduite, ajoutant les éléments d'agrégation de motifs scannés et de reconstruction compressive rapide aux motifs de codage de la matrice circulante du type S. Le système résultant est utilisé pour démontrer l'imagerie ultra-rapide à des vitesses d'images allant jusqu'à 12 000 images par seconde (ips), des taux de modulation allant jusqu'à 14,1 MHz et la visualisation en temps réel d'une vidéo à mono-pixel 101×103 à des vitesses allant jusqu'à 100 ips. Enfin, dans la troisième partie, une application de la plateforme SPI-ASAP à l'imagerie d'émission térahertz (THz) est proposée, consistant en la conception substantiellement achevée d'un microscope chimique térahertz computationnel (TCM pour terahertz chemical microscope). Bien que la construction du système proposé soit actuellement en cours, un mécanisme minimalement intrusif et vérifié expérimentalement pour la modulation de l'émission THz est rapporté, ce qui prouve la faisabilité de cette conception pour améliorer le fonctionnement des systèmes TCM existants.

Mots-clés: imagerie mono-pixel (SPI); détection comprimée; imagerie numérique; dispositif à micromiroir numérique (DMD); S-matrices circulantes; imagerie tridimensionnelle; imagerie à très grande vitesse; imagerie térahertz; Microscopie chimique térahertz (TCM)

TABLE OF CONTENTS

LIST OF FIGURES

LIST OF TABLES

LIST OF ABBREVIATIONS

1D	one-dimensional
2D	two-dimensional
3D	three-dimensional
CS	compressed sensing
CW	continuous wave
DCT	discrete cosine transform
DFT	discrete Fourier transform
DMD	digital micromirror device
FOV	field of view
FPP	fringe projection profilometry
fps	frames per second
fs	femtosecond
GM	galvanometer mirror
GPU	graphic processing unit
kfps	thousand frames per second
LED	light emitting diode
LTEM	laser-excited terahertz emission microscopy
LTM	light transport matrix
MEMS	micro-electromechanical systems
NIR	near-infrared
PCA	photoconductive antenna
ps	picosecond
PSNR	peak signal-to-noise ratio
SLM	spatial light modulator
SNR	signal-to-noise ratio
SOS	silicon-on-sapphire
SPI	single-pixel imaging

SPI-ASAP	single-pixel imaging accelerated via swept aggregate patterns
SSIM	structural similarity index
STDP	single-pixel three-dimensional dual photography
TCM	terahertz chemical microscopy
THz	terahertz
THz-TDS	terahertz time-domain spectroscopy

LIST OF CONTRIBUTIONS

Peer-reviewed Journal Articles

[A1] Jiang, C.[†], **Kilcullen, P.**[†] et al. Real-time high-speed three-dimensional surface imaging using band-limited illumination profilometry with a CoaXPress interface. *Opt. Lett.* **45**(4), 964–967 (2020). doi:10.1364/OL.378939.

[A2] Jiang, C.[†], **Kilcullen, P.**[†], Lai, Y., Ozaki, T. & Liang, J. High-speed dual-view band-limited illumination profilometry using temporally interlaced acquisition. *Photonics Res.* **8**(11), 1808–1817 (2020). doi:10.1364/prj.399492.

[A3] **Kilcullen, P.**, Jiang, C., Ozaki, T. & Liang, J. Camera-free three-dimensional dual photography. *Opt. Express* **28**(20), 29377–29389 (2020). doi:10.1364/OE.402310.

[A4] Jiang, C., **Kilcullen, P.**, Lai, Y., Wang, S., Ozaki, T. & Liang, J. Multi-scale band-limited illumination profilometry for robust three-dimensional surface imaging at video rate. *Opt. Express* **30**(11), 19824–19838 (2022). doi:10.1364/oe.457502.

[A5] **Kilcullen, P.**, Ozaki, T. & Liang, J. Compressed ultrahigh-speed single-pixel imaging by swept aggregate patterns. *Nat. Commun.* **13**, 7879 (2022). doi:10.1038/s41467-022-35585-8.

Conference Papers

[B1] Jiang, C.[†], **Kilcullen, P.**[†], Liu, X., Ozaki, T. & Liang, J. Three-dimensional structured light profilometry using a bandwidth-limited projector. In *Emerging Digital Micromirror Device Based Systems and Applications XI*, Proc. SPIE 10932, 109320K (2019). doi:10.1117/12.2510145.

[B2] **Kilcullen, P.**, Jiang, C., Ozaki, T. & Liang, J. Single-pixel three-dimensional dual photography. In *Emerging Digital Micromirror Device Based Systems and Applications XIII*, Proc. SPIE 11698, 116980L (2021). doi:10.1117/12.2578897.

[B3] Jiang, C.[†], **Kilcullen, P.**[†], Liu, X., Lai, Y., Ozaki, T. & Liang, J. High-speed three-dimensional surface measurement using band-limited illumination profilometry (BLIP). In *Emerging Digital Micromirror Device Based Systems and Applications XIII*, Proc. SPIE 11698, 116980V (2021). doi:10.1117/12.2577076.

Conference Presentations

[C1] **Kilcullen, P.**, Jiang, C., Ozaki, T. & Liang, J. Single-pixel structured light profilometry. In *Proceedings of Photonics North 2021*. IEEE (2021). doi:10.1109/pn52152.2021.9597999.

[C2] Jiang, C.[†], **Kilcullen, P.**[†], Liu, X., Lai, Y., Ozaki, T. & Liang, J. High-speed band-limited illumination profilometry. In *Proceedings of Photonics North 2021*. IEEE (2021). doi:10.1109/PN52152.2021.9597958.

[†] Equal contribution to published article.

Under Peer-Review

[D1] Liu, X., **Kilcullen, P.**, Wang, Y., Helfield, B. & Liang, J. Diffraction-gated real-time ultrahigh-speed mapping photography. Submitted for publication in *Science Advances* (March 2023).

Patent Applications

[E1] Liang, J., Jiang, C. & **Kilcullen, P.** A method and a system for 3d imaging. Patent Application US17/310,489 (United States), CA3129216A (Canada), PCT/CA2020/050149 (WIPO). Submitted Feb, 2020. Published as US20220357151A1, CA3129216A1, WO2020160666A1.

[E2] Liang, J., Jiang, C. & **Kilcullen, P.** Method and system for high-speed dual-view band-limited illumination profilometry. Patent Application US17/444,307 (United States), CA3126592A (Canada). Submitted Aug, 2021. Published as US20220038676A1, CA3126592A1.

1 INTRODUCTION

The multi-pixel digital camera represents one of the most mature technologies employed within science and throughout wider society. The progressive miniaturization and continuing improvement of semiconductor-based integrated circuits has allowed sensor technologies such as charge-coupled devices (CCDs) and complementary metal-oxide semiconductor (CMOS) sensors to revolutionize the tools and techniques of scientific imaging, in particular for high-speed and real-time imaging. Yet for most wavelengths outside of the visible spectrum, or for phenomena occurring on extremely short time scales, the use of these mature silicon-based technologies is not possible; a fact which limits their application in many scientific fields of interest [1]. Traditionally, in cases where the immaturity of sensor technology has precluded the use of multi-pixel detectors, imaging systems have been forced to adopt raster scanning, thereby suppressing image acquisition rates with mechanical limitations often to several orders of magnitude below the bandwidth of the available detector. Besides imposing significant bottlenecks to the speed of measurement acquisition, all approaches to single-point raster scanning, such as motorized object positioning or mirror-actuated beam steering, require imaging times that must scale to accommodate at least one independent measurement for each pixel sampled in the image. Yet, it is clear that for a given photoactive device or material, the development of an electronically integrated array-format photosensor (if feasible) must introduce sacrifices with respect to overall cost, noise performance, and/or time resolution when compared against the same technology in a single-pixel format. Thus, if provided with a sufficiently fast means for achieving sequential two-dimensional (2D) optical sampling, the advantages of single-pixel detectors could be leveraged in the pursuit of developing imaging systems with higher-performance and lower-cost.

Single-pixel imaging (SPI), as an emerging methodology for scientific imaging, aims to avoid the limitations of raster scanning while capitalizing on the performance advantages of single-pixel sensors. In contrast to the operation of imaging systems with conventional multi-pixel sensors, SPI systems capture images by recording a sequence of wide-field optically computed inner products involving the underlying image and a set of deterministic spatial encoding patterns introduced to the imaging beam via a modulation device. These inner products capture the underlying image in an indirect way, with the recovery of actual images depending on the use of a reconstruction algorithm together with knowledge of the encoding pattern sequence used during experiment. Remarkably, the coded and wide-field nature of the measurements used in SPI allows it to benefit from a computational advantage entirely unavailable to raster scanning systems: the potential to recover accurate imagery from a number of detector measurements far below the number of image pixels.

In recent years, the popularity of SPI has grown owing to the increasing availability of spatial light modulation (SLM) hardware, together with the maturity of general-purpose software for the implementation of sophisticated image reconstruction algorithms. For SPI systems working with visible or near-visible wavelengths, the dominant SLM technology has been the digital micromirror device (DMD) which is capable of reconfigurable and non-mechanical display of mega-pixel resolution binary patterns at rates up to 32 kHz [2]. Notably, the compatibility of DMD technology with near-infrared (NIR) wavelengths makes their use with SPI especially attractive as a lower-cost alternative to imaging with multi-pixel NIR detectors, with the commercial costs of the latter technology typically exceeding those of DMDs by as much as two orders of magnitude per pixel [1]. However, despite offering numerous advantages, the kHz pattern refresh rates of DMDs continue to sharply limit the signal acquisition rate of most SPI systems to below the MHz bandwidths of typical single-point photodetector equipment, thus still failing to fully leverage the advantages in time resolution afforded by single-pixel detection. In order to compensate for the kHz display rate limitations of DMDs, most SPI systems have aimed to increase imaging speeds by reducing the number of samples required for image recovery through an appropriately selected reconstruction algorithm. Although a sufficiently large set of pattern and detector signal data may only require statistical averaging or matrix inversion for image reconstruction, the majority of current SPI approaches reduce sampling overhead by utilizing reconstruction algorithms from a family of computational techniques known as compressed sensing (CS) [3–6]. Unfortunately, while having enabled their wide adoption within SPI and elsewhere, the flexibility and generality of most CS algorithms depends on techniques of convex optimization that are inherently iterative, exhibiting widely varying processing times and requiring a large computational overhead [7–9]. While advantageous for imaging experiments that process data after acquisition, the resulting trade-off between the time required for pattern deployment and that required for sophisticated image reconstruction has precluded most SPI systems from achieving real-time visualization, where reconstruction must immediately follow acquisition with tight synchronization.

For SPI systems, overall performance depends critically on both the dedicated hardware used for spatial light modulation, as well as the algorithm chosen for image reconstruction. Although the existence of robust and general-purpose technological solutions for each of these components (e.g. DMDs for modulation and CS algorithms for reconstruction) has made SPI research widely accessible, the use of separate and generic solutions for both modulation and reconstruction has left many of SPI's central performance limitations under-addressed. It is reasonable to expect that addressing these limitations, and thus growing the potential applications of SPI, will require the development of not only specialized modulation hardware, but also reconstruction algorithms that are tightly coupled to their operation. Thus, in contrast to methods seeking to improve either modulation speeds or reconstruction times in isolation from the other, approaches which are able to address these aspects simultaneously may hold the most potential for advancing the technological maturity of SPI.

Within this line of development, this thesis introduces a new approach to SPI called single-pixel imaging accelerated via scanning of aggregate patterns (SPI-ASAP), encompassing both a hardware solution for the rapid modulation of encoding patterns, as well as a complimentary algorithm for image reconstruction. In combination, these techniques allow for offline imaging in both high-speed and ultrahigh-speed regimes, while also supporting real-time and low-latency operation at video framerates. At the heart of its operation, SPI-ASAP's modulation approach augments the performance of a conventional DMD with off-the-shelf laser scanning hardware allowing for the MHz-rate deployment of sets of simultaneously aggregated encoding patterns. The crucial contribution of the laser scanning principle is that it allows for the rapid deployment of individual masking patterns as optically selected sub-regions of larger patterns which are displayed via DMD. Whereas the high-resolution, non-mechanical operation, reconfigurability, and wide availability of DMDs have yet to be matched by any alternative modulation technology employed in SPI, the strategy of scanning and pattern aggregation allows SPI-ASAP to acquire data at rates 50–100 times above the traditional limits of DMD-only modulation, while still retaining the advantages of DMD hardware. Together with this modulation strategy, a particular optimal choice of design basis for the encoding patterns of SPI-ASAP enables the use of a lightweight and heuristically simple reconstruction algorithm which is nonetheless capable of compressed sensing: the recovery of images from significantly under-sampled datasets. Importantly, the structure of this algorithm allows it to be compatible with parallelized execution using multi-core computer hardware such as a graphics processing unit (GPU). Moreover, despite its comparative simplicity and emphasis on low computational overhead, this algorithm shows comparable or better performance to traditional iterative CS algorithms when combined with the sampling strategy implemented by the modulation hardware of SPI-ASAP.

This thesis introduces the platform of SPI-ASAP as well as various applications of SPI to three-dimensional, real-time, ultrahigh-speed, and terahertz imaging, in three parts; each corresponding to the main research projects which have been undertaken in the course of the development of SPI-ASAP. Following a review of the principles and existing techniques of SPI, dual photography, and fringe projection profilometry provided by this introductory chapter, the outline of these parts is as follows:

In the first part (chapter 2, derived from the publication in [10]), an approach to three-dimensional (3D) imaging is explored which, via the use of a dual DMD system design, extends the technique of fringe projection profilometry to SPI. In contrast to previous techniques for 3D SPI which have relied on either highly time-sensitive detection or strong assumptions of surface reflectance behavior, this approach expands the domain of well-known structured light 3D imaging techniques by eliminating the use of 2D imaging sensors. Further, through the principle of Helmholtz reciprocity, the dual DMD SPI system is linked to the concept of dual photography and shown to be capable of artificial scene relighting. Although the real-time and high-speed capable aspects of SPI-ASAP were not yet implemented at the time of this project, the design of the encoding patterns, based on cyclic S-matrices, forms a link between this work and the later design of SPI-ASAP. Indeed, the method of 3D SPI explored is in principle fully compatible with SPI-ASAP, and thus representative of an important future application.

In the second part (chapter 3, derived from the publication in [11]), the SPI-ASAP platform is fully introduced, adding the elements of scanned pattern aggregation and fast compressive reconstruction to the cyclic S-matrix encoding patterns. Stemming from the high flexibility afforded to the choice of encoding pattern sizes by the DMD hardware, the system framerate and resolution were able to be optimized for the measurement of several widely ranging phenomena. The SPI-ASAP system was used to demonstrate high-speed and ultrahigh-speed imaging at framerates up to 12,000 frames-per-second (fps), with modulation rates of up to 14.1 MHz, and real-time visualization of 101×103 single-pixel video at speeds up to 100 fps. In addition to these capabilities, an application to the study of imaging in strong ambient light was explored via the high-speed imaging of the burn-out of incandescent light bulb filaments. By requiring the use of spatial and chromatic filtering, this application leveraged a unique capability of SPI systems to tolerate significant scattering, defocusing, or other optical disruption within the imaging system path preceding the single-point detector.

Finally, in the third part (chapter 4), an ongoing project involving the application of the SPI-ASAP platform to terahertz (THz) emission imaging is described, consisting of the substantially completed design of a computational terahertz chemical microscope (TCM). Based on the sensitivity of THz emission phenomena to microscopic electric field variations at the surface depletion layers of semiconductors, TCM systems have been proposed as an important diagnostic tool for the mapping of surface electrochemical potentials with applications including the visualization of chemical reactions, and the detection of biological materials including cancer cells. Unfortunately, owing to the technical limitations of devices for coherent THz detection, all TCM system designs have to date involved the use of single-point raster scanning. This project therefore aims to improve the technological maturity of TCM systems by incorporating the computational approach of SPI, specifically that implemented by the SPI-ASAP platform. Although the final construction stages of the proposed system are still currently ongoing, a minimally intrusive and experimentally verified mechanism for the modulation of THz emission is reported, substantiating the feasibility of this design to enhance the operation of existing TCM systems.

1.1 Principles of single-pixel imaging

1.1.1 Measurement model and the interpretation of image data

SPI systems fundamentally reconstruct images by integrating and recording light fields that arise from interactions with both an object under examination and a controllable modulator device. Two distinct modes of system architecture thus arise for SPI, depending on the order in which light received by the detector respectively interacts with the object and modulator. A schematic illustration of SPI under these two imaging modes, including virtual cross-sections of the imaging beam arising within each case, is shown in Fig. 1.1. The 'active mode', defined by the interaction order of modulator→object, operates with patterns of structured illumination that are projected onto the object and subsequently sampled by the detector. Conversely, the 'passive mode', defined by the interaction order of object→modulator, uses the modulator as a structured filter that may selectively pass the light field produced by the object towards the detector. The passive mode architecture may be regarded as a generalization of normal photography since, by considering the modulator and detector as a functional 'camera' module, imaging may be undertaken with illumination provided only from the object's environment. In addition, although the interactions between the modulator and object depicted in Fig. 1.1 assume transmission through the modulator and reflection from the object, it should be noted that SPI systems may involve any combination of reflective or transmissive light interactions from these components.

Despite various differences between the active and passive imaging modes when used for experiment, both forms of SPI system architecture may be described within the same theoretical framework. Mathematically, we consider SPI as the recovery of a pixelated image $\boldsymbol{x} = \left[x_1, x_2, \ldots, x_n\right]^T$ from data consisting of a set of pairs $\left(\boldsymbol{s}_i, y_i\right)$ $i = 1 \ldots m$, where the n-element vectors $\boldsymbol{s}_i$ represent pixelated encoding patterns deployed by the modulator, with the m scalars y_i representing the corresponding recordings of intensity measured by the single-pixel detector. Within SPI terminology, each $\boldsymbol{s}_i$ may be referred to as a 'masking pattern' or 'encoding pattern', while each y_i may be referred to as 'bucket signal'. Under conditions such as those shown in Fig. 1.1, each bucket signal measurement y_i occurring with the deployment of an encoding pattern $\boldsymbol{s}_i$ corresponds to an optically computed value of the inner product

$$y_i = \langle \boldsymbol{s}_i, \boldsymbol{x} \rangle = \sum_{j=1}^{n} s_{i,j}\, x_j \quad , \tag{1.1}$$

where the values $s_{i,j}$ represent the modulation input provided to the jth pixel within the ith encoding pattern. As a consequence of equation (1.1), the relationship between the deployed encoding patterns, the received bucket signals, and the unknown image can be summarized in the form of a single matrix equation

$$\boldsymbol{y} = \boldsymbol{S}\boldsymbol{x} \quad , \tag{1.2}$$

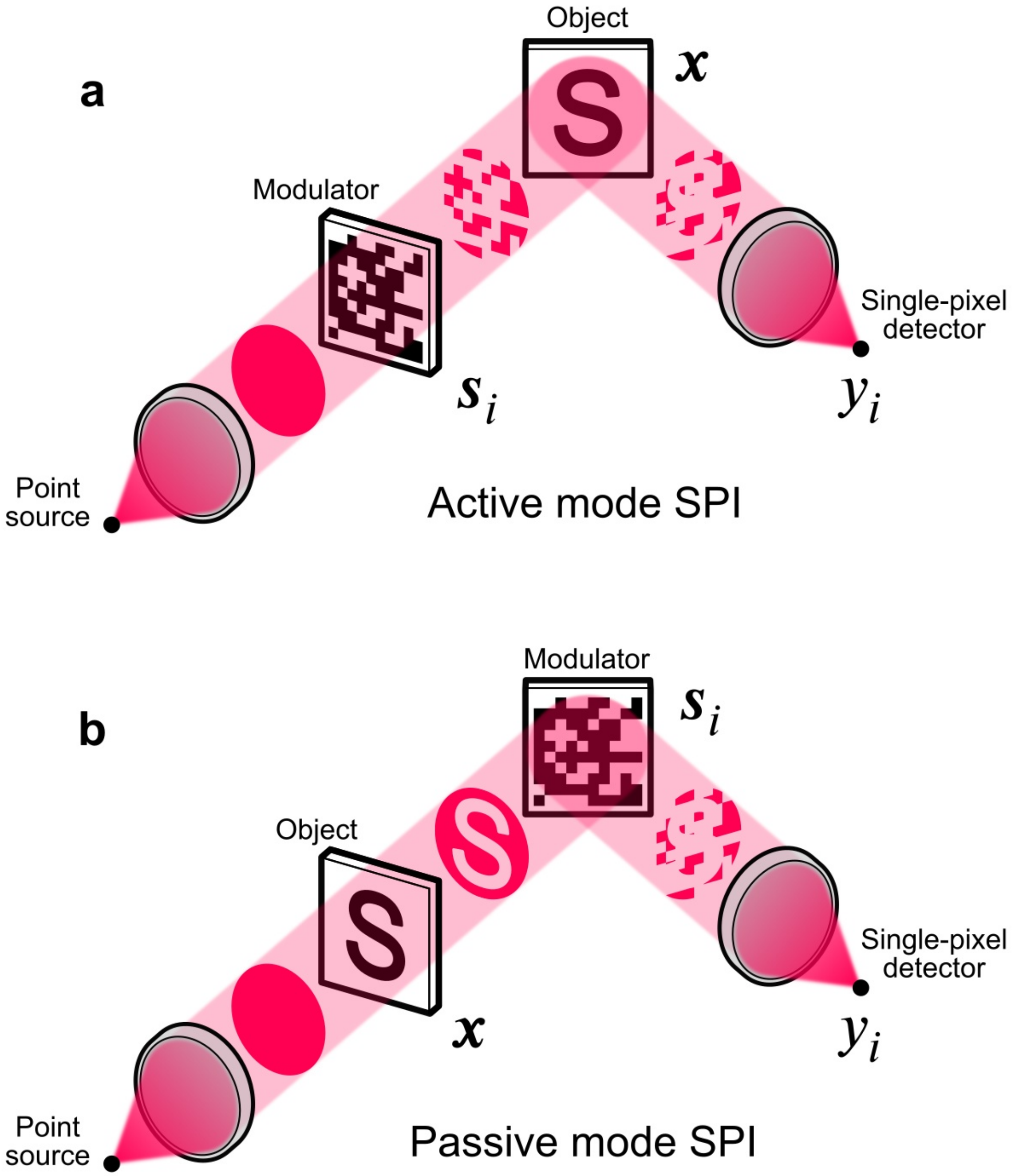

Figure 1.1 Schematic illustration of the principle of single-pixel imaging (SPI). (a) The active imaging arrangement, in which the imaging beam encounters the modulator first, and the object second. **(b)** The passive imaging arrangement, in which the imaging beam encounters the object first, and the modulator second. In either arrangement, imaging proceeds by the measurement of the optically computed inner products $y_i = \langle \boldsymbol{s}_i, \boldsymbol{x} \rangle$ for a sequence of encoding patterns $\boldsymbol{s}_i$ introduced by the modulator. Cross-section profiles of the imaging beam show the changes imparted to its spatial structure by interactions with the object and modulator, with the measurements y_i proportional to the integrated intensity of the final profile.

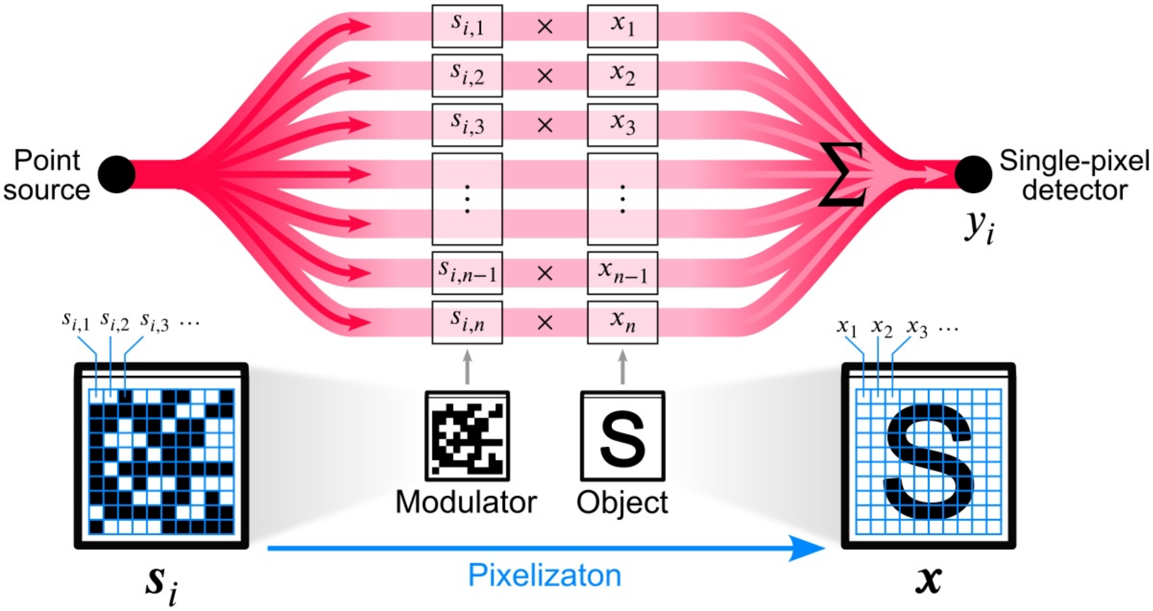

Figure 1.2 Interpretation of single-pixel imaging via light transport channels. For active mode SPI, a modulator separates the imaging beam into separate channels of light transport that are modified by interaction with the modulator and object, and subsequently summed by the single-pixel detector. Objects $\boldsymbol{x}$ recovered from experiment arise conceptually as arrays of light transport coefficients that are spatialized via the pixelization of the modulator.

where $\boldsymbol{y} = [y_1, y_2, \ldots, y_n]^T$ is a vector compiling each bucket signal, and $\boldsymbol{S}$, referred to as the 'measurement matrix' or 'sampling matrix', compiles each encoding pattern into a matrix of size $m \times n$ according to $\boldsymbol{S}_{i,j} = s_{i,j}$, i.e. with the encoding patterns $\boldsymbol{s}_i$ appearing as the rows of $\boldsymbol{S}$. Following the collection of bucket signals $\boldsymbol{y}$, recovery of the image $\boldsymbol{x}$ proceeds as the computational inverse problem of identifying satisfactory solutions to the linear system expressed by equation (1.2).

Equations (1.1) and (1.2) thus summarize the measurement model which underpins the theoretical framework for image recovery in SPI. Implicit in this framework is a linear relationship between the detector response and the effects of light transport introduced by the modulator and object. This relationship, although mathematically simple and universally assumed within SPI, imposes certain operationalizations of $\boldsymbol{x}$ and $\boldsymbol{S}$ which must be recognized in order to interpret the results arising from actual experiments. An illustration showing an interpretation of $\boldsymbol{x}$ and $\boldsymbol{S}$ as arrays of light transport coefficients is provided in Fig. 1.2. Considering the case of active mode imaging (see Fig. 1.1a), the pixelization of the modulator device serves to define channels of light transport along which the influence of the modulator and object takes place. Across each channel, the deployment of an encoding pattern by the modulator corresponds to the introduction of coefficients $s_{i,1}\ s_{i,2}\ \ldots\ s_{i,n}$ which modify the light allowed to propagate further towards the object and detector. The influence of the object is then to introduce additional coefficients $x_1\ x_2\ \ldots\ x_n$ to each channel. Finally, the detection of a bucket signal y_i corresponds to a measurement of the total light transport as a sum across channels. Although having been just carried out for active mode imaging, the above discussion, with slight modification (i.e. reversing the order of modulator and object coefficients Fig. 1.2), may also be directly applied to passive mode imaging. Importantly, within either the active or passive imaging cases, it is the intrinsic pixelization of the modulator that determines the sites of optical measurement of the object, and thus the spatial interpretation of the elements of the reconstructed object $\boldsymbol{x}$ as coefficients of light transport located within a 2D image. Interestingly, the regime of pixelization imposed by a modulator need not obey the layout of a rectangular grid, and indeed the encoding pixels may be given arbitrary shapes and sizes [12, 13]. However, even with the origins of pixelization thus explained, multiple interpretations of the values assigned within $\boldsymbol{S}$ and recovered in $\boldsymbol{x}$ are possible in general (i.e. the inclusion of units), depending on specific conventions used within the settings of an experiment. In keeping with the most common convention used within SPI research, we shall therefore interpret the values assigned to $\boldsymbol{S}$ as representing dimensionless coefficients reflecting the relative changes to light transport imposed by a given encoding pattern. Thus, for the particular example of a binary modulator as depicted in Fig. 1.1 and Fig. 1.2, elements of the matrix $\boldsymbol{S}$ would take on the values $\boldsymbol{S}_{i,j} = 0$ and $\boldsymbol{S}_{i,j} = 1$ for blocking and transparent pixels, respectively. With this convention established, the pixels of $\boldsymbol{x}$ carry the same physical units of the bucket signals, and thus depend on the particular equipment used in experiment.

As a further example to assist interpretation under these conventions, the special case may be considered in which the measurement matrix used for an SPI experiment is set equal to an identity matrix of size $n \times n$. In this case, the ith encoding pattern leads to the modulator blocking all incident light (via transport coefficients of 0) except to the channel designated by the ith pixel which is completely transmitted (via a transport coefficient of 1). As a result, we obtain $y_i = x_i$ for the inner products of equation (1.1), and thus the pixels of the recovered object may be interpreted directly as the detector responses arising from unit activation of the associated pixel of the modulator. Due to the assumptions of linearity found in equations (1.1) and (1.2), this interpretation of the values of $\boldsymbol{x}$ holds in general for arbitrary choices of the sampling matrix $\boldsymbol{S}$. Importantly, all optical effects aside from the influence of the modulator (e.g. non-uniform illumination from the light source) are thus inherited by the values recovered in $\boldsymbol{x}$, which may require additional processing (e.g. flat field correction) to obtain data of interest within a specific experiment.

1.1.2 Hadamard matrices, S-matrices, and the multiplex advantage

Central to the design of SPI systems is the choice of sampling matrix $\boldsymbol{S}$ defining the set of encoding patterns used in experiment. In the most trivial case, the choice of $\boldsymbol{S} = \boldsymbol{I}_n$ for the identity matrix of size $n \times n$, results in the direct relation $y_i = x_i$ between bucket signal and recovered image pixels. However, under the broad design assumption that $\boldsymbol{S}$ possesses an inverse, it is possible to identify measurement matrices that optimize a highly desirable property for SPI experiments: the ability to significantly suppress the influence of random noise on the quality of reconstructed images.

As a motivating example (adapted from [14]), we consider the abstract measurement problem in which a vector of four unknowns $\boldsymbol{x} = \left[x_1, x_2, x_3, x_4\right]^T$ is to be measured experimentally in the presence of random noise that originates from the apparatus used for measurement. In order to conceptualize an apparatus allowing for the elements of the measurement matrix $\boldsymbol{S}$ to be both positive and negative, we adopt the following analogy, drawn from metrology rather than optics. That is, we consider the underlying object $\boldsymbol{x}$ to be a vector of masses corresponding to a collection of objects which is to be measured using a chemical balance (i.e. a scale consisting of two symmetrical weighing pans with which unknown masses are determined through the addition of known masses to achieve balance). The selection of desirable matrices $\boldsymbol{S}$ within this framework, known as ‘weighing designs’, was extensively studied many years before the advent of SPI [14–16]. Continuing with the analogy and identifying the elements x_i as the initially unknown masses of the separate objects, a crucial observation is that placement of groups of objects on either pan of the balance scale, together with a sign convention distinguishing the pans, allows this apparatus to measure linear combinations of the masses with coefficients of $+1$ and -1 due to the balance scales generating opposite moments about the scale’s balancing pivot. Thus for example, measurement of the combination of masses $x_1 - x_2 - x_3 + x_4$ is realizable from placement of the object groups $\{x_1, x_4\}$ and $\{x_2, x_3\}$ in the left and right pans respectively, with the addition of balancing masses to the right or left pans considered respectively as yielding positively and negatively signed measurements. Due to imperfections of the apparatus however, measurements performed with the scale are influenced by additive random errors (i.e. noise), the distribution of which is assumed to be free from influences stemming from the magnitude of masses present on the scale, as well as other errors arising from measurements made at previous times. Considering the errors, denoted by e_i, to therefore be independent and identically distributed (i.i.d.) with mean $\mu = 0$ (feasible for a calibrated scale) and variance $\sigma^2 > 0$, we now consider the experiment that determines the masses $\boldsymbol{x}$ through the choice $\boldsymbol{S} = \boldsymbol{I}_n$:

$$\begin{aligned} y_1 &= x_1 + e_1 \\ y_2 &= x_2 + e_2 \\ y_3 &= x_3 + e_3 \\ y_4 &= x_4 + e_4 \end{aligned} \quad . \tag{1.3}$$

In this case, estimates of the mass of each object are obtained straightforwardly from the measurements y_i, each of which directly inherits the experimental uncertainties of the apparatus characterized by the variance σ^2 and thus standard deviation σ. Now, for a key comparison, the following invertible matrix is introduced as a template for carrying out the same weighing experiment,

$$\boldsymbol{S} = \begin{bmatrix} +1 & +1 & +1 & +1 \\ +1 & -1 & +1 & -1 \\ +1 & +1 & -1 & -1 \\ +1 & -1 & -1 & +1 \end{bmatrix} , \tag{1.4}$$

from which the following measurement equations are obtained

$$\begin{aligned} y_1 &= x_1 + x_2 + x_3 + x_4 + e_1 \\ y_2 &= x_1 - x_2 + x_3 - x_4 + e_2 \\ y_3 &= x_1 + x_2 - x_3 - x_4 + e_3 \\ y_4 &= x_1 - x_2 - x_3 + x_4 + e_4 \end{aligned} \quad . \tag{1.5}$$

Solving this system of equations for the x_i then produces the result

$$\begin{aligned} x_1 &= \frac{1}{4}\left(y_1 + y_2 + y_3 + y_4\right) + \frac{1}{4}\left(e_1 + e_2 + e_3 + e_4\right) &&= \varphi_1 + \varepsilon_1 \\ x_2 &= \frac{1}{4}\left(y_1 - y_2 + y_3 - y_4\right) + \frac{1}{4}\left(e_1 - e_2 + e_3 - e_4\right) &&= \varphi_2 + \varepsilon_2 \\ x_3 &= \frac{1}{4}\left(y_1 + y_2 - y_3 - y_4\right) + \frac{1}{4}\left(e_1 + e_2 - e_3 - e_4\right) &&= \varphi_3 + \varepsilon_3 \\ x_4 &= \frac{1}{4}\left(y_1 - y_2 - y_3 + y_4\right) + \frac{1}{4}\left(e_1 - e_2 - e_3 + e_4\right) &&= \varphi_4 + \varepsilon_4 \end{aligned} \quad , \tag{1.6}$$

where the symbols φ_i and ε_i have been introduced for brevity as the linear combinations of measurements and errors involved in each equation, respectively. Remarkably, using the computed values of $\varphi_1 \ldots \varphi_4$ as estimations for the masses $x_1 \ldots x_4$ leads to the reduction of experimental uncertainty, owing to the fact that in equation (1.6), the random errors ε_i each arise via linear combinations of the four i.i.d. random variables $e_1 \ldots e_4$ resembling arithmetic means with ±1 coefficients. Thus, the errors ε_i (each still with mean $\mu = 0$) are characterized by a variance of $\frac{1}{4}\sigma^2$ and thus a reduced standard deviation of $\frac{1}{2}\sigma$.

This example demonstrates how the careful use of apparatus can produce improvements to the accuracy of experiments; a phenomenon that arises fundamentally by generalizing the functionality of the apparatus for producing measurements of linear combinations of inputs. Although an averaging of four repeated experiments carried out according to equation (1.3) would produce an equivalent improvement to accuracy, the experiment described by equation (1.6) strikingly does not require the use of additional measurements at all. For a fixed apparatus and total number of measurements, the increase in accuracy facilitated by measurements derived from multiple simultaneous inputs is called the ‘multiplex advantage’ [14].

Owing to the linearity of the apparatus and the additive influence of noise, we may view equation (1.6) in the matrix form

$$\boldsymbol{x} = \boldsymbol{S}^{-1}\left(\boldsymbol{y} + \boldsymbol{e}\right) = \boldsymbol{S}^{-1}\boldsymbol{y} + \boldsymbol{S}^{-1}\boldsymbol{e} \quad , \tag{1.7}$$

where we have written $\boldsymbol{e} = \left[e_1, e_2, e_3, e_4\right]^T$ for the vector of random errors. The reduction of noise can be understood by examining the influence of the inverse measurement matrix $\boldsymbol{S}^{-1}$ as a linear transform that acts to modify the volume of space occupied by the distribution of the noise vector $\boldsymbol{e}$. This factor of volume change when generalized to square matrices of arbitrary size is the matrix determinant, which for invertible matrices $\boldsymbol{S}$ obeys the relationship $\det\left(\boldsymbol{S}^{-1}\right) = (\det \boldsymbol{S})^{-1}$. Thus,

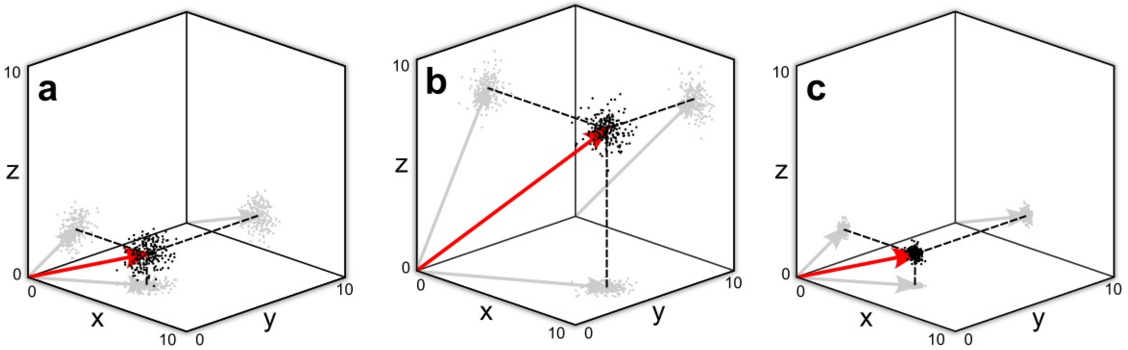

Figure 1.3 Visualization of of the multiplex advantage. **(a)** Conventional sampling of a ground truth vector (red arrow) resulting in 200 measurements influenced by noise (black dots). Other views of the same data are also shown projected as shadows onto each of the xy, yz, and zx axes and connected by dotted black lines. **(b)** Multiplexed sampling under the same conditions as in (a) resulting in 200 measurements exhibiting the same noise influence, however with an increased SNR. **(c)** Recovered ground truth estimates of the data in (b), demonstrating a reduced influence of noise as compared to (a).

selections of $\boldsymbol{S}$ which improve the accuracy of a weighing experiment should minimize $|\det \boldsymbol{S}^{-1}|$, equivalent to maximizing $|\det \boldsymbol{S}|$. By restricting the magnitude of the elements of $\boldsymbol{S}$ to obey $|\boldsymbol{S}_{i,j}| \leq 1$, the problem of identifying matrices $\boldsymbol{S}$ with maximal determinant becomes well-defined, with the solution provided by the Hadamard matrices [14, 17], defined for a given size $n \times n$ as the $\{+1, -1\}$-valued matrices satisfying

$$\boldsymbol{H}\boldsymbol{H}^T = \boldsymbol{H}^T\boldsymbol{H} = n\boldsymbol{I}_n \quad , \tag{1.8}$$

from which it follows that $\boldsymbol{H}^{-1} = \frac{1}{n}\boldsymbol{H}^T$. A Hadamard matrix therefore consists of rows which are mutually orthogonal, and whose elements all take on the maximum allowed absolute value. Stated precisely, Hadamard matrices are distinguished by the following theorem: if $\boldsymbol{H}$ is an $n \times n$ matrix with elements satisfying $|\boldsymbol{H}_{i,j}| \leq 1$, then the determinant of $\boldsymbol{H}$ obeys the inequality $|\det \boldsymbol{H}| \leq n^{n/2}$, with equality occurring if and only if $\boldsymbol{H}$ is a Hadamard matrix [17]. More properties of $\boldsymbol{H}$ include the possible values allowed for n, which must be equal to 1, 2, or 4k for k a positive integer. Although the existence of Hadamard matrices for all sizes 4k is a famous outstanding problem, a simple way to generate Hadamard matrices of order 2^k, known as the Sylvester construction, is as follows,

$$\boldsymbol{H}_1 = [1] \quad , \quad \boldsymbol{H}_2 = \begin{bmatrix} +1 & +1 \\ +1 & -1 \end{bmatrix} \quad , \quad \boldsymbol{H}_{2^{k+1}} = \begin{bmatrix} \boldsymbol{H}_{2^k} & \boldsymbol{H}_{2^k} \\ \boldsymbol{H}_{2^k} & -\boldsymbol{H}_{2^k} \end{bmatrix} \quad . \tag{1.9}$$

This construction for the case of $k = 2$ was used to generate the matrix $\boldsymbol{S}$ in equation (1.4), with the property that $\boldsymbol{S}^{-1} = \frac{1}{n}\boldsymbol{S}^T$ being used to derive equation (1.6).

As a further example and visualization of the multiplex advantage, the results of a numerical simulation using the matrix $\boldsymbol{H}_8$ derived from from the construction of equation (1.9) is presented in Fig. 1.3. Starting from a fixed ground truth vector $\boldsymbol{x}$, the results of 200 simulated non-multiplexed experiments $\boldsymbol{y} = \boldsymbol{I}_8\boldsymbol{x} + \boldsymbol{e}$ for different instances of random noise are shown in Fig. 1.3a, with the elements of the error vector $\boldsymbol{e}$ being generated independently from a normal distribution with zero mean and fixed variance. The resulting simulated measurements $\boldsymbol{y}_1 \ldots \boldsymbol{y}_{200}$ (black dots) as well as the ground truth vector $\boldsymbol{x}$ (red arrow) are visualized in 3D by using the first three elements of each vector. Next, the simulated results of 200 multiplexed experiments $\hat{\boldsymbol{y}} = \boldsymbol{H}_8\boldsymbol{x} + \boldsymbol{e}$ are similarly shown in Fig. 1.3b, with black dots representing the simulated measurements $\hat{\boldsymbol{y}}_1 \ldots \hat{\boldsymbol{y}}_{200}$ and the red arrow representing the vector vector $\boldsymbol{H}_8\boldsymbol{x}$. Finally, Fig. 1.3c shows the estimations of the ground truth derived from the data in Fig. 1.3b, with the red arrow again representing $\boldsymbol{x}$ and the black dots representing the data $\boldsymbol{H}_8^{-1}\hat{\boldsymbol{y}}_1 \ldots \boldsymbol{H}_8^{-1}\hat{\boldsymbol{y}}_{200}$. A comparison between Fig. 1.3a and Fig. 1.3b illustrates how the multiplexed measurement produces an improved signal-to-noise ratio (SNR) by facilitating the increase in magnitude of the measurement vectors relative to the magnitude of the uncertainty due to noise in the measurement apparatus. The linear transformation induced by the matrix $\boldsymbol{H}_8^{-1}$ then leaves this SNR unchanged, thus resulting in the multiplex advantage observed as the reduced size of the distribution of data points in Fig. 1.3c as compared to that of Fig. 1.3a.

Although discussed so far within context of abstract ‘weighing designs’, it is clear that the potential for utilizing the multiplex advantage exists for SPI systems which also obey noise models of the form $\boldsymbol{y} = \boldsymbol{S}\boldsymbol{x} + \boldsymbol{e}$ for random errors introduced by the single-pixel detector. However, as devices affecting coefficients of light transport, modulators used within SPI must typically impose the restriction $0 \leq \boldsymbol{S}_{i,j} \leq 1$ on the measurement matrices used for actual experiments. Despite this, for an underlying object sampled with n pixels, the full multiplex advantage of $\{+1, -1\}$-valued Hadamard matrices may still be utilized within experiments that obtain $m = 2n$ single-pixel measurements. In particular, for a given Hadamard matrix $\boldsymbol{H}$, the $\{0, 1\}$-valued matrices $\boldsymbol{H}_+ = \frac{1}{2}(1 + \boldsymbol{H})$ and $\boldsymbol{H}_- = \frac{1}{2}(1 - \boldsymbol{H})$ may be used to collect the measurements $\boldsymbol{y}_+ = \boldsymbol{H}_+\boldsymbol{x}$ and $\boldsymbol{y}_- = \boldsymbol{H}_-\boldsymbol{x}$, from which the vector of differential measurements can be seen to satisfy

$$\boldsymbol{y} \equiv \boldsymbol{y}_+ - \boldsymbol{y}_- = \boldsymbol{H}_+\boldsymbol{x} - \boldsymbol{H}_-\boldsymbol{x} = \left(\boldsymbol{H}_+ - \boldsymbol{H}_-\right)\boldsymbol{x} = \boldsymbol{H}\boldsymbol{x} \quad , \tag{1.10}$$

and thus may be used to recover $\boldsymbol{x}$ via the Hadamard matrix inverse. Unfortunately, this approach, although still widely popular within SPI [18–21], has the downside of doubling the number of measurements, thus lowering the overall efficiency of image acquisition.

The largest multiplex advantage, i.e. matrix determinant, available from measurement matrices $\boldsymbol{S}$ satisfying $0 \leq \boldsymbol{S}_{i,j} \leq 1$ is therefore of great practical interest. Fortunately, such optimal matrices, known as S-matrices[1], have also been extensively characterized, sharing a close relationship with Hadamard matrices [14, 17, 23]. Given a Hadamard matrix $\boldsymbol{H}$ of size $(n+1) \times (n+1)$, an S-matrix

---

[1] The name ‘S-matrix’ derives from the fact that all distinct pairs of rows from an $n \times n$ S-matrix, when considered as points in an n-dimensional space, are separated by equal Euclidean distances and hence form a geometric object analogous to an equilateral triangle in 3D space known as a *simplex* [14, 22].

may always be obtained by first writing $\boldsymbol{H}$ in the 'normalized' form

$$\boldsymbol{H} = \begin{bmatrix} 1 & 1 & \dots & 1 \\ 1 & & & \\ \vdots & & \boldsymbol{G} & \\ 1 & & & \end{bmatrix} , \tag{1.11}$$

which can always be accomplished by multiplying appropriate rows or columns of a Hadamard matrix by -1, a step which always produces another Hadamard matrix satisfying equation (1.8). From the matrix $\boldsymbol{G}$, an S-matrix of size $n \times n$ is then obtained as

$$\boldsymbol{S} = \frac{1}{2}(\boldsymbol{J} - \boldsymbol{G}) \quad , \tag{1.12}$$

where $\boldsymbol{J}$ is defined as the $n \times n$ matrix consisting of all 1s (i.e. $\boldsymbol{J}_{i,j} = 1$). From this procedure it can be shown that $|\det \boldsymbol{S}| = 2^{-n}|\det \boldsymbol{H}|$ and, by recognizing the reversibility of each step, that $\boldsymbol{S}$ must possess a maximal determinant [17]. Finally, by combining equations (1.8), (1.11) and (1.12), it follows that the inverse of an $n \times n$ S-matrix can be written explicitly as

$$\boldsymbol{S}^{-1} = \frac{2}{n+1}\left(2\boldsymbol{S}^{T} - \boldsymbol{J}\right) \quad . \tag{1.13}$$

S-matrices, being $\{0, 1\}$-valued and affording a maximal multiplex advantage, are thus readily applicable for SPI, especially when using binary modulation devices such as DMDs. As a final specialization towards the later presentation of SPI-ASAP, we note the particular usefulness of 'cyclic S-matrices' which possess a highly regular structure, determined by

$$\boldsymbol{S}_{i,j} = \boldsymbol{S}_{1,M(i+j)} \quad , \tag{1.14}$$

where $i, j = 1 \dots n$ and the function $M(x) = ((x-1) \bmod n) + 1$ performs 1s-based modulo (i.e. wraps the set of integers to the range $1 \dots n$). These matrices are therefore entirely determined from the information given in their initial row, with all subsequent rows being found by iterations of left-wise shifting of elements with circular replacement. Three known methods of generic construction are known for cyclic S-matrices, each of which allowing for the generation of a binary sequence determining the initial row. Across these methods, the possible sequence lengths are $n = 2^k - 1$ for any positive integer k, $n = p$ for any prime p, or $n = pq$ for any pair of twin primes p and $q = p + 2$ [14]. Cyclic S-matrices, as will be fully described in chapter 3, play a fundamental role in the operation of SPI-ASAP, with the cyclic property contributing a highly useful means for the compact display of multiple encoding patterns simultaneously using a DMD. Aside from this, other attractive computational properties of cyclic S-matrices may be noted. As a consequence of cyclic structure, all encoding patterns determined by a cyclic S-matrix may be determined starting from the specification of the initial pattern, with all subsequent patterns arising by the iterative application of a permutation to the pixel order. Moreover, with reference to equation (1.13), it can be seen that the inverse S^{-1} of a cyclic S-matrix is also cyclic, with computation of the initial row of the inverse matrix, up to a scaling factor, amounting to merely the replacement of 0s with -1s in the initial row of S. These properties dramatically lower the storage and computational resources required for the use of cyclic S-matrices in SPI, while also opening up the opportunity for display hardware to entirely generate sequences via embedded processing. Finally, multiplication of a vector by a full-rank cyclic S-matrix can be equivalently described as an operation of discrete convolution, opening up opportunities for reconstruction algorithms leveraging the discrete Fourier transform (DFT) [13].

The ability for cyclic measurement matrices to form compact aggregated expressions of their encoding patterns is illustrated in Fig. 1.4 for the case of an example cyclic S-matrix of order $n = 35$. Beginning from a binary sequence determining its initial row (Fig. 1.4a), the entire content of the measurement matrix then follows from the application of equation (1.14), leading to the appearance of distinct diagonal bands (Fig. 1.4b). From this design, individual encoding patterns deployed in experiment arise from the rows of this matrix subjected to a process of 2D reshaping. Although in general the reshaping procedure need not adhere to equally sized encoding pixels nor a rectangular grid layout [12, 13], the usually adopted choice row-major ordering as the convention for 2D reshaping leads to encoding patterns such as those depicted in Fig. 1.4c. Importantly, owing to the measurement matrix's cyclic structure, the application of row-major reshaping results in a significant overlap between the contents of encoding patterns formed from adjacent rows. By exploiting this overlap, various schemes for encoding pattern aggregation (shown in Fig. 1.4d–f) may be used to increase the efficiency of encoding pattern deployment, either through the construction of physical masks of a reduced size, or, as is the case with SPI-ASAP, the efficient display of multiple patterns simultaneously via DMD.

As a way to conclude the material of this section, an experimental demonstration of the multiplex advantage using cyclic S-matrices is shown in Fig. 1.5, comparing the effect of sampling strategy on the influence of noise in images recovered from two actual SPI experiments. In each case, active mode SPI was performed at a resolution of 137×139 pixels with modulation provided by a DMD. A continuous wave (CW) laser with a wavelength of 671 nm and an output power of 200 mW served as the illumination source. In the first case (Fig. 1.5a), sampling was determined using an identity matrix which produced encoding patterns bearing single points of illumination. The resulting deployment of these patterns produced a 'flying spot' which scanned the object in a manner analogous to a raster scan. In the second case (Fig. 1.5d), sampling was determined using a cyclic S-matrix of order $n = 19{,}043$. Each experiment was carried out under identical conditions using the same equipment and settings. A comparison of the photographs shown in Fig. 1.5a and Fig. 1.5d, illustrates the higher overall illumination brightness achieved using multiplexing, which in the case of cyclic S-matrices resulted in 50% of all pixels supplying illumination throughout the experiment. This higher optical throughput resulted in a significantly improved SNR as seen in the raw data from the cyclic S-matrix experiment (Fig. 1.5e), in stark contrast to the corresponding data from the identity matrix experiment (Fig. 1.5b) which, owing to very low SNR, appeared equally informative to data obtained with the illumination provided by the laser completely blocked (Fig. 1.5c). Applying

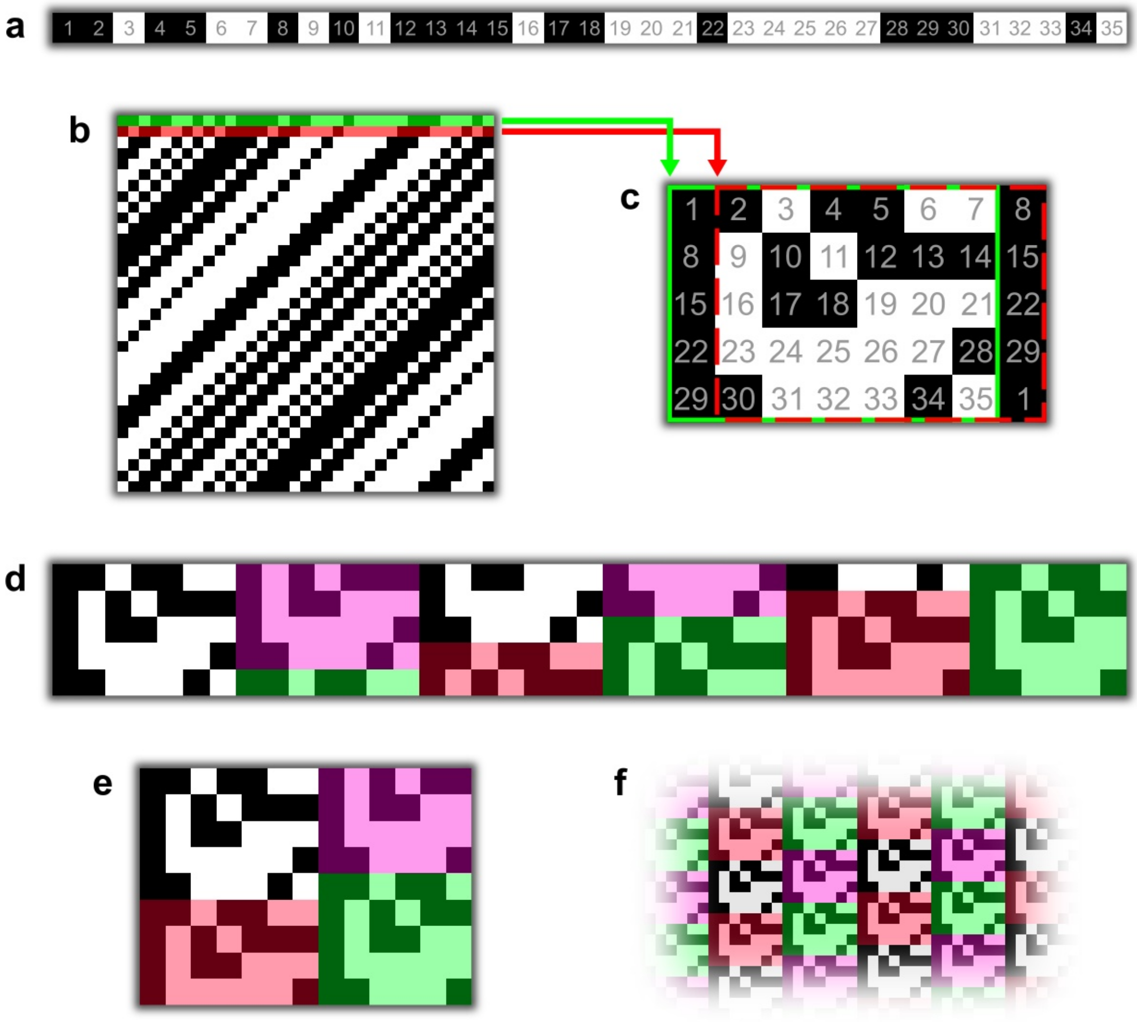

Figure 1.4 Aggregation properties of cyclic measurement matrices. **(a)** Initial row of an example cyclic S-matrix of order $n = 35$, with individual elements numbered. **(b)** The complete cyclic S-matrix corresponding to the binary sequence in (a). Green and red colors are used to highlight the first and second rows, respectively. **(c)** 2D encoding patterns of size 5×7 formed from the rows of the encoding matrix according to row-major ordering. As shown by the green and red highlighting, the reshaping process results in significant overlap between encoding patterns formed from consecutive rows. **(d)** A design of size 5×41 (205 elements) aggregating all possible cyclic encoding patterns formed by continuing the overlap scheme illustrated in (c). Color tinting is used to highlight copies of the encoding pattern formed by reshaping the initial row in (a). **(e)** A more compact aggregation design of size 9×13 (117 elements) also encompassing all the patterns in (d) with color tinting also used to highlight copies of the initial encoding pattern. **(f)** A more general scheme in which copies of the initial encoding pattern are used to tile the plane (color tinting identical to (d) and (e)). All aggregation schemes, including those of (d) and (e), may be identified with particular subsets of this tiling.

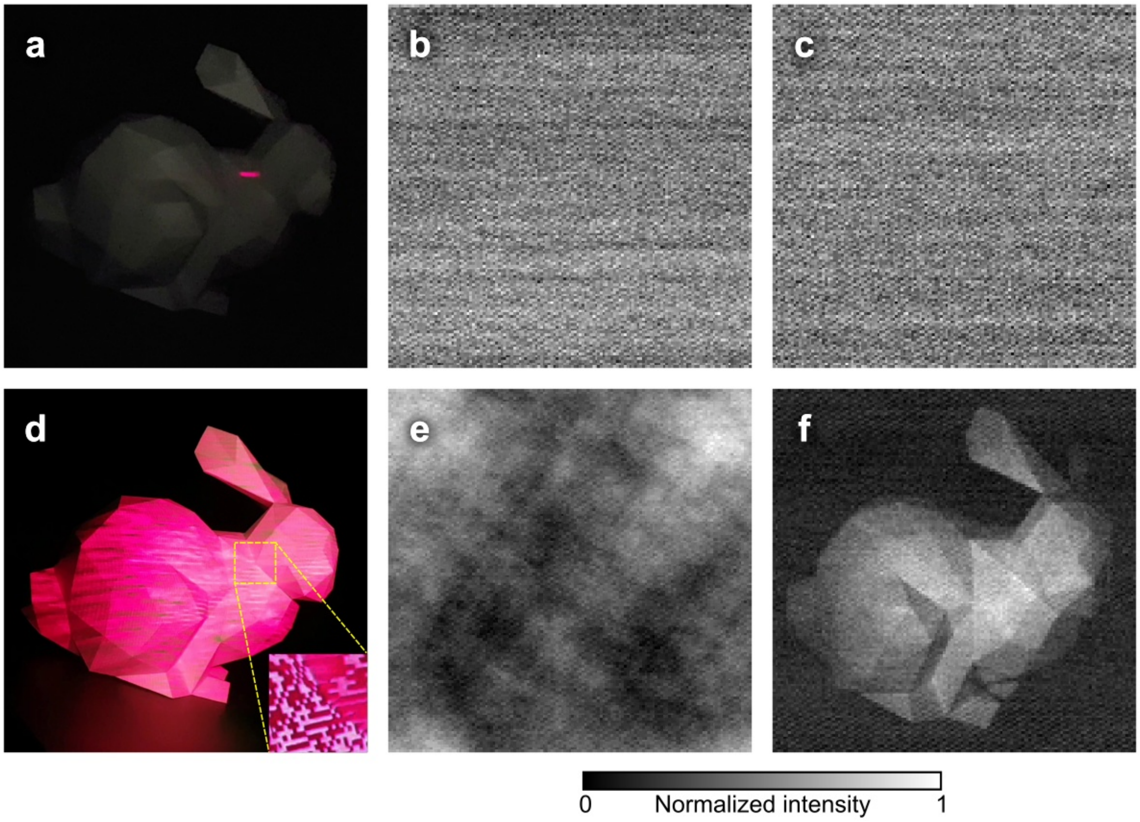

Figure 1.5 Experimental demonstration of the multiplex advantage. **(a)** Photograph of an object (a low-poly paper sculpture of the Stanford bunny) undergoing active mode SPI with sampling carried out according to an identity matrix. The resulting encoding patterns (following row-major reshaping) produced a 'flying spot' of illumination which travelled across the object from left to right. **(b)** Raw data (137×139) produced from the experiment in (a), consisting of the detector values obtained when a corresponding pixel was illuminated by the flying spot. **(c)** Raw data produced from the experiment in (a) with laser illumination blocked, thus illustrating the noise floor against which the measurements in (b) took place. **(d)** Photograph of the object undergoing active mode SPI with measurement sampling determined by a cyclic S-matrix. **(e)** Raw data (137×139) produced from the experiment in (d), colorized the same way as (b) and (c), with values corresponding to the same order of deployment as in the experiment in (a). **(f)** Recovered image obtained using the data in (e) together with the inverse of the cyclic S-matrix used for measurement. No spatial filtering or additional processing was applied to data presented in this figure.

the cyclic S-matrix inverse to the data in Fig. 1.5e then produced the image shown in Fig. 1.5f. The multiplex advantage for the cyclic S-matrix used in this experiment is thus dramatically visible from the comparison of Fig. 1.5b and Fig. 1.5f which, if experimental noise were absent, would have produced equivalent images.

1.1.3 Algorithms for single-pixel image reconstruction

Closely linked to the selection of measurement matrices in SPI is the choice of computational approach used to recover images. Although the number of algorithms having been proposed for SPI reconstruction is large and still growing [5], for the problem of recovering an n-pixel image from a set of m single-pixel measurements, a broad categorization of these approaches may be taken according to the three cases $m > n$, $m = n$, or $m < n$, corresponding to measurement matrices for which equation (1.2) takes the form of an over-determined, exactly determined, or under-determined linear system, respectively. In broad terms, the simplest and most direct reconstruction algorithm arises when both $m = n$ and the linear independence of the encoding patterns occurs, allowing the measurement matrix $\boldsymbol{S}$ to possess an inverse $\boldsymbol{S}^{-1}$ and thus for $\boldsymbol{x}$ to be recovered directly via $\boldsymbol{x} = \boldsymbol{S}^{-1}\boldsymbol{y}$. The considerations of multiplex advantage already discussed apply directly to this case, with the best choices of $\boldsymbol{S}$ corresponding to either Hadamard matrices or S-matrices which are always invertible.

Next in terms of sophistication are cases where $m > n$ in which, although the existence of a unique solution to equation (1.2) may not exist, the excess of data may still enable the accurate reconstruction of images from closed form expressions. Two popular approaches for over-determined SPI reconstruction are as follows. First, the recovery of $\boldsymbol{x}$ may be undertaken as the least squares solution to $\boldsymbol{y} = \boldsymbol{S}\boldsymbol{x}$, i.e. as the vector which solves the optimization problem

$$\arg\min_{\boldsymbol{x}} \|\boldsymbol{S}\boldsymbol{x} - \boldsymbol{y}\|_2^2 \qquad \text{subject to} \qquad \boldsymbol{S}\boldsymbol{x} = \boldsymbol{y} \ , \tag{1.15}$$

where the notation $\arg\min_{\boldsymbol{x}}(\cdot)$ denotes an algorithm that returns a value of the variable $\boldsymbol{x}$ that minimizes the argument, and $\|\boldsymbol{z}\|_2 \equiv \left(\sum_{j=1}^{n} z_i^2\right)^{1/2}$ denotes the euclidean ℓ_2-norm. Subsequently, the solution to equation (1.15) may be then calculated from the closed-form expression [5],

$$\boldsymbol{x} = \left(\boldsymbol{S}^T\boldsymbol{S}\right)^{-1}\boldsymbol{S}^T\boldsymbol{y} \ . \tag{1.16}$$

Second, if a large number of encoding patterns are used (i.e. $m \gg n$) and the individual encoding pixels $\boldsymbol{S}_{i,j}$ are statistically uncorrelated both within and across the set of encoding patterns, then recovery may proceed using ‘ghost imaging’, i.e. statistical correlations of the bucket signals with the corresponding encoding patterns [24, 25],

$$\tilde{\boldsymbol{x}} = \langle \left(y_i - \langle y_i \rangle\right) \boldsymbol{s}_i \rangle \ , \tag{1.17}$$

where $\langle\cdot\rangle \equiv \frac{1}{m}\sum_{i=1}^{m}(\cdot)$ denotes the statistical average taken over the set of m bucket signals and encoding patterns used in the experiment (and $\tilde{\boldsymbol{x}}$ has been written to reflect the fact that this method only recovers $\boldsymbol{x}$ up to a possible constant multiple and offset). Although a wide range of matrices $\boldsymbol{S}$ are compatible with the least squares solution for the $m > n$ case, the most compatible choices for $\boldsymbol{S}$ when $m \gg n$ correspond to random matrices, from which large sets of encoding patterns may be easily generated in order to obtain satisfactory convergence from equation (1.17).

For SPI systems oriented towards performance however, the cases of greatest practical interest and technical difficulty are those with $m < n$, for which the linear system of equations in (1.2) becomes under-determined, and thus potentially accepting of infinitely many solutions. Within this case, algorithms based on the mathematical theory of compressed sensing (CS) have seen wide adoption, with SPI providing some of the first historical applications of CS algorithms [3, 4, 26]. Towards reconstruction problems within SPI, CS algorithms possess two particularly attractive properties. First, CS algorithms in practice are often able to recover useful images from conditions in which the compression ratio, defined as m/n, may be as small or smaller than 0.1 [4, 27]. Second, CS algorithms exhibit a wide flexibility with respect to the choices of sensing matrix $\boldsymbol{S}$ compatible with reconstruction, with random sensing matrices in particular exhibiting a theoretically universal compatibility, while also embodying a choice which is simple to use in practice [8, 28].

In general, CS algorithms recover estimates of $\boldsymbol{x}$ through the introduction of additional constraint functions, known as ‘regularizers’, which encode additional domain-specific assumptions about the properties expected of the structure of objects $\boldsymbol{x}$ as vectors residing within the hyperplane defined by the set of vectors satisfying the measurement matrix equation $\boldsymbol{y} = \boldsymbol{S}\boldsymbol{x}$. Stated in the form of optimization problems, the most widely used CS algorithms obey the forms

$$\arg\min_{\boldsymbol{x}} f(\boldsymbol{x}) \qquad \text{subject to} \qquad \boldsymbol{S}\boldsymbol{x} = \boldsymbol{y} \ , \tag{1.18}$$

$$\arg\min_{\boldsymbol{x}} f(\boldsymbol{x}) \qquad \text{subject to} \qquad \|\boldsymbol{S}\boldsymbol{x} - \boldsymbol{y}\|_2 \leq \epsilon \ , \tag{1.19}$$

$$\arg\min_{\boldsymbol{x}} \frac{1}{2}\|\boldsymbol{S}\boldsymbol{x} - \boldsymbol{y}\|_2^2 + \lambda f(\boldsymbol{x}) \ , \tag{1.20}$$

where the function $f(\boldsymbol{x})$ denotes the chosen regularizer, and the numbers ϵ and λ, selected from the range $[0, \infty)$, are parameters that may restrict the solution search space, or balance the impact of the regularizer against a cost function enforcing agreement with the data, respectively. Common regularizers include the ‘sparsity constraint’ $\|\boldsymbol{\Phi}\boldsymbol{x}\|_1$ and ‘total variation’ TV$(\boldsymbol{x})$, in which $\boldsymbol{\Phi}$ is a matrix of an orthogonal transform such as the discrete Fourier transform (DFT) or discrete cosine transform (DCT), $\|\boldsymbol{z}\|_1 \equiv \sum_{j=1}^{n}|z_i|$ denotes the ℓ_1-norm, and the total variation function TV$(\boldsymbol{x})$ for 2D rectangular images $\boldsymbol{x}$ of dimensions $a \times b$ is defined as

$$\text{TV}(\boldsymbol{x}) = \sum_{i=1}^{a-1}\sum_{j=1}^{b-1}\sqrt{[\boldsymbol{x}(i+1,j) - \boldsymbol{x}(i,j)]^2 + [\boldsymbol{x}(i,j+1) - \boldsymbol{x}(i,j)]^2} \ , \tag{1.21}$$

where we write $\boldsymbol{x}(i, j)$ to indicate the value of the pixel of $\boldsymbol{x}$ with coordinates (i, j). In particular, equations (1.18) and (1.19) when used with the sparsity constraint are known as 'basis pursuit' and 'basis pursuit with inequality constraints', respectively [3, 8, 29]. Popular implementations for equations (1.18) and (1.19) when used with the total variation regularizer include the software libraries ℓ_1-MAGIC [30], NESTA [29], and TVAL3 [31]. Finally, a popular solver for generic optimization problems of equation (1.20) is known as TwIST [32], and is also frequently used with the total variation regularizer.

A commonality of all CS algorithms adhering to the forms above, is that they are each solved in practice within the framework of convex optimization, which approximates solutions to the stated regularized problems by iteratively improving upon an initial solution guess and continuing until a convergence condition is satisfied [5, 7, 32]. Unfortunately, the iterative nature of CS algorithms stemming from the use of complex regularizers, while enabling high robustness and flexibility, also produces their most significant drawback in the form of large computational overheads, with the number of iterations required for convergence strongly dependent on the data input to the algorithm. However, by setting aside the use of regularizers and optimization, much faster non-iterative reconstruction methods are possible, albeit at the cost of requiring stronger assumptions of the underlying data. A particularly simple approach that may be seen as a simplified form of sparsity constraint regularization is known as 'basis scanning'. In this approach, the underlying data $\boldsymbol{x}$ is assumed to be 'sparse' with respect to the encoding patterns of a fixed invertible measurement matrix $\boldsymbol{S}$, meaning that the bucket signals corresponding to specific encoding patterns of $\boldsymbol{S}$ would be of negligible magnitude if measured, and thus may be taken to be zero. Although imposing a significantly stronger assumption than that of the sparsity constraint regularizer, the sparsity of most realistic images is nonetheless a widely recognized property of several orthogonal transformations such as the DFT, DCT, and Hadamard transform [27, 33–35]. Thus, under the assumption of pattern-specific sparsity, only a subset of the encoding patterns determined by $\boldsymbol{S}$ need be deployed during experiment corresponding to the bucket signals with highest expected magnitude. By substituting zeros for the values of all bucket signals not otherwise sampled, a fully determined linear system $\boldsymbol{y} = \boldsymbol{S}\boldsymbol{x}$ is still obtained from an experiment obeying $m < n$, allowing for the non-iterative recovery of $\boldsymbol{x}$ via $\boldsymbol{x} = \boldsymbol{S}^{-1}\boldsymbol{y}$. Finally, whereas the sparsity assumptions of standard basis scanning must assume a fixed set of excluded encoding patterns, in cases where SPI measurements are taken repeatedly such as in video imaging, the excluded set of encoding patterns may be continuously updated based on the sparsity information from previously obtained imagery. By updating the set of deployed encoding patterns via selective randomization, the desired adaptive behavior can be achieved, resulting in an algorithm known as 'evolutionary compressed sensing [36, 37].

Building off of the optimization problem of equation (1.18), the potential for non-iterative compressive reconstruction may also be realized by the selection of specific regularizers amenable to closed-form solution. The least-squares optimization approach of equation (1.15), while consistent with this strategy, is unfortunately incompatible with compressive reconstruction where $m < n$ due to the fact that the solution given by equation (1.16) requires $\boldsymbol{S}^T\boldsymbol{S}$ to possess a matrix inverse;

a situation only possible with $m \geq n$ [5]. To overcome this problem, a recent approach known as 'Fourier domain regularized inversion' has proposed the use of a regularizer based on the ℓ_2-norm and discrete filter convolution [9]. In particular, for the optimization problem given by

$$\underset{\boldsymbol{x}}{\arg\min}\ \|\boldsymbol{x} * \boldsymbol{h}\|_2^2 \qquad \text{subject to} \qquad \boldsymbol{S}\boldsymbol{x} = \boldsymbol{y}\ , \tag{1.22}$$

where $\boldsymbol{x}*\boldsymbol{h}$ denotes discrete circular convolution, with the filter $\boldsymbol{h}$ chosen as a penalty for undesirable features in the reconstruction such as noise or discontinuities. By expressing the regularizer in the form $\|\boldsymbol{x} * \boldsymbol{h}\|_2^2 = \boldsymbol{x}^T\boldsymbol{C}\boldsymbol{x}$ for an invertible and circular matrix $\boldsymbol{C}$ determined by $\boldsymbol{h}$, the solution to the optimization problem (1.22) is given

$$\boldsymbol{x} = \boldsymbol{C}^{-1}\boldsymbol{M}^{\dagger}\left(\boldsymbol{M}\boldsymbol{C}^{-1}\boldsymbol{M}^{\dagger}\right)^{-1}\boldsymbol{y} \tag{1.23}$$

where $\boldsymbol{M}^{\dagger}$ denotes the conjugate transpose of $\boldsymbol{M}$. Within this framework, $\boldsymbol{h}$ may be chosen so as to combining several different kinds of penalty, with examples in practice including penalties for high spacial frequencies and large discrete gradients [9].

Finally, the application of machine learning techniques represents an emerging development within SPI reconstruction. Recently, the use of deep convolutional neural networks (CNNs) has been proposed for improving the quality of image reconstructions obtained from statistical ghost imaging [38]. By functioning as domain-specialized filters for noise reduction and feature enhancement, deep CNNs allowed for the number of measurements to be dramatically reduced in SPI experiments, thus transforming the computationally simple ghost imaging algorithm normally used with $m \gg n$ into an algorithm capable of satisfactory performance even for the compressive case with $m < n$. Whereas SPI reconstruction methods must typically rely on their users for the selection of domain appropriate sensing matrices, certain machine learning architectures can allow for sensing matrices to be optimized simultaneously alongside a network used to reconstruct their measurements. Within this direction, one recent work has demonstrated the use of a deep convolutional auto-encoder network (DCAN) for the simultaneous training of both an SPI reconstruction model and an optimized set of binary encoding patterns [39]. With the optimized encoding patterns deployed via DMD modulation, this approach was able to achieve satisfactory reconstructions from datasets with compression ratios as low as $m/n = 0.02$. Building from this result, another recent work has proposed the use of recurrent neural networks (RNNs) for SPI reconstruction and encoding pattern optimization, with the resulting models requiring fewer training parameters than CNNs, while also showing an improved robustness to noise [40].

The advantages of trained networks for image reconstruction in SPI include their deterministic reconstruction times, relatively low computational overheads, and high performance due to their compatibility with execution on parallelized computer hardware. However, machine learning techniques possess two significant disadvantages. First, a substantial investment in computational resources and example data is always required for the training of sophisticated networks, with the case of SPI reconstruction requiring the use of large sets of imagery (with sizes typically on the order of 10–100 thousand) considered to be representative of the data to be processed in actual experiments. Although the availability of image training datasets applicable to the processing of photographic imagery has become widespread, such data may not exist for SPI which targets specific experimental applications. Second, the performance of many machine learning models is strongly dependent on the exact matching of experimental conditions to the formatting of data imposed by the training infrastructure. As a result, models targeting SPI reconstruction, once trained, are unable to exhibit flexibility with regards to experimental parameters such as image resolution and number of measurements.

1.2 High-speed modulation techniques for single-pixel imaging

Within the vast majority of cases, SPI systems make use of consumer hardware for spatial light modulation, with the technological development of new modulation approaches constituting only a tiny fraction of SPI research. As a result, such hardware has continued to define the technological limitations facing the development of high-speed and real-time capable SPI systems. Today, mature single-chip packaged consumer hardware for spatial light modulation has been achieved with multiple technologies. As has already been observed, the dominant modulation technology used within SPI is the digital micromirror device (DMD), having the advantages of high resolution, high speed, electronic control, and wide availability. The active surfaces of DMDs are arrays of millions of independent micro-electromechanical systems (MEMS), each consisting of a micrometer-scale flat mirror and an integrated compliant hinge that allows the mirror to be tilted between two rest positions through the application of electrostatic forces [41]. DMDs thus function as programmable binary reflection gratings that in practice can perform binary modulation at speeds up to several tens of kHz. Although no other consumer-available technologies currently exist which are able to compete with the modulation speeds of DMDs, the binary and amplitude-only nature of DMD modulation requires the use of holography in order to address applications requiring the continuous modulation of both amplitude and phase. In contrast to this limitation, modulator hardware making use of liquid crystal technology is capable of the direct and continuous control of phase, and may be used for the manufacturing of modulator devices that operate in either reflection or transmission. In construction, liquid crystal spatial light modulators (LC-SLMs) consist of an array of electrodes placed in contact with a layer of nematic liquid crystal, the birefringence of which is controlled via the application of voltages to the electrodes [26]. However, in comparison with the capabilities of DMDs, the speed of LC-SLMs is typically limited to below 100 Hz, precluding them from applications targeting speed performant SPI systems. Nonetheless, a MEMS architecture for spatial phase modulation capable of similar modulation speed to DMDs has been recently introduced [42], with commercial availability anticipated in the near future.

While the limitations of consumer modulation hardware have continued to define the acquisition speeds of most SPI systems below high-speed or real-time operation, a number of recent developments have pushed this goal closer by substituting the use of DMDs with other custom-made modulators and light sources. One recent approach, using a multi-pixel illumination module of 32×32 light emitting diodes (LEDs), has achieved a pattern deployment rate of 3.13 MHz and a CS-assisted imaging rate of 25,000 frames per second (fps) [43, 44]. In contrast to DMDs which rely on the physical actuation of their MEMS mirror components, this approach derives a significant speed advantage from the very short switching times of LEDs which can be compatible with modulation at rates exceeding 10 MHz. In order to derive the precise timing of signals, the illumination module was controlled using a field-programmable gate array (FPGA) that allowed for the control logic of the LED array to be flexibly programmed, while still allowing for operation at the same speeds as a purpose-built integrated circuit. However, owing to the limited number of controllable signal outputs available on the FPGA, the circuitry of the LED array was not compatible with the display of arbitrary modulation patterns, with experiments relying instead on the display of fixed-resolution Hadamard basis patterns. As a more critical disadvantage, SPI carried out with the use of LED illumination is fundamentally incompatible with imaging applications relying on passive detection [45], or the use of specialized light sources or detectors [18, 46].

Another long-established approach for enhancing SPI modulation speeds has been the use of patterned physical masks designed for mechanical motion at high speeds. In this category, the most performant systems have used fast rotating disks placed in the imaging beam as the pattern delivery mechanism, with optimal designs allowing for the deployment of distinct encoding patterns from a rotational shift of only one pattern pixel. While this approach has been well-known in the field of THz and millimeter-wave SPI for over a decade [47–52], the most recent development using visible-band detection has achieved a pattern projection rate of 2.4 MHz, corresponding to the non-compressive recovery of 101×103 pixel images at 72 fps [13]. In another study, an imaging speed of 100 fps was achieved assisted by CS and optimization-based image reconstruction, although with a reduced frame size of 32×32 pixels [53]. However, especially when compared to DMD modulation, the use of physical masks often increases these systems' cost and complexity, while substantially decreasing flexibility. The inherent trade-off between pixel-count and pixel size for fixed disk dimensions, for example, means that higher resolution must come at the cost of increased precision and difficultly in manufacturing. In addition, when encoding pixel sizes reach the dimensional accuracy limits of pattern manufacturing, the use of auxiliary hardware, such as synchronized piezo-controlled steering mirrors [13], may become essential in order to compensate for systematic defects such as pattern non-concentricity.

1.3 Dual Photography and Fringe Projection Profilometry

In chapter 2, an approach to SPI-based three-dimensional (3D) imaging is presented that incorporates two existing techniques: a method of digital image synthesis known as dual photography, and a method of 3D imaging known as fringe projection profilometry (FPP). At the heart of chapter 2's results is a conceptual link that allows for fringe shifting techniques to not only carry out 3D imaging, but also implement a special case of dual photography in a highly efficient manner. In view of this upcoming material, the present section thus aims to provide an introduction to the techniques of dual photography and FPP, while also prioritizing the conceptual link that will be further built upon in chapter 2.

1.3.1 Dual Photography

As discussed in section 1.1.1 and presented in Fig. 1.2, the data recovered from an SPI experiment can be interpreted as an array of light transport coefficients representing the single-pixel detector responses arising from the unit activation of the pixels of the modulator. SPI, when viewed as a methodology of light transport measurement, is thus specialized for the capture of such light transport coefficients in a many-to-one fashion, where each coefficient (i.e. each pixel in the recovered images) represents light transport between a pixel of the modulator and the single-pixel detector. In dual photography however, the role of a single-pixel detector is filled instead by a digital camera with a multi-pixel sensor, with illumination provided by a digital projector serving as an active mode source of structured light patterns. In this way, dual photography extends the concept of light transport measurement in SPI, while generalizing it for the use of multi-pixel detectors. This generalization, while not compatible with the aims of SPI as a technology for addressing the engineering shortcomings of multi-pixel sensors, nonetheless allows dual photography experiments to record datasets far richer than those of SPI, fully capturing light transport in the many-to-many case for multi-pixel light sources and detectors. By analyzing such complete light transport data for a given scene, it is possible to not only synthesize images taken from the perspective of non-imaging devices (i.e. modulators) analogously to SPI, but to also introduce hypothetical patterns of apparent illumination to the recovered images; a capability known as scene relighting. Although hypothetical, the radiometric accuracy of these synthesized images is assured by the principle of Helmholtz reciprocity which guarantees the radiometric equivalence of light transport under the exchange of point sources and detectors [54]. Remarkably, images synthesized via scene relighting can capture complex light transport effects such as mirrored reflections, refractions, caustics, and scattering from diffuse surfaces [55].

In a dual photography experiment, the essential equipment consists of a digital projector and camera, with light transport being completely determined by the acquisition of energy transfer coefficients for each pair of camera and projector pixels. The meaning of these coefficients is described as follows. For a camera containing a focal plane array sensor with n_c pixels, we can associate digital images captured by the camera with n_c-element vectors $\boldsymbol{c}$ whose elements represent the response of each camera pixel to the light received from a scene. Similarly, for a projector with a display field consisting of n_p pixels we may associate an n_p-element illumination vector $\boldsymbol{p}$ whose elements represent the input brightness that each pixel delivers to the scene observed by the camera.

The response of the ith camera pixel due to the illumination of the jth projector pixel is therefore linearly proportional to the projector pixel's brightness with the coefficient being determined by the possibly complicated properties of the scene geometry. This linearity allows these transport coefficients to be arranged into the compact matrix equation:

$$\boldsymbol{c} = \boldsymbol{T}\,\boldsymbol{p} \quad , \tag{1.24}$$

where the vectors $\boldsymbol{c}$ and $\boldsymbol{p}$ represent the pixels comprising the camera image and projector illumination field respectively, and the matrix $\boldsymbol{T}$, known as the light transport matrix (LTM), stores the transport coefficient between the ith camera pixel and jth projector pixel as T_{ij}.

In the context of dual photography and the formalism of the LTM, the meaning of Helmholtz reciprocity is to assert the equivalence of the coefficient of light transport under the conditions of spatially exchanging the ith camera pixel and jth projector pixel in relation to the scene. As a result of this principle, knowledge of the LTM $\boldsymbol{T}$ for a given scene and projector/camera pixelization (collectively referred to as the 'primal view') informs us of the LTM $\boldsymbol{T}'$ of a second hypothetical situation (referred to as the 'dual view') involving the same scene with a camera and projector that are pixelated identically to the former projector and camera, respectively. Relative to the first situation (i.e. the primal view), the second hypothetical situation (i.e. the dual view) effectively swaps the roles of the camera and projector pixels as light sensors and light emitters, respectively. Between these two situations, Helmholtz reciprocity assures the result $\boldsymbol{T}' = \boldsymbol{T}^T$.

Dual photography, as a consequence of Helmholtz reciprocity, operates by synthesizing realistic digital images corresponding to the dual view while operating on data obtained from the primal view. Once the LTM for a given scene is recorded, the synthesis of dual images $\boldsymbol{p}'$ may proceed according to the equation

$$\boldsymbol{p}' = \boldsymbol{T}^T\boldsymbol{c}' \quad , \tag{1.25}$$

where $\boldsymbol{c}'$ represents a virtual field of illumination emerging from the camera, and the matrix $\boldsymbol{T}$ is the same transport matrix in equation (1.24) transposed so that the same coefficients $T^T_{ij} = T_{ji}$ now account for opposite-going light transport from the ith camera pixel to the jth projector pixel. It should be noted that the inverse relationship $\boldsymbol{T}\,\boldsymbol{T}^T = \boldsymbol{I}$ is not entailed by equations (1.24) and (1.25) and is indeed not true in general due to the loss of energy in scenes due to scattering and absorption [55]. Furthermore, provided knowledge of $\boldsymbol{T}$, the substitution of arbitrary illumination patterns for the projector and camera vectors $\boldsymbol{p}$ and $\boldsymbol{c}'$ in equations (1.24) and (1.25) allows for scene relighting: the realistic synthesis of primal and/or dual images under arbitrary illumination conditions.

Experimentally, image-based methods are sufficient to determine the entire LTM $\boldsymbol{T}$, a fact that can be understood by considering its columns $\boldsymbol{T} = \left[\boldsymbol{T}_1, \boldsymbol{T}_2, \ldots, \boldsymbol{T}_n\right]$. By capturing an image $\boldsymbol{c}_j$ under conditions in which the scene is illuminated by only the jth projector pixel of brightness β, equation (1.24) shows that $\boldsymbol{c}_j = \beta\,\boldsymbol{T}_j$ and thus we may determine $\boldsymbol{T}$ up to an arbitrary brightness factor by exhaustion: acquiring camera images of the scene illuminated by each projector pixel individually. However, for projectors and cameras with typically mega-pixel resolutions, it is clear that the size of the fully acquired LTM is extremely large ($10^6 \times 10^6$). As a result, the development of efficient algorithms for determining the LTM has traditionally occupied the largest concern for research in dual photography techniques [55, 56]. Indeed, for many scenes of sufficient interest it is clear that the structure of $\boldsymbol{T}$ is extremely sparse since its columns may be considered as camera images captured under the conditions of illumination from only a single projector pixel, thus resulting in captured images (and thus the columns of $\boldsymbol{T}$) having only small areas of significant brightness. For scenes in which complicated light transport phenomena such as reflection, refraction, and diffuse scattering are absent or may be disregarded, we may consider each column of $\boldsymbol{T}$ as being characterized by only a single brightness value associated with a coordinate representing a central locus of intensity in the captured image. For such scenes, the full problem of measuring light transport between single projector pixels and multiple camera pixels reduces to a one-to-one correspondence problem between projector and camera coordinates mediated by points in the scene under ray transport.

As an alternate basis for approximate dual imaging and relighting, we may consider for each camera pixel (u, v) associating a possibly sub-pixel resolved coordinate (u', v') corresponding to that pixel's underlying scene point within the projector field of view. By acquiring such coordinates for a sufficient set of camera pixels, a dual image can be synthesized via pixel-wise transformation and subsequent grid interpolation of camera pixels in the coordinate space of the projector image plane. Moreover, by also associating new intensity functions with either the camera or projector image planes, hypothetical illumination conditions can be simulated by proportionally modulating transform-associated camera pixel values based on either their (u, v) or (u', v') coordinates before interpolation. Thus, with a means for the recovery of (u', v') coordinates from image data for the pixel (u, v), we may achieve the synthesis of approximate dual images and both primal and dual image scene relighting.

Although there exists a wide range of methods for coding point correspondences through structured illumination [57], of relevance to the later material of chapter 2 is the highly efficient phase-based encoding method of sinusoidal fringe shifting [58–62]. Although many variations on this technique have been developed [63], the most common approach begins with the collection of $N \geq 3$ camera images of the target scene under illumination from a sinusoidally varying fringe pattern whose underlying phase is adjusted by an amount equal to $2\pi/N$ between each capture. Because of this manner of equal fringe shifting, all scene points under illumination, from the camera's point of view, report sinusoidally varying intensities across the acquired images. In particular, for a sequence of camera images $I_k(u, v)$ with $k = 0 \dots N-1$ considered as functions of discrete pixel coordinates (u, v), pixel intensity can be modeled according to the equation

$$I_k(u, v) = I'(u, v) + I''(u, v) \cos\left[\varphi(u, v) - \frac{2\pi k}{N}\right] \quad , \tag{1.26}$$

where $I'(u, v)$ and $I''(u, v)$ represent the spatial distributions of the average pixel intensity and fringe modulation amplitude respectively, and $\varphi(u,v)$ represents a phase parameter associated with the sinusoidal intensity response of each pixel. By defining the sums

$$\begin{aligned} A(u,v) &= \sum_{k=0}^{N-1} I_k(u,v)\sin\left(\frac{2\pi k}{N}\right) \quad , \quad \text{and} \\ B(u,v) &= \sum_{k=0}^{N-1} I_k(u,v)\cos\left(\frac{2\pi k}{N}\right) \quad , \end{aligned} \tag{1.27}$$

as well as taking note of the following identities involving discrete sums of shifted sinusoids:

$$\begin{aligned} &\sum_{k=0}^{N-1}\cos\left(\frac{2\pi k}{N}\right) = \sum_{k=0}^{N-1}\sin\left(\frac{2\pi k}{N}\right) = 0 \quad , \\ &\sum_{k=0}^{N-1}\cos\left(\phi - \frac{2\pi k}{N}\right)\sin\left(\frac{2\pi k}{N}\right) = \frac{N}{2}\sin(\phi) \quad , \\ &\sum_{k=0}^{N-1}\cos\left(\phi - \frac{2\pi k}{N}\right)\cos\left(\frac{2\pi k}{N}\right) = \frac{N}{2}\cos(\phi) \quad , \end{aligned} \tag{1.28}$$

(here $\phi \in \mathbb{R}$ is an arbitrary phase), it follows that the recovery of average intensity, modulation, and phase from equation (1.26) may be directly computed as:

$$\begin{aligned} I'(u,v) &= \frac{1}{N}\sum_{k=0}^{N-1} I_k(u,v) \quad , \\ I''(u,v) &= \sqrt{[A(u,v)]^2 + [B(u,v)]^2} \quad , \\ \varphi(u,v) &= \tan^{-1}\left(\frac{A(u,v)}{B(u,v)}\right) \quad . \end{aligned} \tag{1.29}$$

Taken together, the use of equally shifted fringe patterns with the three deterministic expressions in equation (1.29) are frequently called the ‘fringe shifting algorithm’. Importantly, the condition $N \geq 3$ is necessary in order for all three of the sinusoidal parameters $I'(u,v)$, $I''(u,v)$, and $\varphi(u,v)$ to be uniquely determined from equation (1.29). Generally, larger values of N contribute greater accuracy to the recovery of parameters via equation (1.29) in the presence of noise, although at the cost of acquiring larger input datasets during experiment.

Given any function $\tilde{\varphi}(u',v')$ defined across the coordinates of the projector’s illumination field, a sequence of N ‘fringe patterns’ giving rise to image data satisfying equation (1.26) can specified as

$$M_k(u',v') = \frac{1}{2}\left[1 + \cos\left(\tilde{\varphi}(u',v') - \frac{2\pi k}{N}\right)\right] \quad , \tag{1.30}$$

which for $k = 0 \ldots N-1$ defines the brightness of projector pixel (u',v') in pattern k as a modulation

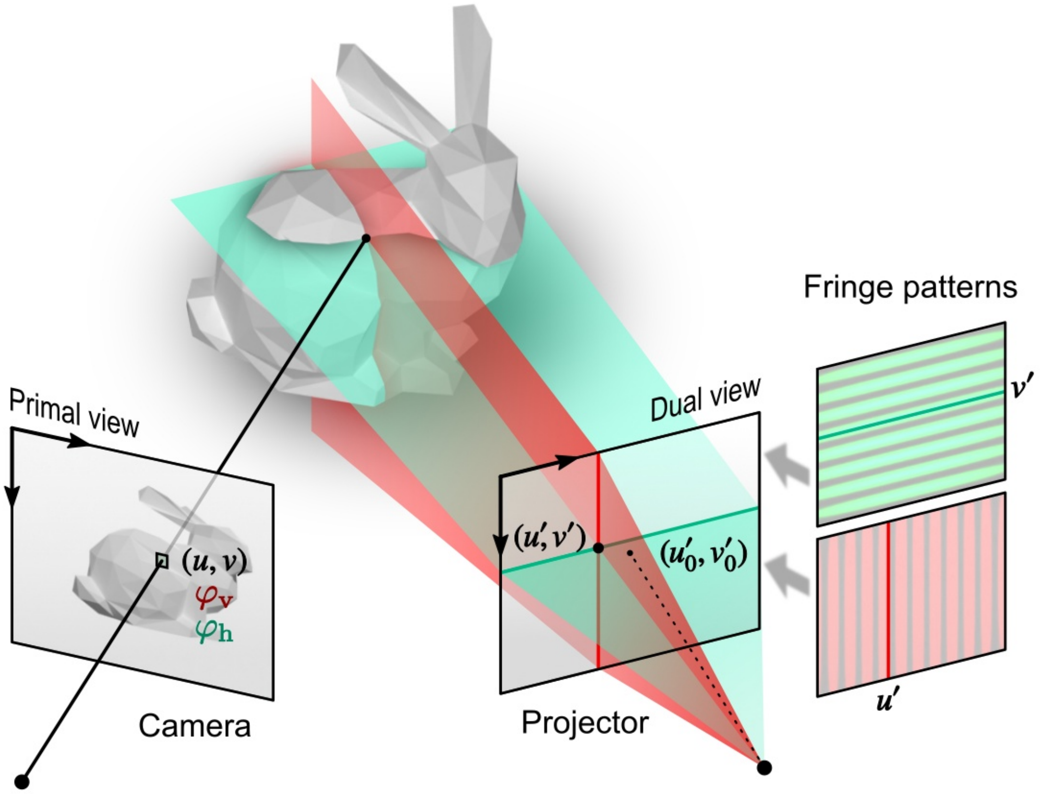

Figure 1.6 Dual photography implemented using fringe shifting.

value normalized within the interval $[0, 1]$. In the context of equation (1.26), the correlation between the intensity of camera pixel (u, v) with the illumination contributed by its matching projector pixel (u', v') implies that information is directly encoded via fringe shifting in the sense that $\varphi(u, v) = \tilde{\varphi}(u', v')$ modulo 2π. From the intensity data obtained by a given camera pixel (u, v), the recovery of horizontal and vertical coordinates corresponding to the location of the matching point in the projector's illumination field can then be accomplished by two sets of orthogonally oriented fringe patterns, defined by setting $\tilde{\varphi}(u', v')$ equal to the linear functions

$$\begin{aligned} \tilde{\varphi}_{\mathsf{h}}(u', v') &= \frac{2\pi}{\lambda_{\mathsf{h}}} \left(v' - v'_0\right) \quad , \\ \tilde{\varphi}_{\mathsf{v}}(u', v') &= \frac{2\pi}{\lambda_{\mathsf{h}}} \left(u' - u'_0\right) \quad , \end{aligned} \tag{1.31}$$

where λ_{v} and λ_{h} represent vertical and horizontal fringe period respectively in units of projector pixels, and the coordinates u'_0 and v'_0 (typically chosen such that the location (u'_0, v'_0) represents the midpoint of the projector's illumination field) serve as a datum to represent projector coordinates with zero phase. As a method for the implementation of dual photography, the geometric meanings of the fringe shifting quantities defined so far are illustrated in figure 1.6.

Fundamentally, equation (1.29) reflects the fact that recovered values of $\varphi(u, v)$ are determined only within multiples of 2π which, using the quadrant sensitive inverse tangent function, may be considered as values restricted (i.e. ‘wrapped’) to the interval $(-\pi, \pi]$. Consequently, it is necessary to make use of a phase ‘unwrapping’ procedure together with an additional projected pattern in order to obtain non-discontinuous phase values from which projector coordinates can be suitably recovered. Although robust and sophisticated algorithms suited for the problem of two-dimensional phase unwrapping exist [64], their necessary use within fringe shifting experiments represents the fundamental trade-off with their high efficiency (i.e. requiring as few as $N = 3$ data points per pixel). Fortunately, phase unwrapping algorithms may be designed so as to make use of auxiliary data such as recovered fringe modulation amplitudes $I''(u, v)$ for the purposes of suppressing the influence of noise [65].

Finally, as a practical scheme used within fringe shifting experiments, an additional projector pattern consisting of a single narrow stripe with appropriate horizontal or vertical orientation may be used to associate the datum coordinates u'_0 and v'_0 with subsets P_v and P_h of camera pixels illuminated by each stripe. Following the use of a suitable phase unwrapping algorithm, we may consider $\varphi_\mathsf{v}(u, v)$ and $\varphi_\mathsf{h}(u, v)$ to represent ‘unwrapped’ phase maps derived from imagery of vertical and horizontal fringes generated by projection sequences corresponding to $\tilde{\varphi}_\mathsf{v}(u', v')$ and $\tilde{\varphi}_\mathsf{h}(u', v')$, respectively. By computing θ_v and θ_h defined as the averages of $\tilde{\varphi}_\mathsf{v}(u', v')$ and $\tilde{\varphi}_\mathsf{h}(u', v')$ taken over the pixel sets P_v and P_h respectively, the complete recovery of projector coordinates (u', v') from associated camera pixels (u, v) may be expressed as

$$\begin{aligned} u' &= \frac{\lambda_\mathsf{v}}{2\pi}\left(\varphi_\mathsf{v}(u, v) - \theta_\mathsf{v}\right) + u'_0 \ , \\ v' &= \frac{\lambda_\mathsf{h}}{2\pi}\left(\varphi_\mathsf{h}(u, v) - \theta_\mathsf{h}\right) + v'_0 \ . \end{aligned} \tag{1.32}$$

1.3.2 Fringe Projection Profilometry

In the previous section, the coordinate encoding method of sinusoidal fringe shifting was introduced as a means by which a point-to-point transformation could be determined that mapped pixels in a camera’s field of view to corresponding locations in a projector’s illumination field; a capability sufficient, given certain assumptions, for performing dual photography and scene relighting. This correspondence ultimately results in a set of points on the surface of an object under study being associated with two pieces of information: that through the front-end optics of the respective devices, they are simultaneously imaged onto a camera pixel (u, v), as well as illuminated by a projector (sub)pixel (u', v'). This information however, when combined with knowledge of the relative positioning and image forming properties of the camera and projector, provides a basis for the recovery of yet more information about the set of object points: their coordinates in 3D space. This capability, when built from the efficient coordinate recovery afforded via the fringe shifting algorithm, is exactly the method of 3D imaging known as fringe projection profilometry.

Towards the recovery of 3D information, a coordinate-based understanding of the image forming behaviors of devices like cameras and projectors can be provided mathematically using the classic 'pinhole' model [66–68], in which the projection of 3D points onto a 2D sensor or modulator is treated analogously to the case of a camera obscura consisting of a flat screen and a small point-like aperture. Mathematically, the pinhole model takes the form of a 3×4 matrix equation

$$\rho \begin{bmatrix} u \\ v \\ 1 \end{bmatrix} = \begin{bmatrix} f_u & \alpha & u_\mathrm{P} \\ 0 & f_v & v_\mathrm{P} \\ 0 & 0 & 1 \end{bmatrix} \begin{bmatrix} \boldsymbol{R} & \boldsymbol{t} \end{bmatrix} \begin{bmatrix} x \\ y \\ z \\ 1 \end{bmatrix} , \tag{1.33}$$

which describes the projection of a point with 3D coordinates (x, y, z) onto an image plane with coordinates (u, v) in terms of several parameters. The 'extrinsic parameters', consisting of a 3×3 matrix $\boldsymbol{R}$ and 3×1 vector $\boldsymbol{t}$, describe the rigid-body rotation and translation respectively between a chosen world coordinate system and device coordinate system. The 'intrinsic parameters' describing the device's image forming properties consist of f_u and f_v which represent effective focal lengths along each axis of the image plane, u_P and v_P which describe the coordinates of the principle point (i.e. the location to which all points on the devices z-axis are imaged), and α which accounts for possible pixel skewness. Finally, the column vectors $[u, v, 1]^T$ and $[x, y, z, 1]^T$ are 'homogeneous coordinate' representations of (u, v) and (x, y, z) that through the arbitrary scalar ρ allow for the numerical extraction of (u, v) from equation (1.33).

For use in actual experiments, knowledge of the parameters involved in equation (1.33) may be obtained for cameras using automated calibration procedures which normally involve the capture of images of a specialized calibration object together with specialized software [68]. Implicit in the determination of extrinsic parameters after calibration is an assignment of a base 'world' coordinate system, usually assigned from a particular image of the calibration object within the calibration dataset. Importantly, while normally described as a projective model for ray-receiving cameras, the pinhole model remains equally valid for projectors from which light rays may originate. Consequently, although projectors do not capture images like cameras, specialized procedures have also been developed for the calibration of projectors [59].

Now building upon the projective model of equation (1.33), a method for the recovery of 3D information from a calibrated imaging system can be described as follows. Suppose that to an object point with coordinates (x, y, z) there correspond camera and projector image plane coordinates (u, v) and (u', v') respectively. It then follows that simultaneous knowledge of any three coordinates from the set $\{u, v, u', v'\}$ constitutes sufficient information for the determination of (x, y, z). More precisely, writing the three coordinates, however chosen, as the triplet (w_1, w_2, w_3), there can be derived a 3×3 linear system of the form $\boldsymbol{a} = \boldsymbol{G}[x, y, z]^T$ in which the 3×1 vector $\boldsymbol{a}$, and the elements of the matrix $\boldsymbol{G}$ are completely determined by w_1, w_2, w_3, and each device's respective calibration parameters. Thus by constructing $\boldsymbol{a}$ and the elements of $\boldsymbol{G}$ and performing matrix inversion, the

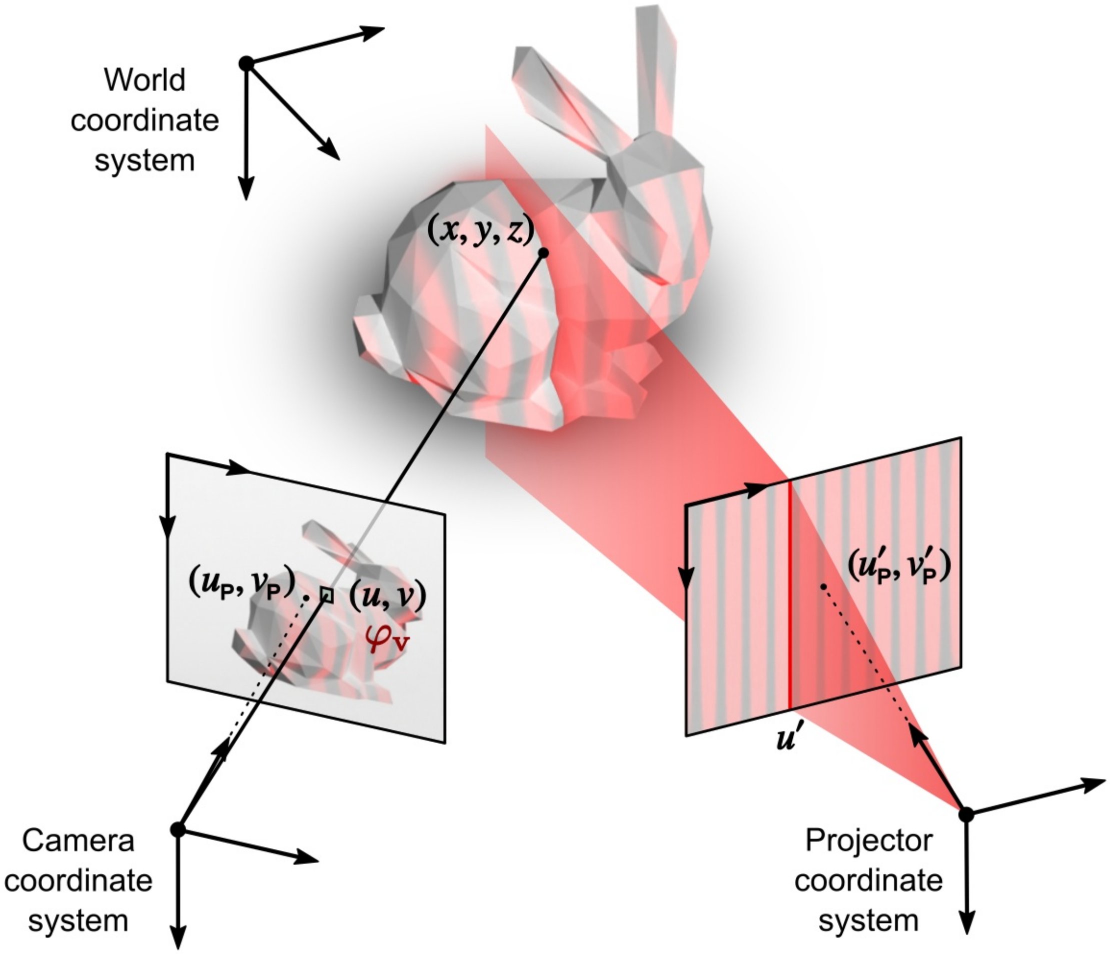

Figure 1.7 Geometric interpretation of 3D imaging using fringe shifting profilometry. The coordinates $(u_\mathrm{P}, v_\mathrm{P})$ and $(u'_\mathrm{P}, v'_\mathrm{P})$ represent the principle points of the camera and projector, respectively.

above method allows 3D information to be extracted for the object point underlying the associated coordinates (u, v) and (u', v').

For the majority of structured light 3D imaging systems, an offset between the viewpoints of the camera and projector occurs in the horizontal plane, with the recovery of 3D information following from the above procedure with the choice of $w_1 = u$, $w_2 = v$, and $w_3 = u'$ for the horizontal projector coordinate. In this context, the defining feature of FPP is that determination of u' follows from the projection of vertically oriented fringe patterns and the fringe shifting algorithm, exactly as shown in equations (1.29) and (1.32). Importantly, the determination of 3D information in this way does not require knowledge of the vertical projector coordinate v', nor the use of any horizontally oriented fringe patterns in experiment.

The geometric meaning of recovering (x, y, z) from u, v, and u' is illustrated in Fig. 1.7. For an object point that is imaged to the camera pixel (u, v), the pinhole model determines a unique ray along which the object point must lie. The indeterminate location of the object point along this ray represents the familiar loss of depth information from 2D images of 3D objects. The role of the additional projector coordinate u' is then to specify the location of the object point along this ray. From a sequence of images obtained with shifted fringe patterns displayed by the projector, the fringe shifting algorithm allows for the recovery of a phase value φ_{v} through which the corresponding horizontal projector coordinate u' is obtained following phase unwrapping. Subsequently, knowledge of u' allows for the identification of a set of rays that emanate from a single column within the projector's illumination field, thus defining a plane that also contains the object point. Finally, the coordinates of the object point (x, y, z) are recovered as the intersection point of the ray and the plane.

Although the geometric interpretation of point recovery shown in Fig. 1.7 is intuitive, it is clear that knowledge of the extrinsic and intrinsic parameters obtained from camera and projector calibration is essential for the quantitative calculation of 3D points. For completeness, we now show how the equations governing the determination of (x, y, z) from u, v, and u' may be obtained explicitly. Assuming knowledge of both the extrinsic and intrinsic parameters for the camera and projector, the projective behavior of each device may be written according to a calibrated pinhole model (1.33):

$$\begin{aligned}
\rho_{\mathrm{c}}\begin{bmatrix} u \\ v \\ 1 \end{bmatrix} &= \begin{bmatrix} a_{11} & a_{12} & a_{13} & a_{14} \\ a_{21} & a_{22} & a_{23} & a_{24} \\ a_{31} & a_{32} & a_{33} & a_{34} \end{bmatrix}\begin{bmatrix} x \\ y \\ z \\ 1 \end{bmatrix} \quad , \\
\rho_{\mathrm{p}}\begin{bmatrix} u' \\ v' \\ 1 \end{bmatrix} &= \begin{bmatrix} b_{11} & b_{12} & b_{13} & b_{14} \\ b_{21} & b_{22} & b_{23} & b_{24} \\ b_{31} & b_{32} & b_{33} & b_{34} \end{bmatrix}\begin{bmatrix} x \\ y \\ z \\ 1 \end{bmatrix} \quad ,
\end{aligned} \tag{1.34}$$

where a_{ij} and b_{ij} have been introduced to represent the general elements of the 3×4 combined pinhole projection matrices of the camera and projector respectively, and the numbers ρ_{c} and ρ_{p} permit extraction of the 2D coordinates (u, v) and (u', v') respectively following the matrix vector multiplication on the right-hand sides. However, by extracting the following relations from (1.34):

$$\begin{aligned}
u\rho_{\mathrm{c}} &= a_{11}x + a_{12}y + a_{13}z + a_{14} \\
v\rho_{\mathrm{c}} &= a_{21}x + a_{22}y + a_{23}z + a_{24} \\
\rho_{\mathrm{c}} &= a_{31}x + a_{32}y + a_{33}z + a_{34} \quad , \\
u'\rho_{\mathrm{p}} &= b_{11}x + b_{12}y + b_{13}z + b_{14} \\
\rho_{\mathrm{p}} &= b_{31}x + b_{32}y + b_{33}z + b_{34}
\end{aligned} \tag{1.35}$$

a 3×3 linear system of equations may be obtained for the unknowns x, y, and z in terms of u, v, u', and the pinhole model parameters:

$$\begin{bmatrix} a_{34}u - a_{14} \\ a_{34}v - a_{24} \\ b_{34}u' - b_{14} \end{bmatrix} = \begin{bmatrix} a_{11} - a_{31}u & a_{12} - a_{32}u & a_{13} - a_{33}u \\ a_{21} - a_{31}v & a_{22} - a_{32}v & a_{23} - a_{33}v \\ b_{11} - b_{31}u' & b_{12} - b_{32}u' & b_{13} - b_{33}u' \end{bmatrix} \begin{bmatrix} x \\ y \\ z \end{bmatrix} . \tag{1.36}$$

Thus, equation (1.36) takes the form of $\boldsymbol{a} = \boldsymbol{G}[x, y, z]^T$, permitting the recovery of 3D point information to take place via matrix inversion.

1.4 Conclusion

Nearly twenty years ago, the field of single-pixel imaging emerged from the confluence of two great technologies: the digital micromirror device which lay at the heart of consumer digital projectors, and the nascent mathematical theory of compressed sensing whose surprising effectiveness was just at the beginning of its rigorous explanation. Since then, the wide accessibility and novelty of SPI's core components has allowed it to flourish as a field of research, encompassing a number of scientific applications that has only continued to grow. However, despite almost two decades of scientific attention, the limitations of SPI's earliest technological ingredients have continued to sharply define its practical limitations up to present day. Despite their status as the leading hardware for spatial light modulation, the pattern refresh rates of DMDs has for many years remained stagnant at a point three orders of magnitude below the MHz bandwidths and sub-microsecond time resolutions of typical single-pixel detectors. Moreover, despite the flexibility and maturity of its theory and software, the development of robust and performant CS reconstruction algorithms has seen only little progress for cases demanding the processing of real-time streaming video. At the intersection of these weaknesses lies the prospect of high-speed and real-time SPI, a prospect whose fulfillment is the topic of the research contained in this thesis.

In the following chapters, a new platform for high-performance SPI will be introduced, along with several applications towards 3D imaging, high-speed and real-time imaging, and finally terahertz imaging. This platform, called SPI-ASAP, supports high-speed and ultrahigh-speed imaging through the scanned deployment of aggregated encoding patterns; an efficient modulation architecture that is implemented through the combination of a motorized polygonal scanning mirror with a conventional DMD. In this way, SPI-ASAP's measurement speed is able to reach two orders of magnitude above the top speeds achievable with DMD-only modulation, while still retaining all of the advantages of DMDs in terms of the flexibility afforded to the size and pixelization of the imaging FOV. Within this framework, cyclic S-matrices form an ideal basis for SPI-ASAP's operation, with their key mathematical properties serving several important roles, in particular, enabling the construction of an efficient reconstruction algorithm that is both compatible with compressive under-sampling, as well as highly parallelized computation via the use of GPU hardware. In this way, the modulation hardware and reconstruction algorithm of SPI-ASAP embody a unique and mutually complementary system, whose design features are tightly linked. Conceptualized as a platform for SPI systems targeting high-speed and real-time performance, SPI-ASAP thus represents a step towards SPI architectures that surpass separate and generic solutions for modulation and reconstruction, advancing the technologies available for the development of imaging systems that see what 2D image sensors can’t.

2 THREE-DIMENSIONAL SINGLE-PIXEL IMAGING

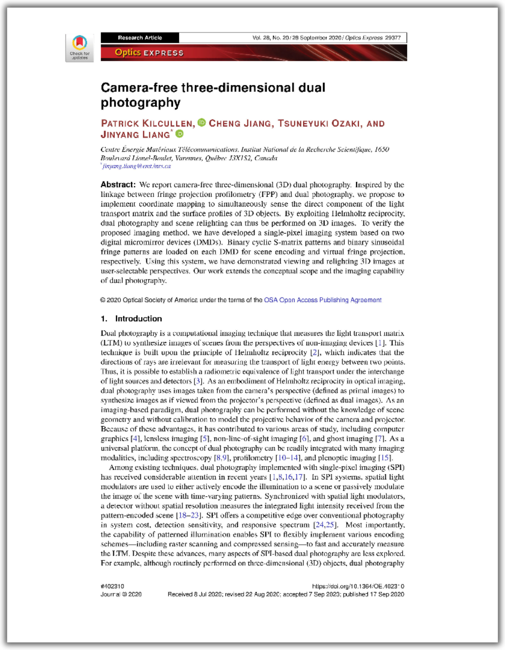

Research Article Vol. 28, No. 20 / 28 September 2020 / *Optics Express* 29377

Optics EXPRESS

Camera-free three-dimensional dual photography

PATRICK KILCULLEN, CHENG JIANG, TSUNEYUKI OZAKI, AND JINYANG LIANG*

Centre Énergie Matériaux Télécommunications, Institut National de la Recherche Scientifique, 1650 Boulevard Lionel-Boulet, Varennes, Québec J3X1S2, Canada

*jinyang.liang@emt.inrs.ca

Abstract: We report camera-free three-dimensional (3D) dual photography. Inspired by the linkage between fringe projection profilometry (FPP) and dual photography, we propose to implement coordinate mapping to simultaneously sense the direct component of the light transport matrix and the surface profiles of 3D objects. By exploiting Helmholtz reciprocity, dual photography and scene relighting can thus be performed on 3D images. To verify the proposed imaging method, we have developed a single-pixel imaging system based on two digital micromirror devices (DMDs). Binary cyclic S-matrix patterns and binary sinusoidal fringe patterns are loaded on each DMD for scene encoding and virtual fringe projection, respectively. Using this system, we have demonstrated viewing and relighting 3D images at user-selectable perspectives. Our work extends the conceptual scope and the imaging capability of dual photography.

1. Introduction

Dual photography is a computational imaging technique that measures the light transport matrix (LTM) to synthesize images of scenes from the perspectives of non-imaging devices [1]. This technique is built upon the principle of Helmholtz reciprocity [2], which indicates that the directions of rays are irrelevant for measuring the transport of light energy between two points. Thus, it is possible to establish a radiometric equivalence of light transport under the interchange of light sources and detectors [3]. As an embodiment of Helmholtz reciprocity in optical imaging, dual photography uses images taken from the camera's perspective (defined as primal images) to synthesize images as if viewed from the projector's perspective (defined as dual images). As an imaging-based paradigm, dual photography can be performed without the knowledge of scene geometry and without calibration to model the projective behavior of the camera and projector. Because of these advantages, it has contributed to various areas of study, including computer graphics [4], lensless imaging [5], non-line-of-sight imaging [6], and ghost imaging [7]. As a universal platform, the concept of dual photography can be readily integrated with many imaging modalities, including spectroscopy [8,9], profilometry [10–14], and plenoptic imaging [15].

Among existing techniques, dual photography implemented with single-pixel imaging (SPI) has received considerable attention in recent years [1,8,16,17]. In SPI systems, spatial light modulators are used to either actively encode the illumination to a scene or passively modulate the image of the scene with time-varying patterns. Synchronized with spatial light modulators, a detector without spatial resolution measures the integrated light intensity received from the pattern-encoded scene [18–23]. SPI offers a competitive edge over conventional photography in system cost, detection sensitivity, and responsive spectrum [24,25]. Most importantly, the capability of patterned illumination enables SPI to flexibly implement various encoding schemes—including raster scanning and compressed sensing—to fast and accurately measure the LTM. Despite these advances, many aspects of SPI-based dual photography are less explored. For example, although routinely performed on three-dimensional (3D) objects, dual photography

#402310 https://doi.org/10.1364/OE.402310
Journal © 2020 Received 8 Jul 2020; revised 22 Aug 2020; accepted 7 Sep 2020; published 17 Sep 2020

Camera-free three-dimensional dual photography
Photographie bimode tridimensionnelle sans caméra

Patrick Kilcullen[1], Cheng Jiang[1], Tsuneyuki Ozaki[1], and Jinyang Liang[1*]

[1]*Centre Énergie Matériaux Télécommunications, Institut National de la Recherche Scientifique, 1650 Boulevard Lionel-Boulet, Varennes, Québec J3X1S2, Canada*

*jinyang.liang@emt.inrs.ca

Publication: *Optics Express* **28**(20), pp. 29377–29389 (2020). doi:10.1364/OE.402310

Published: 17 Sep 2020

Author Contributions: The initial concept of extending fringe projection profilometry (FPP) to single-pixel imaging was proposed by JL. A later contribution by PK clarified the necessity of a second DMD used in the experimental setup. Subsequently, JL proposed the theoretical link to dual photography. Design and construction of the experimental system was carried out by PK which included the development of software necessary for the automation of data collection, and subsequent data analysis. Collection of experimental data was performed by PK. CJ and TO engaged in consultation with the authors.

Abstract: We report camera-free three-dimensional (3D) dual photography. Inspired by the linkage between fringe projection profilometry (FPP) and dual photography, we propose to implement coordinate mapping to simultaneously sense the direct component of the light transport matrix and the surface profiles of 3D objects. By exploiting Helmholtz reciprocity, dual photography and scene relighting can thus be performed on 3D images. To verify the proposed imaging method, we have developed a single-pixel imaging system based on two digital micromirror devices (DMDs). Binary cyclic S-matrix patterns and binary sinusoidal fringe patterns are loaded on each DMD for scene encoding and virtual fringe projection, respectively. Using this system, we have demonstrated viewing and relighting 3D images at user-selectable perspectives. Our work extends the conceptual scope and the imaging capability of dual photography.

2.1 Introduction

Dual photography is a computational imaging technique that measures the light transport matrix (LTM) to synthesize images of scenes from the perspectives of non-imaging devices [55]. This technique is built upon the principle of Helmholtz reciprocity [54], which indicates that the directions of rays are irrelevant for measuring the transport of light energy between two points. Thus, it is possible to establish a radiometric equivalence of light transport under the interchange of light sources and detectors [69]. As an embodiment of Helmholtz reciprocity in optical imaging, dual photography uses images taken from the camera's perspective (defined as primal images) to synthesize images as if viewed from the projector's perspective (defined as dual images). As an imaging-based paradigm, dual photography can be performed without the knowledge of scene geometry and without calibration to model the projective behavior of the camera and projector. Because of these advantages, it has contributed to various areas of study, including computer graphics [70], lensless imaging [71], non-line-of-sight imaging [72], and ghost imaging [73]. As a universal platform, the concept of dual photography can be readily integrated with many imaging modalities, including spectroscopy [56, 74], profilometry [75–79], and plenoptic imaging [80].

Among existing techniques, dual photography implemented with single-pixel imaging (SPI) has received considerable attention in recent years [55, 56, 81, 82]. In SPI systems, spatial light modulators are used to either actively encode the illumination to a scene or passively modulate the image of the scene with time-varying patterns. Synchronized with spatial light modulators, a detector without spatial resolution measures the integrated light intensity received from the pattern-encoded scene [6, 45, 83–86]. SPI offers a competitive edge over conventional photography in system cost, detection sensitivity, and responsive spectrum [1, 18]. Most importantly, the capability of patterned illumination enables SPI to flexibly implement various encoding schemes—including raster scanning and compressed sensing—to fast and accurately measure the LTM. Despite these advances, many aspects of SPI-based dual photography are less explored. For example, although routinely performed on three-dimensional (3D) objects, dual photography has not been performed on 3D images. In addition, scene relighting is provided merely from primal and dual perspectives. Finally, previous dual photography work has been dominated by the use of commercial projectors, which have to produce grayscale patterns via weighted temporal integration [60]. The resulting dark noise and digitization error [41] limit the performance of SPI-based dual photography systems.

2.2 Methods

2.2.1 Linkage of light transport matrix (LTM) to fringe projection profilometry (FPP)

To overcome these limitations, in this paper, we report camera-free 3D dual photography implemented in an SPI platform. Our method is inspired by observing the analogy between the function-

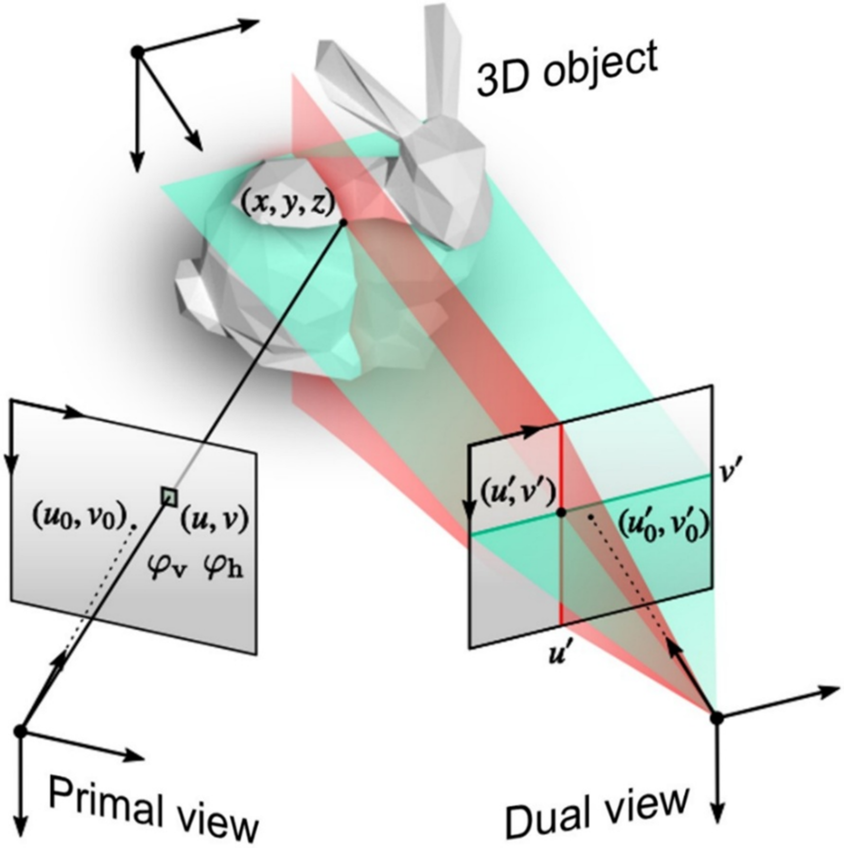

Figure 2.1 Coordinate settings of 3D dual photography using fringe projection profilometry (FPP)-based coordinate mapping.

ality of the LTM and the operating principle of fringe projection profilometry (FPP) [87].

An LTM associates the illumination from each projector's pixel to corresponding camera pixels. Each LTM's element, determined by the properties of the scene geometry, is determined by using imaging-based methods, such as raster scanning of a single illuminating pixel while measuring the intensity of responsive camera pixels [88]. The LTM is comprised of columns that represent vectorized images of the impulse scattering response of the scene. The information recorded by the LTM can be divided into a direct component (which accounts for light paths that experience only one interaction with the scene) and a global component (which accounts for all other paths reaching the camera) [89]. Since the former considers light that reflects/scatters from a single point in the scene, the direct component of the LTM obeys epipolar geometry and can serve as the basis for building a two-dimensional (2D) pixel-to-pixel mapping between the projector and camera.

A 2D pixel-to-pixel mapping can also be recorded by structured light methods in a projector-camera system. For example, in the context of projector calibration used in FPP [66], sinusoidal fringe patterns are used to associate phase-encoded projector coordinates with camera pixels of an image of a flat calibration grid. After the measurement of phase values $\varphi_\text{h}(u, v)$ and $\varphi_\text{v}(u, v)$ by the projection of horizontal and vertical fringe patterns respectively, each camera pixel (u, v) is linked with their corresponding projector pixel (u', v') without the knowledge of calibration parameters of either device (Fig. 2.1).

These results indicate that the 2D pixel correspondence established by the FPP method can equivalently represent the direct component of the LTM. Thus, a dual image with sub-pixel precision can be synthesized via pixel-wise transformation and subsequent grid interpolation of camera pixels in the coordinate space of the projector. Moreover, hypothetical illumination conditions from perspectives of either the camera or the projector can be synthesized by adjusting transform-associated camera pixel values based on their coordinates before interpolation.

Besides elucidating the 2D pixel-to-pixel relationship between the camera and the projector, the FPP-based method also describes the projective relationship of a 3D point (x, y, z) onto the camera pixel (u, v) and the projector pixel (u', v') by using the projective model of a pinhole camera [67], expressed by

$$\rho_0 \left[u', v', 1\right]^T = \boldsymbol{A}_0 \left[x, y, z, 1\right]^T \quad \text{and} \quad \rho_1 \left[u', v', 1\right]^T = \boldsymbol{A}_1 \left[x, y, z, 1\right]^T \tag{2.1}$$

where $\boldsymbol{A}_0$ and $\boldsymbol{A}_1$ are matrices that characterize the projective behavior of the projector and the camera, which are available after the FPP-based system calibration [58, 68]. ρ_0 and ρ_1 are arbitrary scalar factors for the numerical extraction of (u', v') and (u, v). Geometrically, prior knowledge of coordinates (u, v) together with the recovery of a horizontal projector coordinate u' determine a ray and a plane that emanate from the camera and projector, respectively. The intersection of this ray and the plane determines the recovery of a 3D coordinate (Fig. 2.1). Mathematically, knowledge of the coordinate set $\{u, v, u'\}$ together with camera modeling in Eq. (2.1) is sufficient for establishing three linearly independent equations that recover (x, y, z). Thus, simultaneous LTM detection and 3D imaging provided by the FPP-based method should allow performing dual photography and scene relighting on 3D images.

2.2.2 System

To verify the proposed imaging method, we have developed a single-pixel three-dimensional dual photography (STDP) system consisting of an illumination module and a collection module (Fig. 2.2). In the illumination module, a continuous-wave laser (CNI Lasers MRL-III-671) is the light source. Following beam expansion and collimation (via lenses L1 through L4), mirrors M1 and M2 steer the beam onto a 0.45” digital micromirror device (DMD 1, Ajile Light Industries AJD-4500), from which the diffraction order with the maximum efficiency is selected by an iris placed on the Fourier plane of a 4*f* imaging system consisting of lenses L5 and L6. The image of DMD 1, formed at the intermediate image plane, is projected by a projection lens PL (Nikon AF-P DX NIKKOR 18–55 mm *f*/3.5–5.6) onto a 3D object. The light scattered from the 3D object enters the collection module.

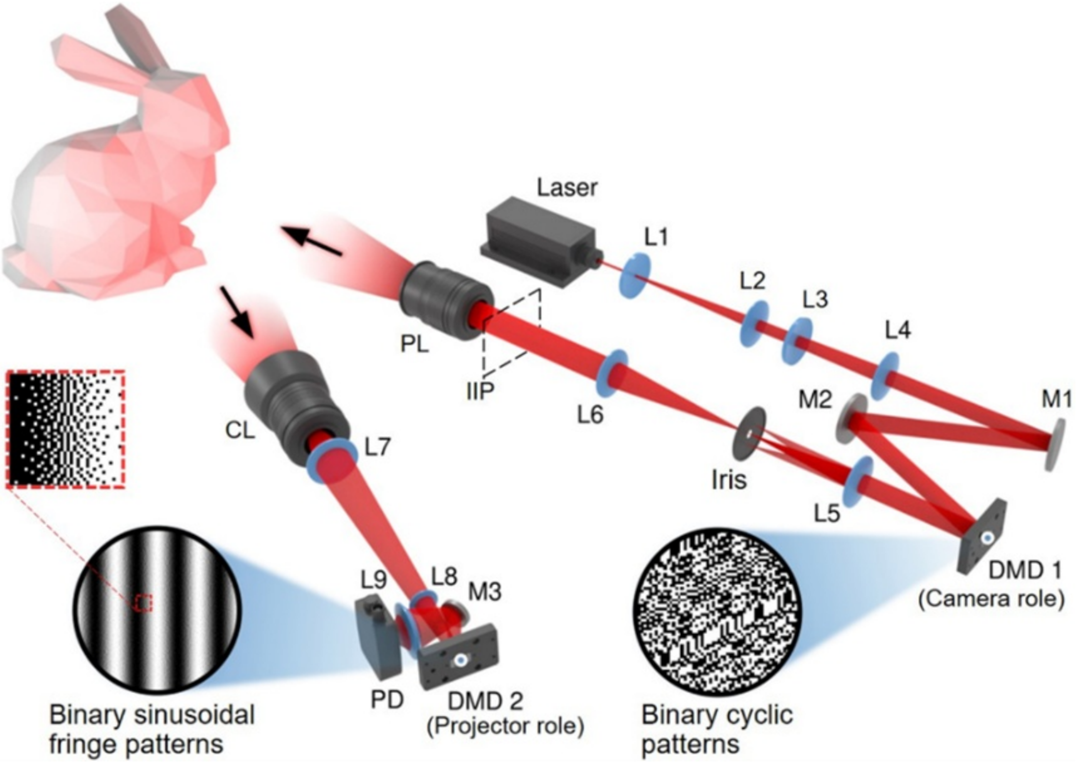

Figure 2.2 Schematic of the single-pixel three-dimensional dual photography (STDP) system. CL, Collection lens; DMD 1 and DMD 2, Digital micromirror device; IIP, Intermediate image plane; L1–L9, Lens; M1–M3, Mirror; PD, Photodiode; PL, Projection lens.

The light is collected by a collection lens CL (Opteka 85 mm *f*/1.8). The formed image is relayed by lenses L7 and L8 onto another 0.45” digital micromirror device (DMD 2, Ajile Light Industries AJD-4500). A mirror M3 reflects the light modulated by DMD 2 to a condenser lens L9 that focuses the light onto a photodiode (Thorlabs DET100A2). Photocurrent signals, digitized by a data acquisition card (National Instruments PCIe-6321), are transferred to a computer for image processing.

2.2.3 Data acquisition

Calibration of the STDP system is first carried out using single-pixel imaging to determine the matrices of $\boldsymbol{A}_0$ and $\boldsymbol{A}_1$ in Eq. (2.1). For the illumination module, calibration imaging is performed by displaying, on DMD 1, a sequence of masking patterns the same as the ones used in data acquisition (to be explained below), together with a fixed all-“on” pattern on DMD 2. Several single-pixel images of a planar calibration object featuring a checkerboard pattern are obtained in this way across various poses. These images, combined with knowledge of the checkerboard pattern dimensions, allows for estimating $\boldsymbol{A}_0$ with appropriate software [68]. The same method is applied to the calibration of the collection module by swapping the displayed patterns on DMD 1 and DMD 2. This procedure produces single-pixel images of the calibration object centered on DMD 2, from which $\boldsymbol{A}_1$ is estimated.

For data acquisition, DMD 1 displays complete sets of binary masking patterns generated by a cyclic S-matrix [14, 23], which is known for enhancing the signal-to-noise ratio in SPI reconstruction [90, 91]. Generated by the twin-prime construction [15, 16, 92], the cyclic S-matrix of size $MN \times MN$ can be obtained for each pair of twin primes M and $N = M+2$. Denoting the elements of such a matrix by $\boldsymbol{S} = \left[s_{ji}\right]$, where $j, i = 0, \ldots, MN-1$, the first row of this matrix is defined by

$$s_{0i} = \begin{cases} 0 & \text{if } [f(i) - g(i)]\, g(i) = 0 \\ +1 & \text{otherwise} \end{cases} , \tag{2.2}$$

where functions $f(i)$ and $g(i)$ are defined by

$$\begin{aligned} f(i) &= \begin{cases} +1 & \text{if } i \text{ is a quadratic residue (mod } M\text{)} \\ 0 & \text{if } i \equiv 0 \ \text{(mod } M\text{)} \\ -1 & \text{otherwise} \end{cases} , \text{ and} \\ g(i) &= \begin{cases} +1 & \text{if } i \text{ is a quadratic residue (mod } N\text{)} \\ 0 & \text{if } i \equiv 0 \ \text{(mod } N\text{)} \\ -1 & \text{otherwise} \end{cases} . \end{aligned} \tag{2.3}$$

Each subsequent row is then derived from the previous row by the element-wise left circular shifting of the initial row. In our experiments, each row was reshaped to a 2D binary masking pattern, $e_j(u, v)$, with $M \times N$ encoding pixels in size. For our experiments, we chose $M = 137$ and $N = 139$, which generated a total of $MN = 19043$ binary masking patterns. Each encoding pixel had a size of approximately 2.5 mm × 2.5 mm at the object plane. DMD 1 operated at 250 Hz. Photodiode signals were digitally acquired at the same rate. Thus, the acquisition time of each single-pixel image was 77 seconds.

In the collection module, a total of six sinusoidal fringe patterns are displayed on DMD 2 for virtual fringe projection [93, 94]. They are divided into two groups. The first three patterns have horizontal fringes with a period of $\lambda_\mathrm{h} = 864$ µm. The second group have vertical fringes with an equal period $\lambda_\mathrm{v} = 864$ µm. These grayscale sinusoidal fringes are converted into binary patterns for DMD 2 using an error diffusion algorithm [95], with an example shown by the inset in Fig. 2.2. Because each encoding pixel in the masking patterns, when imaged onto DMD 2, occupies an array of micromirrors, the high-spatial-frequency noise carried by these binary sinusoidal patterns is filtered. Therefore, the original grayscale sinusoidal fringes are virtually projected to the 3D object. As a result, a representative signal c_{jk} measured by the photodiode during display of masking pattern j and fringe pattern k can be expressed by

$$c_{jk} = \sum_{u,v} e_j(u, v) p_k(u, v) \ . \tag{2.4}$$

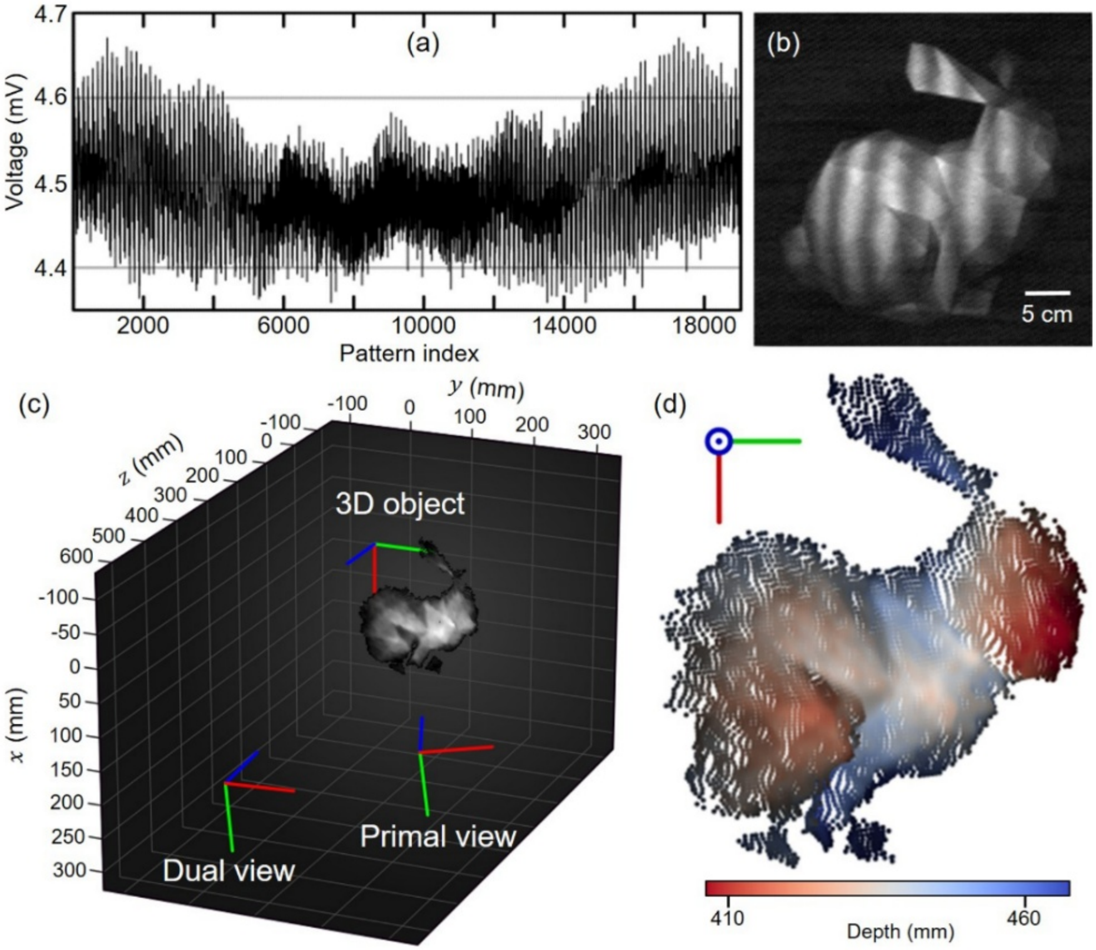

Figure 2.3 Imaging a low-poly sculpture of the Stanford bunny using the STDP system. **(a)** Signal acquired by the photodiode for a fringe image. **(b)** A reconstructed fringe image of the object. **(c)** World coordinate system containing point cloud data of the object. **(d)** A recovered 3D image.

Here, p_k, representing the fringe images produced by the virtual fringe projection, is expressed by

$$p_k(u, v) = I_{\mathrm{m}}(u, v) + I_{\mathrm{va}}(u, v) \cos\left[\varphi_{\mathrm{d}}(u, v) - 2\pi k/3\right] \quad , \tag{2.5}$$

where $k = 0, \ldots, 5$. $I_{\mathrm{m}}(u, v)$ and $I_{\mathrm{va}}(u, v)$ represent the mean intensity and intensity variation, respectively. $\varphi_{\mathrm{d}}(u, v)$ is written as $\varphi_{\mathrm{v}}(u, v)$ for $k = 0, 1, 2$ and $\varphi_{\mathrm{h}}(u, v)$ for $k = 3, 4, 5$ which represent depth-indicated phases for vertical and horizontal fringes, respectively. The sinusoidal fringe patterns, sequentially displayed on DMD 2, remain unchanged during the projection of the cyclic pattern sequence of DMD 1. As an example, the signal trace for a specific fringe pattern is shown in Fig. 2.3(a).

Besides these fringe patterns, two additional projector patterns consisting of a single narrow stripe with either vertical or horizontal orientation are used to illuminate subsets of camera pixels, denoted by $\mathrm{P_v}$ and $\mathrm{P_h}$. These patterns also associate the datum coordinates u_0' and v_0', chosen as the center of vertical and horizontal coordinates of the projector.

2.2.4 Image reconstruction

The image reconstruction starts by recovering the vectorized fringe image $\boldsymbol{p}_k$ by

$$\boldsymbol{p}_k = \boldsymbol{S}^{-1}\boldsymbol{c}_k \quad . \tag{2.6}$$

Here, $\boldsymbol{c}_k$ represents the photodiode measurements for the kth fringe pattern in a vectorized form. The inverse of the cyclic S-matrix is given by $\boldsymbol{S}^{-1} = 2(2\boldsymbol{S} - \boldsymbol{J})/(MN+1)$, where $\boldsymbol{J}$ is an all-ones matrix of size $MN \times MN$. $\boldsymbol{p}_k$ is then reshaped to a 2D fringe image $M \times N$ in size, and an example is shown in Fig. 2.3(b). Then, the wrapped phases associated with the vertical and horizontal fringe patterns are recovered by

$$\begin{aligned} \tilde{\varphi}_{\mathrm{h}} &= \tan^{-1}\left(\frac{\sum_{k=0}^{2} p_k(u,v)\ \sin\left(2\pi k/3\right)}{\sum_{k=0}^{2} p_k(u,v)\ \cos\left(2\pi k/3\right)}\right) \quad , \text{ and} \\ \tilde{\varphi}_{\mathrm{v}} &= \tan^{-1}\left(\frac{\sum_{k=3}^{5} p_k(u,v)\ \sin\left(2\pi k/3\right)}{\sum_{k=3}^{5} p_k(u,v)\ \cos\left(2\pi k/3\right)}\right) \quad . \end{aligned} \tag{2.7}$$

Using the quadrant sensitive inverse tangent function, the computed values from Eq. (2.7) are wrapped in the interval $(-\pi, \pi]$. Consequently, a procedure based on the discrete cosine transformation is used for the weighted phase unwrapping [64, 65] to obtain non-discontinuous phase values from which projector coordinates can be recovered. In addition, based on the single stripe patterns, averages of φ_{v} and φ_{h} taken over the pixel sets P_{v} and P_{h} are computed as θ_{v} and θ_{h}. In this way, the associated projector coordinates (u', v') are recovered by

$$\begin{aligned} u' &= \lambda_{\mathrm{v}}\ \left[\varphi_{\mathrm{v}}(u,v) - \theta_{\mathrm{v}}\right]/2\pi + u'_0 \quad , \text{ and} \\ v' &= \lambda_{\mathrm{h}}\ \left[\varphi_{\mathrm{h}}(u,v) - \theta_{\mathrm{h}}\right]/2\pi + v'_0 \quad . \end{aligned} \tag{2.8}$$

Finally, with the knowledge of $\boldsymbol{A}_0$ and $\boldsymbol{A}_1$, the coordinate set $\{u, v, u'\}$ is used with Eq. (2.1) to generate 3D point clouds [Figs. 2.3(c) and (d)].

We characterized the spatial resolution and the depth resolution of the STDP system. For the quantification of spatial resolution, we analyzed the images of the checkerboard target used in system calibration. The line profiles of both vertical and horizontal edges of a selected square were averaged to calculate the edge spread functions (ESFs). Taking the derivative of the ESFs yielded the line spread functions (LSFs). The spatial resolutions of the STDP system, defined by the averaged full-width at half-maximum of the LSFs in the horizontal and vertical directions, were determined to be 2.98 mm. To calculate the depth resolution, we analyzed the variation in the point-cloud geometry observed for a tilted white planar target with no pattern. The standard deviation of measured depth over an area of 14 cm × 17 cm was calculated as the system's noise level. The depth resolution, defined as twice the system's noise level [60], was quantified to be 2.59 mm.

2.2.5 Dual photography and scene relighting

Because the cyclic-S-matrix-based masking patterns actively illuminate the 3D object, the reconstructed primal images take the perspective of the illumination module. Accordingly, the dual view is defined from the direction of the collection module. The STDP system allows two methods for dual photography and scene relighting. First, the obtained 2D-to-2D [i.e., (u, v)-to-(u', v')] coordinate mapping allows generating 2D dual images with scene relighting akin to previous dual photography methods. In particular, from the primal image pixels (u, v) with intensities $I(u, v)$ and an optional relighting function $r(u, v)$, an intensity $I_r(u', v') = I(u, v)\, r(u, v)$ can be defined on the points (u', v'), from which the 2D dual image and 2D relit dual image can be obtained via interpolation. Moreover, using additional 3D-to-2D [i.e., (x, y, z)-to-(u, v) and (x, y, z)-to-(u', v')] coordinate mappings with known calibrations, 3D dual images with scene relighting can be generated by projecting recovered point data (x, y, z) and associated intensity values $I(x, y, z)$. For any choice of suitable matrices $\boldsymbol{A}_{\text{vp}}$ ("vp" stands for "virtual projector") and $\boldsymbol{A}_{\text{vc}}$ ("vc" stands for "virtual camera""), the projective relationship, $\rho_{\text{vp}}[u', v', 1]^T = \boldsymbol{A}_{\text{vp}}[x, y, z, 1]^T$ and $\rho_{\text{vc}}[u', v', 1]^T = \boldsymbol{A}_{\text{vc}}[x, y, z, 1]^T$, can be used to synthesize images centered on the matrix $\boldsymbol{A}_{\text{vc}}$ with optional relighting $r(u, v)$ from the projective matrix $\boldsymbol{A}_{\text{vp}}$ achieved from interpolation of the scattered data, i.e., $I_r(u', v') = I(x, y, z)\, r(u, v)$. By setting $\boldsymbol{A}_{\text{vp}} = \boldsymbol{A}_0$ and $\boldsymbol{A}_{\text{vc}} = \boldsymbol{A}_1$ from the experimental calibration, the 3D-to-2D coordinate mapping performs equivalent dual image synthesis as to the 2D-to-2D coordinate mapping. With the relighting choice $r(u, v) = 1$, both methods yield $I_r(u', v') = I_r(u, v)$, which is equivalent to the statement of Helmholtz reciprocity. For other choices of $\boldsymbol{A}_{\text{vc}}$ and $\boldsymbol{A}_{\text{vp}}$, in general, the reciprocity principle no longer assures the radiometric accuracy of output images. However, the synthesis of realistic dual imaging and scene relighting can still be achieved from user-selectable perspectives by the 3D-to-2D coordinate mapping.

2.3 Results

2.3.1 3D dual photography

To verify the performance of STDP, we imaged two 3D objects: a tilted plane with a laser hazard symbol and a low-poly sculpture of the Stanford bunny. Figure 2.4(a) shows the primal images. Synthetic 2D dual images using the 2D-to-2D coordinate mapping are shown in Fig. 2.4(b). We also recovered 3D dual images of each object. As a comparison, the results obtained by using the 3D-to-2D coordinate mapping are shown in Figs. 2.4(c) and (d). Figure 2.4(c) was produced by projecting the 3D information to 2D datasets, whose results show good resemblance to Fig. 2.4(b).

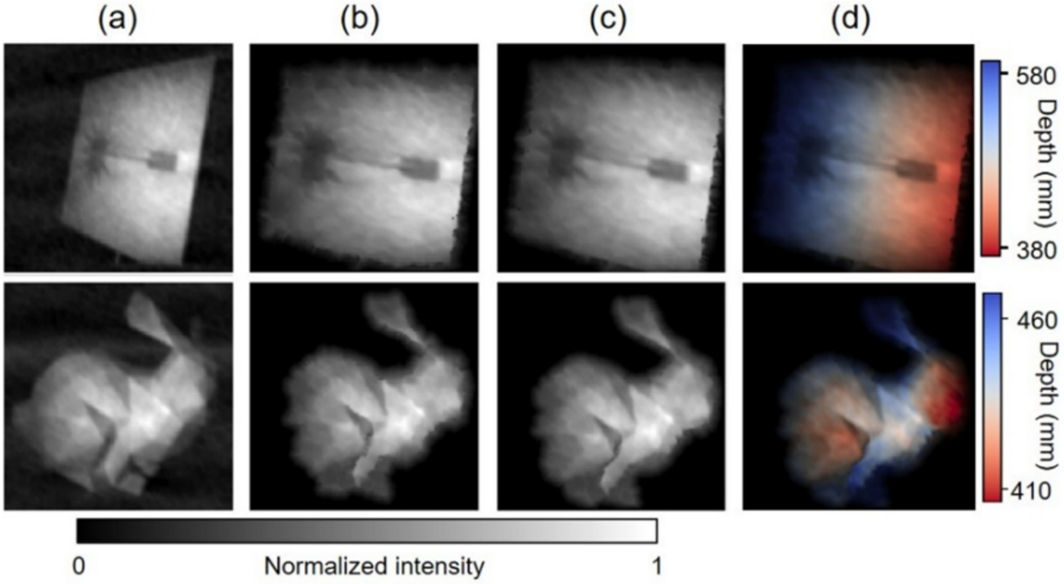

Figure 2.4 3D dual photography. **(a)** Primal images. **(b)** 2D dual images synthesized by using the 2D coordinate mapping. **(c)**–**(d)** 2D dual images (c) and depth-encoded 3D dual images (d) synthesized by using the FPP-based 3D-to-2D coordinate mapping.

Finally, Fig. 2.4(d) shows dual photography retaining 3D information.

2.3.2 3D scene relighting at the primal and dual perspectives

To demonstrate scene relighting using STDP, we digitally illuminated the same objects in Fig. 2.4 with a relighting pattern consisting of bright circles in a hexagonal arrangement, from both the primal view and the dual view. Figures 2.5(a) and (b) show results generated by using the 2D-to-2D coordinate mapping. As a comparison, 3D dual images, produced by using the 3D-to-2D coordinate mapping, are shown in Fig. 2.5(c). We also verified these results experimentally by displaying the relighting pattern on DMD 2 [Fig. 2.5(d)]. A detailed comparison of a local feature [insets in Fig. 2.5(d)] demonstrates the feasibility of our method.

2.3.3 3D dual photography and scene relighting beyond the primal and dual perspectives

We further explored the imaging capability of STDP to synthesize photography from user-selectable perspectives between the primal and dual perspectives. This capability is demonstrated with a 3D object of a tilted plane with a maple leaf symbol for various choices of $\boldsymbol{A}_{\mathrm{vc}}$ and $\boldsymbol{A}_{\mathrm{vp}}$ interpolated between the primal and dual view projection matrices (Figs. 2.6 and 2.7). In particular, to generate 3D dual imaging with user-selectable perspectives, $\boldsymbol{A}_{\mathrm{vc}}$ was interpolated by $\boldsymbol{A}_{\mathrm{vc}} = (1-t)\boldsymbol{A}_0 + t\boldsymbol{A}_1$ for t varying from 0 to 1 (see Visualization 1). Images at five representative views (for $t = 0$, 0.25, 0.50,

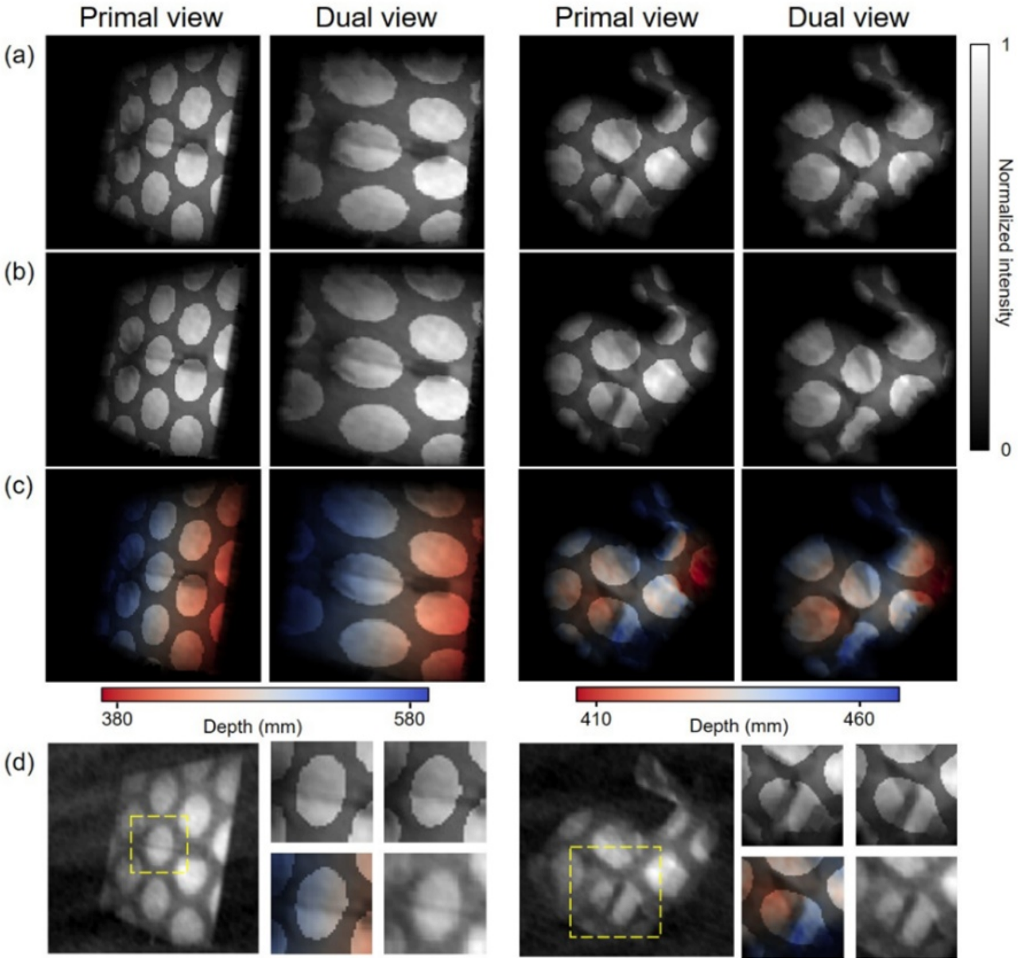

Figure 2.5 3D scene relighting. **(a)** 2D relit primal and dual images of the laser hazard symbol object and the bunny object synthesized by using the 2D-to-2D coordinate mapping. **(b)** 3D relit primal and dual images synthesized by using the 3D-to-2D coordinate mapping. **(c)** As in (b), but with depth information displayed. **(d)** Experimental verification of scene relighting at the primal view. Comparison of a local feature (marked by the yellow dashed boxes) in (a)–(d) are shown in the zoomed views on the top left, top right, bottom left, and bottom right, respectively.

0.75, and 1) are shown in Fig. 2.6. Synthetic images in Fig. 2.6(a) correspond to uniform relighting [i.e., $r(u, v) = 1$]. In Figs. 2.6(b) and (c), the same relighting pattern used in Section 2.3.2 was implemented, with $\boldsymbol{A}_{\text{vp}}$ set equal to $\boldsymbol{A}_0$ and $\boldsymbol{A}_1$, respectively. The images corresponding to values of $t = 0$ in Fig. 2.6(b) and $t = 1$ in Fig. 2.6(c) indicate $\boldsymbol{A}_{\text{vp}} = \boldsymbol{A}_{\text{vc}}$, in which case the alignment of views causes the relighting pattern to appear undistorted by scene geometry. We also demonstrated synthetic relit images for which the perspectives of the relighting pattern were varied as $\boldsymbol{A}_{\text{vp}} = (1 - t)\boldsymbol{A}_0 + t\boldsymbol{A}_1$ for t ranging from 0 to 1 (see Visualization 2). Figures 2.7(a) and (b) show five representative images with $\boldsymbol{A}_{\text{vc}}$ fixed at $\boldsymbol{A}_0$ and $\boldsymbol{A}_1$, respectively. As before, it was noted that the situation $\boldsymbol{A}_{\text{vc}} = \boldsymbol{A}_{\text{vp}}$ produced an undistorted relighting pattern for the values of $t = 0$ and $t = 1$ in Fig. 2.7(a) and (b), respectively.

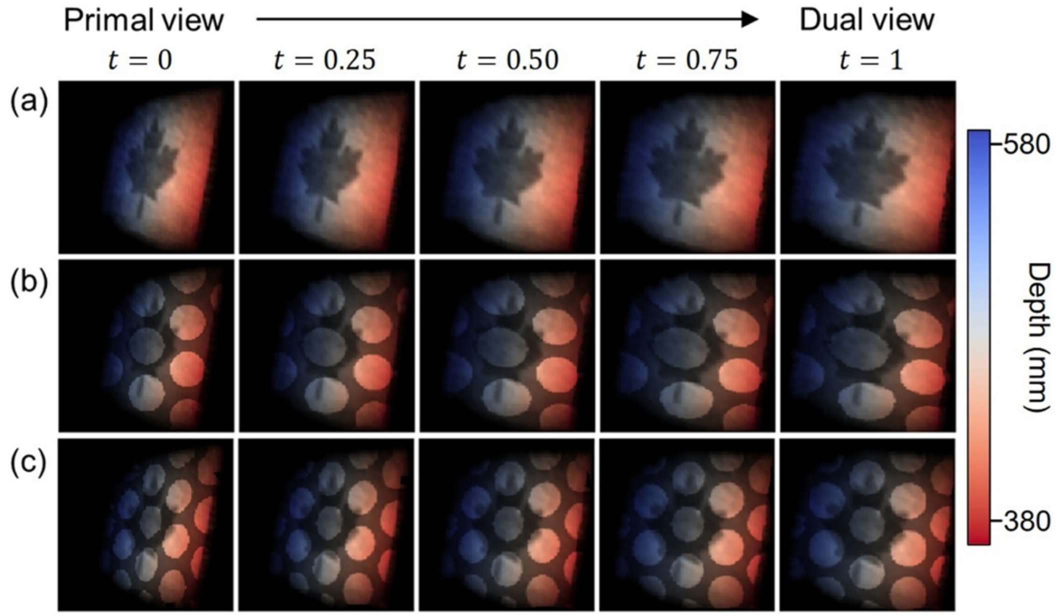

Figure 2.6 3D dual photography and scene relighting with user-selectable camera views. 3D dual photography **(a)** and scene relighting **(b)**–**(c)** with user-selectable camera views. Each column labels a value of t for which $\boldsymbol{A}_{\text{vc}} = (1 - t)\boldsymbol{A}_0 + t\boldsymbol{A}_1$ was chosen to interpolate views between the experimental primal (t = 0) and dual (t = 1) views. In (a), $r(u, v) = 1$. In (b) and (c), $r(u, v)$ was chosen to be a pattern featuring a hexagonal arrangement of circles, while $\boldsymbol{A}_{\text{vp}}$ was set equal to $\boldsymbol{A}_0$ and $\boldsymbol{A}_1$, respectively.

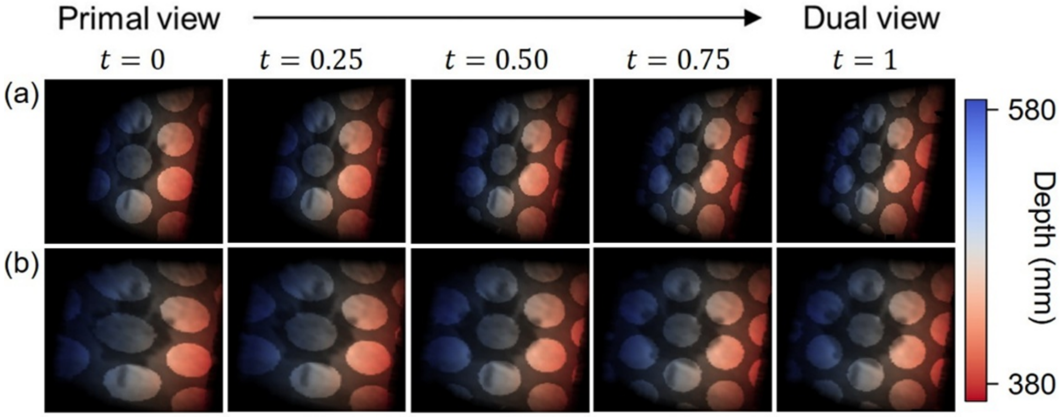

Figure 2.7 3D scene relighting with user-selectable perspectives of illumination. Each column labels a value of t for which $\boldsymbol{A}_{\text{vp}} = (1 - t)\boldsymbol{A}_0 + t\boldsymbol{A}_1$ was chosen to interpolate relighting perspectives between the primal (t = 0) and dual (t = 1) views. The same relighting pattern used in Fig. 2.6(b) and Fig. 2.6(c) was applied to **(a)** and **(b)**, for which $\boldsymbol{A}_{\text{vc}}$ was set equal to $\boldsymbol{A}_0$ and $\boldsymbol{A}_1$, respectively.

2.4 Discussion and conclusions

We have demonstrated camera-free 3D dual photography. FPP-based 3D-to-2D coordinate matching is used both to sense the direct component of the LTM and to associate 3D coordinates with 2D pixels of the camera and the projector. We have developed the STDP system employing two DMDs for both active illumination and virtual fringe projection on an SPI platform. The STDP system has enabled dual photography and scene relighting on 3D images. It has also extended dual photography and scene relighting to user-selectable perspectives between the primal and dual views.

The STDP system possesses several advantages. First, akin to conventional dual photography techniques, the synthesis of 2D dual images in STDP can be achieved without the knowledge of scene geometry, camera/projector parameters, and surface properties. Moreover, STDP extends the performance of dual photography on 3D images. Finally, binary patterns are displayed on both DMDs employed in the STDP system, and grayscale fringe patterns are virtually projected to the 3D objects. These features assure the accuracy in 3D surface profilometry with high pattern stability by avoiding dark noise and digitization error.

The spatial resolution of the STDP system is mainly limited by two factors. First, the number of encoding pixels in each masking pattern sets the upper bound of the spatial resolution. Nonetheless, these masking patterns must be projected with high fidelity. Thus, the number of encoding pixels is ultimately limited by the pixel count of DMD and the optical bandwidth of the illumination module. Second, the photodiode needs to resolve a varying signal across the used masking patterns. As the size of the encoding pixels is decreased, the magnitude of the difference in photodiode signals for displayed masking patterns will diminish. Thus, the signal-to-noise ratio of the photodiode practically limits the spatial resolution of the STDP system.

The future work will focus on further enhancing the imaging capability of the STDP system for new applications. The use of a laser and a photodiode with each DMD, together with Helmholtz reciprocity, makes the STDP system functionally symmetric. This structure allows flexibly implementing many widely adapted algorithms, including ones used in compressed sensing [3, 4, 21, 96] and non-line-of-sight imaging [45, 97, 98], to improve the imaging speed and to measure the global components of the LTM. Meanwhile, by exploiting the advantages of photodiodes in their high sensitivities and broad responsive spectra [99, 100], the STDP system may open new opportunities in few-photon imaging and infrared 3D dual photography, which could facilitate multi-spectral photorealism in computer graphics [55, 56]. Furthermore, the use of multiple collection modules could also generalize our experiment while reducing 3D occlusion and enhancing resolution. STDP is an attractive technique when side-view imaging is exclusively allowed. The possible scenarios include in-situ and undisturbed imaging of animals in their natural habitats (e.g., in cracks at a corner of a stone) [101]. It will also create new FPP-based applications for computer graphics and entertainment. All of these directions are promising research topics in the future.

Funding

Natural Sciences and Engineering Research Council of Canada (ALLRP 551076-20, ALLRP-549833-2020, CRDPJ-532304-18, RGPAS-507845-2017, RGPIN-2017-05959); Canada Foundation for Innovation (37146); Fonds de recherche du Québec – Nature et technologies (2019-NC-252960); Fonds de Recherche du Québec – Santé (267406, 280229).

Acknowledgements

The authors thank Jeremy Gribben and Alan Boate from Ajile Light Industries for their assistance with DMD equipment and software.

Disclosures

The authors declare no conflicts of interest.

Supplementary materials

[**Visualization 1**] Animated GIF image file (6.49 MB).
doi:10.6084/m9.figshare.12624899.v1.

[**Visualization 2**] Animated GIF image file (4.36 MB).
doi:10.6084/m9.figshare.12624902.v1.

References

See collected Bibliography (page 134).

3 ULTRAHIGH-SPEED AND REAL-TIME SINGLE-PIXEL IMAGING

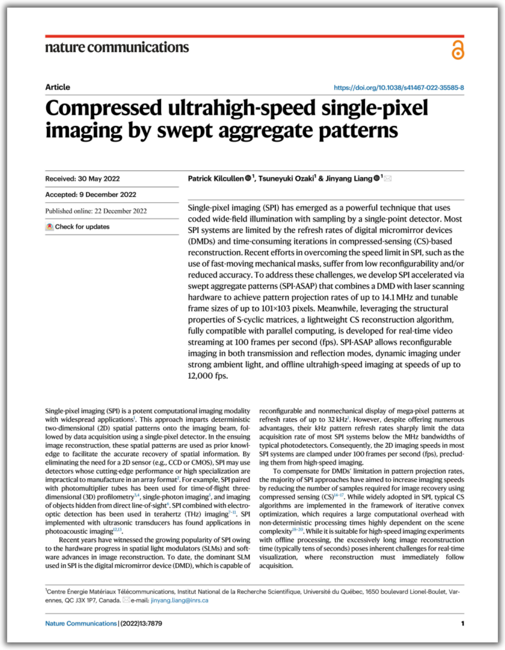

nature communications

Article

https://doi.org/10.1038/s41467-022-35585-8

Compressed ultrahigh-speed single-pixel imaging by swept aggregate patterns

Received: 30 May 2022

Accepted: 9 December 2022

Patrick Kilcullen[1], Tsuneyuki Ozaki[1] & Jinyang Liang[1]

Single-pixel imaging (SPI) has emerged as a powerful technique that uses coded wide-field illumination with sampling by a single-point detector. Most SPI systems are limited by the refresh rates of digital micromirror devices (DMDs) and time-consuming iterations in compressed-sensing (CS)-based reconstruction. Recent efforts in overcoming the speed limit in SPI, such as the use of fast-moving mechanical masks, suffer from low reconfigurability and/or reduced accuracy. To address these challenges, we develop SPI accelerated via swept aggregate patterns (SPI-ASAP) that combines a DMD with laser scanning hardware to achieve pattern projection rates of up to 14.1 MHz and tunable frame sizes of up to 101×103 pixels. Meanwhile, leveraging the structural properties of S-cyclic matrices, a lightweight CS reconstruction algorithm, fully compatible with parallel computing, is developed for real-time video streaming at 100 frames per second (fps). SPI-ASAP allows reconfigurable imaging in both transmission and reflection modes, dynamic imaging under strong ambient light, and offline ultrahigh-speed imaging at speeds of up to 12,000 fps.

Single-pixel imaging (SPI) is a potent computational imaging modality with widespread applications[1]. This approach imparts deterministic two-dimensional (2D) spatial patterns onto the imaging beam, followed by data acquisition using a single-pixel detector. In the ensuing image reconstruction, these spatial patterns are used as prior knowledge to facilitate the accurate recovery of spatial information. By eliminating the need for a 2D sensor (e.g., CCD or CMOS), SPI may use detectors whose cutting-edge performance or high specialization are impractical to manufacture in an array format[2]. For example, SPI paired with photomultiplier tubes has been used for time-of-flight three-dimensional (3D) profilometry[3,4], single-photon imaging[5], and imaging of objects hidden from direct line-of-sight[6]. SPI combined with electro-optic detection has been used in terahertz (THz) imaging[7–11]. SPI implemented with ultrasonic transducers has found applications in photoacoustic imaging[12,13].

Recent years have witnessed the growing popularity of SPI owing to the hardware progress in spatial light modulators (SLMs) and software advances in image reconstruction. To date, the dominant SLM used in SPI is the digital micromirror device (DMD), which is capable of reconfigurable and nonmechanical display of mega-pixel patterns at refresh rates of up to 32 kHz[1]. However, despite offering numerous advantages, their kHz pattern refresh rates sharply limit the data acquisition rate of most SPI systems below the MHz bandwidths of typical photodetectors. Consequently, the 2D imaging speeds in most SPI systems are clamped under 100 frames per second (fps), precluding them from high-speed imaging.

To compensate for DMDs' limitation in pattern projection rates, the majority of SPI approaches have aimed to increase imaging speeds by reducing the number of samples required for image recovery using compressed sensing (CS)[14–17]. While widely adopted in SPI, typical CS algorithms are implemented in the framework of iterative convex optimization, which requires a large computational overhead with non-deterministic processing times highly dependent on the scene complexity[18–20]. While it is suitable for high-speed imaging experiments with offline processing, the excessively long image reconstruction time (typically tens of seconds) poses inherent challenges for real-time visualization, where reconstruction must immediately follow acquisition.

---

[1] Centre Énergie Matériaux Télécommunications, Institut National de la Recherche Scientifique, Université du Québec, 1650 boulevard Lionel-Boulet, Varennes, QC J3X 1P7, Canada. e-mail: jinyang.liang@inrs.ca

Compressed ultrahigh-speed single-pixel imaging by swept aggregate patterns

Imagerie mono-pixel comprimée ultrarapide par balayage de motifs agrégés

Patrick Kilcullen[1], Tsuneyuki Ozaki[1], and Jinyang Liang[1*]

[1] Centre Énergie Matériaux Télécommunications, Institut National de la Recherche Scientifique, Université du Québec, 1650 Boulevard Lionel-Boulet, Varennes, Québec J3X1P7, Canada
[*]jinyang.liang@emt.inrs.ca

Publication: *Nature Communications* **13**:7879 (2022). doi:10.1038/s41467-022-35585-8
Published: 22 Dec 2022

Author Contributions: The initial concept of accelerating pattern deployment via a combination of DMD patterning and optical sweeping was proposed by JL. Later contributions by PK emphasized the potential role of cyclic S-matrices, and the practical advantages of polygonal mirror scanning. Design and construction of the experimental system was carried out by PK which included the development of software necessary for the automation of data collection, and subsequent data analysis. Collection of experimental data was performed by PK. TO engaged in consultation with the authors, particularly with regards to potential applications to terahertz imaging.

Abstract: Single-pixel imaging (SPI) has emerged as a powerful technique that uses coded wide-field illumination with sampling by a single-point detector. Most SPI systems are limited by the refresh rates of digital micromirror devices (DMDs) and time-consuming iterations in compressed-sensing (CS)-based reconstruction. Recent efforts in overcoming the speed limit in SPI, such as the use of fast-moving mechanical masks, suffer from low reconfigurability and/or reduced accuracy. To address these challenges, we develop SPI accelerated via swept aggregate patterns (SPI-ASAP) that combines a DMD with laser scanning hardware to achieve pattern projection rates of up to 14.1 MHz and tunable frame sizes of up to 101×103 pixels. Meanwhile, leveraging the structural properties of cyclic S-matrices, a lightweight CS reconstruction algorithm, fully compatible with parallel computing, is developed for real-time video streaming at 100 frames per second (fps). SPI-ASAP allows reconfigurable imaging in both transmission and reflection modes, dynamic imaging under strong ambient light, and offline ultrahigh-speed imaging at speeds of up to 12,000 fps.

3.1 Introduction

Single-pixel imaging (SPI) is a potent computational imaging modality with widespread applications [1]. This approach imparts deterministic two-dimensional (2D) spatial patterns onto the imaging beam, followed by data acquisition using a single-pixel detector. In the ensuing image reconstruction, these spatial patterns are used as prior knowledge to facilitate the accurate recovery of spatial information. By eliminating the need for a 2D sensor (e.g., CCD or CMOS), SPI may use detectors whose cutting-edge performance or high specialization are impractical to manufacture in an array format [6]. For example, SPI paired with photomultiplier tubes has been used for time-of-flight three-dimensional (3D) profilometry [21, 102], single-photon imaging [20], and imaging of objects hidden from direct line-of-sight [103]. SPI combined with electro-optic detection has been used in terahertz (THz) imaging [19, 46, 104–106]. SPI implemented with ultrasonic transducers has found applications in photoacoustic imaging [83, 107].

Recent years have witnessed the growing popularity of SPI owing to the hardware progress in spatial light modulators (SLMs) and software advances in image reconstruction. To date, the dominant SLM used in SPI is the digital micromirror device (DMD), which is capable of reconfigurable and non-mechanical display of mega-pixel patterns at refresh rates of up to 32 kHz [1]. However, despite offering numerous advantages, their kHz pattern refresh rates sharply limit the data acquisition rate of most SPI systems below the MHz bandwidths of typical photodetectors. Consequently, the 2D imaging speeds in most SPI systems are clamped under 100 frames per second (fps), precluding them from high-speed imaging.

To compensate for DMDs' limitation in pattern projection rates, the majority of SPI approaches have aimed to increase imaging speeds by reducing the number of samples required for image recovery using compressed sensing (CS) [3, 4, 27, 108]. While widely adopted in SPI, typical CS algorithms are implemented in the framework of iterative convex optimization, which requires a large computational overhead with non-deterministic processing times highly dependent on the scene complexity [7–9]. While it is suitable for high-speed imaging experiments with offline processing, the excessively long image reconstruction time (typically tens of seconds) poses inherent challenges for real-time visualization, where reconstruction must immediately follow acquisition.

Towards this goal, many ensuing developments have substituted DMDs with new light sources and modulators [13, 43, 44, 109]. One recent approach has used a high-speed illumination module comprised of an array of 32×32 light-emitting diodes (LEDs) [43, 44]. Although this method has demonstrated a pattern deployment rate of 3.13 MHz and a CS-assisted 2D imaging rate of 25 thousand frames per second (kfps), the performance of its patterned light source, which requires custom hardware, is closely tied to the display of Hadamard patterns that possess certain symmetry properties. Moreover, because the patterns were directly provided by LED illumination, this approach is inapplicable to many types of SPI requiring either passive detection [45] or specialized light sources, such as lasers [18].

Alternatively, the speed of SPI systems can be enhanced by using patterned transmissive masks mechanically scanned at high speeds [13, 53]. Coded patterns etched onto printed circuit boards have been used in THz and millimeter-wave SPI for over a decade [47–52]. Systems of this sort frequently employ fast rotating disks to impart spatial modulation to the illumination [110, 111]. To enhance pattern deployment from continuous rotation, much emphasis in pattern design and reconstruction has been placed on the use of cyclic matrices [90, 91, 112–114], which allow for the deployment of a new masking pattern from a translational shift of only one pattern pixel [115]. The latest development in this approach reported a pattern projection rate of 2.4 MHz, which transferred to a non-CS recovery of a frame size of 101×103 pixels at 72 fps [13]. In another study [53], assisted by CS and optimization-based image reconstruction, the imaging speed reached 100 fps despite a reduced frame size of 32×32 pixels. However, in contrast to the advantages of reconfigurable DMDs, these physical masks often increase the systems' complexity and considerably reduce their flexibility. For example, the inherent trade-off between pixel count and pixel size for fixed disk dimensions suggests an increased difficulty in manufacturing for larger encoding masks. Consequently, auxiliary tools, such as a synchronized steering mirror [13], may be required to correct inaccurate radial motion caused by the non-concentricity of the patterns.

To overcome these limitations, we develop single-pixel imaging accelerated via swept aggregate patterns (SPI-ASAP). The implementation of laser scanning rapidly deploys individual encoding masks as optically selected sub-regions of larger aggregate patterns that are displayed via DMD. In this way, pattern aggregation enhances SPI data acquisition rates to more than two orders of magnitude above the limitations of DMD-only modulation, while still retaining the high pixel count and flexibility of pattern display with DMDs. Meanwhile, a fast CS reconstruction algorithm, which is tightly coupled with the architecture of pattern deployment, is developed with full compatibility with parallel computing for real-time visualization. Altogether, SPI-ASAP projects encoding patterns at a rate of up to 14.1 MHz, allowing for reconfigurable 2D imaging offline at up to 12 kfps. Unrestricted by the iterative optimization of conventional CS-based image reconstruction, SPI-ASAP empowers real-time video operation at 100 fps for frame sizes of up to 101×103 pixels.

3.2 Results

3.2.1 System setup

A schematic of the SPI-ASAP system is shown in Fig. 3.1. A 200 mW continuous-wave laser operating at 671 nm is used as the light source. The ultrahigh-speed pattern sweeping is generated by a 16-facet polygonal mirror, a 0.45" DMD, and associated optical components (lenses L1–L5 in Fig. 3.1). The incident beam is first reflected by a facet of the polygonal mirror, which creates illumination that rapidly moves across the DMD surface at a 24° angle of incidence. Binary patterns, represented numerically as $\{0, 1\}$-valued 2D arrays, are displayed on this DMD. Containing an array

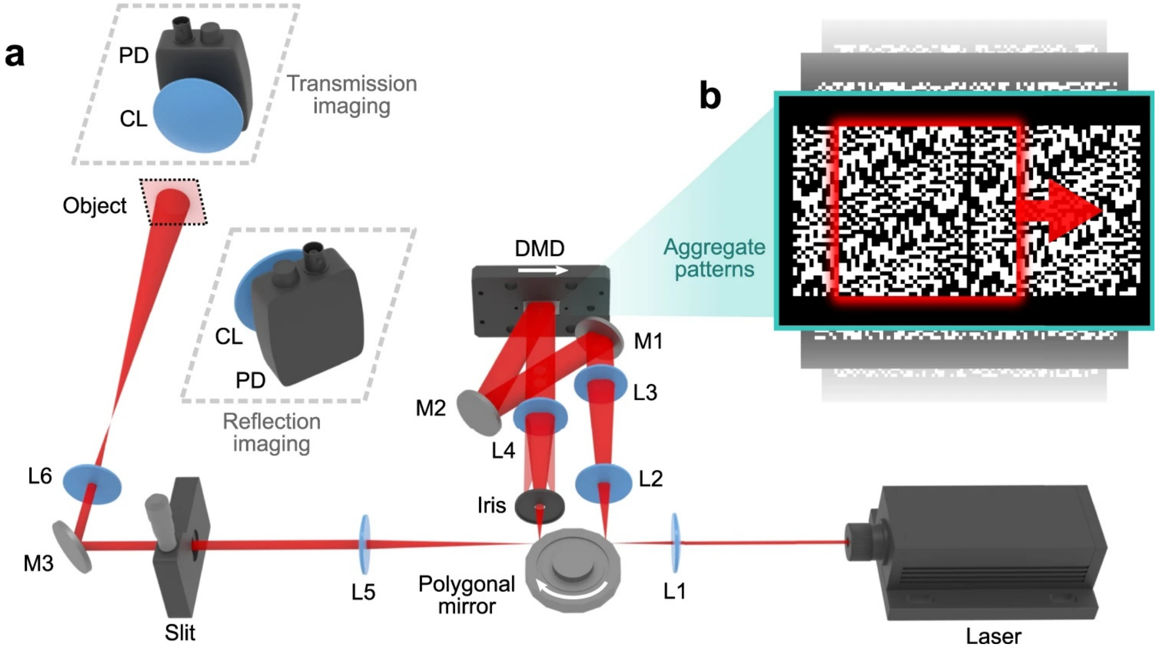

Figure 3.1 Schematic of SPI-ASAP. **(a)** System illustration showing beam scanning of a DMD-displayed aggregate pattern by rotation of a polygonal mirror. White arrows indicate directions of polygonal mirror rotation and illumination scanning. CL, condenser lens; DMD, digital micromirror device; L1–L6, lenses; M1–M3, mirrors; PD, photodiode. **(b)** Closeup of an example aggregate pattern in a sequence suitable for imaging at a frame size of 41×43 pixels. Red box: a representative encoding pattern. Red arrow: scanning direction.

of 912×1140 square micromirrors (7.6 μm pitch), the DMD uses tilt actuation to either discard the beam (via the 0-valued pixels) or reflect it (via the 1-valued pixels) back to the polygonal mirror. An iris, positioned near the back focal plane of L4, selects the strongest diffraction order. Owing to the symmetry of the optical path, the second reflection by the polygonal mirror imparts an equal and opposite scanning motion to the imaging beam, which stabilizes its position at an adjustable slit. Meanwhile, because this slit receives an image of the illuminated part of the DMD's surface, stabilization by the second reflection also imparts a rapid scanning motion to the patterns that tracks with the motion of the scanned illumination. This dual-scanning operation increases the optical efficiency of SPI-ASAP over that of a single-scanned design because illumination is concentrated on only the parts of the DMD surface that are conveyed to the adjustable slit.

During operation, each scan induced by a polygonal mirror facet is synchronized with the display of a new aggregate binary pattern pre-stored by the DMD. After transmitting through the slit, the structured illumination interrogates the structure of objects placed in the image plane (imaged by lens L6). A portion of light transmitted or reflected by an object is focused by a condenser lens to a photodiode that is positioned to receive light in either the transmission mode or the reflection mode. The recorded data points, referred to as "bucket signals", are transferred to a computer for ensuing image processing. The full details of the experimental setup, principles of laser beam encoding and de-scanning, as well as system synchronization, are discussed in Methods, Supplementary Notes 1–2, and Supplementary Figs. 3.7–3.8. A discussion of the advantages of polygonal mirror scanning in SPI-ASAP, as well as a performance comparison with previous scanning SPI systems, is provided in Supplementary Note 3, Supplementary Fig. 3.9, and Supplementary Table 3.1.

3.2.2 Coding strategy and image recovery

The bucket signals, denoted by an m-element vector $\boldsymbol{y}$, can be regarded as the optically computed inner products between an n-pixel image $\boldsymbol{x}$ and the set of encoding patterns $\{\boldsymbol{s}_i, i = 1, \ldots, m\}$. This process can be expressed in the form of a single m by n matrix equation

$$\boldsymbol{y} = \boldsymbol{S}\boldsymbol{x} \quad , \tag{3.1}$$

where the measurement matrix $\boldsymbol{S}$ contains each encoding pattern written in row form and corresponding to the order of the bucket signals in $\boldsymbol{y}$. SPI-ASAP uses cyclic S-matrices to generate encoding patterns, with Fig. 3.2a illustrating an example for $n = 35$. Individual encoding patterns arise from the 2D reshaping of the rows of $\boldsymbol{S}$ by row-major ordering. Writing $n = pq$ for the dimensions of the reshaped rows, it is possible to restructure the information in $\boldsymbol{S}$ to form a $(2p-1)\times(2q-1)$ pattern that exactly encompasses all 2D encoding patterns determined by its rows. An example of such restructuring is shown in Fig. 3.2b, from which it can be seen that each $p \times q$ sub-region represents a 2D reshaped row of $\boldsymbol{S}$, with the corresponding row index appearing as the number in the top leftmost corner element. In each scan, a $p \times (2q-1)$ sub-region of the restructured matrix pattern displays on the DMD. The scanning action of the optical system then sequentially illuminates and projects each $p \times q$ sub-area of this pattern, resulting in the deployment of q encoding patterns (see an example in Fig. 3.2b). This process then repeats, each time using a different $p \times (2q-1)$ sub-region of the restructured matrix pattern to aggregate the deployment of q encoding patterns in each scan. After p scans, a full measurement is completed when the DMD-displayed aggregate patterns traverse through the entire restructured matrix pattern. More details of cyclic S-matrices are discussed in Methods.

Owning to the 2D packing relationship of the encoding patterns within the restructured matrix pattern, their deployment in SPI-ASAP can be regarded as an operation of 2D discrete convolution on the $(2p-1)\times(2q-1)$ restructured matrix pattern, with the underlying image used as a kernel of size $p \times q$. Thus, because of the high similarity in the structures of spatially adjacent encoding patterns, the bucket signals $\boldsymbol{y}$ exhibit 2D smoothness when reshaped to a matrix $\boldsymbol{Y}$ of the same size as the image (Fig. 3.2c). Moreover, periodic boundary conditions are exhibited by $\boldsymbol{Y}$, allowing 2D smoothness to extend to all elements. Therefore, in general, a bucket signal indexed to row i of $\boldsymbol{S}$ will exhibit a high similarity with the bucket signals that surround it in $\boldsymbol{Y}$, with the four nearest neighbouring bucket signals in particular corresponding to the rows $i-1$, $i+1$, $i-q$, and $i+q$ in $\boldsymbol{S}$, with q denoting the width of the reshaped rows and indices interpreted modulo n.

This property motivates a strategy to incorporate CS (i.e., $m < n$) in rapid image recovery. By

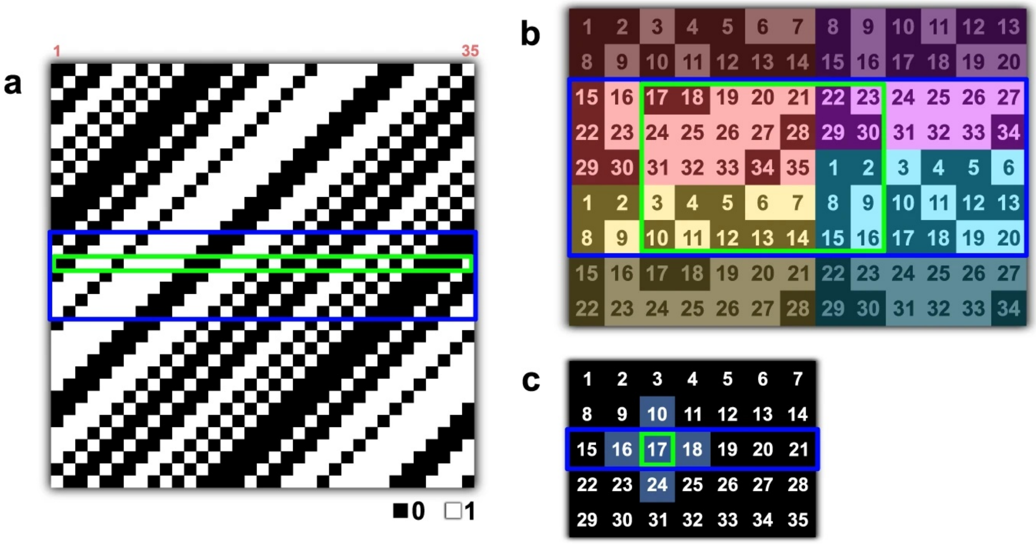

1	2	3	4	5	6	7	8	9	10	11	12	13
8	9	10	11	12	13	14	15	16	17	18	19	20
15	16	17	18	19	20	21	22	23	24	25	26	27
22	23	24	25	26	27	28	29	30	31	32	33	34
29	30	31	32	33	34	35	1	2	3	4	5	6
1	2	3	4	5	6	7	8	9	10	11	12	13
8	9	10	11	12	13	14	15	16	17	18	19	20
15	16	17	18	19	20	21	22	23	24	25	26	27
22	23	24	25	26	27	28	29	30	31	32	33	34

1	2	3	4	5	6	7
8	9	10	11	12	13	14
15	16	17	18	19	20	21
22	23	24	25	26	27	28
29	30	31	32	33	34	35

Figure 3.2 Coding strategy of SPI-ASAP. (a) Binary cyclic S-matrix of order $n = 35$ (i.e., $p = 7$ and $q = 5$). Green boxes (also appearing in (b) and (c)) highlight the role of a single encoding pattern. Blue boxes (also appearing in (b) and (c)) highlight a range of p rows deployed together in each scan. **(b)** Restructured matrix pattern formed from the matrix shown in (a). The numbers represent the corresponding column indices of each element of the first row of the matrix shown in (a), with shaded colors highlighting four tiled copies of the reshaped initial row. The blue-boxed region shows an aggregate pattern that is displayed via DMD. The green-boxed region shows the single encoding pattern (corresponding to row 17) also highlighted in (a). **(c)** Arrangement of the bucket signals as a 2D array with numbers corresponding to row indices of the matrix in (a). Gray shading highlights an expected neighbourhood of similar values surrounding the measurement from the encoding pattern highlighted in green in (b). The blue-boxed region shows a row of bucket signals acquired from the deployment of the aggregate pattern high-lighted in (b).

using carefully selected encoding patterns, a set of evenly distributed samples is selected on $\boldsymbol{Y}$. Then, the values of non-sampled elements can be estimated by interpolation, which empowers image recovery by direct inversion of Eq. (3.1). The architecture of SPI-ASAP enables a particular sampling strategy in which bucket signals corresponding to complete rows of $\boldsymbol{Y}$ are acquired in each scan. Aggregate patterns are thus formed in the manner shown by the purple boxes in Fig. 3.2, with the displayed DMD pattern sequence determined by an evenly distributed selection of rows from $\boldsymbol{Y}$.

In this case of row-wise subsampling, non-sampled data in $\boldsymbol{Y}$ can be approximated by one-dimensional (1D) interpolation along columns with a method such as spline interpolation. This operation, along with optional low-pass filtering, can be implemented using only matrix multiplication with the assistance of pre-computed elements. Thus, SPI-ASAP's reconstruction algorithm is compatible with the architecture of a graphic processing unit (GPU) for real-time visualization. Meanwhile, by sectioning streams of bucket signals generated by continuous scanning, videos can be reconstructed with tunable frame rates. Details regarding the sequencing of aggregate patterns, data segmentation for video reconstruction, determination of imaging speeds, and implementation of image reconstruction using matrix multiplication are provided in Methods. Simulated comparisons of SPI-ASAP to existing CS-based reconstruction algorithms [5] are provided in Supplementary Note 4. The results of this comparison (see Supplementary Fig. 3.10) show that SPI-ASAP

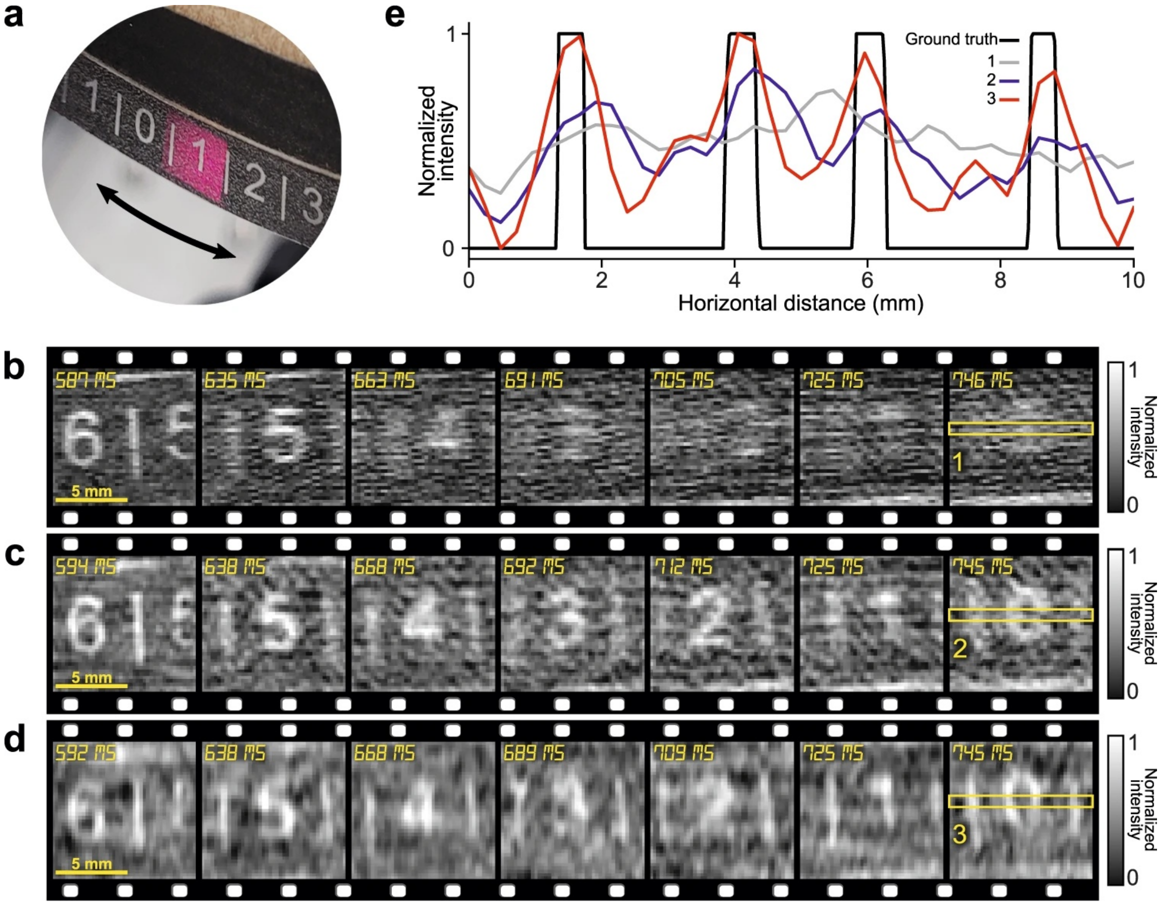

Figure 3.3 SPI-ASAP of motion of a transmissive position ruler attached to a pendulum. **(a)** Photograph of position ruler and illuminated FOV of 10 mm × 10 mm. **(b)**–**(d)** Selected frames from reconstructions with 100% sampling at 145 fps (b), 50% sampling at 298 fps (c), and 25% sampling at 598 fps (d). **(e)** Normalized average intensity profiles from a selected region with a size of 5×43 pixels (marked by the yellow boxes in (b)–(d)), compared to the ground truth.

accelerates reconstruction speeds by 2–3 orders of magnitude while maintaining comparable or superior reconstructed image quality.

3.2.3 Demonstration of SPI-ASAP in transmission mode

To prove the concept of SPI-ASAP, we imaged the dampened oscillations of a pendulum object with a 10 cm radius. As shown in Fig. 3.3a, on the bottom of this pendulum is a scale consisting of the digits “0” to “9” separated by vertical lines. “0” is placed at the pendulum’s rest position, and the remaining digits are placed symmetrically at increasing distances. Working in transmission mode, the SPI-ASAP system had a frame size of 41×43 pixels ($n = 1{,}763$), corresponding to a field-of-view (FOV) of approximately 10 mm × 10 mm.

The motion of the pendulum was recorded over 1.54 seconds during which the pendulum exhibited dampened oscillations and came to rest at equilibrium. Supplementary Movie 1 shows three videos reconstructed from this dataset corresponding to sampling rates of 100%, 50%, and 25%, with imaging speeds of 145 fps, 298 fps, and 598 fps, respectively. Fig. 3.3b–d show representative frames from each reconstructed video. Unlike conventional imaging for which fast-moving objects may exhibit only localized motion blurring, the sequential and wide-field nature of SPI's data acquisition produces global artifacts for highly dynamic scenes. As illustrated by the profiles compared in Fig. 3.3e, increased frame rates by CS-assisted SPI-ASAP reduce these blur artifacts, allowing details of fast-moving objects to be resolved. Attractively, this flexibility is controlled entirely at the reconstruction stage, thus allowing a balance between overall image quality and frame rate to be optimized to suit specific datasets.

3.2.4 Demonstration of SPI-ASAP in reflection mode

To test the SPI-ASAP system in reflection mode, we imaged the internal components of a running mechanical watch movement (Fig. 3.4a). The balance wheel, which controlled the intermittent motion of the escape wheel, underwent sustained oscillatory motion at approximately 2.5 Hz. The SPI-ASAP system had a FOV of 14 mm × 14 mm, a frame size of 59×61 pixels, and an imaging speed of 103 fps (with 100% sampling). Fig. 3.4b illustrates selected frames from the reconstructed videos, with the full sequence shown in Supplementary Movie 2. Intensity data from three pixels are plotted in Fig. 3.4c to study the motion of the internal wheels. Pixel 1 selects a position that is darkened once per full oscillation of the balance wheel and thus allows for quantification of the 2.5 Hz oscillation frequency. Pixels 2 and 3 select positions that are alternatively darkened by the passage of one tooth of the escape wheel that intermittently moves twice per balance wheel oscillation.

Another reflection-mode experiment captured the heating-induced rupture of a popcorn kernel. As shown in Fig. 3.4d, the kernel was held upright by a metal holder and heated by a forced stream of hot air from a heat gun. The SPI-ASAP system imaged this event at 298 fps (with 50% sampling) and with a FOV of 14 mm × 14 mm (41×43 pixels). The reconstructed movie is shown in Supplementary Movie 3 with selected frames shown in Fig. 3.4e. As visualized in Fig. 3.4f, the rupture of the kernel's shell initiated on its upper right side, with the subsequent expansion of the kernel's interior causing the kernel to be pulled from the holder by the air stream.

3.2.5 SPI-ASAP in strong ambient light

Since an imaging relationship need not exist between object and detector in SPI, SPI systems can tolerate optical disruption of the imaging beam that may occur between the pattern-illuminated object and detection with the non-imaging sensor [34, 45, 103, 116, 117]. This characteristic well-positions SPI for scenarios requiring extreme optical filtering, such as for scenes involving intense and varying ambient light. To demonstrate this capability in high-speed SPI-ASAP, we studied the

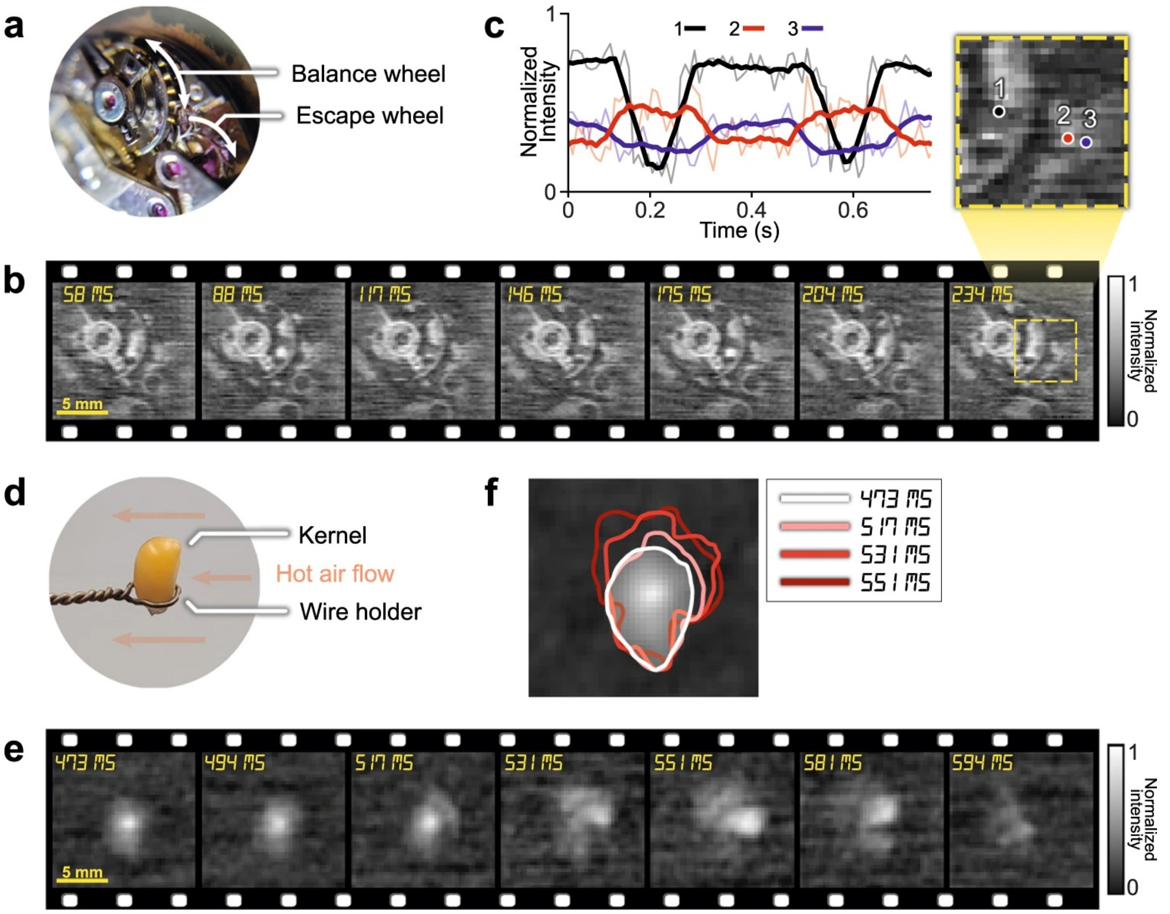

Figure 3.4 SPI-ASAP in reflection mode. **(a)** Photo of the internal components of the mechanical watch. **(b)** Selected frames of the running mechanical watch movement imaged at 103 fps. **(c)** Time evolution of the intensity of the three selected pixels (marked in the expanded inset from (b)), illustrating the approximate 2.5 Hz motion of the balance wheel and the 5.0 Hz intermittent motion of the escape wheel. Thick lines show moving averages (7-frame window) with raw data shown by the thin lines. **(d)** Experimental setup for imaging the rupture of a popcorn kernel. **(e)** Selected frames of the heating-induced rupture imaged at 298 fps with 50% sampling. **(f)** Traced outlines of the kernel from selected frames showing its expansion during rupture.

current-induced failure of incandescent light bulb filaments in two experimental conditions (Fig. 3.5). To remove the strong and time-varying incandescence, we built spatial and chromatic filtering stages on the detection side (see details in Supplementary Note 5 and Supplementary Fig. 3.11). SPI-ASAP operated at 298 fps (50% sampling) and with a FOV of 11 mm × 11 mm (41×43 pixels).

The first experiment used a sealed un-modified bulb (Fig. 3.5a). Selected frames from the reconstructed video (Supplementary Movie 4) are shown in Fig. 3.5b. The burn-out of the filament occurred after 3–5 seconds of increasing incandescence. The result reveals that the failure occurred at the left connection between the filament and the supporting wire lead, followed by the deposition of the vaporized metal from the supporting wires on the interior of the glass bulb surface. This process led to a reduced transmission through the bulb, which is observed in Fig. 3.5b as an overall darkening following the initiation of the failure (Fig. 3.5c).

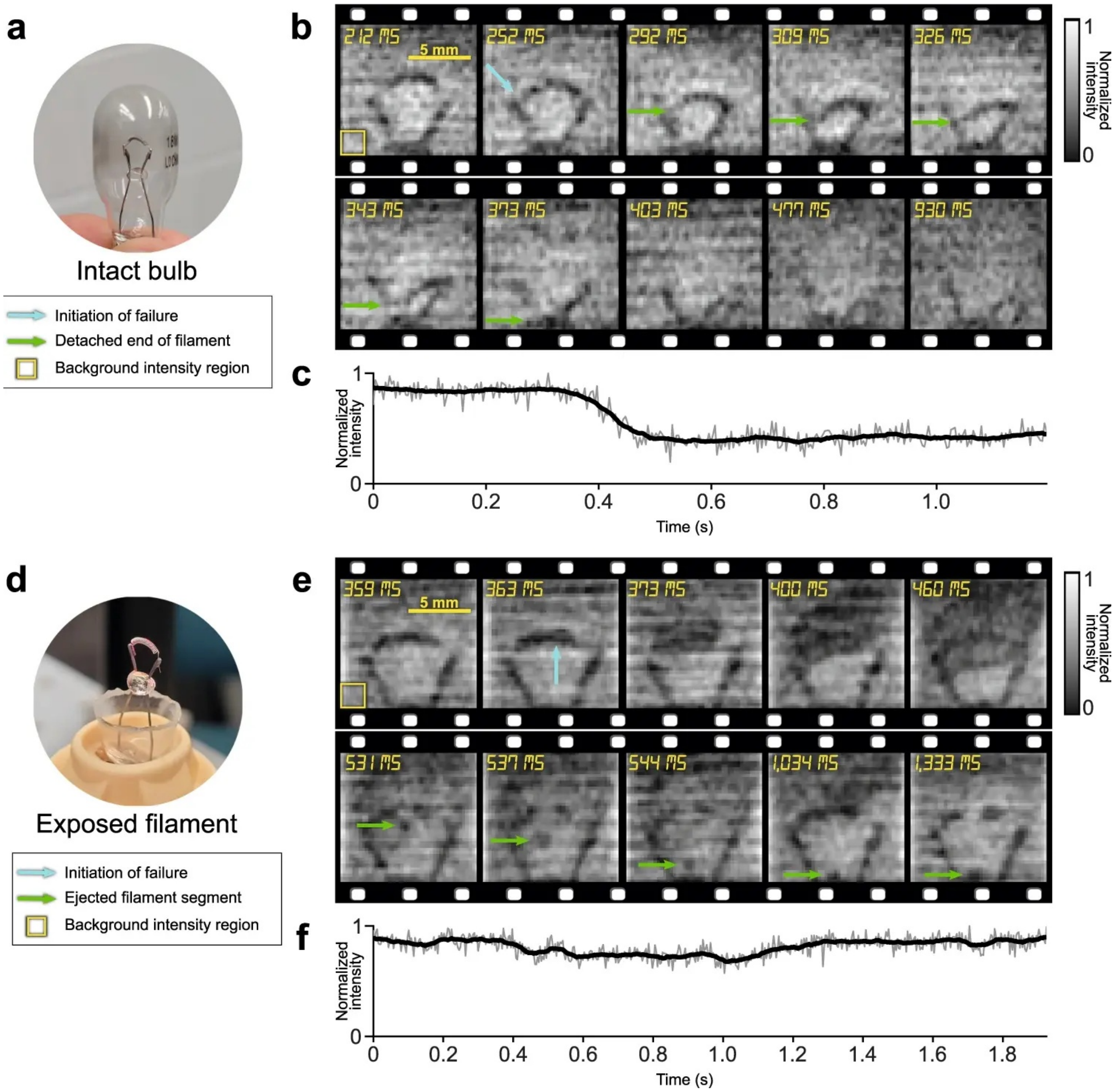

Figure 3.5 SPI-ASAP of the burn-out of incandescent filaments. **(a)** Photo of an unmodified bulb showing the enclosed filament. **(b)** Selected frames of the reconstructed video of the unmodified bulb. **(c)** Time evolution of the intensity of a background region (8×8 pixels) highlighted in (b). Thick line shows the moving average (21 frame window) with raw data shown by the thin line. **(d)** Photo of a modified bulb showing direct exposure of filament to air. **(e)** Selected frames of the reconstructed video of the modified bulb. **(f)** As (c), but from the background region in (e).

As a comparison, in the second experiment the cover glass of the bulb was removed (Fig. 3.5d). The evolution of this dynamic event is shown in Supplementary Movie 5, with selected frames presented in Fig. 3.5e. In contrast to the first experiment, the filament exposed to air had a quicker failure, which initiated after 1–2 seconds of increasing incandescence. Moreover, failure occurred in the filament material itself from combustion due to the presence of oxygen in air. The result also reveals the emission of smoke and vaporized material as well as the ejection of a section of filament material that fell onto and fused with the portion of glass bridging between the filament support wires. Finally, Fig. 3.5f shows the time evolution of the background intensity of an identical

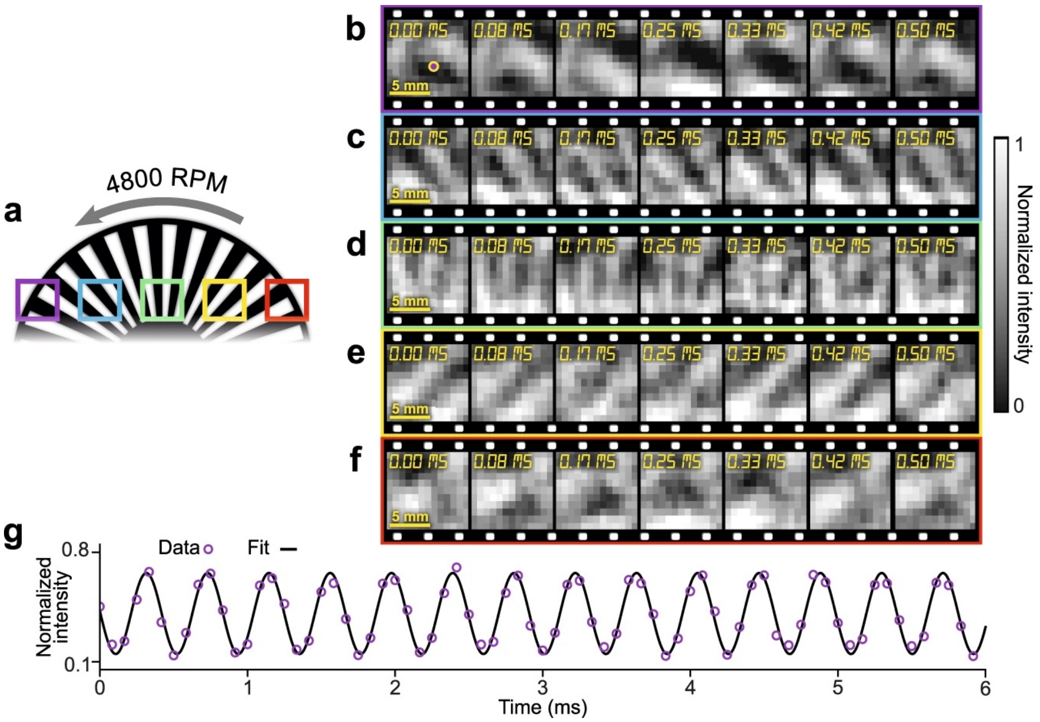

Figure 3.6 Ultrahigh-speed SPI-ASAP of an optical chopper rotating at 4,800 RPM. **(a)** Schematic of the experimental setup. Color boxes show regions imaged by SPI-ASAP. **(b)**–**(f)** Consecutive frames of reconstructed ultrahigh-speed videos with outline colors corresponding to the FOV positions shown in (a). **(g)** Time history of normalized intensity for a selected pixel (marked by the purple point in (b)).

region of background pixels as that shown in Fig. 3.5c.

3.2.6 Ultrahigh-speed SPI-ASAP at 12 kfps

For the above-discussed experiments, the operation of SPI-ASAP requires the scan-synchronized deployment of multiple aggregate patterns by the DMD, whose maximum refresh rate limits the system's performance. To further increase the imaging speed, data acquisition was carried out at the maximum scan rate of the polygonal mirror (i.e., 12 kHz) with a single static mask that combined a sufficient number of aggregate patterns to allow for reconstruction at 55% sampling (more details about the pattern generation and signal timing are included in Supplementary Note 6 and Supplementary Fig. 3.12). Using this experimental configuration, we imaged a 30 slot optical chopper rotating at 4,800 RPM (Fig. 3.6a). The SPI-ASAP system imaged five different locations, each with a FOV of 10 mm × 10 mm and a frame size of 11×13 pixels.

Fig. 3.6b–f show consecutive frames from dynamic videos (see Supplementary Movie 6) captured at 12 kfps, thus demonstrating the maximum possible frame rate of SPI-ASAP based on its current hardware. A time history of normalized intensity from a selected pixel is shown in Fig. 3.6g. By using a sinusoidal fitting, the wheel chop rate was determined to be 2408.9 Hz corresponding to a linear speed at the edge of the wheel of 25.7 ms^{-1}, in agreement with the experimental conditions.

3.2.7 Demonstration of real-time SPI-ASAP

The reconstruction algorithm adopted by SPI-ASAP is well-suited for real-time operation, in which recovery and display of images must follow acquisition immediately with minimal delay. A filmed demonstration of SPI-ASAP operating in real-time for a variety of scenes, frame sizes, and frame rates is included in Supplementary Movie 7. It shows the system operating at a frame size of 59×61 pixels with a real-time display at 51 fps and 100 fps (corresponding to 100% and 50% sampling, respectively), a 71×73 pixel frame size at 84 fps (50% sampling), and a 101×103 pixel frame size at 97 fps (30% sampling). GPU-computed matrix multiplications for image reconstruction typically required 0.4 ms. Data processing times, encompassing the registration of photodiode signals, image reconstruction, and display, were typically 1.0 ms.

3.3 Discussion

We have developed SPI-ASAP based on the concept of swept aggregate patterns to enhance the capabilities of SPI for ultrahigh-speed and real-time imaging. In contrast to existing SPI methods, SPI-ASAP synergizes DMD modulation and polygonal mirror scanning to retain the practical advantages of DMDs in flexible and reconfigurable pattern projection, while extending the rate of pattern deployment by over two orders of magnitude. We have demonstrated SPI-ASAP for high-speed and real-time imaging by recording various dynamic scenes in both reflection and transmission across various frame sizes. In both the reflection and transmission modes, SPI-ASAP shows its flexibility for frame size and frame rate, resilience to strong ambient light, and its capability of ultrahigh-speed imaging at up to 12 kfps.

While currently limited by the specifications of core components, SPI-ASAP's performance could be further enhanced by optimized selections of DMD and laser scanning hardware. The pattern deployment rate of the current SPI-ASAP system is limited by the maximum display rate of the DMD (i.e., 6.37 kHz), which was approximately 53% of the 12 kHz maximum scan rate of the polygonal mirror. As discussed in Supplementary Note 3, the scan duty cycle of the current SPI-ASAP system is compatible with an approximately 10× increase in mirror facet count, which would correspond to a maximum scan rate of 120 kHz using 45,000 RPM motorization. If the fastest DMD (with a 32 kHz refresh rate) were used, the performance of SPI-ASAP could be increased by five times, while ultrahigh-speed SPI-ASAP performance would be increased by a factor of 10. Finally, the currently deployed interpolation method for SPI-ASAP is designed to maximally leverage the parallel computing ability of GPUs. Undoubtedly, other sophisticated interpolation methods [118, 119] could also be explored to potentially improve reconstruction quality while maintaining fast reconstruction.

As primarily a source of structured illumination, DMDs also impose restrictions for the optical sources compatible with SPI-ASAP, which must be compatible with both the 1̃0 μm size of individual

DMD micromirrors and the transmission properties of the DMD's cover window. Frame size and FOV are also influenced by the DMD's size and pixel count, as well as the noise and bandwidth properties of the photodiode. Owing to the correlative behavior of the swept masks, information of image structure is represented in small variations in photodetector signals, which in general fluctuate more rapidly and with decreased amplitude as the frame size of deployed patterns is increased. Consequently, the photodiode's signal-to-noise ratio would ultimately limit frame size and scanning rate under the coding strategy of SPI-ASAP. Meanwhile, the focal lengths and clear apertures of the optics that image the DMD-displayed patterns to the object (i.e., L4–L6 in Fig. 3.1 and Supplementary Fig. 3.7) constrain the optical bandwidth of pattern projection, which thus limits SPI-ASAP's frame sizes by constraining the minimum pixel size of encoding patterns to be compatible with the system's optical point spread function. Additionally, timing inaccuracies caused by polygonal mirror defects as well as the continuous motion of the encoding patterns contribute to an anisotropic spatial resolution. Investigation of this property of SPI-ASAP and an analysis of contributing factors are provided in Supplementary Note 7 and Supplementary Fig. 3.13.

As a coded-aperture imaging modality [96], SPI-ASAP holds promises in terms of broad application scope. Besides the active-illumination-based applications demonstrated in this work, the principle of SPI-ASAP is readily applicable to high-speed imaging with passive detection, which will open new routes to applications that rely on self-luminescent events, such as optical property characterization of nanomaterials [120] and the monitoring of neural activities [121]. SPI-ASAP for imaging in strong ambient light conditions could also be adopted for the study of combustion phenomena [122]. The non-imaging relationship between object and detector in SPI-ASAP indicates its potential applications for non-line-of-sight imaging [45]. Combining SPI-ASAP with 3D profilometry will lead to the immediate application of scene relighting on high-speed 3D objects [10]. Extending the operational spectral range of SPI-ASAP will enable fast hazardous gas detection [18]. Finally, SPI-ASAP may find applications in inducing patterned regions of high conductivity in semiconductor materials for high-speed 2D THz imaging [19, 33, 46].

3.4 Methods

3.4.1 Geometry of beam scanning

The design of SPI-ASAP uses a rotating polygonal mirror in a double-reflection arrangement, which translates scanned illumination of the DMD surface into the swept deployment of encoding patterns. Closeups of the polygonal mirror and DMD reflections producing the desired scan behavior are illustrated in Supplementary Fig. 3.8. The basis of this behavior is the angular correlation of the scanned and de-scanned beams during mirror rotation. This requirement can be expressed by $\varphi_1 = \varphi_2$ for scan angles φ_1 and φ_2 (see Supplementary Fig. 3.8a) for light that respectively illuminates and is reflected by the DMD surface. At the position of the DMD shown in Supplementary Fig. 3.8b, this requirement transfers to the correlation of lateral beam shifts as the DMD surface is scanned by illumination with an incident angle of $\theta = 24°$. If scan optics with a focal length f_1 are used to collimate the illuminating beam, the generated lateral shift is expressed by $d_1 = f_1\varphi_1$. Subsequent reflections of the beam by planar mirrors (M1 and M2 in Supplementary Fig. 3.7a) do not alter such lateral shifts. As illustrated by the geometry of Supplementary Fig. 3.8b, the diffraction of the DMD produces a lateral shift of $d_2 = d_1 \sec\theta$. De-scanning optics of focal length f_2, re-focusing the reflected beam, then produce an angular variation of $\varphi_2 = d_2/f_2$. Combining this information produces the design requirement $f_1 = f_2 \cos\theta$, which dictated the selection of lenses L2–L4 in the SPI-ASAP system. For de-scanning, a single lens (L4) was chosen. For scanning, two lenses (L2 and L3) with specific positioning were used to produce the required effective focal length. Complete details of lens selection and positioning are included in Supplementary Note 1.

3.4.2 Cyclic S-matrices

SPI-ASAP encodes measurements by using cyclic S-matrices. In general, S-matrices are defined as the class of $\{0,1\}$-valued matrices that possess a maximal possible value of the determinant [14, 17]. It can be shown that for a non-trivial S-matrix $\boldsymbol{S}$ of order n [10, 15],

$$\boldsymbol{S}^{-1} = \frac{2}{n+1}\left(2\boldsymbol{S}^{T} - \boldsymbol{J}\right) \quad , \tag{3.2}$$

where $\boldsymbol{J}$ denotes the all-ones matrix with size $n \times n$, $\boldsymbol{S}^T$ denotes the matrix transpose of $\boldsymbol{S}$, and n must be of the form $4k - 1$ for some positive integer k. In the case of cyclic S-matrices, an additional cyclic structure is imposed by which the initial row determines all subsequent rows via left-wise circular shifts. Let $\boldsymbol{S}_{i,j}$ denote the element of $\boldsymbol{S}$ with row index i and column index j. The initial row $\boldsymbol{S}_{0,j}$ $(j = 0, \ldots, n-1)$ then determines all elements of $\boldsymbol{S}$ according to

$$\boldsymbol{S}_{i,j} = \boldsymbol{S}_{0,i+j} \quad , \tag{3.3}$$

where $i = 0, \ldots, n-1$, and the indices are interpreted modulo n. The consequences of the circular structure are that $\boldsymbol{S}$ is symmetric (i.e. $\boldsymbol{S} = \boldsymbol{S}^T$) and that $\boldsymbol{S}^{-1}$ is also circular. Several methods are known for the construction of cyclic S-matrices. For imaging, it is desirable that n can be factorized into parts of approximately equal size. Fortunately, given any pair of twin primes p and $q = p + 2$, it is possible to construct a cyclic S-matrix of order $n = pq$ [23, 92].

The computation of $\boldsymbol{S}_{0,j}$ depends on the following property. An integer x is called a quadratic residue (mod y) if $x \neq 0$ (mod y) and there exists another integer z such that $x \equiv z^2$ (mod y). In this case, the following functions can be defined:

$$f(j) = \begin{cases} +1 & \text{if } j \text{ is a quadratic residue (mod } p) \\ 0 & \text{if } j \equiv 0 \pmod{p} \\ -1 & \text{otherwise} \end{cases}, \tag{3.4}$$

and

$$g(j) = \begin{cases} +1 & \text{if } j \text{ is a quadratic residue (mod } q) \\ 0 & \text{if } j \equiv 0 \pmod{q} \\ -1 & \text{otherwise} \end{cases}, \tag{3.5}$$

from which $\boldsymbol{S}_{0,j}$ of a cyclic S-matrix of order $n = pq$ can be computed by

$$\boldsymbol{S}_{0,j} = \begin{cases} 0 & \text{if } [f(j) - g(j)]\, g(j) = 0 \\ +1 & \text{otherwise} \end{cases}. \tag{3.6}$$

3.4.3 Aggregate pattern sequencing and data segmentation for video reconstruction

For video reconstruction, the smallest units of data considered for frame segmentation corresponded to the scans of individual aggregate patterns. Each scan produces a sequence of q bucket signals comprising a completed row of $\boldsymbol{Y}$ (Fig. 3.2c). Each frame of reconstructed video is then produced from a fixed number of scans (denoted by L) allocated into consecutive non-overlapping segments from a dataset recorded continuously during experiments. Additional scans of three registration patterns appended to the start of the pre-stored sequence (see Supplementary Note 2) are excluded during frame segmentation. As a result, the average framerate f_r of recovered videos is selectable at the time of reconstruction according to the equation

$$f_\mathrm{r} = \begin{cases} \frac{f_\mathrm{s}}{L+3} & \text{if } L = p \\ \frac{f_\mathrm{s}}{L+3\frac{L-1}{p}} & \text{if } L < p \end{cases}, \tag{3.7}$$

where f_s is the scan rate of the polygonal mirror which for our experiments (except for ultrahigh-speed imaging), was 6.37 kHz, limited by the maximum refresh rate of our DMD.

In operation, a complete sequence of aggregate patterns is pre-stored by the DMD and displayed iteratively. To support under-sampling, aggregate patterns are displayed in a permuted order that allows groups of $L < p$ consecutive scans to fill the rows of $\boldsymbol{Y}$ with approximately uniform spacing. By numbering the aggregate patterns with $k = 0, \dots, p-1$ corresponding to the rows of $\boldsymbol{Y}$, the display of the aggregate patterns took place in the order $d_0, d_1, \dots, d_{p-1}$ where the sequence of values d_k was defined by

$$\begin{aligned} d_0 &= 0 \ , \ \text{and} \\ d_{k+1} &= d_k + c \ \ (\text{mod } p) \end{aligned} \ . \tag{3.8}$$

Here, c is a constant chosen from an inspection of the sampling uniformity for various values of L. As a consequence of using cyclic S-matrices derived from the twin-prime construction, p is prime, and thus Eq. (3.8) defines a permutation for any value of $c \neq 0$ (mod p). The preferred values of c used for our experiments are summarized in Supplementary Table 3.2.

3.4.4 Interpolation-based image reconstruction using matrix operations

To take full advantage of GPU hardware for real-time visualization, SPI-ASAP's image reconstruction is developed based on matrix multiplication for direct parallelization. In general, it consists of two computational steps: interpolation and image recovery. For a segment of L consecutive scans deployed in a permuted order, recorded data are represented by a $L \times q$ matrix $\boldsymbol{M}$ whose elements $\boldsymbol{M}_{i,j}$ respectively denote the jth bucket signal ($j = 0, \ldots, q-1$) acquired from the deployment of the ith aggregate pattern ($i = 0, \ldots, L-1$).

The goal of interpolation is to transform $\boldsymbol{M}$ into an estimate of the smooth bucket signal matrix $\boldsymbol{Y}$. This transformation can be computed by the matrix product

$$\boldsymbol{Y} = \boldsymbol{W}\boldsymbol{M}\boldsymbol{V} \ , \tag{3.9}$$

where the matrices $\boldsymbol{V}$ (size $q \times q$) and $\boldsymbol{W}$ (size $p \times L$) are carefully designed to carry out optional row-wise low-pass filtering, and column-wise interpolation, respectively. Both the matrices $\boldsymbol{V}$ and $\boldsymbol{W}$ can be pre-computed and stored with low overhead owing to their sizes scaling linearly to the frame size of reconstructed images. Full details of the pre-computations involved for the elements of the matrices $\boldsymbol{W}$ and $\boldsymbol{V}$ are provided in Supplementary Note 8 and Supplementary Fig. 3.14.

Then, by reshaping $\boldsymbol{Y}$ back into an n-element vector $\boldsymbol{y}$, the reconstruction of a 2D image $\boldsymbol{x}$ then follows by direct inversion according to Eq. (3.1). Because the structure of $\boldsymbol{S}^{-1}$ is cyclic, computation of $\boldsymbol{x}$ becomes equivalent to a convolution of $\boldsymbol{y}$ with the initial row of $\boldsymbol{S}^{-1}$,

$$\boldsymbol{x} = \boldsymbol{y} * \boldsymbol{s}_0^{-1} \ , \tag{3.10}$$

where $\boldsymbol{s}_0^{-1}$ is the initial row of $\boldsymbol{S}^{-1}$, and the operator $*$ denotes discrete circular convolution.

During real-time operation, parallelization of reconstruction computations was facilitated with the use of a GPU (GeForce GTX 1060, NVIDIA). Frame rates were limited by the rate of data acquisition from scanning, with reconstruction and display taking place quickly enough to consume all incoming data.

Data availability

All data needed to evaluate the findings of this study are present in the paper and Supplementary Information. Raw data for Fig. 3.3 and Fig. 3.6 are provided with the software package described in the code availability statement. All other raw data in this study are available from the corresponding author upon request.

Code availability

A MATLAB software implementation of SPI-ASAP is available at https://doi.org/10.5281/zenodo.7227472.

References

See collected Bibliography (page 134).

Acknowledgements

The authors thank Jeremy Gribben and Alan Boate from Ajile Light Industries and Cheng Jiang from Institut National de la Recherche Scientifique for technical assistance. J.L. acknowledges the support by the Natural Sciences and Engineering Research Council of Canada (NSERC) (RGPIN-2017-05959, RGPAS-2017-507845, I2IPJ-555593-20), Canada Foundation for Innovation and Ministère de l'Économie et de l'Innovation du Québec (37146), Canadian Cancer Society (707056), New Frontier in Research Fund (NFRFE-2020-00267), Fonds de Recherche du Québec–Nature et Technologies (203345 - Centre d'optique, photonique et lasers), and Fonds de Recherche du Québec–Santé (267406, 280229). P.K. acknowledges the support from the Alexander Graham Bell CGS-D scholarship from NSERC.

Author contributions

P.K., J.L., and T.O. conceived the idea. P.K. created the experimental setup and developed all software. P.K. performed the experiments and data analysis. P.K. wrote the manuscript, with J.L. and T.O. providing editorial input. J.L. proposed the concept, contributed to experimental design, and supervised the project.

Competing interests

The authors disclose the patent application of US Provisional 63/380,620 (P.K., J.L., and T.O.).

Additional information

Supplementary information The online version contains supplementary material available at https://doi.org/10.1038/s41467-022-35585-8.

Correspondence and requests for materials should be addressed to Jinyang Liang.

Peer review information *Nature Communications* thanks Liheng Bian and the other, anonymous, reviewer(s) for their contribution to the peer review of this work. Peer reviewer reports are available.

Reprints and permissions information is available at http://www.nature.com/reprints

Index of supplementary information

[**Supplementary Movie 1**] MP4 movie file (30 seconds, 13.82 MB).
doi:10.6084/m9.figshare.21973607.v1.

[**Supplementary Movie 2**] MP4 movie file (8 seconds, 1.29 MB).
doi:10.6084/m9.figshare.21973595.v1.

[**Supplementary Movie 3**] MP4 movie file (9 seconds, 1.14 MB).
doi:10.6084/m9.figshare.21973601.v1.

[**Supplementary Movie 4**] MP4 movie file (11 seconds, 1.88 MB).
doi:10.6084/m9.figshare.21973598.v1.

[**Supplementary Movie 5**] MP4 movie file (17 seconds, 3.17 MB).
doi:10.6084/m9.figshare.21973604.v1.

[**Supplementary Movie 6**] MP4 movie file (4 seconds, 1.70 MB).
doi:10.6084/m9.figshare.21973592.v1.

[**Supplementary Movie 7**] MP4 movie file (117 seconds, 19.63 MB).
doi:10.6084/m9.figshare.21973589.v1.

See also Supplementary information (page 69).

3.5 Supplementary information

3.5.1 Supplementary Note 1: Details of system setup

A detailed illustration of the experimental setup of single-pixel imaging accelerated via swept aggregate patterns (SPI-ASAP) is shown in Supplementary Fig. 3.7a. Light from a continuous-wave laser source (200 mW power, 671 nm wavelength, MRL-III-671, CNI Laser) illuminates a high-speed projection module, whose core components are a polygonal mirror (Gecko-45-HSS, Precision Laser Scanning) and a digital micromirror device (DMD, AJD-4500, Ajile Light Industries). This high-speed polygonal mirror consists of 16 planar facets and has scanning rates at 2.7–12 kHz (corresponding to 10,000–45,000 RPM). It is used in a double-reflection arrangement [123] that increases optical efficiency by allowing illumination to be concentrated on only the parts of the DMD surface that are transmitted by the system. In particular, the laser beam is focused by the lens L1 (30 mm focal length) to a moving facet of the polygonal mirror placed at the lens' focal plane. The reflected beam is collimated by lenses L2 (75 mm focal length) and L3 (125 mm focal length) that are separated by 63.2 mm (Supplementary Fig. 3.7b) so as to produce an effective focal length

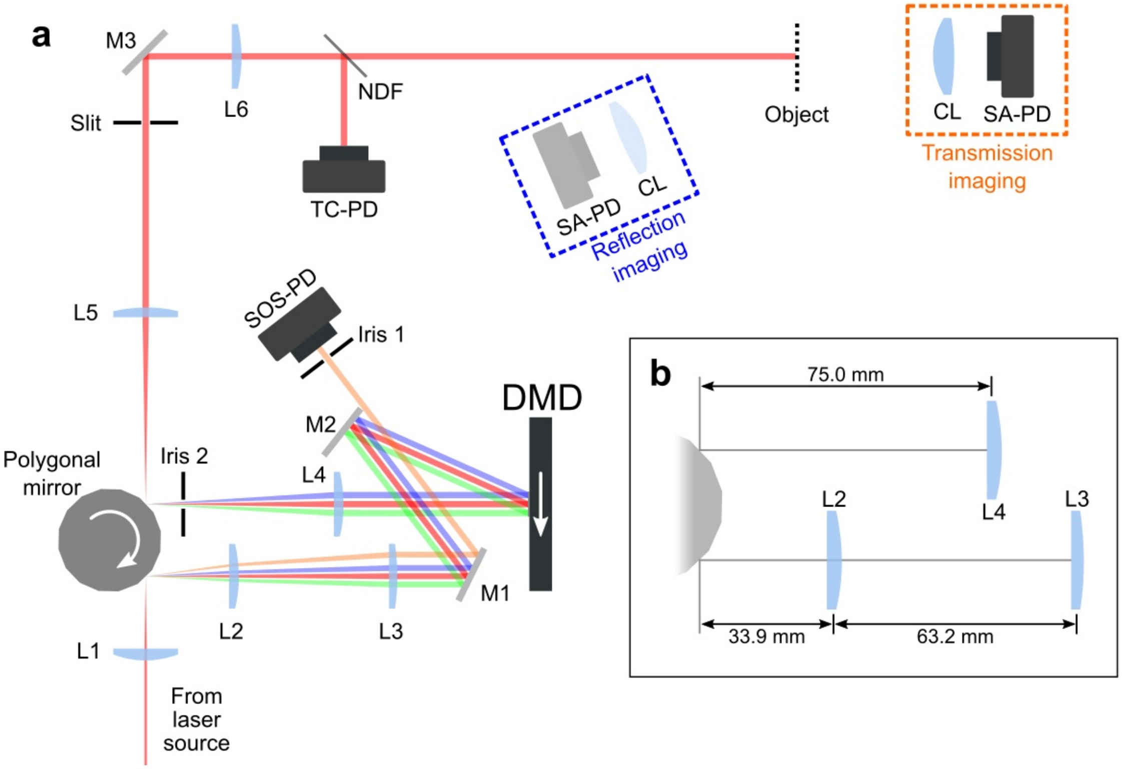

Supplementary Figure 3.7 Detailed system schematic of SPI-ASAP. **(a)** Scale illustration of system components. Four beam paths highlighting the scanning action are shown by the colors orange, blue, red, and green, in the order of appearance during scanning. **(b)** Closeup showing positions of lenses for beam scanning and de-scanning. CL: condenser lens. DMD: digital micromirror device. L1-L6: lenses. M1-M3: mirrors. NDF: neutral density filter. SA-PD: signal-acquisition photodiode. SOS-PD: start-of-scan photodiode. TC-PD: time-coding photodiode.

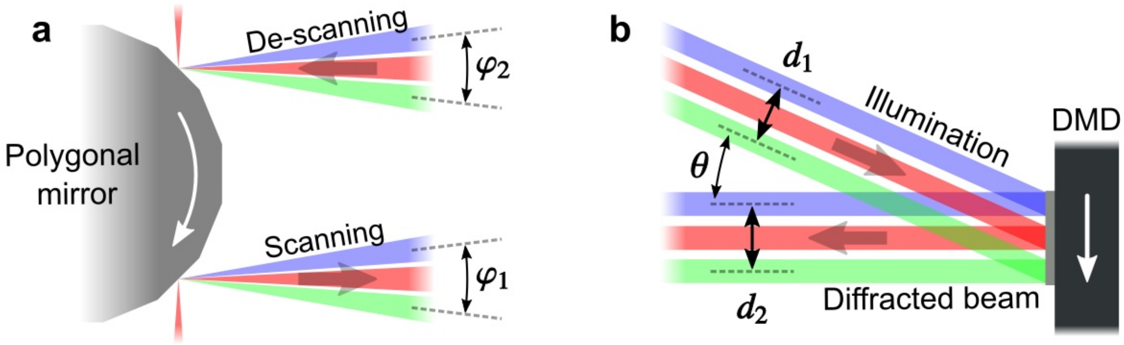

Supplementary Figure 3.8 Geometry of beam scanning. **(a)** Closeup of polygonal mirror reflections showing the correlation of beam angle necessary for scanning and de-scanning. **(b)** Closeup of DMD surface showing the effect of diffraction angle on lateral beam translation distances. In (a) and (b), white arrows indicate directions of polygonal mirror rotation and illumination scanning. Gray arrows show the laser beams' propagation direction.

appropriate for de-scanning by lens L4 (75 mm focal length). In this way, the mirror rotation is transferred to the lateral translation of the beam with its chief ray parallel to the optical axis (detailed in Methods). Then, the beam is reflected by two flat mirrors M1 and M2. A small portion of the beam passes beyond the edge of M2 and enters Iris 1 so that the "start-of-scan" photodiode (SOS-PD, DET100A2, Thorlabs) triggers the display of a new aggregate pattern that is pre-stored by the DMD. The rest of the beam scans across the DMD surface with an incident angle of $\theta = 24°$.

The diffracted beam from the DMD, which is spatially modulated by the displayed aggregate pattern, is imaged to a slit via a 4-*f* imaging system consisting of lenses L4 and L5 (75 mm focal lengths) as well as a moving facet of the polygonal mirror placed at L4's focal plane. Iris 2, positioned close to the polygonal mirror, selects the strongest diffraction order. The width of the slit determines the encoding patterns by optically selecting the sub-regions in the aggregate pattern. The intermediate image at the slit is further relayed by lens L6 (100 mm focal length) to the object with a varied magnification of 1.5–14×. Along the beam path, an adjustable neutral density filter (NDF) controls the illumination intensity while sending the reflected beam to the "time coding" photodiode (TC-PD, DET36A2, Thorlabs). Depending on the operational mode, the transmitted or reflected light of the object is focused by a condenser lens (CL) to the "signal acquisition" photodiode (SA-PD, DET36A2, Thorlabs) whose output waveforms are amplified by a transimpedance amplifier (OPA1S2384EVM, Texas Instruments).

3.5.2 Supplementary Note 2: System timing and data registration

The SOS-PD and TC-PD are used in the synchronization and data registration of SPI-ASAP. Signal path and timing diagrams are illustrated in Supplementary Fig. 3.9. As shown in Supplementary Fig. 3.7, each mirror scan produces a pulsed signal from the SOS-PD. From these signals, a delay generator (DG645, Stanford Research Systems) generates a per-scan timing datum via

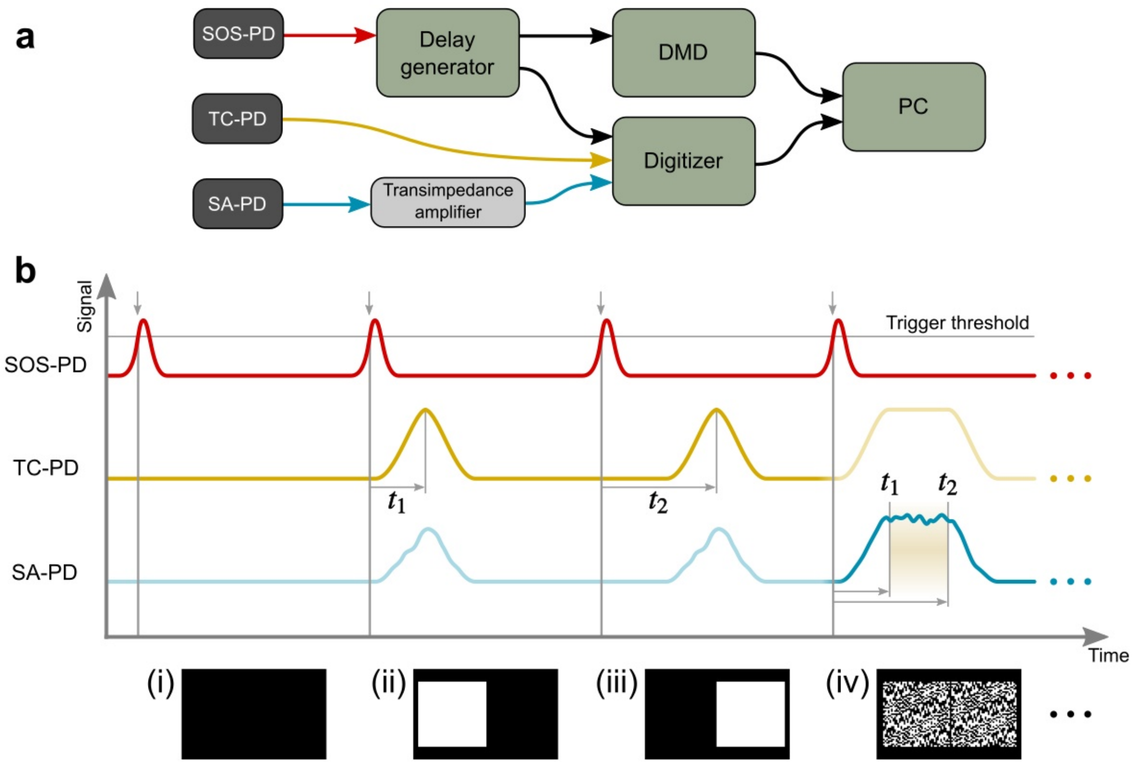

Supplementary Figure 3.9 Illustration of synchronization and data registration in SPI-ASAP. **(a)** Block diagram illustrating the paths of signals involved in timing and acquisition. **(b)** Schematic timing diagram illustrating synchronization and data registration. Insets show the initial frames of a DMD sequence for 41×43-pixel resolution imaging: (i) blank frame, (ii) initial pattern region, (iii) final pattern region, and (iv) the first aggregate pattern.

triggering on the rising edge of a pre-set voltage threshold. Outputs from the delay generator then trigger the refresh of DMD patterns as well as the acquisition of data using a digitizer card (ATS9350, AlazarTech) that interfaces with a computer. Data from both the TC-PD and SA-PD are synchronously stored as waveforms consisting of 1024 points of 12-bit measurements sampled at a rate of 20 MHz.

SA-PD waveforms are registered with the corresponding sub-areas in each aggregate pattern by using three special-purpose registration patterns appended to the beginning of the pre-stored DMD pattern sequence. Illustrated examples of SOS-PD, TC-PD, and SA-PD waveforms corresponding to these registration patterns are shown in Supplementary Fig. 3.9b. The first pattern (marked as (i) in Supplementary Fig. 3.9b) is all dark and serves as a datum for matching the waveforms measured by the TC-PD and SA-PD to the aggregate pattern sequence. The second and third patterns (marked as (ii) and (iii) in Supplementary Fig. 3.9b) consist of "On" DMD pixels in the initial and final encoding pattern sub-regions of the aggregate pattern, respectively. In SPI-ASAP, these patterns produce triangular TC-PD waveforms, whose peak locations supply timing offsets t_1 and t_2 that identify the positions of the initial and final deployed masking patterns (see an example labeled by (iv) in Supplementary Fig. 3.9b) in the SA-PD waveform. Sampling of bucket signal values then follows by linear interpolation of sample locations within the $[t_1, t_2]$ interval.

3.5.3 Supplementary Note 3: Performance comparison for SPI using polygonal mirror scanning

Compared to the existing work on scanning-enhanced SPI [124, 125], the design used in SPI-ASAP has several advantages. In the SPI system demonstrated by Wang et al. [124], a pair of galvanometer mirrors (GMs) were used to implement bi-directional sweeping of DMD-modulated patterns for compressed imaging at a speed of 42 fps and a frame size of 80×80 pixels. However, although the roles of the two GMs were functionally similar to the double-reflection arrangement of SPI-ASAP, the use of galvo-actuation limited the GM's scan rate to 200 Hz. In addition, the scanning geometry required the motion of the independent GMs to be calibrated and tightly synchronized. In another work, the SPI system demonstrated by Zhang et al. [125] achieved a higher scan rate by using a GM in tandem with a resonant scanning mirror that operated at 8 kHz. Sampling was thus achieved with the use of an optimized low-resolution DMD pattern that was scanned in a 2D fashion across the FOV. Although this modality achieved a modulation rate above 1 MHz, the fixed actuation frequency of the resonant scanning mirror ultimately limited the scan rate while still requiring both calibration and synchronization.

In contrast, the choice of a polygonal mirror for SPI-ASAP simultaneously addresses several limitations of designs based on GMs and resonant scanning mirrors. First, the ability to simultaneously deflect off of separate mirror facets in the same device allows for scanning hardware to be consolidated, thus avoiding the synchronization of multiple mechanical devices. Second, because the angular speed of the facets on the polygon mirror remains constant in operation, motorization is simplified thus allowing for many-faceted polygons to achieve scan rates above 10 kHz. Scan rates may also be continuously varied with the rotational speed of the motor, thus increasing flexibility over resonant scanning mirrors whose period of oscillation is fixed. In addition, the time dependence of the scan angle for polygonal mirrors is linear, thus avoiding the need for precise calibration of control signals. Finally, by eliminating the deceleration period required by GMs and resonant scanning mirrors, polygonal mirrors allow for increased scan duty cycles, which may be optimized via the correct selection of facet count.

For the SPI-ASAP system, the use of off-the-shelf hardware dictated the use of a 16-sided mirror polygon. For aggregate patterns making use of the full DMD surface, this restriction resulted in a pattern deployment duty cycle of approximately 8%. Consequently, the rate of pattern modulation for SPI-ASAP is non-constant, with the current system compatible with roughly a 10× increase in polygon facets. To reflect the potential performance of SPI-ASAP with optimized facet count, modulation rates shown in Supplementary Table 3.1 are computed relative to the pattern deployment interval, thus reflecting the peak modulation rate during operation.

	Scanning hardware	Mirror scanning rate	Modulation rate
DeCIOPS (Ref. [124])	1× Resonant scanner 1× GM	Resonant scanner: 8 kHz GM: 125 Hz	1.02 MHz$^{(1)}$
Ref. [125]	2× GMs$^{(2)}$	200 Hz	97 kHz
SPI-ASAP	1× polygonal mirror	Multi-pattern: 6.37 kHz$^{(3)}$ Single-pattern: 12 kHz$^{(4)}$	Multi-pattern: 3.0–5.0 MHz Single-pattern: 14.1 MHz

Notes:
(1) Computed according to the sampling of a 64×64 grid carried out in 4 ms
(2) Operation is synchronized
(3) Limited by the DMD's refresh rate
(4) Limited by the 16-facet polygon mirror

Supplementary Table 3.1 Performance comparison of SPI-ASAP with state-of-the-art techniques in the same category.

3.5.4 Supplementary Note 4: Comparison of conventional compressed-sensing methods with SPI-ASAP

To verify the performance of SPI-ASAP's reconstruction method, we compared image reconstruction between SPI-ASAP and two widely used compressive reconstruction algorithms implemented with the L1-Magic software library [30]. The first algorithm, termed "MinTV", is regularized based on the total variation (TV). The second algorithm, termed "MinDCT", is regularized from sparse representations using the basis of the discrete cosine transform (DCT) [5]. We define the "MinTV" and "MinDCT" reconstruction algorithms based on the following optimization programs found in the L1-Magic software package:

$$\arg\min_{\boldsymbol{x}} \mathrm{TV}(\boldsymbol{x}) \quad \text{subject to} \quad \|\boldsymbol{S}\boldsymbol{x}-\boldsymbol{y}\|_2 \leq \epsilon \ , \tag{MinTV}$$

$$\arg\min_{\boldsymbol{x}} \|\boldsymbol{\Psi}\boldsymbol{x}\|_1 \quad \text{subject to} \quad \|\boldsymbol{S}\boldsymbol{x}-\boldsymbol{y}\|_2 \leq \epsilon \ , \tag{MinDCT}$$

where $\boldsymbol{x}$ is the image to be recovered, $\boldsymbol{y}$ is the vector of bucket signals, $\boldsymbol{S}$ is the measurement matrix, ϵ is a user-specified parameter, and $\|\cdot\|_1$ denotes the L1-norm. For an image with a frame size of $p \times q$, the total variation $\mathrm{TV}(\boldsymbol{x})$ is defined as

$$\mathrm{TV}(\boldsymbol{x}) = \sum_{i=1}^{p-1}\sum_{j=1}^{q-1} \sqrt{[\boldsymbol{x}(i+1,j)-\boldsymbol{x}(i,j)]^2 + [\boldsymbol{x}(i,j+1)-\boldsymbol{x}(i,j)]^2} \ , \tag{3.11}$$

where we write $\boldsymbol{x}(i, j)$ to indicate the value of the pixel of $\boldsymbol{x}$ with coordinates (i, j). Finally, $\boldsymbol{\Psi}$ denotes the real orthogonal matrix that induces the DCT.

For quantitative comparison of the agreement between a reconstruction $\boldsymbol{x}$ and ground truth image $\hat{\boldsymbol{x}}$ we used both the peak signal-to-noise ratio (PSNR) and structural similarity index (SSIM) as metrics to compute reconstruction error [27, 126]. The PSNR and SSIM are defined as

$$\text{PSNR}(\boldsymbol{x}, \hat{\boldsymbol{x}}) = 10 \log_{10} \left(\frac{(\max(\hat{\boldsymbol{x}}))^2}{(1/pq) \|\boldsymbol{x} - \hat{\boldsymbol{x}}\|_2^2} \right) , \tag{3.12}$$

and

$$\text{SSIM}(\boldsymbol{x}, \hat{\boldsymbol{x}}) = \frac{(2\mu_1\mu_2 + C_1)(2\sigma_{12} + C_2)}{(\mu_1^2 + \mu_2^2 + C_1)(\sigma_1^2 + \sigma_2^2 + C_2)} . \tag{3.13}$$

Here, $\max(\hat{\boldsymbol{x}})$ denotes the maximum intensity value of the ground truth image. μ_1 and μ_2 denote the mean intensity values of $\boldsymbol{x}$ and $\hat{\boldsymbol{x}}$, respectively. σ_1^2 and σ_2^2 denote the variances of the intensity values of $\boldsymbol{x}$ and $\hat{\boldsymbol{x}}$, respectively. σ_{12} denotes the covariance of $\boldsymbol{x}$ and $\hat{\boldsymbol{x}}$. The constants C_1 and C_2 are used to prevent indeterminate values of SSIM and were set to the conventional values $(0.01 \max(\hat{\boldsymbol{x}}))^2$ and $(0.03 \max(\hat{\boldsymbol{x}}))^2$, respectively [126].

Similar to other iterative reconstruction methods based on convex optimization, the selection of the user-defined parameter ϵ plays a crucial role in the performance of MinTV and MinDCT. For this numerical experiment, we selected ϵ based on a golden section search that first optimized the PSNR against the ground truth image. Thus, the results of the MinTV and MinDCT methods in Supplementary Fig. 3.10 could be interpreted as optimized with respect to the selection of ϵ.

We also measured the time overhead required for reconstructions provided by each method using a computer with an Intel® Core™ i5-8250U CPU (1.60 GHz) and 8 GB RAM. Input to each reconstruction method included identical measurement matrices and simulated bucket signals. All measurement matrices were composed in accordance with SPI-ASAP's aggregate pattern coding strategy. No noise was injected in this experiment.

The results of this comparison, shown in Supplementary Fig. 3.10, indicate that in terms of PSNR and SSIM, the performance of SPI-ASAP largely meets or exceeds that of the iterative methods, in particular outperforming them across both metrics for the case of sampling rates below 50%. This observation is qualitatively matched by the subset of image reconstruction results shown in Supplementary Fig. 3.10d. For the case of 100% sampling, we note highly accurate convergence across all methods as indicated by the pronounced maxima exhibited by the PSNR metric. Measurements of reconstruction time required for each algorithm (Supplementary Fig. 3.10c) provide the most striking comparison between SPI-ASAP and the conventional methods, with SPI-ASAP reconstructions exhibiting consistent running times 2–3 orders of magnitude below those of both conventional methods.

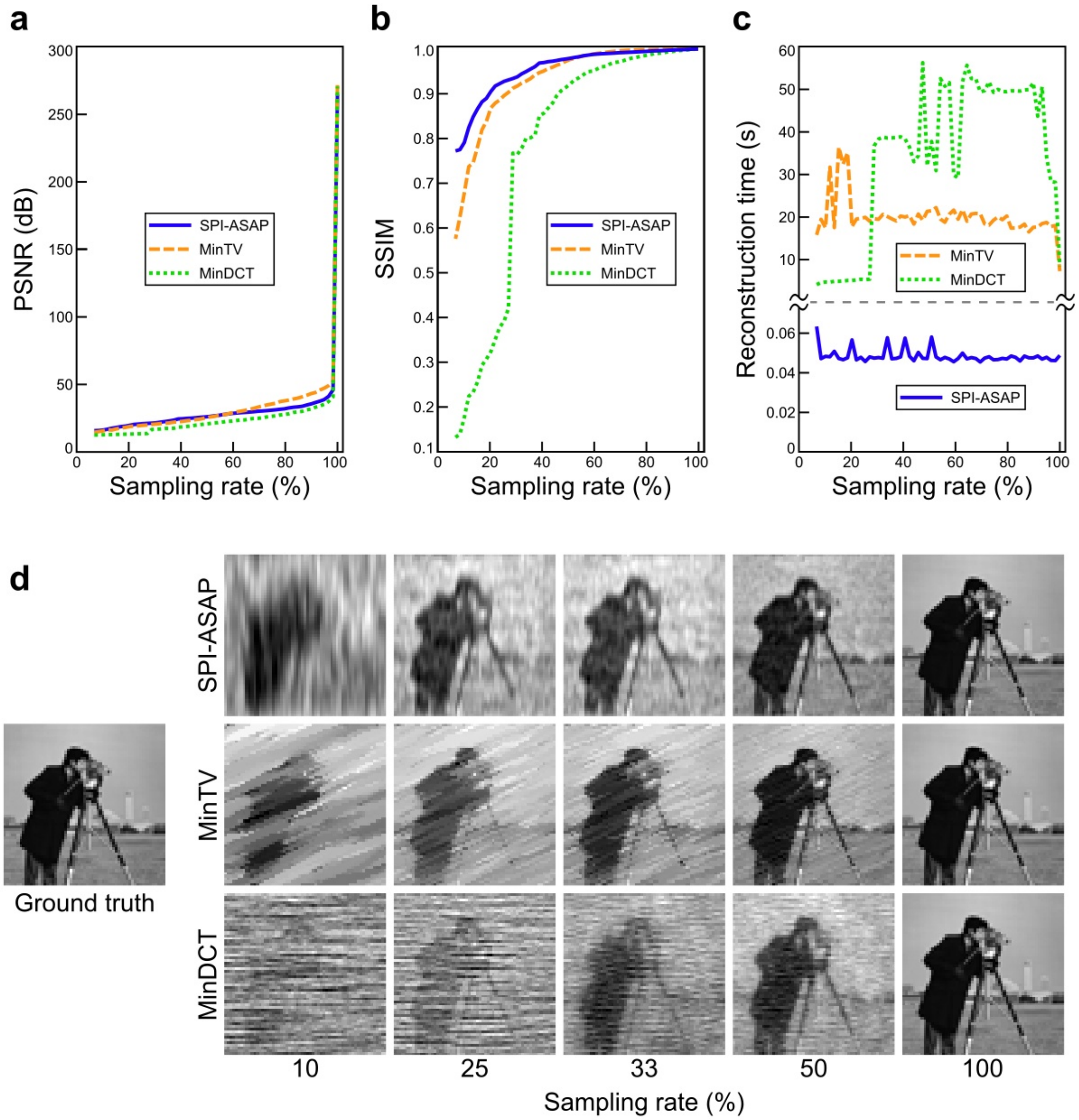

Supplementary Figure 3.10 Comparison of image reconstruction between SPI-ASAP and two widely used compressed-sensing algorithms. The ground truth is the “Cameraman” image with a frame size of 59×61 pixels. **(a)**–**(c)** Reconstruction quality evaluated by peak signal-to-noise ratio (PSNR) (a), structural similarity index (SSIM) (b), and running time (c) for SPI-ASAP, MinTV, and MinDCT plotted as a function of sampling rate for the ground truth image. Note that the vertical axis in (c) is discontinuous. **(d)** Visual comparison of a subset of reconstructed images.

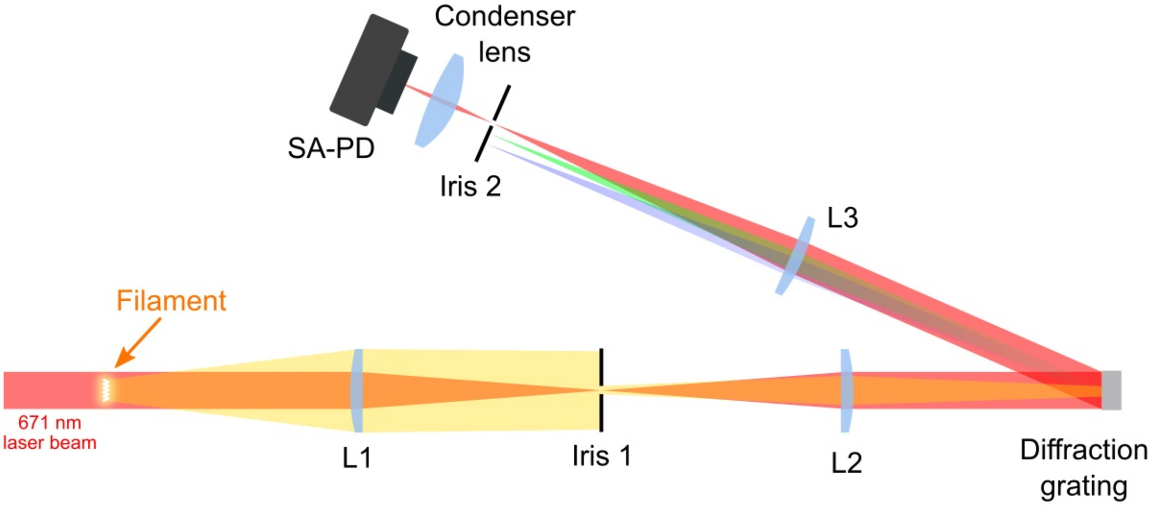

Supplementary Figure 3.11 Illustration of system setup for the high light interference imaging of incandescent filaments. L1–L3: lenses. SA-PD: signal-acquisition photodiode

3.5.5 Supplementary Note 5: Details of imaging of incandescent filaments

The setup for acquiring optically filtered bucket signals is illustrated in Supplementary Fig. 3.11. The incandescent filament was placed at SPI-ASAP's image plane, which was in the front focal plane of lens L1 (75 mm focal length). Iris 1, positioned in the back focal plane of L1, blocked the majority of incandescent rays that were approximately collimated. Lens L2 (75 mm focal length), in a 4-*f* configuration with L1, relayed the image of the filament to the surface of a diffraction grating (600 lines per mm, GR13-0605, Thorlabs) from which the first diffraction order was selected. The grating was positioned on the focal plane of lens L3 (100 mm focal length), which produced a chromatically dispersed image of Iris 1 at Iris 2. Finally, 671 nm light chromatically selected by Iris 2 was focused by the condenser lens to the SA-PD.

The light bulbs used in the experiments were designed for low-power applications (rated 12 V, 18 W) and were commercially sourced. In each experiment, filament burn-out was initiated by the application of 24 V with a DC power supply. Imaging experiments were repeated several times for each case with consistent results, with representative videos being presented in Main Text and Supplementary Movies 4 and 5.

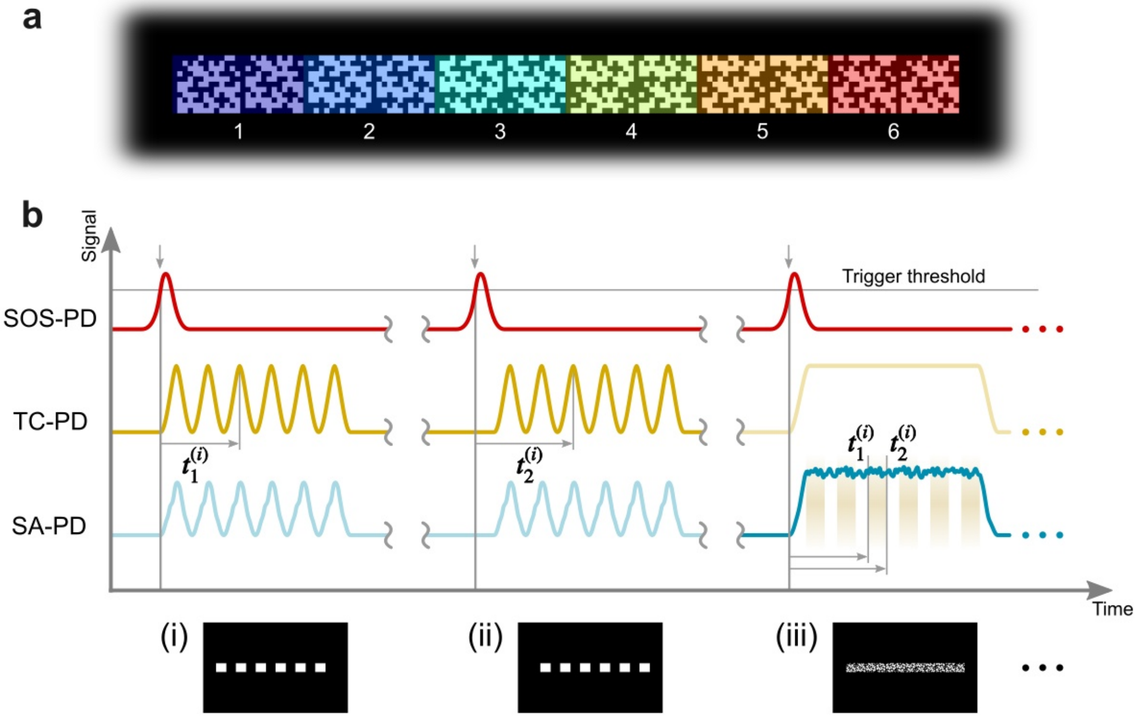

Supplementary Figure 3.12 Illustration of aggregate patterning and system timing for ultra-high-speed imaging at 12 kfps. **(a)** Multi-aggregate pattern scheme for 11×13-pixel resolution imaging consisting of six joint aggregate patterns (distinguished by the shaded colors). **(b)** Schematic timing diagram illustrating synchronization and data registration for the multi-aggregate pattern. Example waveforms corresponding to the display of initial (i) and final (ii) sub-regions on the mask, as well as (iii) the static multi-aggregate pattern.

3.5.6 Supplementary Note 6: Details of ultra-high-speed imaging at 12 kfps

The timing and data registration scheme used for ultra-high-speed imaging with SPI-ASAP is illustrated in Supplementary Fig. 3.12. For this imaging arrangement, bucket signals are generated from a single displayed DMD pattern that remains static during the scanning of the polygonal mirror at its maximum speed of 12 kHz. The static DMD pattern is comprised of six jointly arranged aggregate patterns, each designed with a resolution of 11×13 pixels. Thus, this DMD pattern carried a total of 78 masking patterns corresponding to a sampling rate of 55%.

Data registration for the joint aggregate pattern proceeded similarly to the procedure described in Supplementary Note 3.5.2 with two exceptions. First, multiple intervals were used to derive bucket signals. Second, registration patterns were not displayed synchronously with the collection of data. The registration patterns, shown by insets (i) and (ii) in Supplementary Fig. 3.12, consisted of joint copies of the registration patterns appropriate for each segment of the joint aggregate pattern. Waveforms for the TC-PD and SA-PD were sampled at 50 MHz with TC-PD waveforms being collected separately for each registration pattern. The locations of the six triangular peaks within each TC-PD waveform then supplied timing offsets $t_1^{(i)}$ and $t_2^{(i)}$ $(i = 1, \ldots, 6)$ that identified the positions of the initial and final encoding patterns deployed by each segment of the multi-aggregate pattern. Linear interpolation of sample locations within the six intervals $[t_1^{(i)}, t_2^{(i)}]$ $(i = 1, \dots, 6)$ then determined bucket signal values from SA-PD waveforms collected during the experiment.

Video reconstruction was carried out in a one-to-one fashion with SA-PD waveforms, with the 78 bucket signals derived from each waveform leading to the reconstruction of individual frames in sequence. The time interval to acquire each frame was approximately 6.7 µs.

3.5.7 Supplementary Note 7: Investigation of the spatial resolution of SPI-ASAP

To investigate the spatial resolution of SPI-ASAP, we imaged a resolution target (1951 USAF) at four rotation angles between 0° and 90°. The SPI-ASAP system had a frame size of 59×61 pixels across a FOV of size 5.5 mm (i.e., each pixel is 90 µm in size), which was the most typical setting used in our work. At each rotation position, the image was obtained as temporal averages of 89 consecutively collected frames. For frame reconstruction, spatial filtering was disabled via the choice of $T = (q-1)/2$ in equations (3.15) and (3.16), which set the spatial filtering matrix V equal to the identity (see Supplementary Note 8). Line profiles of normalized intensity were then extracted that were tracked to individual elements of the resolution target over each rotation position.

Imaging results are illustrated in Supplementary Fig. 3.13. Evidence of a non-isotropic spatial resolution can be observed in the variation of line profile modulation depth with the rotation angle of the resolution target. Using the criterion of 5% contrast, we determined a horizontal resolution of 198.4 µm identified as the resolution target line width (Group 1, Element 3) corresponding to profile 2 shown in Supplementary Fig. 3.13a. Similarly, we determined a vertical resolution of 88.4 µm identified as the resolution target line width (Group 2, Element 4) corresponding to profile 2 shown in Supplementary Fig. 3.13b.

Two factors can be identified as contributing to the resolution anisotropy. First, to prioritize speed, SPI-ASAP's data registration procedure (see Supplementary Note 3.5.2) does not compensate for encoding pattern motion that occurs during intervals sampled for each bucket signal. For a scan rate of 6.37 kHz and a modulation duty cycle of 8%, the time interval containing bucket measurements is of duration 0.08 / 6.37 kHz = 12.6 µs. Consequently, for 59×61-pixel imaging, a shift of one encoding pixel occurs after a period of 12.6 µs / 61 = 0.21 µs. Thus, with 20 MHz sampling of SA-PD waveforms, a pattern shift of ±0.12 encoding pixels occurs within the sampling interval. Second, the TC-PD waveforms exhibited a 16-period timing variation produced from minute errors in the facet geometry of the polygonal mirror. For high-speed imaging, this resulted in a timing variation of 0.19 µs, equivalent to ±0.45 encoding pixels. Although the extraction of appropriate timing offsets for data registration was stabilized by temporal averaging, timing variations affecting the registration of bucket signals is still capable of affecting reconstruction results via row-wise misalignment of data within the bucket signal matrix $\boldsymbol{Y}$.

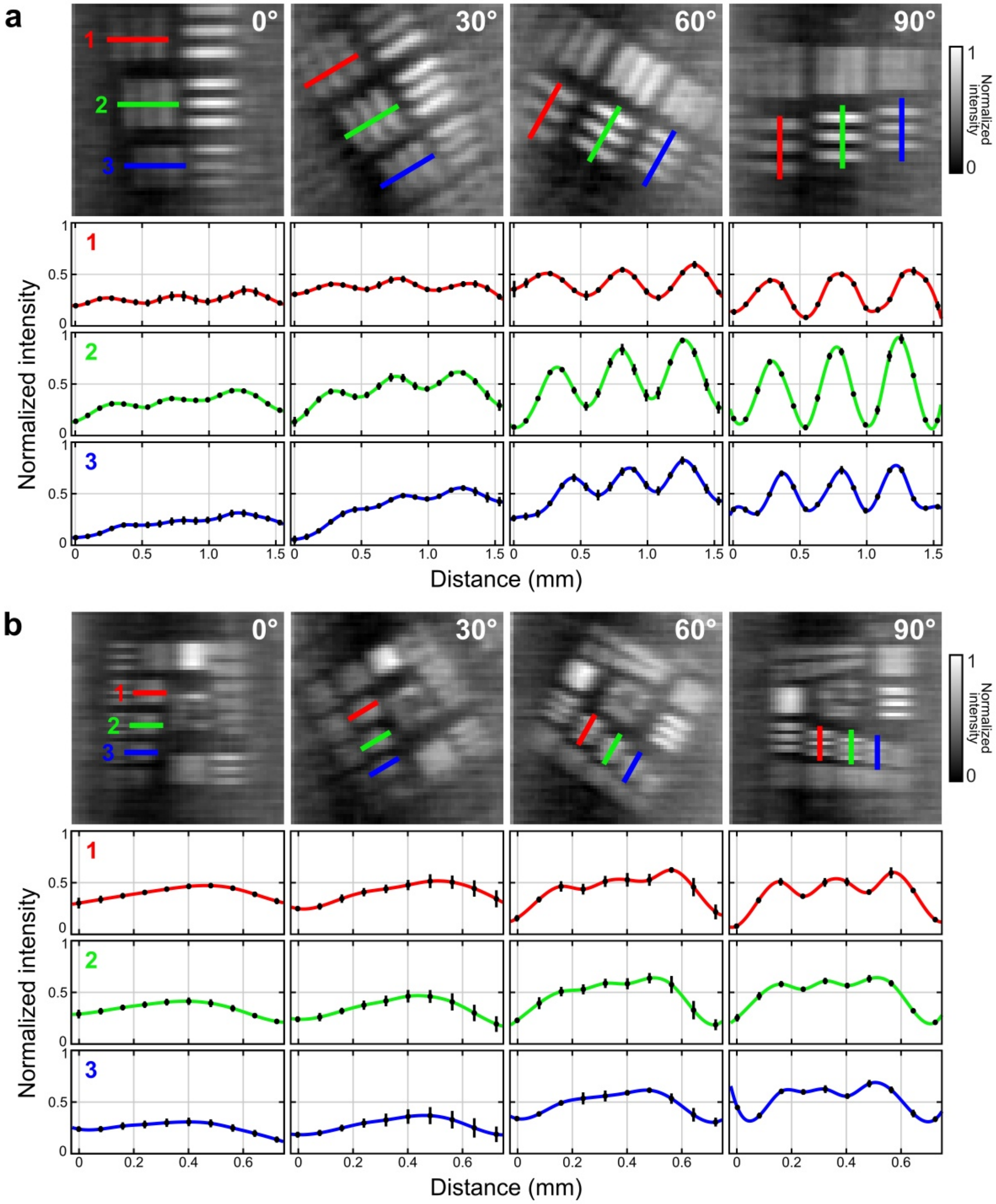

Supplementary Figure 3.13 Investigation of SPI-ASAP's spatial resolution. **(a)** Averaged image sequence and normalized intensity profiles of a resolution target (1951 USAF) rotated through 90°. Profiles 1–3 correspond to the vertical line pairs of Group 1 Elements 2–4, respectively. **(b)** As in a, but with profiles 1–3 corresponding to the vertical line pairs of Group 2 Elements 3–5, respectively. Error bar: standard deviation.

3.5.8 Supplementary Note 8: Details of matrix pre-computations for interpolation-based image reconstruction

3.5.8.1 Derivation of $\boldsymbol{V}$

Let $\boldsymbol{F}$ denote the $q \times q$ matrix of the discrete Fourier transform (DFT) of order q, which is defined by $\boldsymbol{F}_{i,j} = \omega^{-ij}$, where i and j range over $(0, \ldots, q-1)$, and ω is a primitive qth root of unity. The inverse of this matrix can be computed by $\boldsymbol{F}^{-1} = (1/q)\boldsymbol{F}^*$, where $\boldsymbol{F}^*$ denotes the complex conjugate transpose of $\boldsymbol{F}$. The row-wise spatial filtering of a matrix $\boldsymbol{M}$ can be written as

$$\boldsymbol{M}\boldsymbol{V} = \left(\frac{1}{q}\boldsymbol{F}^*\boldsymbol{D}\boldsymbol{F}\boldsymbol{M}^T\right)^T = \boldsymbol{M}\left(\frac{1}{q}\boldsymbol{F}\boldsymbol{D}\boldsymbol{F}^*\right) \quad , \tag{3.14}$$

where the matrix $\boldsymbol{D}$ is diagonal and selects the spatial frequencies retained from the DFT. For a symmetric low-pass filter whose cut-off frequency is denoted by T $(2T \leq q)$, the diagonal elements of $\boldsymbol{D}$ can be defined as:

$$\boldsymbol{D}_{i,i} = \begin{cases} 0 & \text{if } T < i < q - T \\ 1 & \text{otherwise} \end{cases} \quad , \tag{3.15}$$

from which the elements of $\boldsymbol{V}$ can be computed as:

$$\boldsymbol{V}_{i,j} = \frac{1}{q}\left[1 + 2\sum_{k=1}^{T} \cos\left(2\pi(i-j)k/q\right)\right] \quad . \tag{3.16}$$

Across our experiments, only mild low-pass filtering was used, with values of T selected to retain 70%–80% of the spectrum of the DCT.

3.5.8.2 Derivation of $\boldsymbol{W}$

Column-wise interpolation was developed as a special case of piece-wise cubic spline interpolation with cyclic boundary conditions. As illustrated in Supplementary Fig. 3.14, from the four data points shown, a cubic interpolating polynomial $f(x)$ can be specified for values $x_1 \leq x < x_2$, according to the boundary conditions

$$\begin{aligned} f(x_1) &= y_1 \quad , \\ f(x_2) &= y_2 \quad , \\ f'(x_1) &= g_1 \quad , \quad \text{and} \\ f'(x_2) &= g_2 \quad , \end{aligned} \tag{3.17}$$

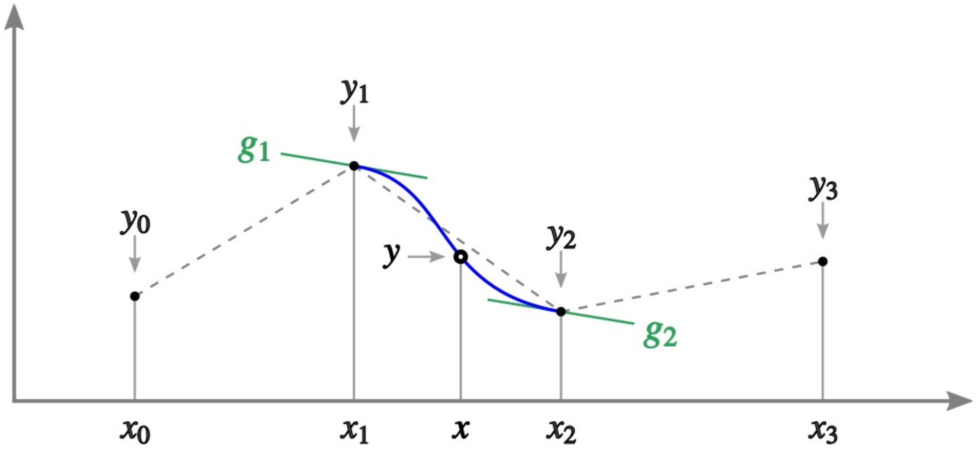

Supplementary Figure 3.14 Illustration of the parameters for cubic spline interpolation.

where the values of g_1 and g_2 are chosen as the average slopes between the two line-segments that meet at positions x_1 and x_2, respectively, i.e.,

$$\begin{aligned} g_1 &= \frac{1}{2}\left(\frac{y_1 - y_0}{x_1 - x_0} + \frac{y_2 - y_1}{x_2 - x_1}\right) \quad , \quad \text{and} \\ g_2 &= \frac{1}{2}\left(\frac{y_2 - y_1}{x_2 - x_1} + \frac{y_3 - y_2}{x_3 - x_2}\right) \quad . \end{aligned} \tag{3.18}$$

For fixed values of $x_0, \ldots, x_3$ and x, values of the resulting interpolation function $y = f(x)$ are linear with respect to the y-coordinate data $y_0, \ldots, y_3$ and can be computed according to

$$y = H(x_0, x_1, x_2, x_3, x) \begin{bmatrix} y_0 \\ y_1 \\ y_2 \\ y_3 \end{bmatrix} \quad , \tag{3.19}$$

where $H(x_0, x_1, x_2, x_3, x)$ is defined as

$$H(x_0, x_1, x_2, x_3, x) = \begin{bmatrix} x^3 & x^2 & x & 1 \end{bmatrix} \begin{bmatrix} x_1^3 & x_1^2 & x_1 & 1 \\ x_2^3 & x_2^2 & x_2 & 1 \\ 3x_1^2 & 2x_1 & 1 & 0 \\ 3x_2^2 & 2x_2 & 1 & 0 \end{bmatrix}^{-1} \begin{bmatrix} 0 & 1 & 0 & 0 \\ 0 & 0 & 1 & 0 \\ -\delta_1 & \delta_1 - \delta_2 & \delta_2 & 0 \\ 0 & -\delta_2 & \delta_2 - \delta_3 & \delta_3 \end{bmatrix} \quad , \tag{3.20}$$

and where $\delta_i = 1 / [2(x_i - x_{i-1})]$.

The function $H(x_0, x_1, x_2, x_3, x)$ is now used to define a pre-computed matrix $\widehat{\boldsymbol{W}}$ as follows. For imaging with resolution $p \times q$ and segmentation length L, the numbers u_k ($k = 0, \ldots, L-1$) are defined according to $u_k = d_{a+k}$ (see equation (3.8) in Main Text) where a is the index of the first aggregate pattern deployed in the data segment and the index $a + k$ is interpreted modulo p. We then define $\sigma(k)$ to be the permutation that sorts the u_k into strictly increasing order: $u_{\sigma(0)} < \ldots < u_{\sigma(L-1)}$. By relabeling these numbers as $v_0 < \ldots < v_{L-1}$ and by making the following definitions:

$$\begin{aligned} v_{-2} &= v_{L-2} - p \ , \\ v_{-1} &= v_{L-1} - p \ , \\ v_L &= v_0 + p \ , \ \text{and} \\ v_{L+1} &= v_1 + p \ , \end{aligned} \tag{3.21}$$

an expanded sequence is obtained satisfying $v_{-2} < v_{-1} < v_0 < \ldots < v_{L-1} < v_L < v_{L+1}$. For any $i = 0, \ldots, p-1$, we then define $\rho(i)$ to be the unique integer from $0 \ldots L-1$ satisfying the relations

$$v_{\rho(i)-1} < v_{\rho(i)} \le i < v_{\rho(i)+1} < v_{\rho(i)+2} \ , \tag{3.22}$$

which is well-defined as a result of the definitions in equation (3.21). As a result of these definitions, $\rho(i)$ allows for the selection of appropriate data from the columns of $\boldsymbol{M}$ (stored in a permuted order from the sequencing of aggregate patterns) to implement piece-wise interpolation with cyclic boundary conditions matching the indexing of $\boldsymbol{Y}$ (stored in non-permuted order).

With i fixed, four coefficients $h_0, \ldots, h_3$ are then computed:

$$\begin{bmatrix} h_0 & h_1 & h_2 & h_3 \end{bmatrix} = H\big(v_{\rho(i)-1}, v_{\rho(i)}, v_{\rho(i)+1}, v_{\rho(i)+2}, i\big) \ , \tag{3.23}$$

from which the ith row of $\widehat{\boldsymbol{W}}$ is then found as:

$$\widehat{\boldsymbol{W}}_{i,j} = \begin{cases} h_0 & \text{if } j = \sigma^{-1}\left(\rho(i) - 1\right) \\ h_1 & \text{if } j = \sigma^{-1}\left(\rho(i)\right) \\ h_2 & \text{if } j = \sigma^{-1}\left(\rho(i) + 1\right) \\ h_3 & \text{if } j = \sigma^{-1}\left(\rho(i) + 2\right) \\ 0 & \text{otherwise} \end{cases} \ , \tag{3.24}$$

where $j = 0 \ldots L-1$, and the arguments to σ^{-1} are each interpreted modulo L.

For any segment of scan data, the index a for the aggregate pattern corresponding to the first row of $\boldsymbol{M}$ is known at the time of reconstruction. In general, with $\widehat{\boldsymbol{W}}$ pre-computed and stored in memory, the matrix $\boldsymbol{W}$ used for interpolation of $\boldsymbol{M}$ depends on a according to

$$\boldsymbol{W}_{i,j} = \widehat{\boldsymbol{W}}_{i-a,j} \ , \tag{3.25}$$

where the index $i - a$ is interpreted modulo p.

Experiment	p	c
Fig. 3.6, Supplementary Movie 6	11	2
Figs. 3.3b–d, 3.4b, 3.5b, 3.5e, Supplementary Movies 1, 3, 4, 5,	41	12
Figs. 3.4a, Supplementary Movie 2, Supplementary Movie 7 (Demonstrations 3, 4)	59	18
Supplementary Movie 7 (Demonstration 1)	71	21
Supplementary Movie 7 (Demonstration 2)	101	39

Supplementary Table 3.2 Summary of parameters used to determine the sequencing of aggregate patterns.

4 TOWARDS A REAL-TIME TERAHERTZ CHEMICAL MICROSCOPE

4.1 Introduction

Terahertz (THz) radiation lies on the electromagnetic spectrum (Fig. 4.1) between the microwave and infrared regions, corresponding to a range of frequencies with millimeter to sub-millimeter wavelengths, extending from several tens of gigahertz (GHz) to several tens of THz. Although named according to the metric prefix *tera* (T, 10^{12}), the THz region has been historically distinguished by the range of unique technologies required for its generation and detection [105, 127]. For many years, the relative lack of convenient and inexpensive technology for THz generation, detection, and imaging resulted in a technological 'THz gap' that arose form the simultaneous limitations of electronic technologies on one hand (limited to below ≈100 GHz) and optical technologies on the other (limited to above ≈10 THz) [128]. Nonetheless, interest in the THz region as a frontier for experimental photonics has over the past 30 years continued to grow, with current applications including fields such as spectroscopy [129, 130], non-destructive testing [131–133], industrial monitoring [134, 135], and cultural conservation [136–138].

In particular, the development of imaging systems has been of paramount importance to research within THz science [139]. Driven by the operation of pulsed femtosecond (fs) lasers, the majority of THz imaging systems use dedicated crystals or antennas as the means of generating THz radiation that subsequently illuminates an object or sample after a period of free-space propagation. This separation of THz source and object, by the necessary physics of electromagnetic wave propagation, imposes limits on maximum spatial resolution which, for 1.0 THz radiation under the diffraction limit, must be on the order of the wavelength, i.e. 300 μm (see Fig. 4.1). For certain materials however, the generation of THz waves can occur directly from fs laser interaction. By tightly focusing the pulsed illumination, the THz emission response of the material itself can be probed with a far higher spatial resolution, on the order of a few micrometers, determined instead by the central wavelength of the laser source [140]. This technique, known as laser-excited THz emission microscopy (LTEM), was initially proposed for the non-destructive testing and inspection of electronic devices such as semiconductor integrated circuits [141–143]. Shortly after the emergence of LTEM, a generalization of the technique, known as THz chemical microscopy (TCM),

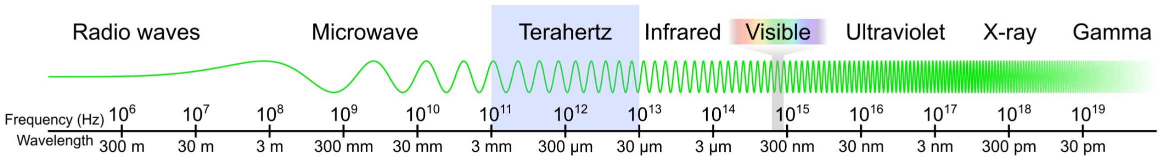

Figure 4.1 Location of the terahertz region within the electromagnetic spectrum.

was proposed for targeting the diagnostic imaging of chemical and biological samples [144, 145]. However, a shortcoming shared by current LTEM and TCM systems is their dependence on single-point mechanical scanning of samples, the necessity of which has sharply limited their range of observable phenomena, sampling resolution, and richness of collected data due to significant time overheads needed for imaging acquisition. This necessity of single-point scanning stems from the limitations of detection equipment which, owing to the technical requirements of coherent THz detection, are not feasible to construct in an array format. Despite these difficulties, the potential for computational imaging approaches to LTEM and TCM imaging has to date remained unexplored.

Within this context, the ongoing work presented in this chapter aims to enhance the performance capabilities of these technologies, in particular TCM imaging, by utilizing the computational principles of SPI to eliminate raster scanning and thus expand the horizons of TCM technology as a platform for diagnostic imaging. Towards this goal, the author proposes an experimentally verified technique for modulating the THz emission process using continuous wave (CW) laser illumination. By introducing structured CW illumination to an expanded region of fs laser-induced THz emission, SPI-ASAP may be incorporated through minimal modifications to the architecture of established TCM systems, while crucially avoiding interference with the chemical and physical phenomena recorded by the system. Although having not yet reached the data collection stage, the author's work towards a functional prototype has to date produced an effectively completed design, the components of which have been fully sourced and assembled in laboratory. A description of the design aspects of this prototype, as well as experimental evidence of the modulation potential of CW laser illumination, are the subjects of this chapter.

4.2 Principles of computational imaging for terahertz chemical microscopy

4.2.1 Mechanism of terahertz emission

For semiconductors probed under LTEM or TCM, the THz emission response reflects the dynamic motion of photoexcited carriers which, via the laws of classical electrodynamics, leads to the generation of THz radiation as a result of a time-varying current density,

$$E_{\text{THz}} \propto \frac{\partial \boldsymbol{J}(t)}{\partial t} = e\, v(t) \frac{\partial n(t)}{\partial t} + e\, n(t) \frac{\partial v(t)}{\partial t} \tag{4.1}$$

where $\boldsymbol{J}(t) = e\, n(t)\, v(t)$ is the instantaneous current density, e is the elementary charge, and $n(t)$ and $v(t)$ are the instantaneous carrier density and mean carrier velocity, respectively. Normally, the time derivative of the carrier density $\partial n(t)/\partial t$ is related to the pulse characteristics of the fs laser used for excitation and is therefore of non-varying influence under fixed laser conditions [146]. However, in situations where the photoexcited portion of the semiconductor is subject to the influence of local electric fields, the emission of THz becomes modulated due to the proportional impact of electric fields on carrier acceleration $\partial v(t)/\partial t$. Combined with the fact that many chemically and

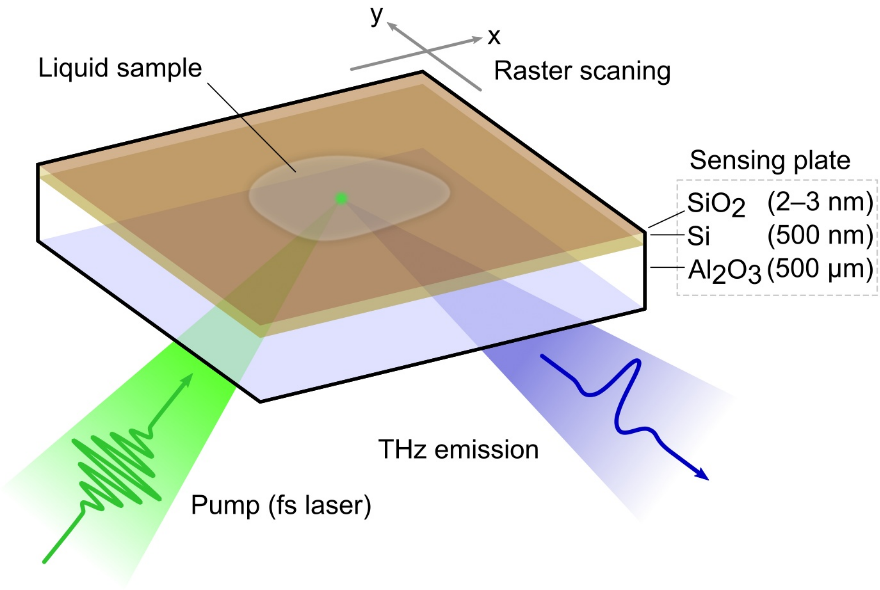

Figure 4.2 Principles of conventional TCM imaging. Schematic diagram of an arrangement for conventional TCM imaging showing the composition of a SOS sensing plate (dimensions in parentheses indicate typical layer thicknesses).

biologically relevant phenomena can sensitively impact microscopic electric fields near the surfaces of semiconductors [140, 146, 147], it is through this influence that the method of TCM imaging derives its chief diagnostic value.

In contrast to LTEM imaging which relies solely on the unmodified material composition of its targets for compatibility with laser-induced THz emission, the experimental arrangement of TCM imaging provides a dedicated semiconductor component, referred to as the 'sensing plate', that is placed into contact with a liquid sample and used to provide the source of THz emission. A schematic diagram of a TCM system sensing plate can be found in Fig. 4.2. In operation, chemically or biologically relevant molecules placed in solution are used to wet the surface of the sensing plate, which is subsequently imaged via single-point scanning of the focused laser spot, together with the coherent detection of THz waveforms. Although sometimes modified by the addition of other molecules, the sensing plate component traditionally chosen for TCM imaging is silicon-on-sapphire (SOS), a composite material consisting of an epitaxially grown thin film of silicon (Si) deposited on a sapphire (Al_2O_3) wafer. Importantly for the emission of THz radiation, exposure to air leads to a native layer of silicon oxide (SiO_2) being present on the SOS material, a fact which produces a static depletion layer electric field near the surface of the semiconductor that may be modified by the interaction of chemical reagents [140]. With the sapphire substrate serving as a structure that is transparent to both THz and optical wavelengths, a chemical solution placed on the top surface of the horizontally oriented sensing plate is illuminated by a focused fs laser from the bottom side, with subsequent THz detection taking place at the reflection angle of the laser illumination, thus avoiding influence by the absorption properties of the liquid sample.

4.2.2 Detection of terahertz radiation

The method of THz wave sensing and analysis used by LTEM and TCM imaging systems is known as THz time-domain spectroscopy (THz-TDS) [105], a pump-probe experimental technique in which measurements of electric field transients are obtained directly in the time-domain via the use of an optically triggered detector in conjunction with an optical delay line. Historically, THz-TDS was introduced as a methodology for the spectroscopic characterization of materials in the THz region, in particular for the study of certain molecular gases [148, 149]. When used for the measurement of THz-range spectra, THz-TDS experiments include a dedicated opto-electronic means for the generation of THz pulses that propagate through or reflect from samples before detection. In contrast, when THz-TDS is used within LTEM or TCM experiments, the sample itself takes the place of a dedicated THz source. Typical THz pulses generated/acquired via THz-TDS take the shape of single-cycle or few-cycle electric field oscillations with periods on the order of 1 picosecond (ps), and spectral content spanning the range between 100 GHz and 5 THz [127]. As a well-established means of THz measurement, the strengths of THz-TDS include its high temporal resolution (typically below 0.1 ps), combined with the ability to recover both amplitude and phase information from spectroscopic measurements derived via computational Fourier transforms performed on time-domain data [129].

Although the properties of nonlinear crystals may be used for either the generation or detection of THz pulses in THz-TDS, the majority of implementations of THz-TDS, in particular for LTEM and TCM imaging, utilize photoconductive antennas (PCAs). Notable for their growing commercial availability in recent years, PCAs are semiconductor-based opto-electronic devices which may be used for both the generation and detection of THz radiation depending on their incorporation with auxiliary electronic equipment. In their most basic form, PCAs consist of a pair of metallic (typically gold) electrodes deposited on a semiconductor substrate. The correct selection of semiconductor material, electrode separation distance, and overall electrode geometry, allow PCAs to operate as optically controlled sub-picosecond electronic switches when optical excitation is provided to the small region (typically <10 µm across) of semiconductor material lying between the electrodes [105]. When a constant voltage is applied across the electrodes during switching induced by a short-duration optical pulse, acceleration of the photocarriers under the applied electric field leads to the generation of THz radiation according to equation (4.1). Conversely, when the photocarrier lifetime of the semiconductor substrate is sufficiently short (i.e. sub-picosecond), a PCA may serve as a THz detector via the measurement of charge transport between the electrodes caused by ambient electric fields during the brief interval of photocarrier-induced conductivity.

A schematic of the THz-TDS technique illustrating the use of PCAs for the generation and detection of THz pulses is depicted in Fig. 4.3a. During the system's operation, input optical pulses from a femtosecond laser source are split into two beam paths labeled 'pump' and 'probe' that are used to drive the generation and detection of THz, respectively. At the end of the pump beam path,

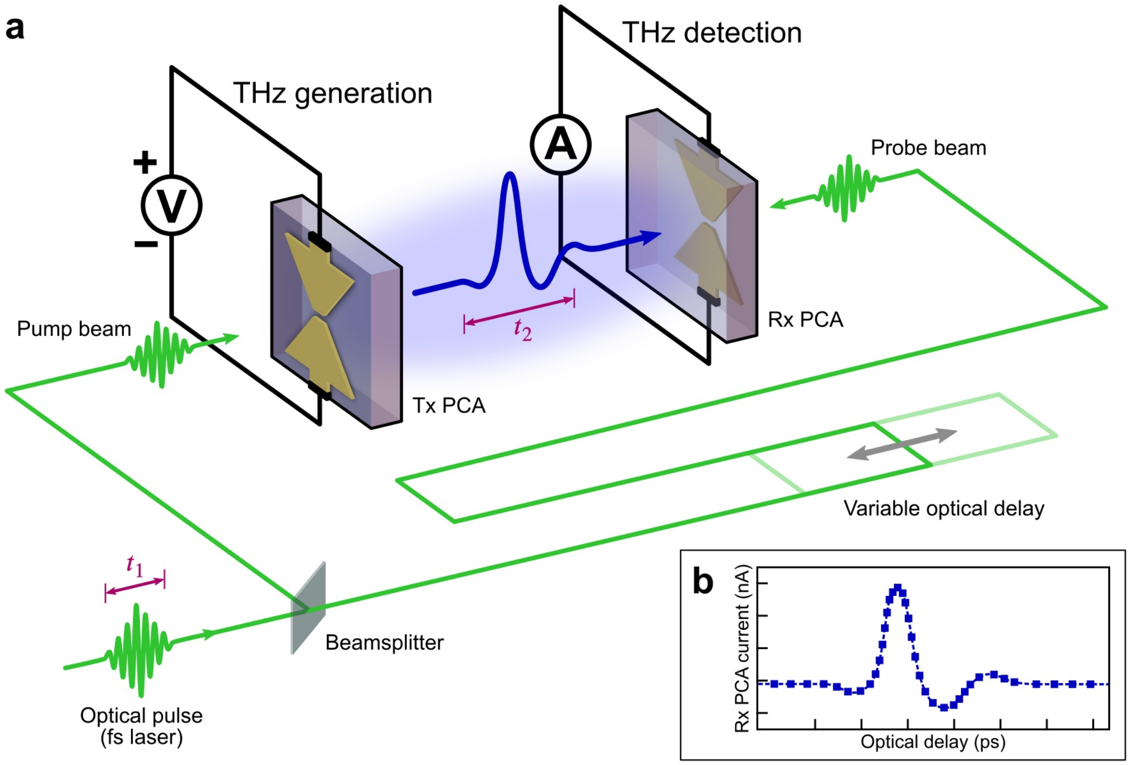

Figure 4.3 Principle of THz-TDS using photoconductive antennas (PCAs). **(a)** Schematic illustration of the experimental layout of THz-TDS. THz generation occurs via the interaction of a pump beam optical pulse with the transmission PCA (Tx PCA) which is held under a DC bias. THz detection occurs via the interaction of a separate but temporally correlated probe beam pulse with the reception PCA (Rx PCA), resulting in a time-varying current. t_1, optical pulse width; t_2, THz pulse width. **(b)** Measurement of THz waveforms resulting from detection of Rx PCA current as a function of optical delay.

interaction of a fs laser pulse with a PCA connected to a voltage source leads to the generation of THz via a time varying inter-electrode photocurrent. Conversely at the end of the probe beam path, interaction of a separate fs laser pulse with a PCA connected to equipment for the measurement of electrical current enables THz detection via sensing of field-induced electrode charge transport. Crucial for the operation of THz-TDS are the time-gated and time-correlated aspects of the mechanisms used for THz generation and detection. Firstly, whether PCAs or nonlinear crystals are used to implement THz-TDS, the use of short optical pulses is mandatory, as they serve as impulse-like triggers whose duration impacts the characteristics of generated THz pulses, as well as the temporal resolution at which the electric field of such pulses is sampled. The accurate retrieval of THz measurements therefore requires $t_1 \ll t_2$ for t_1 and t_2 representing the durations of optical and THz pulses, respectively, with values of $t_2 \approx 1$ ps necessitating the use of fs lasers in practice. Secondly, the use of a beamsplitter to generate the pump and probe beam paths is also of high importance, as it intrinsically leads to the time-correlated arrivals of optical pulses to both the means of THz generation and detection. Finally, with the time-gated and time-correlated aspects of a THz-TDS system in place, current signals from the detection PCA will thus correspond to the charge transport induced by a fixed sub-picosecond portion of the generated THz response, with time-domain measurement of the entire THz waveform thus taking place via scanning of a variable optical delay (Fig. 4.3b).

In practice, several details often modify the picture of THz-TDS illustrated by Fig. 4.3. Firstly, PCAs are often fabricated with additional lens components (typically constructed out of high-resistivity silicon) that, when placed on the side of the semiconductor substrate opposite the electrodes, facilitate THz collimation and focusing. Secondly, the detection of THz signals via charge transport is almost always assisted by the use of lock-in detection for the amplification of weak current signals, for which a lock-in signal may be introduced via modulation of the THz generating PCA's bias voltage, or via the use of an optical chopper in either the pump or probe beam paths. Thirdly, reflective optics (typically off-axis parabolic mirrors, OAPMs) are often used by THz-TDS systems to manage the focusing and collimation of THz radiation onto and from samples placed in the THz beam path. Finally, for THz-TDS measurements requiring high accuracy, the sensitive absorption of THz radiation to water vapor present in air often makes the use of physical enclosures necessary in order to mitigate atmospheric humidity within the THz beam path, with common strategies including air displacement with dry nitrogen gas and the use of chemical desiccants.

Although the richness of time-domain measurement is well-matched for the diagnostic imaging needs of LTEM and TCM systems, as a means of THz image sensing THz-TDS suffers from several limitations. Most prominent among these is the inherent complexity of optically triggered detection which, by requiring input from the same fs laser dedicated to THz generation, creates enormous difficulties for the prospect of array-format detectors whose required optical input power and intricacy of alignment would both necessarily scale with increasing pixel count. This has led to THz-TDS in practice being limited to exclusively the single-point detection of THz waveforms. Moreover, in conjunction with the limitations of single-point detection for imaging, the measurement of THz waveforms via THz-TDS generally requires long acquisition times during which the position of the optical delay line must be mechanically scanned with high precision. As a result, imaging systems making use of THz-TDS for time-resolved or spectral imaging must contend with the acquisition of 3D datasets, with the vast majority of approaches incurring massive time overheads from the use of mechanical scanning for both the 2D imaging plane, as well as the temporal axis of each THz waveform on a per-pixel basis.

In reaction to these limitations, the potential of computational methods as a means to enhance the performance of THz-TDS imaging systems has long been recognized, with the first demonstrations of SPI under THz-TDS measurement being carried out almost immediately after the advent of compressive sensing techniques and the single-pixel imaging concept [3, 47, 48]. Owing to the fact that sampling with THz-TDS amounts to the measurement of a time-varying electric field in the vicinity of the single-point sensor, the application of SPI techniques for imaging with THz-TDS is enabled via the superposition principle for electromagnetic radiation, which guarantees the linearity of electric field components combined under simultaneous detection. Subsequently, THz SPI attracted much interest with initial research focusing on means for modulating free-space THz beams with mechanically scanned masks [49, 50, 115], and later by masks implemented with optically pumped semiconductors controlled via DMD [19, 33, 46]. However, in contrast to the widespread interest in THz-TDS driven SPI carried out with dedicated THz sources, there have been as yet no demonstrations of single-pixel computational methods applied to TCM systems which rely on the sample-dependent generation of THz.

4.2.3 Techniques for spatial modulation

To generalize the operation of TCM systems to utilize SPI, a means of spatially modulating the THz response is required. Returning to the expression of the THz electric field response in equation (4.1), it can be seen that aside from the influence of local electric fields on the carrier acceleration term $\partial v(t)/\partial t$, the photocarrier density itself $n(t)$ provides an independent means for the external control of THz signals. Considering the options for the optical control of $n(t)$, one obvious approach, depicted in Fig. 4.4a, is the spatial modulation of the fs laser itself, replacing focused single-point illumination with an expanded field of structured illumination that selectively patterns the photocarrier density, and thus sites of THz emission, within the field of view (FOV). This direct approach, although conceptually simple, would suffer from several drawbacks in practice if used with DMD hardware. First, given the fact that most TCM systems operate with limited fs laser power, the inherently low diffraction efficiency of DMDs would introduce a significant waste (typically on the order of 80–90%) of the optical power available for sample illumination [95]. Second, since DMDs in practice function as both binary modulators and blazed gratings, the modulation of pulsed (i.e. wide bandwidth) optical signals must introduce a tilted pulse front via dispersion [150]; the compensation of which, being potentially necessary given the time sensitivity of THz-TDS, would require the use of additional dispersion-inducing optics, thus increasing system cost and complexity while further decreasing optical efficiency [151, 152]. For TCM systems, the loss of optical power available for sample illumination must consequently reduce both the strength of THz emission and the signal-to-noise ratio (SNR) of subsequent waveform measurements. As a result, designs prioritizing the conservation of optical power available for THz generation must effectively preclude the use of DMD hardware for direct spatial modulation in TCM, producing a sharp disadvantage for system speed and flexibility.

However, in order to maximize optical efficiency while retaining the use of DMD hardware, modulation of the carrier density may instead be provided by a separate optical source with photon energies sufficient for photoexcitation. This arrangement, depicted in Fig. 4.4b, features an expanded area of fs laser illumination that is also illuminated by a CW optical beam carrying the spatial patterns necessary for coded sampling. Under selective illumination by the CW beam, each site of THz emission within the FOV could then be subject to a controlled background photocarrier density, thus providing a means for the modulation of the THz emission process. As will be soon discussed, experiments observing the effect of such CW illumination on THz signals from SOS sensing plates have shown that a ‘quenching’ (i.e. reduction) of THz waveform amplitude does in fact occur under

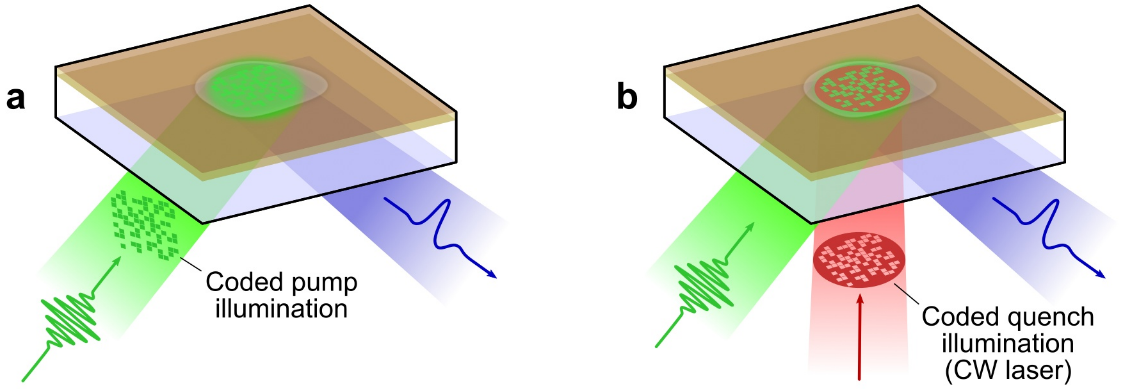

Figure 4.4 Principles of computational TCM imaging. **(a)** Schematic of computational TCM imaging using spatial patterning of the optical pump used to illuminate the sensing plate. **(b)** Schematic of computational TCM imaging using spatial patterning of a separate CW quenching beam.

CW illumination. As such, the encoding pattern shown in Fig. 4.4b is depicted as the inverse of that shown in Fig. 4.4a in order to visualize circumstances resulting in equivalent coded measurements. Crucially, the strategy of spatial encoding with a separate CW source allows for the unproblematic integration of DMD hardware both by eliminating the possibility of front pulse tilt effects, while also conserving the optical power available for THz generation. Moreover, by isolating the components used for THz generation and detection from the components used for modulation, this strategy allows SPI to be implemented with existing TCM systems with minimal necessary modification (i.e. expansion of the area of pump illumination to cover the FOV).

Based on these considerations, the strategy of CW quenching is proposed by the author for the implementation of computational terahertz chemical microscopy. As the key to this proposed technique, experimental results demonstrating the quenching effect will be presented in the following section 4.3.1. Although any means of spatial modulation compatible with CW light could be suited for computational TCM imaging, the proven high-speed and real-time capabilities of SPI-ASAP make it an attractive option for structured illumination and pipelined reconstruction, with the envisioned operation depicted in Fig. 4.4b matching well with the already proven approach shown in chapter 3. Nonetheless, many design considerations must still accompany the integration of SPI-ASAP with TCM. Details of these considerations, having been accounted for in the construction of the current system prototype, are discussed in section 4.4.

4.3 Results

4.3.1 Experimental investigation of THz emission quenching

In order to demonstrate the potential of CW modulation for the control of THz emission signals, an existing conventional TCM system available at the INRS was used as a convenient testing platform prior to construction of the final prototype. Although more complete details of the existing system have been published elsewhere [147, 153], a schematic illustration of the system and the experimental setup is shown in Fig. 4.5. The optical source used for THz generation was a ytterbium (Yb)-doped fs laser (Newport Spectra-Physics HighQ-2) which had a pulse duration of 250 fs, a center wavelength of 1045 nm, and a pulse repetition rate of 63 MHz. The fs laser source was split into two beams that facilitated the use of THz-TDS for waveform measurement. One beam was diverted to a motorized optical delay line and subsequently used to optically trigger a commercial PCA (Batop bPCA-180-05-10-1060-h). The other part of the pump beam was focused and frequency-doubled using a type I BBO crystal to produce the second harmonic at 523 nm. An optical band-pass filter was placed after the BBO crystal to remove the fundamental from the pump signal delivered to the sensing plate, at which the frequency doubled pump was focused to a spot size of 2 mm. At the same time, 671 nm light from a CW laser (CNI Laser MRL-III-671) was focused to an equal spot size and superimposed on the location of pump illumination. To enhance the SNR of the measured signals, lock-in amplification was used (Stanford Research Systems SR830) in conjunction with a motorized optical chopper that was placed in the pump arm of the system before the BBO crystal. Optical power in the 523 nm pump and the CW quench beams was controlled with the use of neutral density filters. The maximum optical power available for THz generation and CW quenching was approximately 50 mW and 240 mW, respectively. The SOS sensing plate was used without a liquid sample. During experiment, each THz waveform consisted of 100 samples recorded over a 10 ps duration that captured the peak of the THz signal transient, corresponding to a total travel distance by the motorized delay line of approximately 1.5 mm. The optical chopper was operated at a chop frequency of 110 Hz that provided the reference frequency for lock-in amplification, with acquisition of each waveform occurring over a period of 5 minutes.

The resulting THz waveforms recorded as a function of both pump and quench power are illustrated in Fig. 4.6. The results demonstrate the existence of a spectrally uniform quenching effect whose proportional effect is independent of incident pump laser power. Importantly for the possibility of computational TCM, these results indicate that controlled patterns of CW illumination are capable of reducing the peak-to-peak amplitude of THz signals by as much as 35% at the limit of the optical power available in the experiment. Within the framework of SPI, this modulation strength, although partial, is nonetheless wholly sufficient for the execution of computational imaging (a point demonstrated in section 4.4.2). Of interest within the results of Fig. 4.6 is the relative uniformity of the quenching effect as a function of incident pump power. In particular, Fig. 4.6f demonstrates that a 35% modulation is produced uniformly across pump powers spanning an order of magnitude, corresponding to pump powers ranging between 21% and 2.1% of the power used for CW quenching. Moreover, a steady plateau in the strength of CW quenching is observed, with the trend in Fig. 4.6f suggesting an ultimate limit of the effect occurring below 50% modulation against increasing quench laser power.

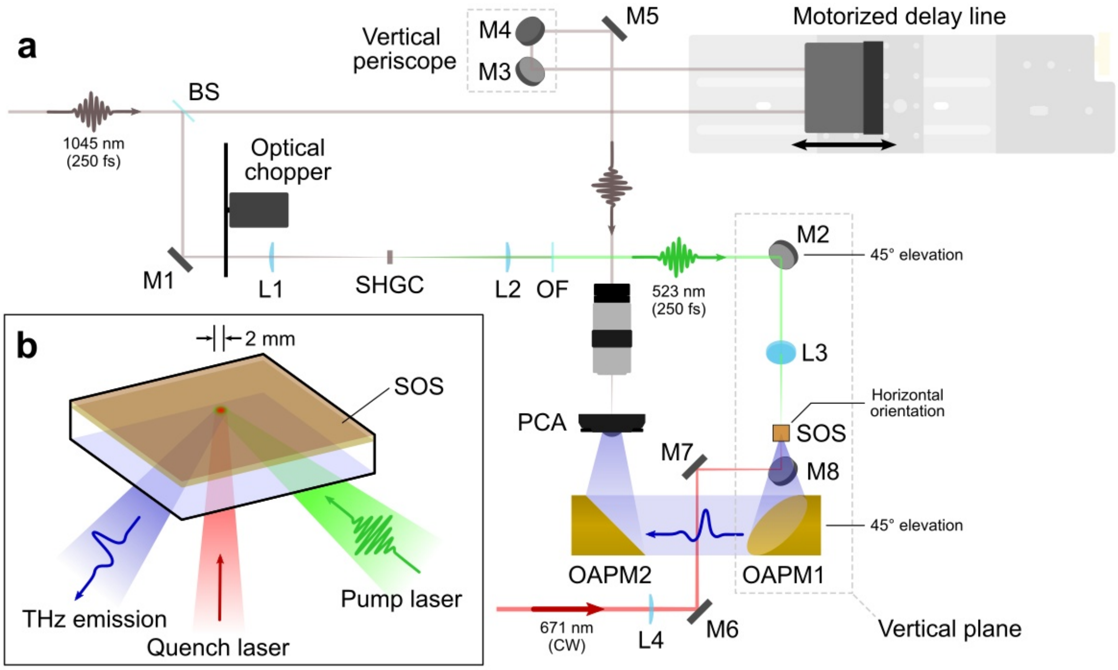

Figure 4.5 Experimental setup for observing the effects of THz emission quenching. **(a)** Schematic illustration of the system setup in the form of a conventional TCM with the sensing plate oriented horizontally. Alignment of the pump laser, quench laser, and direction of THz emission detection occurred in a vertical plane with elevations as noted. BS, beamsplitter; M1–M8, mirrors; PCA, photoconductive antenna; L1–L4 lenses, OAPM1–OAPM2, off-axis parabolic mirrors; SHGC, second harmonic generation crystal; OF, optical bandpass filter; SOS, silicon-on-sapphire sensing plate. **(b)** Close-up illustration of the sensing plate showing the incident orientations of the optical beams.

4.3.2 A qualitative model for THz emission quenching

Within the scope of the research yet undertaken by the author, a quantitative explanation for the quenching effect incorporating the material properties of SOS epitaxial films has not yet been obtained. Nonetheless, a simple qualitative model incorporating the basic principle of equation (4.1) can be supplied as a first step. Under constant illumination by a CW laser, a portion of a photosensitive material such as silicon can be expected to reach equilibrium with respect to the density $n(t)$ of photocarriers which are generated within the material. This equilibrium density should be expected to both increase with increasing intensity of illumination, while also gradually reaching a point of saturation owing to the finite number of photocarrier donor atoms present in the lattice. A generic qualitative plot of equilibrium photocarrier density illustrating these characteristics is shown in Fig. 4.7. Given a certain condition of constant illumination corresponding to a point along the equilibrium curve, the addition of a pulse of illumination from a fs laser may be regarded as a perturbation that temporarily disrupts the equilibrium of photocarriers, leading to a time-dependence of $n(t)$ from which THz emission proceeds via the term $\partial n(t)/\partial t$ in equation (4.1). However, the magnitude of the time-dependent perturbation induced by the pump pulse should be proportional to the derivative at the point of equilibrium which, owing to the shape of the equilibrium curve,

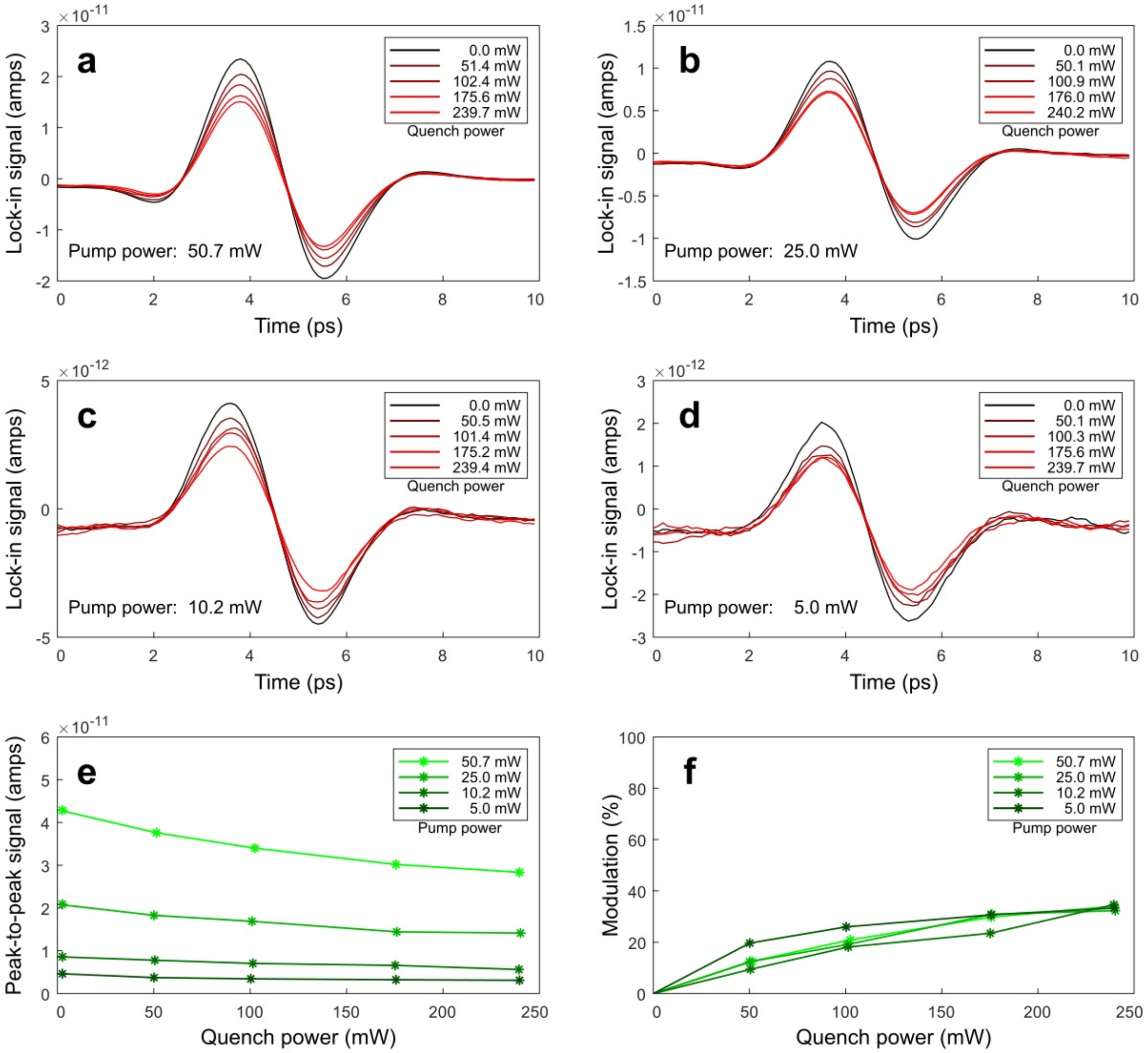

Figure 4.6 Evidence for CW laser quenching of THz emissions. (a)–(d) Time-domain THz waveforms measured from SOS with varying fs (pump) laser powers, with each plot showing superimposed waveforms from a series of CW (quenching) laser powers. Raw waveform data has been smoothed with the use of a moving average of 11 data points. **(e)** Plots of peak-to-peak signal amplitude as a function of quenching power for various pump powers. **(f)** Modulation depth, defined as relative peak-to-peak amplitude difference, shown for the same data presented in (e).

should decrease as equilibrium points are chosen with increasing CW illumination intensity. Thus, by the equilibrium curve's shape, we should conclude that increased intensity of CW illumination will result in reduced variation in the perturbed time-dependent photocarrier density $n(t)$, reducing the maximum rate of change $\partial n(t)/\partial t$ and thus providing a mechanism for suppressing the strength of THz emission signals via equation (4.1).

Although non-quantitative, the hypothesis that changes in $n(t)$ under fs illumination should be mediated by derivatives along the photocarrier equilibrium curve is able to explain three central aspects of the data at hand: the existence of a quenching effect itself, the increasing dependence of modulation strength with increased illumination intensity, and the constancy of modulation strength as a function of pump laser power. For constant pump laser power, increasing the illumination intensity moves the equilibrium point towards regions where the curve's derivative decreases, thus suppressing the magnitude of perturbations seen by the photocarrier density. Alternatively, varying pump intensities, corresponding to the perturbations visualized by the green arrows in Fig. 4.7, are seen to produce proportionally varying perturbations in photocarrier density with the proportionality being determined by the curve's derivative which is constant for fixed CW illumination.

Although presented as a 'first step' towards a full understanding of the observed effect of CW illumination, it is clear that this model comes with limitations beyond those incurred as a qualitative model. First, although able to account for THz emission quenching through the photocarrier density's rate of change $\partial n(t)/\partial t$, the mechanism of THz emission given by equation (4.1) is also dependent on the photocarrier density itself which increases in magnitude with increasing illumination intensity. Thus the explanation of a net quenching effect requires additional information, not supplied by the qualitative model, in order to predict the influence of $\partial n(t)/\partial t$ outweighing the opposing influence of $n(t)$ as illumination intensity is increased (this additional information, still keeping with the mechanism of equation (4.1), would take the form of material properties influencing the mobility of photocarriers). Second, the assumptions of a photocarrier equilibrium curve that is strictly increasing and bounded above would seemingly imply that a 100% modulation strength is achievable in the limit of increasing CW intensity, a prediction which does not appear consistent with the results of Fig. 4.6f. Third, another plausible mechanism not addressed by this model for the quenching of THz signals is the screening of emitted THz by the increased conductivity produced in the silicon layer of the sensing plate under CW illumination. Indeed, this effect when used in bulk semiconductor materials has already formed the basis of much experimental work implementing SPI with THz-TDS [19, 33, 46]. However, the contribution of such screening effects would suggest a modulation depth that would increase as pump power was decreased, a behavior inconsistent with the data of Fig. 4.6f. Evidently, the lack of a screening effect is likely due to the reduced thickness of the semiconductor layer present in the SOS sensing plate (500 nm), in contrast to the bulk semiconductors (i.e. thicknesses typically above 0.1 mm) employed by previous experiments [19, 46, 104].

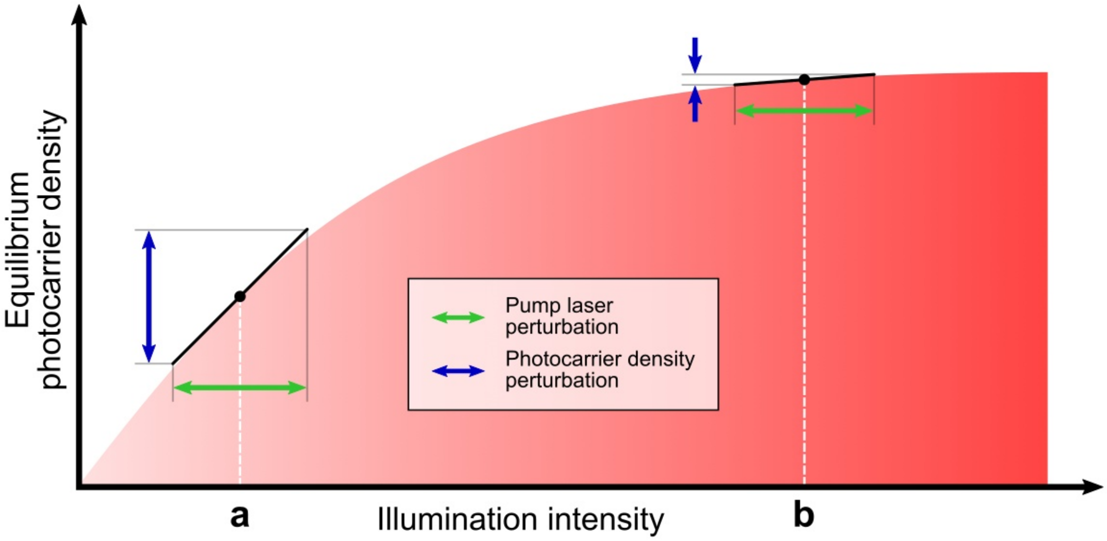

Figure 4.7 Preliminary qualitative model of THz emission quenching. (a) Photocarrier equilibrium under low illumination intensity showing perturbations proportional to the intensity perturbation introduced by the pump laser according to the derivative of the equilibrium curve. **(b)** Same as (a) with the equilibrium point under high illumination intensity showing reduced perturbations owing to the smaller derivative near saturation.

4.4 Design and construction of a prototype system for computational terahertz chemical microscopy

4.4.1 Considerations influencing the optical design and selection of components

Based on the positive evidence of THz emission quenching with CW illumination, the design and construction of a prototype system for computational TCM has been carried out by the author. The design of the prototype system was approached from the perspective of mirroring the functionality and component selection of the already existing TCM system available at the INRS [147, 153]. This dictated the selection of most components related to THz generation and detection including the PCA used for THz detection, and the desire to support the option for generating the second pump harmonic[1]. An additional constraint was the re-use of laser equipment already used by the existing TCM system. This dictated the optical parameters of the pumping laser whose maximum average power output was 1.6 W (1045 nm, 250 fs, 63 MHz). Adoption of the same PCA hardware for THz detection also dictated the parameters of the beamsplitter selected for the system which had a power splitting ratio of 95%/5% (reflection/transmission) for the beams dedicated for the

---

[1] Although not a feature of other TCM systems, an ongoing requirement of the existing TCM system is to support research into the use of alternate semiconductor materials used in the fabrication of sensing plates. To this end, the use of nonlinear crystals for SHG has been established in order to accommodate a wider range of semiconductor materials with larger band gap energies. Although frequency doubling of the 1045 nm pump laser source is not necessary to exceed the band gap of silicon (1.12 eV, 1.1 µm photon wavelength) for THz emission from SOS sensing plates, considerations for the use of SHG have still been undertaken to continue the research objectives of the existing system with the design of the prototype computational TCM.

pump and probe arms, respectively. Selection of this splitting ratio was determined based on the desire to maximize pump illumination power, the relatively low optical power needs of the PCA (20 mW maximum input), and commercial availability. Although during initial testing, the use of the 671 nm CW laser (240 mW) used in the initial experiments of the SPI-ASAP system was convenient, the use of other CW sources capable of higher output power was not precluded from the design considerations. Finally, as a more convenient embodiment of the TCM system depicted in Fig. 4.5, it was desired to eliminate the complication of having the pump beam and direction THz emission aligned in a vertical plane. Reasons for this alteration included reducing the difficulty of system alignment, as well as reducing the hazards of laser safety, both factors associated with systems whose beam paths leave the plane of the optical table.

As was already described in section 4.2, the central advantage of modulation performed via CW quenching is that it allows for the conservation of optical pump power available for sample illumination and thus THz emission. In order to quantify this advantage, measurements of the optical efficiency of the SPI-ASAP system and components of the existing TCM system were obtained in order to evaluate various design scenarios involving the use of either pump or quench beam modulation, as well as second harmonic generation. An evaluation of the four possible design scenarios stemming from these variations as well as the aforementioned equipment selections is presented in Fig. 4.8. For these calculations, the optical efficiency of the SPI-ASAP system was measured as 14.5% using 671 nm laser light with a DMD pattern conducive to full-field uniform illumination. However, in order to account for 'OFF' pixels present in the actual encoding patterns deployed by SPI-ASAP, a further 50% reduction of throughput power is necessary, resulting in the net optical efficiency of 7.5% for SPI-ASAP with 671 nm light. The efficiency of the frequency doubling implemented with the nonlinear crystal of the existing TCM system (BBO, 2 mm thickness) was also measured as 11.3%, although this conversion efficiency was considered to be below optimal due to laser induced optical damage exhibited by the crystal. Therefore, 11.3% was regarded as a conservative estimate for the potential efficiency of SHG for the purposes of design calculations. Nonetheless, of significance for the overall design of the prototype system, the optical efficiencies across the design scenarios shown in Fig. 4.8 demonstrate a marked advantage for the strategy of separate CW illumination taking advantage of THz emission quenching.

In order to adopt SPI for TCM imaging, an important departure from the design of traditional TCM systems must be made concerning the optics which collect, relay, and focus emitted THz signals onto the point detector. Whereas traditional TCM systems need only consider the point-to-point refocusing of emitted THz from the sensing plate to the detector, the wide-field nature of SPI measurement demands the implementation of area-to-point refocusing, the practical capabilities of which must set the limits of the system FOV. Fortunately, owing to relatively long optical wavelengths, the millimeter-scale diffraction limited spot sizes achievable by focusing THz radiation in free-space leads to some flexibility for accommodating collection areas a few millimeters in size. This flexibility for the existing TCM system was confirmed by observations made by the author which found that the system's ability to detect THz waveforms, although diminished, was largely

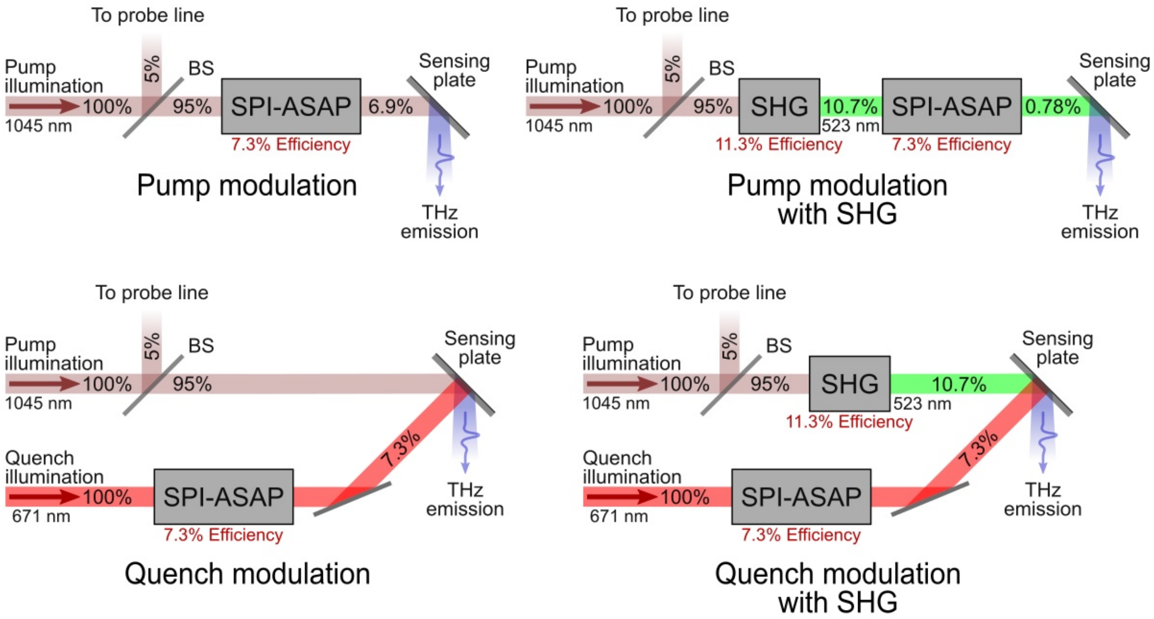

Figure 4.8 Evaluations of optical efficiency for various design scenarios of the computational TCM. Four scenarios are presented, covering each possible variation of (i) SPI-ASAP used as a means of pump or quench beam modulation, and (ii) the inclusion of a crystal for second harmonic generation. Percentages written on each beam reflect fractions of optical power available as a fraction of the total power of the illumination source. BS, beamsplitter; SHG, second harmonic generation.

retained when the spot of focused pump illumination was moved away from the position of optimal alignment by distances of up to approximately 3 mm. This suggests that FOV sizes on the order of 5 mm could be feasible for computational imaging via the appropriate use of the THz-dedicated optics already present in the existing TCM design. In particular, these optics consist of a pair of 90° off-axis parabolic mirrors (OAPMs) used in the configuration depicted in Fig. 4.5a. Using these optical components, one potential strategy for enlarging the sensing plate area available for THz detection is the slight defocusing of the position of the PCA detector, for example, by repositioning the PCA closer or further from the position of OAPM2 in Fig. 4.5a. For a given point on the sensing plate surface, such defocusing, although coming at the cost of detection SNR, would have the effect of expanding the region to which THz signals emitted from that point were focused in the plane of the detector, thus leading to the enhancement of THz detection for sites of THz emission positioned away from the point of optimum focus.

Working within these constraints, consideration was made for the configuration of OAPMs most conducive to the sensor defocusing strategy. Although the particular problem of area-to-spot focusing of THz using 90° OAPMs was not found to be addressed by existing literature, research does exist which consistently identifies an arrangement of OAPMs which minimizes optical aberrations of relevance for wide-area THz detectors [154–156]. This configuration consists of two OAPMs in the 'tip-to-tip' arrangement, in which both mirrors share a common axis of collimation that is coplanar with the off-axis focal points, and the overall shape possesses a left-right mirror symmetry (it should be noted that the arrangement of the OAPMs in Fig. 4.5a does not match this arrangement owing to the rotation of OAPM1 about the collimation axis). The ‘tip-to-tip’ OAPM configuration, though optimized for the performance of imaging, nonetheless inherits attractive properties for the problem of area-to-point focusing in that it achieves the consistent management of simulated spot sizes across entire areas of the input and output planes.

Of high relevance towards the proposed integration of SPI-ASAP with THz-TDS is the matter of accessory equipment used for the acquisition of THz signals. In most THz-TDS systems, including the existing TCM, THz detectors such as PCAs are used in conjunction with lock-in amplifiers which use a reference frequency imparted to the phenomenon under test to separate desired signals from backgrounds of strong noise interference. Unfortunately, the filtering benefits of lock-in amplification come at the cost of increasing the time required for signal acquisition, with low SNR signals incurring longer averaging times set by the characteristics of the internal filters utilized for noise rejection. For the case of the experiments in section 4.3.1 carried out with the existing TCM, acquisition of waveforms with satisfactory SNR required acquisition times of 1.5 seconds (doubled in the experiment to 3 seconds due to a lack of synchronization between the lock-in amplifier and the mechanical delay line). It is therefore clear that the use of lock-in amplification to perform the THz-TDS measurements of the proposed system, if necessary, would preclude the use of the high-speed modulation capabilities of SPI-ASAP. However, for systems which are able to exhibit a sufficiently high SNR, the THz-TDS measurement of waveforms without lock-in amplification is possible [46]. Unfortunately, confident prediction of the necessity of lock-in amplification for the computational TCM system is not realistic, owing to the high number of variables to be optimized in the course of constructing THz systems generally. Given this uncertainty, the outlook of the current project has thus been designed to accommodate a range of possible scenarios for the integration of SPI-ASAP. In the ‘worst-case’ scenario, reflecting the necessary use of lock-in amplification with acquisition times comparable to the existing TCM (i.e. on the order of seconds), the encoding and reconstruction scheme of SPI-ASAP may still be utilized without the aspect of rapid aggregated pattern scanning. In this case, pattern projection rates implemented with a DMD alone may be slowed arbitrarily to match the speed of lock-in amplification, with the motorized polygonal mirror either immobilized or removed. Although this modulation approach would no-longer conceptually meet the definition of SPI-ASAP, on a practical level the reuse of the hardware components of the as-built SPI-ASAP system would be convenient, with minimal modifications preferred. However, by making design decisions prioritizing the THz-relevant aspects of optical pump power and OAPM configuration, the feasibility of THz detection without lock-in amplification may be maximized to the greatest possible, thus increasing the likelihood of the full integration of SPI-ASAP.

4.4.2 Considerations of SPI-ASAP with limited modulation strength

Although the previously described results indicate that CW quenching is able to achieve partial modulation using THz emission from SOS, the establishment of any modulation effect is, in principle, sufficient for the implementation of SPI. In particular for the reconstruction framework of SPI-ASAP, the use of S-matrices as the basis for encoding pattern design and image recovery allows SPI-ASAP to remain fully compatible with modulation depths below 100%. We prove this assertion in this section.

To begin, let $\boldsymbol{S}$ represent an S-matrix of size $n \times n$ (within the discussion that follows, it is unnecessary to assume that $\boldsymbol{S}$ is cyclic), $\boldsymbol{J}$ represent the $n \times n$ matrix entirely consisting of 1s (i.e. $\boldsymbol{J}_{i,j} = 1$), and $\alpha \in [0, 1]$ be a given constant. Then under deployment of a set of encoding patterns determined by the rows of $\boldsymbol{S}$, we may represent an effective measurement matrix $\hat{\boldsymbol{S}}$ with modulation strength α as the linear combination of $\boldsymbol{S}$ and $\boldsymbol{J}$,

$$\hat{\boldsymbol{S}} = \alpha \boldsymbol{S} + (1 - \alpha)\, \boldsymbol{J} \quad . \tag{4.2}$$

Thus the elements of $\hat{\boldsymbol{S}}$ take on the values $1 - \alpha$ and 1, corresponding to when the elements of $\boldsymbol{S}$ are 0 or 1, respectively. Now we let the n-element vector $\boldsymbol{x}$ represent an underlying image subject to SPI measurement by $\hat{\boldsymbol{S}}$. As the framework of SPI-ASAP includes an interpolation step that allows for an invertible recovery problem to proceed even from under-sampled data, it is sufficient to consider the fully sampled case in which deployment of the encoding patterns formed by the rows of $\hat{\boldsymbol{S}}$ results in the measurement of the n-element vector $\boldsymbol{y}$ according to

$$\boldsymbol{y} = \hat{\boldsymbol{S}} \boldsymbol{x} \quad . \tag{4.3}$$

Image recovery proceeding via the direct application of $\boldsymbol{S}^{-1}$ then produces an estimated image $\hat{\boldsymbol{x}}$ according to

$$\begin{aligned} \hat{\boldsymbol{x}} &= \boldsymbol{S}^{-1} \boldsymbol{y} \\ &= \left(\alpha \boldsymbol{S}^{-1} \boldsymbol{S} + (1 - \alpha)\, \boldsymbol{S}^{-1} \boldsymbol{J} \right) \boldsymbol{x} \\ &= \alpha \boldsymbol{x} + (1 - \alpha)\, \boldsymbol{S}^{-1} \boldsymbol{J} \boldsymbol{x} \quad . \end{aligned} \tag{4.4}$$

Further simplification now occurs by recognizing certain properties of $\boldsymbol{S}$. By the relationship that S-matrices share with Hadamard matrices, it can be shown that each row and column of $\boldsymbol{S}$ contains exactly $\frac{n+1}{2}$ 1s and $\frac{n-1}{2}$ 0s. From this, the relations $\boldsymbol{S}\boldsymbol{J} = \boldsymbol{S}^T \boldsymbol{J} = \frac{n+1}{2} \boldsymbol{J}$ follow. Combined with the formula for the inverse of an S-matrix,

$$\boldsymbol{S}^{-1} = \frac{2}{n+1} \left(2\boldsymbol{S}^T - \boldsymbol{J} \right) \quad , \tag{4.5}$$

we obtain the equation $\boldsymbol{S}^{-1}\boldsymbol{J} = \frac{2}{n+1}\boldsymbol{J}$, and thus from equation (4.4) we obtain

$$\hat{\boldsymbol{x}} = \alpha \boldsymbol{x} + \frac{2(1-\alpha)}{n+1} \boldsymbol{J} \boldsymbol{x} = \alpha \boldsymbol{x} + \beta \frac{2(1-\alpha)}{n+1} \boldsymbol{e} \quad . \tag{4.6}$$

where β is a constant equal to the total intensity of the image $\boldsymbol{x}$, and $\boldsymbol{e}$ denotes a constant vector of 1s with n elements. Thus, equation (4.6) shows that up to a uniform background and a scaling factor, application of SPI-ASAP's recovery strategy is able to recover images $\boldsymbol{x}$ from bucket signal data $\boldsymbol{y}$ without modification in cases of limited modulation strength. Since $\hat{\boldsymbol{x}}$ retains the structural and contrast information present in $\boldsymbol{x}$, this methodology would suffice for the purposes of most applications of TCM imaging, which in practice use data normalization.

However, we note that the unknown and experimentally dependent constants α and β may each be inferred from simple auxiliary data that may be collected from within the same SPI experimental setup. In particular, we note that the deployment of 2D encoding patterns determined from the n-element zero vector and $\boldsymbol{e}$ (represented as column vectors) must correspond under our assumptions of limited modulation depth to the effective encoding patterns $(1-\alpha)\boldsymbol{e}$ and $\boldsymbol{e}$, respectively. Deployment of these encoding patterns would then provide the corresponding data points y_0 and y_1 according to,

$$y_0 = (1-\alpha)\,\boldsymbol{e}^T\boldsymbol{x} \quad \text{and} \quad y_1 = \boldsymbol{e}^T\boldsymbol{x} \ , \tag{4.7}$$

from which α and β may be found:

$$\alpha = \frac{y_1 - y_0}{y_1} \ , \qquad \beta = y_1 \ . \tag{4.8}$$

Thus by summarizing the results of equations (4.4), (4.6), and (4.8), we obtain

$$\boldsymbol{x} = \frac{y_1}{y_1 - y_0}\left[\boldsymbol{S}^{-1}\boldsymbol{y} - \frac{2y_0}{n+1}\boldsymbol{e}\right] = \frac{y_1}{y_1 - y_0}\boldsymbol{S}^{-1}\left[\boldsymbol{y} - y_0\boldsymbol{e}\right] \ , \tag{4.9}$$

which gives the exact recovery of $\boldsymbol{x}$ from $\boldsymbol{y}$. Intuitively, thanks to the linearity of the measurement model, this result indicates that correct recovery of $\boldsymbol{x}$ amounts to a correction of DC bias in the data $\boldsymbol{y}$, together with a rescaling equal to the inverse modulation strength $1/\alpha$.

4.4.3 The constructed prototype

Following the considerations and constraints described in section 4.4.1, material procurement and construction of a prototype system for computational TCM has been substantially completed. The to-scale system design plan together with a photograph of the prototype system are shown in Fig. 4.9. Though the overall layout of components resembles that of the existing TCM illustrated in Fig. 4.5, an important difference lies in the vertical orientation of the sensing plate, allowing for the alignment of all beam paths to remain within the plane of the optical table, while also allowing for the desired 'tip-to-tip' configuration of the OAPMs used for the collection and focusing of the THz signal. Although advantageous with respect to the compactness of system layout, the use of a vertical sensing plate comes at the cost of requiring special measures for the containment of liquid samples. Fortunately, apparatus for the containment of liquid samples compatible with the operation of sensing plates have already been present in the TCM literature, with various experiments demonstrating the construction of fluidic chips that in layered combination with sensing plates may form reservoirs and channels suited for the flow of aqueous reagents [144, 157, 158]. Of particular interest, owing to their ease of fabrication, are fluidic chips cast from polydimethylsiloxane (PDMS) elastomer [158]. Conveniently, casting of PDMS chips with millimeter-scale features is especially feasible by using molds fabricated using 3D printing methods such as resin lithography [159]. Preparations for the future construction of such fluidic chips, including the procurement of equipment and materials for PDMS casting and resin 3D printing, have been carried out for the present project.

In order to minimize system footprint, the design shown in Fig. 4.9 incorporates elevated platforms and shelving to accommodate active parts of the optical system, as well as various electronic equipment. One platform, positioned at a 9” elevation above the optical table, will be used to support both the SPI-ASAP modulation system as well as the CW laser source. Another platform constructed out of lumber materials provides a rigid shelf for the placement of a lock-in amplifier, delay generator, oscilloscope, and personal computer used for system automation and data analysis. In operation using CW quenching, encoding patterns generated by the elevated SPI-ASAP system will be imaged to the sensing plate via a vertical mirror periscope and relay optics.

In order to support a variety of imaging modes anticipated to be carried out over its experimental lifetime, several accommodations are made by the design of the prototype system. To allow for a wide range of pump illumination and imaging FOV conditions, the system supports the variable positioning of various lens components (L2–L5) with sliding rails. For controlling pump illumination, the combination of lenses L1 and L2 (also used for focusing onto an optional crystal for second harmonic generation) allows for variable spot sizes to be used on the sensing plate, with expansion and contraction of the illuminated area controlled by the positioning of L2 along the beam path. For controlling the imaging FOV, the combination of lenses L4 and L5 is provided, which relay the image of the adjustable slit at the output of the SPI-ASAP system to the sensing plate. Through the positioning of both lenses, a range of magnifications can be obtained, with L4 providing an easy means for focus adjustment by sliding it along the vertical post used for the support of the mirrors M7 and M8. In order to replicate conventional TCM operation, tight focusing of the pump beam can be controlled with the addition of lens L3. Finally, depending on the needs for THz-TDS measurement during operation, lock-in detection can be accommodated with the use of an optical chopper that may be positioned in the probe path as shown.

4.5 Conclusion

This chapter, although lacking the polished conclusion of a working imaging system for terahertz chemical microscopy, has had the purpose of describing the various building blocks that the author hopes will lead to such a conclusion in the near future. Separated from the many technical details, these building blocks consist of a platform for cutting edge single-pixel imaging, an attractive and relevant application within terahertz science, and a newly recognized means for introducing one to

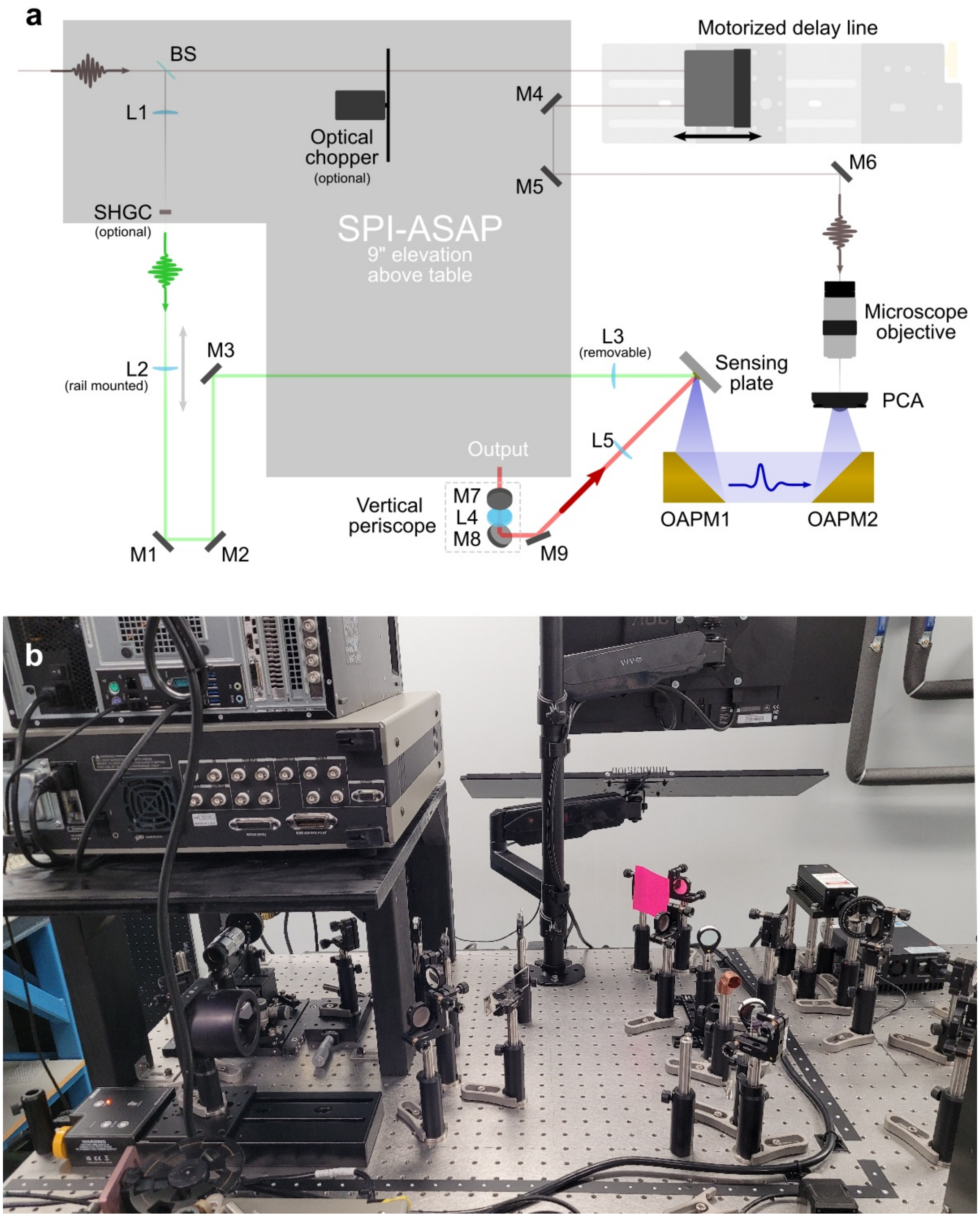

Figure 4.9 Design and construction of the prototype computational TCM system. **(a)** To-scale diagram of the system footprint, showing the components for coherent waveform detection. Structured CW illumination is provided by the SPI-ASAP system which is installed at a 9” above table elevation and imaged to the sensing plate with the use of a vertical periscope and relay optics. BS, beamsplitter; M1–M6, mirrors; PCA, photoconductive antenna; L1–L4 lenses, OAPM1–OAPM2, off-axis parabolic mirrors; SHGC, second harmonic generation crystal. **(b)** Photograph of the presently constructed system (SPI-ASAP module not shown).

the other.

The main future work envisioned within the scope of this project is self-evidently the completion of the working system prototype. Towards this goal however, the chief hurdles of design, procurement, and construction have already been cleared. In addition, a mechanism for the spatial modulation of THz emission has been identified and proposed for the integration of single-pixel imaging, and potentially the entire platform of SPI-ASAP, into the operation of TCM systems. Although a complete and quantitative picture of this mechanism is not yet at hand, it is clear that this mechanism represents a significant opportunity for the innovations of computational imaging to advance the state of the art for THz emission imaging.

Once completed, several future experiments are envisioned by the author and the author's collaborators for the working computational TCM prototype. In keeping with the research objectives of the current TCM system, the computational TCM could serve as test bed for for the use of other semiconductor materials for sensing plate construction, both under conventional TCM operation, as well as operation taking advantage of THz emission quenching. Materials so far procured by the author for these experiments include custom fabricated test targets and sensing plates made from epitaxially grown gallium arsenide (GaAs) and germanium (Ge). For the treatment of liquid samples, the higher imaging speeds of the computational TCM could find application in experiments that measure the pH of chemical solutions which interact in fluidic chips [144, 157, 158]. Beyond existing applications, the prospect of high-speed and real-time imaging holds great promise not only to expand the horizons of chemical and biological phenomena that may be studied through TCM imaging, but to also significantly advance the state of TCM systems as a technology ready for commercial development and widespread diagnostic use. With coded CW illumination able to provide a means for fast 2D imaging, the overheads of motorized scanning required for the collection of per-pixel waveform data could be reduced from the scanning of a 3D dataset, to scanning of only the 1D temporal axis, thus increasing the availability and richness of waveform data available from TCM experiments. Finally, in order to most fully investigate the potential of the proposed approach for computational TCM, the development of a theoretical model for the phenomenon of THz emission quenching, incorporating the quantitative properties of semiconductor materials, can be anticipated for the scope of future work.

5 CONCLUSION

The diverse landscape of scientific imaging, although dominated in the visible spectrum by array-format silicon-based photosensors, nonetheless requires a diversity of methods and technologies to fill the gaps, both spectral and temporal, where multi-pixel sensors can't see. As a strategy for addressing the fundamental engineering constraints affecting photosensor technologies at the frontiers of development, single-pixel imaging seeks to make the most out of the sensors that exist in the present; allowing the speeds of image acquisition to surpass the mechanical limitations of single-point scanning, and thus approach the full utilization of detector bandwidths.

This thesis has introduced SPI-ASAP, a platform for SPI designed to enable applications to high-speed and real-time imaging. By augmenting the performance of conventional DMDs with off-the-shelf laser scanning hardware, SPI-ASAP supports high-speed and ultrahigh-speed imaging through the scanned deployment of aggregated encoding patterns, thus allowing modulation rates to reach MHz bandwidths over two orders of magnitude above the top speeds achievable with DMD hardware alone. Furthermore, by recognizing the limitations inherent in the use of separate and generic approaches for modulation and reconstruction, SPI-ASAP supports video-rate real-time imaging through a tightly coupled modulation and reconstruction pipeline based on the optimal mathematical properties of cyclic S-matrices. Importantly and in contrast to other competing methods in the field of high-speed and real-time SPI, the construction of SPI-ASAP makes use of only off-the-shelf components. In particular, through its incorporation of DMD hardware, SPI-ASAP maintains superior flexibility with respect to imaging parameters such as pixel count and framerate, while also remaining compatible with a wide variety of specialized light sources.

The applications explored in this thesis for 3D imaging, ultrahigh-speed imaging, real-time imaging, and THz imaging, although wide ranging, reflect only a fraction of the imaging scenarios to which the techniques of SPI have so far been applied. Indeed, because SPI embodies a collection of computational approaches for the sampling of data in general, potential applications of SPI may be considered to arise wherever a means for deterministic light modulation can be implemented within an existing imaging methodology. Yet much work remains to be done within the area of SPI research in order to seek out those imaging methodologies lacking the tools of multi-pixel sensors, and successfully advance their capabilities. In this sense, the capabilities of high-speed and real-time operation should be seen as lucrative goals of SPI technology, the achievement of which has the power to dramatically transform the usability, maturity, application scope, and commercial potential of any imaging modality previously limited to single-point scanning. It is within this ambitious context that the work to realize SPI-ASAP has taken place.

However, it is clear that development must continue in order to fully realize the potential of SPI methodology within imaging science. Chief among the priorities of ongoing SPI research is the generalization to wavelengths outside of the visible spectrum. Indeed, the results presented in this thesis, in keeping with the majority of results produced within the field of SPI research, have utilized sources and single-pixel detectors operating in the visible band. This fact, while often a byproduct of minimizing the cost and design complexity of prototype SPI systems, has ultimately resulted in a continued scarcity of proven applications for which SPI technology is fully spared from competition with array-format sensors. Nonetheless, the ongoing improvements of visible band SPI systems represent significant steps toward addressing this scarcity of applications. In the case of SPI-ASAP, two considerations reflect its significance for non-visible SPI applications. Firstly, since it's fundamental components operate using reflection, SPI-ASAP remains compatible with ultraviolet (UV) and NIR radiation, with the range of operating wavelengths dictated mostly by the properties of the DMD used for experiments [18, 36, 160]. Secondly, the ability for visible or near-visible wavelengths to couple encoding patterns into diverse experimental scenarios makes SPI-ASAP potentially effective for implementing SPI using wavelengths which are not compatible with its optical components. This class of applications prominently includes the state-of-the-art for high-speed single-pixel THz imaging systems [19, 33, 46], as well as the proposed approach for computational THz chemical microscopy described in chapter 4.

The most immediate focus of the future work of SPI-ASAP will be its application to a computational THz chemical microscope. Beyond this goal, other opportunities in THz imaging exist for SPI-ASAP, in particular for systems which modulate free-space THz radiation with the use of patterned photoexcitation in semiconductor masks [19, 33, 46]. Improving the basic hardware components of SPI-ASAP via use of faster DMDs and polygonal mirror hardware would immediately lead to imaging speed improvements by up to a factor of 10 [11]. As previously noted, SPI-ASAP could be used to implement high-speed and/or real-time 3D single-pixel profilometry by extending the STDP system described in chapter 2 [10]. Although so far used for active mode SPI, the hardware of SPI-ASAP could be used for passive mode imaging for applications that rely on self-luminescent events, such as the optical property characterization of nanomaterials [120] and the monitoring of neural activities [121]. As demonstrated by its successful imaging of incandescent filaments, SPI-ASAP for imaging in strong ambient light conditions could be adopted for the study of other combustion phenomena [122]. Extending the operational spectral range of SPI-ASAP with suitable light sources and detectors could further enhance the fast detection of hazardous gases, an application already proven within SPI [18]. Finally, the trade-off between image quality and computational speed for the reconstruction method of SPI-ASAP could no-doubt be further explored by the application of machine learning techniques [38–40].

6 SOMMAIRE RÉCAPITULATIF

6.1 Introduction

L'appareil photo numérique multi-pixel représente l'une des technologies les plus avancées utilisées dans le domaine scientifique et dans la société en général. La miniaturisation progressive et l'amélioration continue des circuits intégrés à base de semi-conducteurs ont permis aux technologies de capteurs telles que les dispositifs à couplage de charge (CCD pour charge-coupled devices) ou les capteurs complémentaires métal-oxyde-semiconducteur (CMOS pour complementary metal-oxide semiconductor) de révolutionner les outils et les techniques d'imagerie scientifique, en particulier pour l'imagerie à grande vitesse et en temps réel. Pourtant, pour la plupart des longueurs d'onde en dehors du spectre visible, ou pour les phénomènes se produisant sur des échelles de temps extrêmement courtes, l'utilisation de ces technologies matures à base de silicium n'est pas possible ; un fait qui limite leur application dans de nombreux domaines d'intérêt scientifique [1]. Traditionnellement, dans les cas où l'immaturité de la technologie des capteurs a empêché l'utilisation de détecteurs multi-pixels, les systèmes d'imagerie ont été contraints d'adopter le balayage de trame, supprimant ainsi les vitesses d'acquisition d'images avec des limitations mécaniques souvent à plusieurs ordres de grandeur en dessous de la bande passante du détecteur disponible. En plus d'imposer d'importants obstacles à la vitesse d'acquisition des mesures, toutes les approches du balayage de trame à point unique, comme le positionnement motorisé de l'objet ou le guidage du faisceau par miroir, nécessitent des temps d'imagerie qui doivent être mis à niveau pour permettre au moins une mesure indépendante pour chaque pixel échantillonné dans l'image. Pourtant, il est clair que pour un dispositif ou un matériau photo-actif donné, le développement d'un photodétecteur électroniquement intégré en forme de matrice (si possible) doit apporter des compromis en ce qui concerne le coût global, les performances en matière de bruit et/ou la résolution temporelle par rapport à la même technologie dans un format à un seul pixel. Ainsi, si l'on dispose d'un moyen suffisamment rapide pour réaliser un échantillonnage optique bidimensionnel (2D) séquentiel, les avantages des détecteurs à un mono-pixel pourraient être exploités dans le but de développer des systèmes d'imagerie plus performants et moins coûteux.

L'imagerie mono-pixel (SPI de Single-pixel imaging), une nouvelle méthode d'imagerie scientifique, vise à éviter les limites du balayage de trame tout en tirant parti des avantages de performance des capteurs à un seul pixel. Contrairement au fonctionnement des systèmes d'imagerie dotés de capteurs multi-pixels classiques, les systèmes SPI (voir Fig. 6.1) capturent des images en enregistrant une séquence de produits internes à large champ calculés optiquement, impliquant l'image sous-jacente et un ensemble de motifs de codage spatial déterministes introduits dans le faisceau d'imagerie via un dispositif de modulation. Ces produits internes enregistrent l'image sous-jacente de manière indirecte, le redressement des images réelles dépendant de l'utilisation

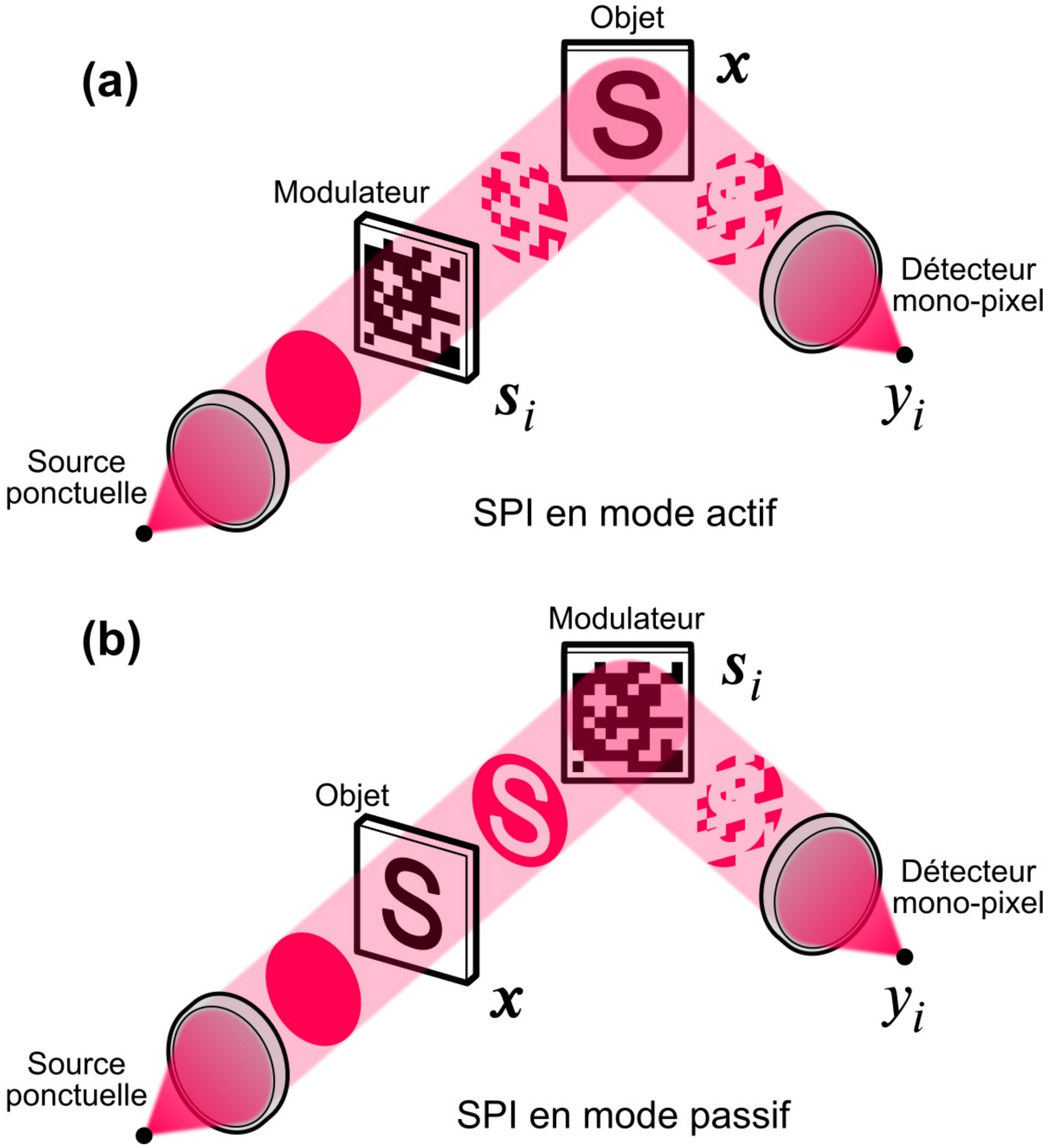

Figure 6.1 Illustration schématique du principe de l'imagerie à mono-pixel (SPI). **(a)** Le dispositif d'imagerie active, dans lequel le faisceau d'imagerie rencontre d'abord le modulateur, puis l'objet. **(b)** Le dispositif d'imagerie passive, dans lequel le faisceau d'imagerie rencontre d'abord l'objet, puis le modulateur. Dans l'une ou l'autre de ces dispositions, la formation d'image se fait par la mesure des produits internes calculés optiquement $y_i = \langle \boldsymbol{s}_i, \boldsymbol{x} \rangle$ pour une séquence de motifs codés $\boldsymbol{s}_i$ introduits par le modulateur. Les profils de section transversale du faisceau d'imagerie montrent les modifications apportées à sa structure spatiale par les interactions avec l'objet et le modulateur, les mesures y_i étant proportionnelles à l'intensité intégrée du profil final.

d'un algorithme de reconstruction et de la connaissance de la séquence de motifs de codage utilisée pendant l'expérience. Il est à remarquer que la structure codée et à large champ des mesures utilisées dans le SPI lui permet de bénéficier d'un avantage informatique totalement inaccessible aux systèmes de balayage de trame : la possibilité de récupérer une imagerie précise à partir d'un nombre de mesures du détecteur bien inférieur au nombre de pixels de l'image.

Ces dernières années, la popularité de la SPI s'est accrue en raison de la disponibilité croissante du matériel de modulation spatiale de la lumière (SLM de l'anglais spatial light modulation), ainsi que de la maturité des logiciels polyvalents pour la mise en œuvre d'algorithmes de reconstruction d'images sophistiqués. Pour les systèmes d'imagerie mono-pixel SPI fonctionnant avec des longueurs d'onde visibles ou proches du visible, la technologie SLM dominante est le dispositif à micromiroir numérique (DMD), capable d'afficher de manière reconfigurable et non mécanique des motifs binaires d'une résolution de l'ordre du méga-pixel à des fréquences pouvant atteindre 32 kHz [2]. Cependant, malgré les nombreux avantages qu'ils offrent, les fréquences de rafraîchissement des motifs en kHz des dispositifs DMD continuent de limiter fortement le taux d'acquisition des signaux de la plupart des systèmes d'imagerie mono-pixel SPI à un niveau inférieur aux bandes passantes en MHz des photodétecteurs à capteur ponctuel typique, ce qui ne permet pas d'exploiter pleinement les avantages de la résolution temporelle offerte par la détection à un mono-pixel. Afin de compenser les limitations de la fréquence d'affichage en kHz des dispositifs numériques à micromiroir DMD, la plupart des systèmes d'imagerie mono-pixelique SPI ont cherché à augmenter les vitesses d'imagerie en réduisant le nombre d'échantillons nécessaires à la récupération de l'image grâce à un algorithme de reconstruction sélectionné de manière adaptée. Bien qu'un ensemble suffisamment grand de motifs et de détecteurs de données puisse ne nécessiter qu'une inversion de matrice ou une moyenne statistique pour la reconstruction de l'image, la majorité des approches actuelles de l'imagerie mono-pixel SPI réduisent l' accroissement d'échantillonnage en utilisant des algorithmes de reconstruction d'une famille de techniques de calcul connues sous le nom de détection comprimée (CS pour compressed sensing) [3–6]. Malheureusement, bien que cela ait permis leur adoption au sein de SPI et ailleurs, la flexibilité et la généralité de la plupart des algorithmes CS dépendent de techniques d'optimisation convexe qui sont intrinsèquement répétitives, présentant des temps de traitement très variables et nécessitant des calculs supplémentaires [7–9]. Bien qu'avantageux pour les expériences d'imagerie qui traitent les données après acquisition, le compromis qui en résulte entre le temps requis pour le déploiement du motif et celui requis pour la reconstruction sophistiquée de l'image a empêché la plupart des systèmes à imagerie mono-pixel SPI de réaliser une visualisation en temps réel, où la reconstruction doit suivre immédiatement l'acquisition avec une synchronisation étroite.

Pour les systèmes SPI, la performance globale dépend essentiellement du matériel spécialisé utilisé pour la modulation spatiale de la lumière, ainsi que de l'algorithme choisi pour la reconstruction de l'image. Bien que l'existence de solutions technologiques robustes et polyvalentes pour chacun de ces composants (par exemple, les DMD pour la modulation et les algorithmes CS pour la reconstruction) ait rendu la recherche sur l'imagerie mono-pixel largement accessible, l'utilisation de solutions distinctes et génériques pour la modulation et la reconstruction n'a pas permis de remédier à bon nombre des limitations de rendement essentielles de la SPI. Il est donc raisonnable de s'attendre à ce que la résolution de ces problèmes, et donc l'augmentation des applications potentielles de la SPI, nécessite des solutions personnalisées pour les composants de base de l'imagerie mono-pixel. Heureusement, un certain nombre de développements récents ont permis de se rapprocher de cet objectif en remplaçant l'utilisation de DMD et/ou de CS conventionnels par d'autres modulateurs, des sources lumineuses et des algorithmes personnalisés [9, 13, 36, 43, 44]. Cependant, bien que ces travaux et d'autres aient continué à traiter séparément les limitations de vitesse de la modulation et de la reconstruction, ces efforts n'ont pas encore été suffisants pour établir une forme robuste, flexible et largement applicable de l'imagerie mono-pixel à grande vitesse ou en temps réel. Les progrès futurs vers cet objectif nécessiteront presque certainement le développement non seulement de matériel de modulation spécialisé, mais aussi d'algorithmes de reconstruction étroitement rattachés à leur fonctionnement. Ainsi, contrairement aux méthodes qui cherchent à améliorer les vitesses de modulation ou les temps de reconstruction de manière isolée, les approches qui sont capables de traiter ces aspects simultanément peuvent avoir le plus grand potentiel pour faire progresser la maturité technologique de l'imagerie mono-pixel SPI.

Dans cette ligne de développement, cette thèse introduit une nouvelle approche de la SPI appelée imagerie mono-pixel ultra-rapide par balayage de motifs agrégés (SPI-ASAP de l'anglais single-pixel imaging accelerated via scanning of aggregate patterns), comprenant à la fois une solution matérielle pour la modulation rapide des motifs de codage, ainsi qu'un algorithme complémentaire pour la reconstruction de l'image. Combinées, ces techniques permettent l'imagerie en différé dans les catégories de haute et de très haute vitesse, tout en permettant un fonctionnement en temps réel et à faible latence à des fréquences d'images vidéo. Au cœur de son fonctionnement, l'approche de modulation de SPI-ASAP augmente les performances du dispositif numérique à micromiroir DMD conventionnel avec du matériel de balayage laser disponible sur le marché, ce qui permet le déploiement à une vitesse de MHz d'ensembles de motifs de codage agrégés simultanément. La contribution cruciale du principe du balayage laser est qu'il permet le déploiement rapide de motifs de masquage distincts en tant que sous-régions sélectionnées optiquement de motifs plus grands qui sont affichés par le DMD. Alors que la haute résolution, le fonctionnement non mécanique, la reprogrammation et la grande disponibilité des DMD n'ont pas encore été égalés par une autre technologie de modulation utilisée dans SPI, la stratégie de balayage et d'agrégation de motifs permet à SPI-ASAP d'acquérir des données à des taux 50 à 100 fois supérieurs aux limites traditionnelles de la modulation par dispositif numérique à micromiroir DMD uniquement, tout en conservant les avantages du matériel DMD. En plus de cette stratégie de modulation, un choix optimal particulier de la base de conception des motifs de codage de SPI-ASAP permet l'utilisation d'un algorithme de reconstruction léger et simple d'un point de vue heuristique, qui est néanmoins capable de réaliser une détection comprimée : le redressement d'images à partir d'ensembles de données nettement sous-échantillonnées. Il est important de noter que la structure de cet algorithme lui permet d'être compatible avec une exécution parallélisée à l'aide d'un matériel informatique multiprocesseur tel qu'une unité de traitement graphique (GPU de l'anglais graphics processing unit). De plus, malgré sa simplicité relative et l'accent mis sur une faible charge de calcul, cet algorithme montre des performances comparables ou supérieures aux algorithmes CS traditionnels répétitifs lorsqu'il est combiné à la stratégie d'échantillonnage mise en œuvre par le matériel de modulation de SPI-ASAP.

Cette thèse présente la plateforme de l'imagerie mono-pixel accélérée par balayage de motifs agrégés SPI-ASAP ainsi que diverses applications d'imagerie mono-pixel SPI à l'imagerie tridimensionnelle, en temps réel, à ultra-haute vitesse et térahertz, en trois parties, chacune correspondant aux principaux projets de recherche qui ont été entrepris au cours du développement de SPI-ASAP. Le plan de ces parties est le suivant :

Dans la première partie (chapitre 2, extrait de la publication dans [10]), une approche de l'imagerie tridimensionnelle (3D) est explorée qui, par le biais de l'utilisation d'un système DMD bimode, étend la technique de profilométrie par projection de franges à la SPI. Contrairement aux techniques précédentes de SPI 3D qui reposaient sur une détection très sensible au temps ou sur des hypothèses fortes concernant le comportement du facteur de réflexion de la surface, cette approche élargit le domaine des techniques d'imagerie 3D à lumière structurée bien connues en éliminant l'utilisation de capteurs d'imagerie 2D. En outre, grâce au principe de réciprocité de Helmholtz, le système SPI à double DMD est lié au concept de photographie bimode et se révèle capable d'éclaircir artificiellement une scène. Bien que les aspects temps réel et haute vitesse de SPI-ASAP n'aient pas encore été établis à l'époque de ce projet, la conception des modèles de codage, basés sur des matrices circulantes de type S, constitue un lien entre ce travail et la conception ultérieure de SPI-ASAP. En effet, la méthode de SPI 3D explorée est en principe entièrement compatible avec SPI-ASAP, et donc représentative d'une importante application potentielle.

Dans la deuxième partie (chapitre 3, extrait de la publication dans [11]), la plateforme SPI-ASAP est entièrement présentée, en ajoutant les éléments d'agrégation de motifs balayés et de reconstruction par compression rapide aux motifs d'encodage cycliques de la matrice S. Grâce à la grande flexibilité offerte par le matériel DMD dans le choix de la taille des motifs de codage, la fréquence d'images et la résolution du système ont pu être optimisées pour la mesure de plusieurs phénomènes. Le système SPI-ASAP a été utilisé pour démontrer l'imagerie à haute et ultra-haute vitesse à des fréquences d'images allant jusqu'à 12 000 images par seconde (ips), avec des taux de modulation allant jusqu'à 14,1 MHz, et la visualisation en temps réel de vidéos à un seul pixel 101×103 à des vitesses allant jusqu'à 100 ips. En plus de ces capacités, une application à l'étude de l'imagerie dans une lumière ambiante intense a été explorée par le biais de l'imagerie à grande vitesse lors de la rupture des filaments d'ampoules à incandescence. En exigeant l'utilisation d'un filtrage spatial et chromatique, cette application a exploité une capacité unique des systèmes SPI à tolérer une diffusion, une défocalisation ou une autre perturbation optique importante dans le trajet du système d'imagerie précédant le capteur ponctuel.

Enfin, dans la troisième partie (chapitre 4), un projet en cours impliquant l'application de la plateforme SPI-ASAP à l'imagerie par émission térahertz (THz) est décrit, consistant en la conception pratiquement achevée d'un microscope chimique térahertz (TCM) computationnel. Sur la base de la sensibilité des phénomènes d'émission THz aux variations microscopiques du champ électrique au niveau des couches de déplétion de surface des semi-conducteurs, les systèmes TCM ont été proposés comme un outil de diagnostic important pour la cartographie des potentiels électrochimiques de surface, avec des applications comprenant la visualisation des réactions chimiques et la détection de matériaux biologiques, y compris les cellules cancéreuses [140]. Malheureusement, en raison des limitations techniques des dispositifs de détection cohérente du THz, toutes les conceptions de systèmes TCM ont jusqu'à présent impliqué l'utilisation d'un balayage de trame ponctuel. Ce projet vise donc à améliorer la maturité technologique des systèmes TCM en incorporant l'approche computationnelle de SPI, plus précisément celle implantée par la plateforme SPI-ASAP. Bien que les étapes finales de la construction du système proposé soient actuellement en cours, un mécanisme peu intrusif et vérifié expérimentalement pour la modulation de l'émission THz est rapporté, justifiant la faisabilité de cette conception pour améliorer le fonctionnement des systèmes TCM existants.

6.2 Imagerie tridimensionnelle à un seul pixel et photographie bimodale

L'imagerie bimodale, également connue sous le nom de photographie bimode (de l'anglais dual photography), est une technique d'imagerie informatique qui synthétise des images réalistes de scènes capturées à partir des perspectives de dispositifs d'éclairage non formateurs d'images [55]. Pour une scène vue par un appareil photo et éclairée par un projecteur, les « images bimodales » synthétiques représentent l'inversion hypothétique des rôles des pixels du projecteur et de l'appareil photo, ce qui équivaut aux conditions d'imagerie et d'éclairage se produisant respectivement du point de vue du projecteur et de l'appareil photo. Bien qu'hypothétique, la nature réaliste de ces images synthétisées est assurée par le principe de réciprocité de Helmholtz qui garantit l'équivalence radiométrique du transport de la lumière sous l'échange de sources ponctuelles et de détecteurs [54, 69]. Il est remarquable que la généralité de ce principe permette aux images bimodales de synthétiser avec précision des scènes complexes impliquant un comportement arbitraire du transport de la lumière, comme les réflexions, les caustiques, les ombres, les inter-réflexions diffuses et la diffusion sous la surface. En tant que paradigme basé sur l'imagerie, la photographie bimodale peut être réalisée sans connaissance de la géométrie de la scène et sans étalonnage pour modéliser le comportement projectif de la caméra et du projecteur. De plus, avec une connaissance suffisante des propriétés de transport de la lumière d'une scène donnée, il est possible de synthétiser des images physiquement exactes d'objets éclairés par des modèles d'éclairage arbitraires.

En photographie bimodale, l'information complète suffisante pour synthétiser des images bimodales et arbitrairement éclairées est modélisée par la matrice de transport de la lumière (LTM de l'anglais light transport matrix), dont la mesure constitue un aspect expérimental critique. Bien

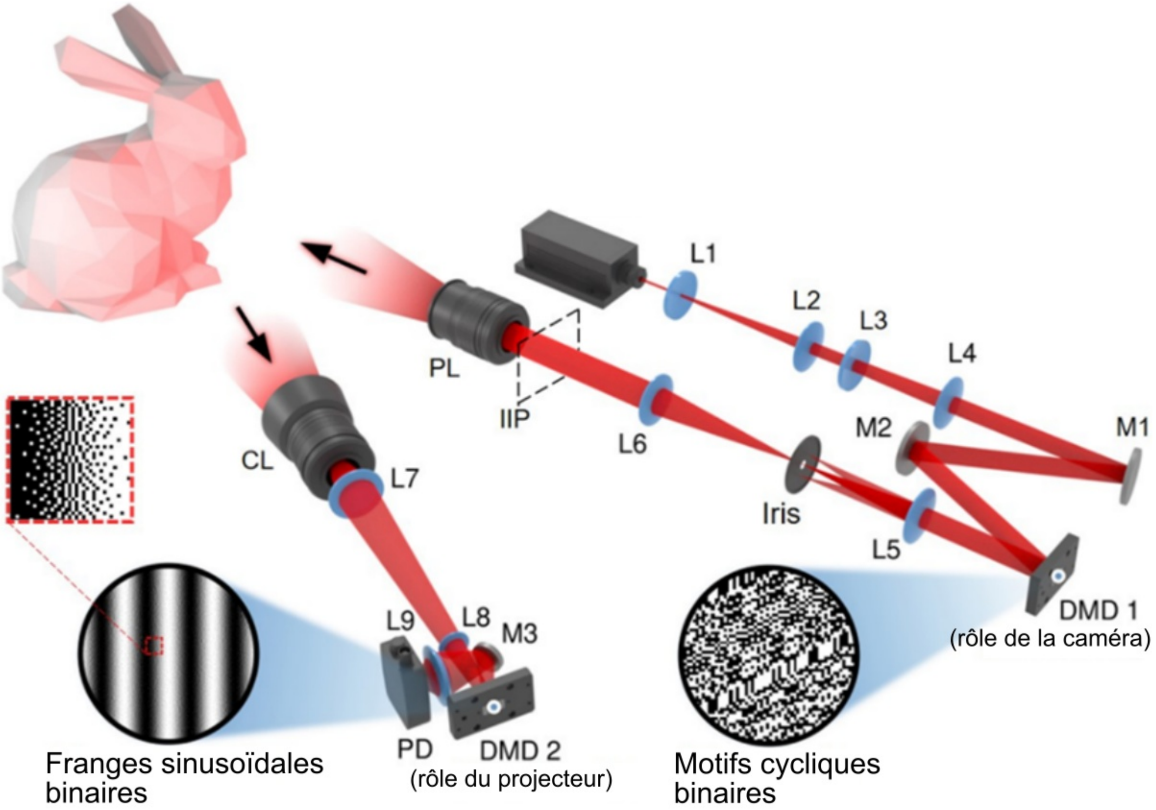

Figure 6.2 Schéma du système de photographie bimodale tridimensionnelle à mono-pixel (STDP). CL, lentille de collecte ; DMD 1 et DMD 2, dispositif numérique à micromiroir ; IIP, plan d'image intermédiaire ; L1-L9, lentille ; M1-M3, miroir ; PD, photodiode ; PL, lentille de projection.

que les appareils photo numériques classiques soient le plus souvent utilisés, la photographie bimodale mise en œuvre avec des appareils photo à mono-pixel a fait l'objet d'une attention considérable [55, 56, 81, 82]. Cependant, de nombreux aspects de la photographie bimodale basée sur l'imagerie mono-pixel SPI sont moins explorés. En particulier, bien que la connaissance de la matrice de transport de la lumière LTM soit suffisante pour l'extraction d'informations 3D des objets, la procédure inverse, qui consiste à utiliser des informations 3D pour approximer le LTM, n'a pas été explorée. Ainsi, bien qu'elle soit couramment réalisée sur des objets tridimensionnels (3D), la photographie bimodale n'a pas été réalisée sur des images 3D.

Pour surmonter ces limitations, ce travail présente une méthode sans caméra pour la photographie bimodale 3D mise en œuvre dans une plateforme à imagerie mono-pixel SPI. Notre système de photographie bimodale tridimensionnelle à mono-pixel (STDP de l'anglais single-pixel three-dimensional dual photography) s'inspire de l'analogie entre la fonctionnalité du LTM et le principe de fonctionnement de la profilométrie par projection de franges (FPP de l'anglais fringe projection profilometry) [87]. Le système résultant, illustré à la Fig. 6.2, intègre deux dispositifs numériques à micromiroir DMD pour la modulation spatiale et possède par conséquent une symétrie fonctionnelle en ce qui concerne les propriétés du transport de la lumière entre la source lumineuse et le capteur à pixel unique, la scène étant soumise à la fois à un éclairage structuré et à une détection structurée. Cette symétrie permet au système d'incarner une méthode de photographie bimodale, tout en comprenant également une méthode fonctionnelle de l'imagerie mono-pixel SPI 3D.

Méthodes

En représentant le transport de la lumière entre chaque paire distincte de projecteurs et de pixels de la caméra, le LTM est composé de colonnes qui représentent des images vectorisées de la réponse de diffusion impulsionnelle de la scène. L'information enregistrée par le LTM peut être divisée en une composante directe (qui tient compte des trajets lumineux qui n'ont qu'une seule interaction avec la scène) et une composante globale (qui tient compte de tous les autres trajets qui atteignent la caméra) [89]. Comme la première traite de la lumière qui se réfléchit/se diffuse à partir d'un seul point de la scène, la composante directe du LTM obéit à la géométrie épipolaire et peut servir de base à la construction d'une cartographie 2D pixel à pixel entre le projecteur et la caméra. Une cartographie 2D pixel à pixel peut également être enregistrée par des méthodes de lumière structurée dans un système projecteur-caméra. Dans un exemple important, dans le contexte de la calibration de projecteur utilisée dans FPP [66], des motifs de franges sinusoïdaux sont utilisés pour associer les coordonnées du projecteur codées en phase aux pixels de la caméra d'une image d'une grille de calibration plate. Après la mesure des valeurs de phase $\varphi_{\mathrm{h}}(u,v)$ et $\varphi_{\mathrm{v}}(u,v)$ par la projection de motifs de franges horizontaux et verticaux respectivement, chaque pixel de caméra (u,v) est lié à un pixel de projecteur correspondant FPP sans la connaissance des paramètres d'étalonnage de l'un ou l'autre dispositif. Ce fait indique que la correspondance 2D des pixels établie par la méthode FPP peut représenter de manière équivalente la composante directe du LTM. Ainsi, une image bimodale avec une précision inférieure au pixel peut être synthétisée par le biais d'une transformation pixel par pixel et d'une interpolation de grille subséquente des pixels de la caméra dans l'espace de coordonnées du projecteur. De plus, des conditions d'éclairage hypothétiques à partir des perspectives de la caméra ou du projecteur peuvent être synthétisées en ajustant les valeurs des pixels de la caméra associées à la transformation sur la base de leurs coordonnées avant interpolation.

En tant que méthode de profilométrie 3D, la méthode basée sur la FPP décrit également la relation projective d'un point 3D (x,y,z) sur le pixel de la caméra (u,v) et le pixel du projecteur (u',v') en utilisant le modèle projectif d'une caméra à sténopé [67], exprimée par

$$\rho_0\left[u',v',1\right]^T = \boldsymbol{A}_0\,[x,y,z,1]^T \quad \text{et} \quad \rho_1\left[u',v',1\right]^T = \boldsymbol{A}_1\,[x,y,z,1]^T \tag{6.1}$$

où $\boldsymbol{A}_0$ et $\boldsymbol{A}_1$ sont des matrices qui caractérisent le comportement projectif du projecteur et de la caméra, qui sont disponibles après l'étalonnage du système basé sur le FPP [58, 68]. Les valeurs ρ_0 et ρ_1 sont des facteurs scalaires arbitraires pour l'extraction numérique de (u',v') et (u,v). D'un point de vue géométrique, la connaissance préalable des coordonnées (u,v) ainsi que le redressement d'une coordonnée horizontale du projecteur u' déterminent un rayon et un plan qui émanent respectivement de la caméra et du projecteur. L'intersection de ce rayon et du plan détermine le redressement d'une coordonnée 3D. Mathématiquement, la connaissance de l'ensemble des coordonnées $\{u, v, u'\}$ ainsi que la modélisation de la caméra dans l'équation (6.1) sont suffisantes pour établir trois équations linéairement indépendantes qui récupèrent (x, y, z).

Pour la collecte des données, le dispositif numérique à micromiroir DMD 1 affiche des ensembles complets de motifs de masquage binaires générés à partir d'une matrice circulante [14, 23], connue pour améliorer le rapport signal sur bruit dans la reconstruction de l'imagerie mono-pixel SPI [90, 91]. En utilisant la construction des nombres premiers jumeaux [15, 16, 92], une matrice circulante $\boldsymbol{S}$ de taille $MN \times MN$ peut être obtenue pour chaque paire de nombres premiers jumeaux M et $N = M + 2$. Dans nos expériences, chaque ligne a été remodelée en un motif de masquage binaire 2D $e_j(u, v)$ dont la taille est de $M \times N$ pixels d'encodage. Pour nos expériences, nous avons choisi $M = 137$ et $N = 139$, ce qui a généré un total de $MN = 19{,}043$ modèles de masquage binaire. Pour le DMD 2, un total de six motifs de bandes sinusoïdales est affiché pour la projection de bandes virtuelles [93, 94]. Les trois premiers motifs présentent des bandes horizontales avec une période de $\lambda_{\mathrm{h}} = 864$ µm. Le deuxième groupe présente des bandes verticales avec une période égale à $\lambda_{\mathrm{v}} = 864$ µm. Ces bandes sinusoïdales en niveaux de gris sont converties en motifs binaires pour le DMD 2 à l'aide d'un algorithme de diffusion des erreurs [95], dont un exemple est illustré par l'encart de la Fig. 6.2. Comme chaque pixel de codage dans les motifs de masquage, lorsqu'il est imagé sur le DMD 2, occupe un réseau de micromiroirs, le bruit à haute fréquence spatiale transporté par ces motifs sinusoïdaux binaires est filtré, ce qui entraîne la projection virtuelle des bandes sinusoïdales en niveaux de gris sur l'objet 3D dans les images récupérées. Un signal représentatif c_{jk} mesuré par la photodiode lors de l'affichage du motif de masquage j et du motif de bandes k peut s'exprimer ainsi

$$c_{jk} = \sum_{u,v} e_j(u, v) p_k(u, v) \quad . \tag{6.2}$$

Ici, p_k, représentant les images de bandes produites par la projection de franges virtuelles, est exprimé par l'équation suivante

$$p_k(u, v) = I_{\mathrm{m}}(u, v) + I_{\mathrm{va}}(u, v) \cos\left[\varphi_{\mathrm{d}}(u, v) - 2\pi k/3\right] \quad , \tag{6.3}$$

où $k = 0, \ldots, 5$. $I_{\mathrm{m}}(u, v)$ et $I_{\mathrm{va}}(u, v)$ représentent respectivement l'intensité moyenne et la variation d'intensité. L'expression $\varphi_{\mathrm{d}}(u, v)$ s'écrit $\varphi_{\mathrm{v}}(u, v)$ pour $k = 0, 1, 2$ et $\varphi_{\mathrm{h}}(u, v)$ pour $k = 3, 4, 5$ qui représentent les phases indiquées par la profondeur pour les bandes verticales et horizontales, respectivement. Les motifs de bandes sinusoïdales, affichés séquentiellement sur le DMD 2, restent inchangés pendant la projection de la séquence de motifs cycliques du DMD 1. À titre d'exemple, la Fig. 6.3a montre la trace du signal pour un motif de bandes spécifique. La reconstruction de l'image commence par la récupération de l'image vectorisée de la bande $\boldsymbol{p}_k$, par la méthode suivante

$$\boldsymbol{p}_k = \boldsymbol{S}^{-1} \boldsymbol{c}_k \quad . \tag{6.4}$$

Ici, $\boldsymbol{c}_k$ représente les mesures de la photodiode pour le $k$ième motif de bandes sous une forme vectorisée. L'image de bandes $\boldsymbol{p}_k$ est ensuite transformée en une image de bandes 2D de taille $M \times N$, dont un exemple est illustré à la Fig. 6.3b.

L'algorithme de décalage des bandes [63], associé à un algorithme approprié de déballage de phase 2D [64, 65], permet ensuite, pour un pixel donné de la caméra avec coordonnées (u, v), le redressement des coordonnées du projecteur associé (u', v'). Enfin, l'ensemble de coordonnées $\{u, v, u'\}$ est utilisé avec l'équation (6.1) pour générer des images 3D, avec un exemple de nuage de points visualisé à la Fig. 6.3c et Fig. 6.3d.

Dans le cadre de l'imagerie bimodale, comme les motifs de masquage éclairent activement l'objet 3D, les images primaires reconstruites adoptent la perspective du module d'éclairage contenant le DMD 1. Par conséquent, la vue bimodale est définie à partir de la direction du module de collecte contenant le DMD 2. Le système STDP permet deux méthodes pour la photographie bimodale et le ré-éclairage de la scène. Tout d'abord, le repérage des coordonnées de 2D à 2D (c'est-à-dire de (u, v) à (u', v')) permet de générer des images bimodales en 2D avec un éclairage de la scène similaire aux méthodes précédentes de photographie bimodale. En particulier, à partir des pixels de l'image primaire (u, v) avec des intensités $I(u, v)$ et une fonction de ré-éclairage optionnelle $r(u, v)$, une intensité $I_r(u', v') = I(u, v)\, r(u, v)$ peut être définie sur les points (u', v'), à partir desquels l'image bimodale 2D et l'image bimodale relit 2D peuvent être obtenues par biais d'une interpolation. De plus, en utilisant des mappages de coordonnées supplémentaires de 3D à 2D (c'est-à-dire de (x, y, z) à (u, v) et de (x, y, z) à (u', v')) avec des calibrations connues, il est possible de générer des images bimodales 3D avec ré-éclairage de la scène en projetant les données ponctuelles récupérées (x, y, z) et les valeurs d'intensité associées $I(x, y, z)$.

Résultats

Pour vérifier les performances du système STDP, nous avons imagé deux objets 3D : un plan incliné avec un pictogramme de danger laser et une sculpture basse densité du lapin de Stanford. La Fig. 6.4a montre les images primaires. Les images synthétiques bimodales 2D utilisant le repérage des coordonnées 2D vers 2D sont présentées à la Fig. 6.4b. Le repérage des coordonnées 3D vers 2D a permis de récupérer des images bimodales 3D de chaque objet, présentées à titre de comparaison sur les Fig. 6.4c et Fig. 6.4d. La Fig. 6.4c a été produite en projetant les informations 3D sur un ensemble de données 2D avec interpolation, les résultats montrant une ressemblance presque parfaite avec la Fig. 6.4d. Enfin, la Fig. 6.4d montre les mêmes images bimodales avec des informations 3D transmises par la coloration de profondeur.

Pour démontrer les capacités de ré-éclairage de scène du système STDP, nous avons éclairé numériquement les mêmes objets de la Fig. 6.4 avec un motif de ré-éclairage composé de cercles lumineux disposés en hexagone, à la fois en vue primaire et en vue bimodale. Les Fig. 6.5a et Fig. 6.5b montrent les résultats générés par l'utilisation du repérage des coordonnées 2D vers 2D.

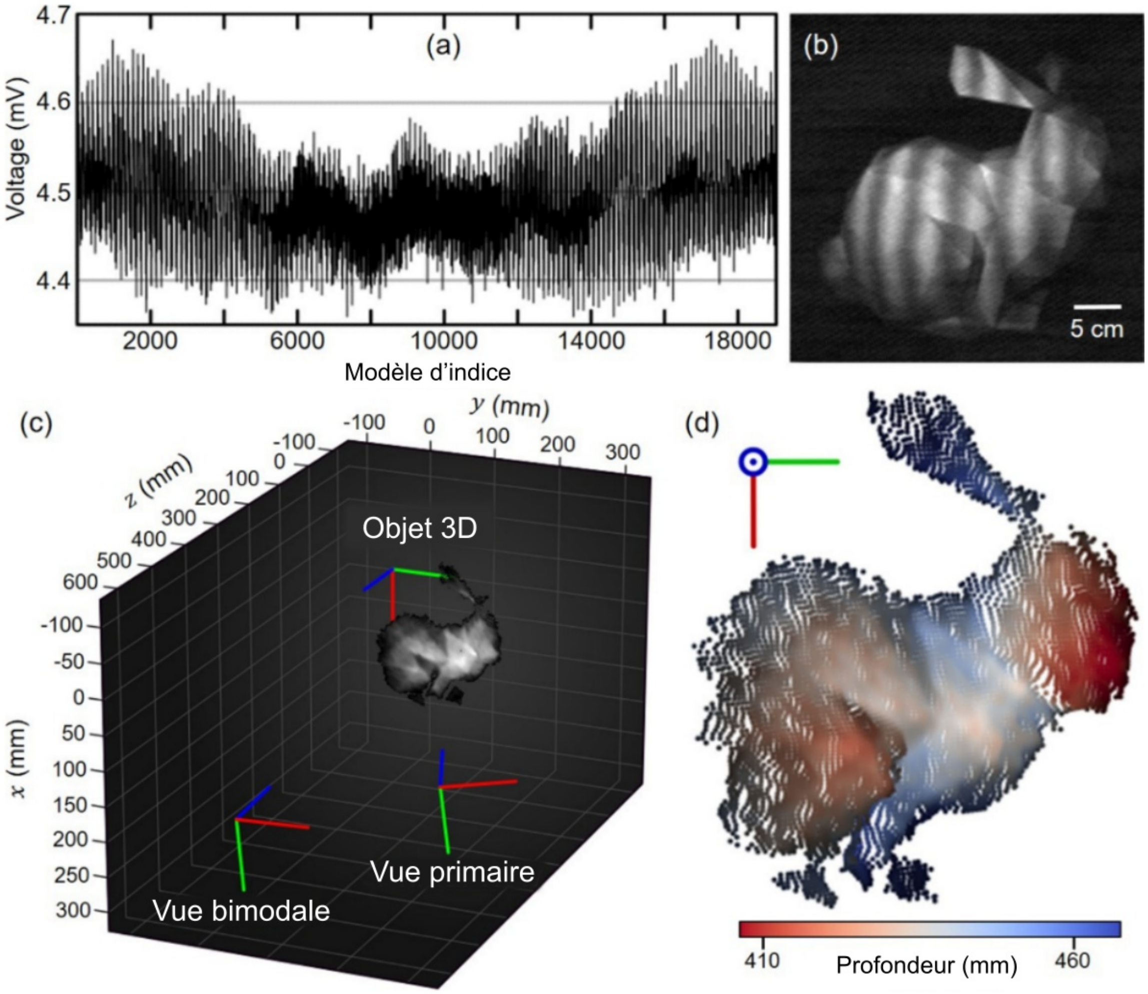

Figure 6.3 Imagerie d'une sculpture à faible polyvalence du lapin de Stanford à l'aide du système STDP. **(a)** Signal acquis par la photodiode pour une image en bande. **(b)** Image de bande reconstruite de l'objet. **(c)** Système de coordonnées mondiales contenant les données du nuage de points de l'objet. **(d)** Nuage de points d'une image 3D récupérée.

À titre de comparaison, la Fig. 6.5c montre des images bimodales 3D produites à l'aide du repérage des coordonnées 3D vers 2D. En affichant le motif de ré-éclairage sur le DMD 2 (Fig. 6.5d), l'aspect détection codée du système STDP a permis de vérifier expérimentalement les résultats du ré-éclairage.

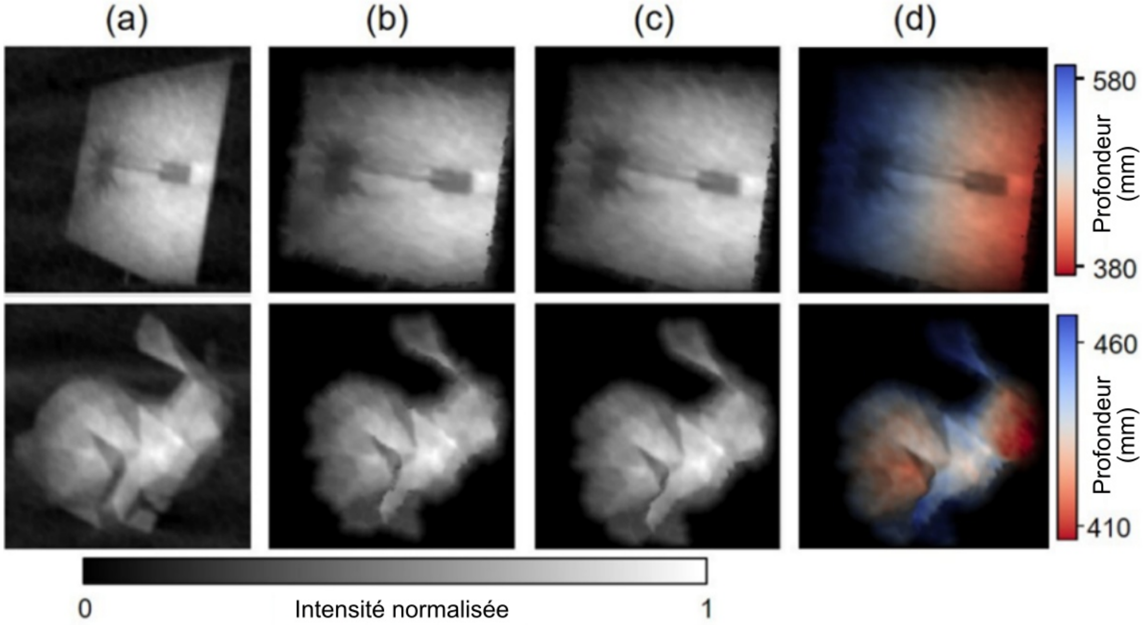

Figure 6.4 Photographie bimodale en 3D. (a) Images primaires. **(b)** Images bimodales 2D synthétisées à l'aide de la cartographie de coordonnées 2D. **(c)–(d)** Images bimodales 2D (c) et images bimodales 3D codées en profondeur (d) synthétisées à l'aide du mappage de coordonnées 3D à 2D basé sur le FPP.

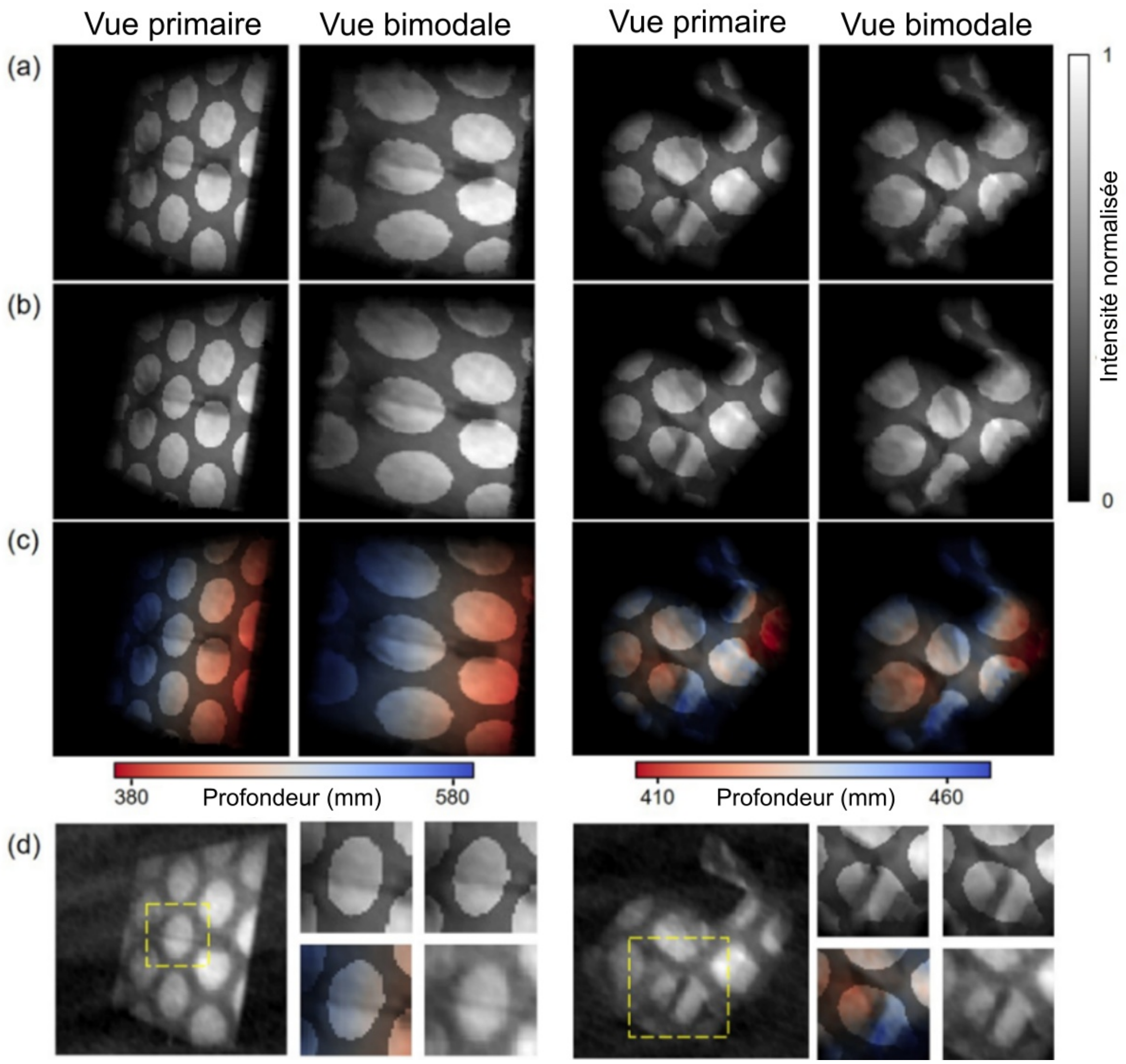

Figure 6.5 Ré-éclairage de la scène en 3D. **(a)** Images primaires et bimodes de relit 2D de l'objet symbole de danger laser et de l'objet lapin synthétisées à l'aide du mappage de coordonnées 2D vers 2D. **(b)** Images primaires et bimodales relit 3D synthétisées à l'aide du mappage de coordonnées 3D vers 2D. **(c)** Comme en (b), mais avec les informations de profondeur affichées. **(d)** Vérification expérimentale du ré-éclairage de la scène sur la vue primaire. La comparaison d'une caractéristique locale (marquée par les cases pointillées jaunes) dans (a)–(d) est montrée dans les vues zoomées en haut à gauche, en haut à droite, en bas à gauche et en bas à droite, respectivement.

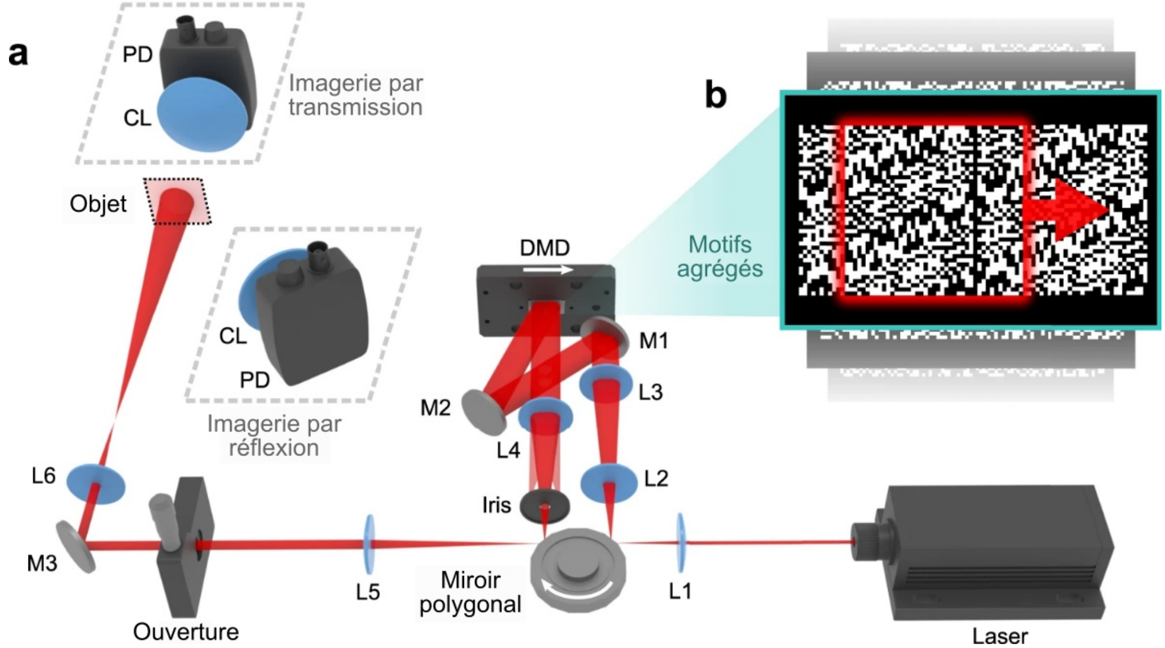

Figure 6.6 Schéma de SPI-ASAP. **(a)** Illustration du système montrant le balayage par faisceau d'un motif agrégé affiché par DMD par la rotation d'un miroir polygonal. Les flèches blanches indiquent les directions de rotation du miroir polygonal et de balayage de l'illumination. CL, lentille de condenseur ; DMD, dispositif numérique à micromiroir ; L1-L6, lentilles ; M1-M3, miroirs ; PD, photodiode. **(b)** Gros plan d'un exemple de motif d'agrégation dans une séquence adaptée à l'imagerie à une taille d'image de 41×43 pixels. Boîte rouge : un motif de codage représentatif. Flèche rouge : direction de balayage.

6.3 Imagerie mono-pixel à ultra-haute vitesse et en temps réel

Comme nous l'avons déjà décrit, les limites de performance de la modulation du dispositif numérique à micromiroir DMD et de la reconstruction par compression CS itérative ont empêché la plupart des systèmes d'imagerie mono-pixel SPI de cibler un fonctionnement à grande vitesse ou en temps réel. Pour surmonter ces limitations, ce travail a introduit l'imagerie à mono-pixel accélérée par biais de motifs agrégés balayés (SPI-ASAP). Au cœur de ce système se trouve une application du balayage laser qui déploie rapidement des masques de codage individuels sous forme de sous-régions sélectionnées optiquement dans des motifs agrégés plus grands qui sont affichés par le dispositif DMD. De cette façon, l'agrégation de motifs et le balayage optique améliorent les vitesses de collecte des données de l'imagerie à mono-pixel accélérée par balayage de motifs agrégés SPI-ASAP à plus d'un facteur de 100 au-dessus des limites de la modulation par le dispositif DMD uniquement, tout en conservant le nombre élevé de pixels et la flexibilité de l'affichage de motifs avec les dispositifs DMD. En outre, un algorithme de reconstruction rapide de la détection par compression CS, étroitement couplé au déploiement de l'architecture de motifs de SPI-ASAP, est présenté et démontre une compatibilité totale avec le calcul parallèle pour la visualisation en temps réel.

La Fig. 6.6 présente un schéma du système SPI-ASAP. Le balayage rapide du motif est généré par un miroir polygonal à 16 facettes, un dispositif numérique à micromiroir DMD de 0,45" et des composants optiques associés. Le faisceau incident est d'abord réfléchi par une facette du miroir polygonal, ce qui crée une illumination qui se déplace rapidement sur la surface du dispositif DMD. En raison d'une symétrie angulaire imposée à l'angle d'incidence, la seconde réflexion par le miroir polygonal transmet un mouvement de balayage égal et opposé au faisceau d'imagerie, qui stabilise sa position au niveau d'une ouverture réglable. En même temps, comme cette ouverture reçoit une image de la partie illuminée de la surface du dispositif DMD, la stabilisation par la seconde réflexion transmet également un mouvement de balayage rapide aux motifs qui suit le mouvement de l'illumination balayée. Cette opération de balayage bimodal augmente l'efficacité optique du l'imagerie à mono-pixel accélérée par le balayage de motifs agrégés SPI-ASAP par rapport à celle d'une conception à balayage unique, car l'éclairage est concentré uniquement sur les parties de la surface du dispositif DMD qui sont acheminées vers l'ouverture réglable.

Pendant le fonctionnement, chaque balayage induit par une facette du miroir polygonal est synchronisé avec l'affichage d'un nouveau motif binaire agrégé préalablement enregistré par le dispositif numérique à micromiroir DMD. Après avoir traversé l'ouverture, l'éclairage structuré interroge la structure des objets placés dans le plan image. Une partie de la lumière transmise ou réfléchie par un objet est focalisée par une lentille condensatrice vers une photodiode qui est positionnée pour recevoir la lumière pour l'imagerie en mode transmission ou en mode réflexion.

Méthodes

SPI-ASAP utilise des matrices circulantes pour générer des modèles d'encodage, les modèles d'encodage individuels provenant du remodelage en 2D des lignes d'une matrice $\boldsymbol{S}$ qui est générée en utilisant la méthode de construction nombres premiers jumeaux (twin-prime). En écrivant $n = pq$ pour les dimensions des lignes remodelées, il est possible de restructurer les informations contenues dans $\boldsymbol{S}$ pour former un motif $(2p-1) \times (2q-1)$ de telle sorte que l'ensemble des $p \times q$ sous-régions distinctes sélectionnées dans ce motif englobe exactement tous les motifs de codage déterminés par $\boldsymbol{S}$ dans le cadre du remodelage 2D. À chaque balayage, une tranche horizontale de $p \times (2q-1)$ du motif complet $(2p-1) \times (2q-1)$ s'affiche sur le DMD. L'action de balayage du système optique illumine et projette ensuite séquentiellement chaque $p \times q$ sous-zone de ce motif, ce qui entraîne le déploiement de q motifs de codage (voir Fig. 6.6b). Ce processus se répète ensuite, chaque balayage utilisant une tranche différente de $p \times (2q-1)$ pour agréger le déploiement de q motifs de codage.

En raison de la relation d'empilement en 2D des motifs de codage, leur déploiement dans l'imagerie à mono-pixel accélérée par balayage de motifs agrégés SPI-ASAP peut être considéré comme une opération de convolution discrète en 2D sur le motif complet $(2p-1) \times (2q-1)$, l'image sous-jacente étant utilisée comme un noyau de taille $p \times q$. Ainsi, les mesures acquises d'un seul pixel présentent un effet lisse en 2D lorsqu'elles sont remodelées en une matrice de la même taille que l'image sous-jacente. Cette propriété motive une stratégie visant à incorporer la détection par compression CS dans une méthode de redressement rapide d'images. Étant donné que les données d'une mesure entièrement échantillonnée peuvent former une matrice avec un lissage en 2D, une distribution uniforme des mesures obtenues permet d'estimer les valeurs des mesures non échantillonnées par interpolation, ce qui permet ensuite de récupérer l'image par l'inversion directe très efficace d'une matrice circulante. Cette stratégie, associée à l'architecture de balayage spécifique de SPI-ASAP, permet de réduire cette méthode d'interpolation à un ensemble d'interpolations unidimensionnelles (1D) indépendantes qui peuvent être calculées efficacement à l'aide de splines. Cette opération, ainsi qu'un filtrage passe-bas spatial facultatif, peut être mise en œuvre en utilisant uniquement une multiplication matrice-matrice avec l'aide d'éléments précalculés. De cette façon, on obtient un algorithme de reconstruction capable de fonctionner en temps réel et facilement compatible avec le calcul parallèle, tel que celui offert par les unités de traitement graphique GPU.

Résultats

Contrairement à l'imagerie conventionnelle pour laquelle les objets en mouvement rapide ne présentent qu'une prise d'empreintes floues, la nature séquentielle et le vaste domaine de la collecte de données de SPI produit des artefacts globaux pour les scènes hautement dynamiques. Cependant, en permettant la récupération d'images à partir de données sous-échantillonnées, l'algorithme de reconstruction de l'imagerie à mono-pixel accélérée par balayage de motifs agrégés SPI-ASAP permet de contrôler de manière flexible la fréquence d'images au stade de la reconstruction, ce qui permet d'optimiser l'équilibre entre la qualité globale de l'image et la fréquence d'images pour répondre à des ensembles de données spécifiques. Pour démontrer ce concept, SPI-ASAP a été utilisé pour visualiser les oscillations amorties d'un pendule d'un rayon de 10 cm. Comme le montre la Fig. 6.7a, le bas de ce pendule comportait une échelle composée des chiffres “0” à “9” séparés par des lignes verticales. Fonctionnant en mode transmission, le système SPI-ASAP avait une taille d'image de 41×43 pixels avec un champ de vision (FOV) d'environ 10 mm × 10 mm. Le mouvement du pendule a été enregistré pendant 1,54 seconde, au cours de laquelle le pendule a présenté des oscillations amorties et s'est arrêté à l'équilibre. Comme l'illustrent les résultats de la Fig. 6.7b–d, ainsi que les profils comparés dans la Fig. 6.7e, l'augmentation de la fréquence d'images par SPI-ASAP assisté par CS a conduit à une réduction des artefacts de flou de mouvement, permettant de résoudre les détails de l'objet en mouvement rapide.

Comme il n'est pas nécessaire qu'il y ait une relation d'imagerie entre l'objet et le détecteur dans le cas de l'imagerie mono-pixel SPI, les systèmes SPI peuvent tolérer la perturbation optique du faisceau d'imagerie qui peut se produire entre l'objet éclairé par le motif et la détection par le capteur ponctuel. Cette caractéristique permet à l'imagerie mono-pixel SPI de se positionner dans des scénarios nécessitant un filtrage optique extrême, par exemple pour des scènes impliquant une lumière ambiante intense et variable. Pour démontrer cette capacité dans le SPI-ASAP haute

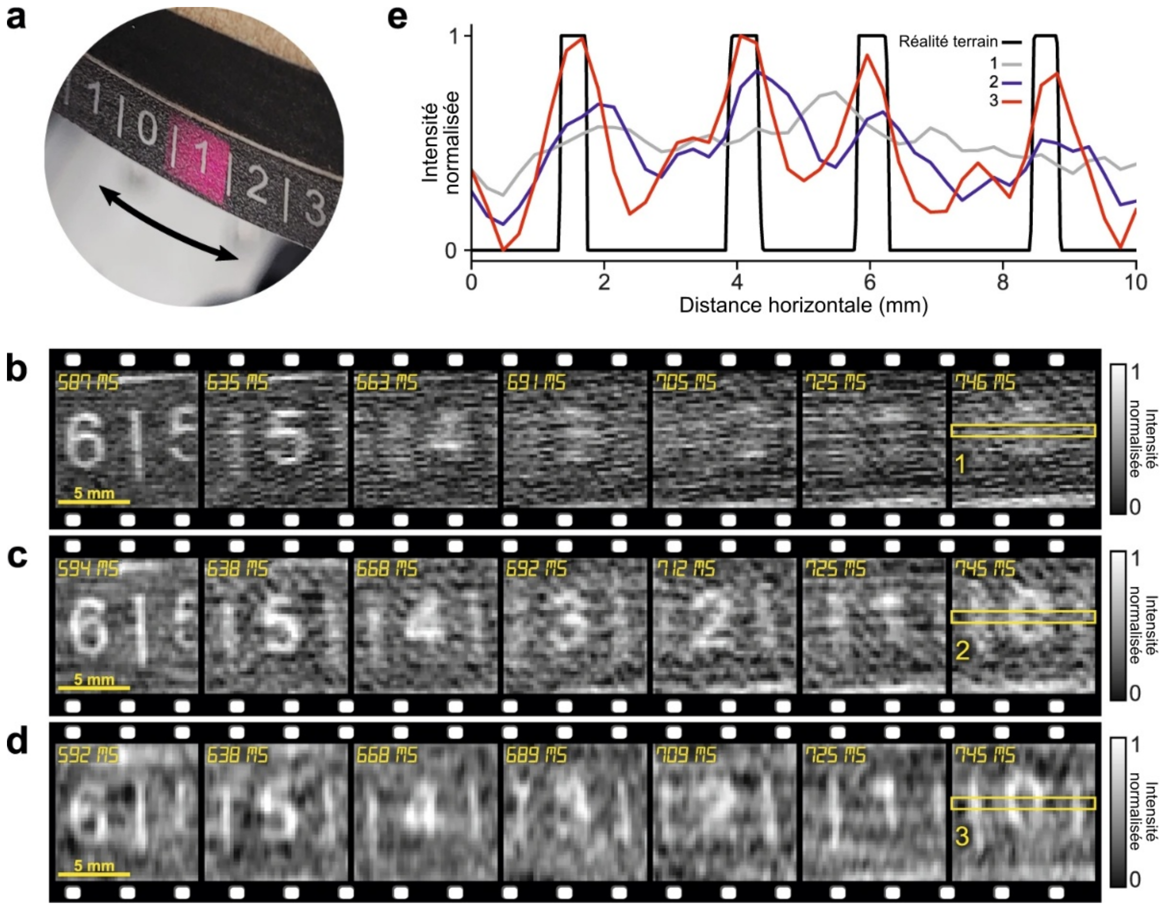

Figure 6.7 SPI-ASAP du mouvement d'une règle de position transmissive attachée à un pendule. **(a)** Photographie de la règle de position et FOV illuminé de 10 mm × 10 mm. **(b)**–**(d)** Images sélectionnées à partir de reconstructions avec un échantillonnage de 100% à 145 fps (b), 50% à 298 fps (c), et 25% à 598 fps (d). **(e)** Profils d'intensité moyenne normalisée d'une région sélectionnée d'une taille de 5×43 pixels (marquée par les cases jaunes dans (b)–(d)), comparée à la vérité terrain.

vitesse, la rupture induite du courant des filaments d'ampoules à incandescence a été étudiée dans deux conditions expérimentales, qui impliquaient l'ajout d'étapes de filtrage spatial et chromatique devant le détecteur à mono-pixel. Le SPI-ASAP a fonctionné à 298 ips (échantillonnage de 50%) et avec un FOV de 11 mm × 11 mm (41×43 pixels). Les résultats de cette expérience, présentés dans la Fig. 6.8, ont permis de mettre en évidence des différences significatives dans les modes de rupture des filaments dans des ampoules normalement scellées (Fig. 6.8a–c), et des filaments exposés directement à l'air (Fig. 6.8e–f). L'un des effets, causé par le dépôt de métal vaporisé à l'intérieur de l'ampoule scellée, est illustré sur la Fig. 6.8b et Fig. 6.8c par un assombrissement général après le début de la rupture.

Pour l'imagerie avec des images de grande taille, le fonctionnement de SPI-ASAP nécessite le déploiement synchronisé par balayage de plusieurs motifs agrégés par le dispositif numérique à micromiroir DMD, dont la fréquence de rafraîchissement maximale (6,37 kHz) limite les performances du système. Afin d'augmenter encore la vitesse d'imagerie de SPI-ASAP pour l'imagerie

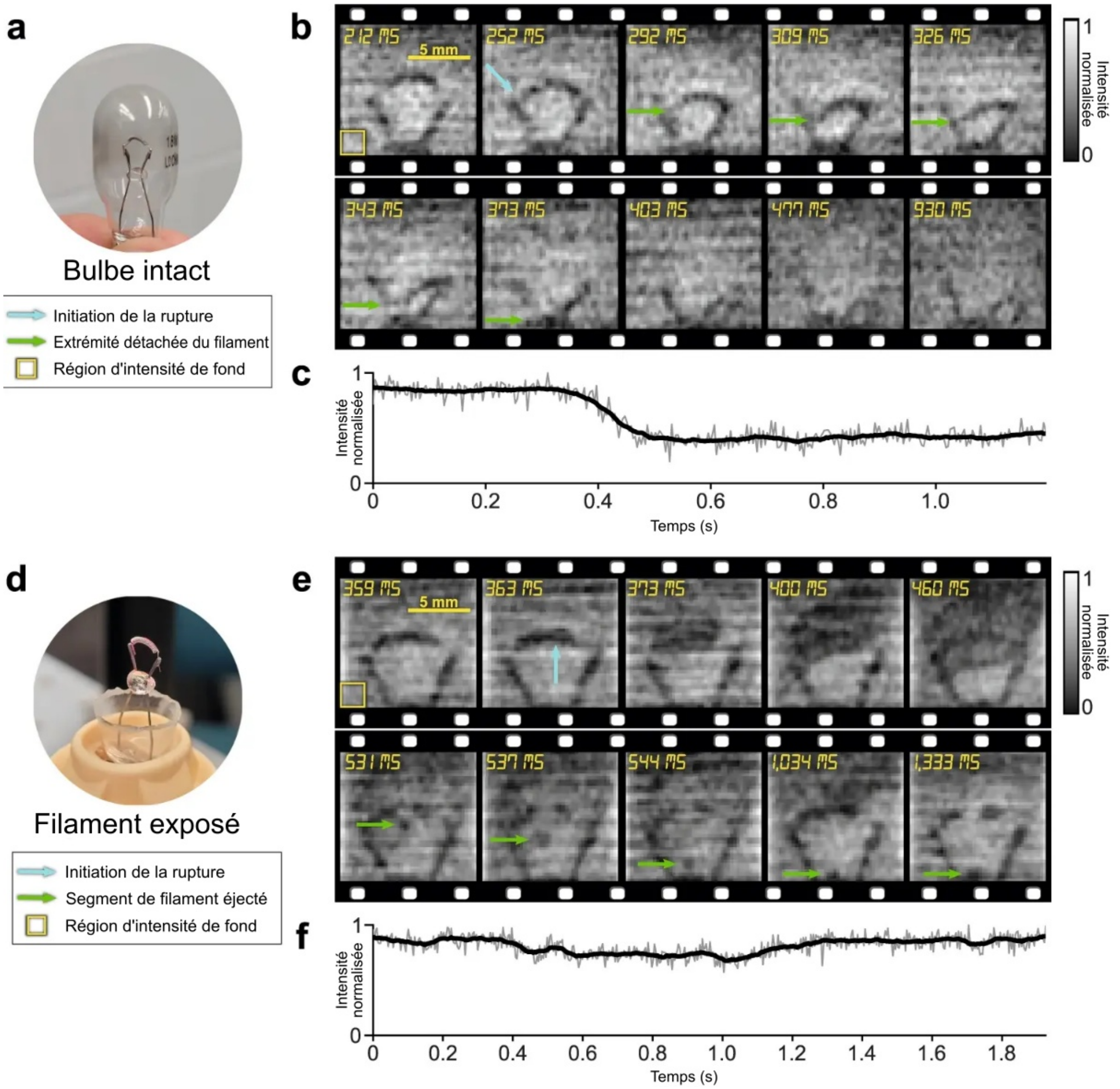

Figure 6.8 SPI-ASAP de la combustion des filaments incandescents. **(a)** Photo d'une ampoule non modifiée montrant le filament enfermé. **(b)** Images sélectionnées de la vidéo reconstruite de l'ampoule non modifiée. **(c)** Évolution temporelle de l'intensité d'une région de fond (8×8 pixels) mise en évidence en (b). La ligne épaisse montre la moyenne mobile (fenêtre de 21 images), les données brutes étant représentées par la ligne fine. **(d)** Photo d'une ampoule modifiée montrant l'exposition directe du filament à l'air. **(e)** Images sélectionnées de la vidéo reconstruite de l'ampoule modifiée. **(f)** Comme en (c), mais à partir de la région de l'arrière-plan en (e).

avec des tailles d'images plus petites, la collecte des données a été effectuée à la fréquence de balayage maximale du miroir polygonal (12 kHz) avec un seul masque statique qui combinait un nombre suffisant de motifs agrégés pour permettre une reconstruction à 55% d'échantillonnage. En utilisant cette configuration expérimentale, SPI-ASAP a été utilisé pour imager un hacheur optique à 30 fentes tournant à 4800 tours/minute (RPM, Fig. 6.9). Le système SPI-ASAP a imagé cinq emplacements différents, chacun avec un champ visuel de 10 mm et une taille d'image de 11×13 pixels. La Fig. 6.9b–f montre des images consécutives de vidéos dynamiques capturées à 12 000 images par seconde (kfps), démontrant ainsi la fréquence d'images maximale possible

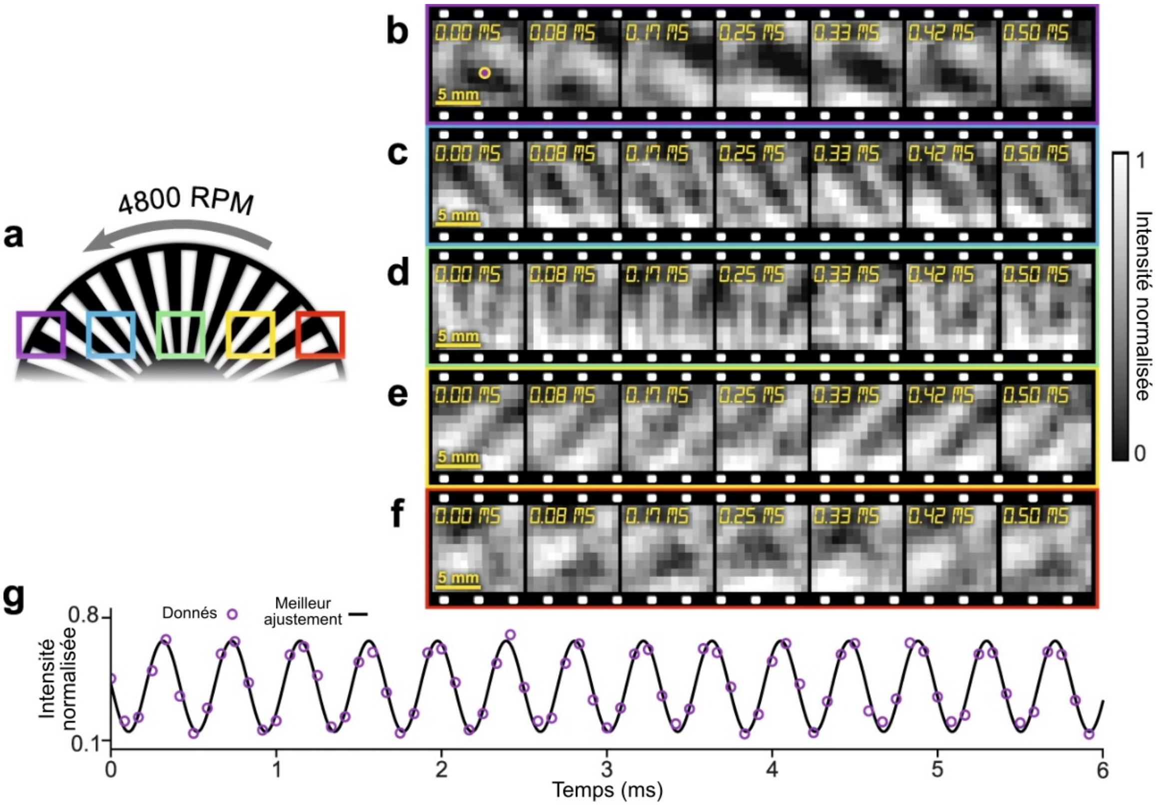

Figure 6.9 SPI-ASAP à ultra-haute vitesse d'un hacheur optique tournant à 4800 RPM. (a) Schéma de la configuration expérimentale. Les boîtes de couleur montrent les régions imagées par SPI-ASAP. **(b)**–**(f)** Images consécutives de vidéos reconstruites à ultra-haute vitesse avec des couleurs de contour correspondant aux positions du FOV montrées dans (a). **(g)** Historique de l'intensité normalisée pour un pixel sélectionné (marqué par le point violet en (b)).

de SPI-ASAP avec son matériel actuel. Un historique temporel de l'intensité normalisée d'un pixel sélectionné, illustré à la Fig. 6.9g, a ensuite permis de déterminer que le taux de hachage de la roue était de 2408,9 Hz, correspondant à une vitesse linéaire au bord de la roue de 25,7 ms^{-1}, en accord avec les conditions de l'expérience.

6.4 Vers un microscope chimique THz en temps réel

Propulsés par le fonctionnement de lasers femtoseconde (fs) à impulsions, la majorité des systèmes d'imagerie THz utilisent des cristaux ou des antennes dédiées pour générer un rayonnement THz qui illumine ensuite un objet ou un échantillon après une période de propagation en espace libre. Cette séparation de la source THz et de l'objet, par la physique de la propagation des ondes, impose des limites à la résolution spatiale maximale qui, pour un rayonnement de 1,0 THz sous la limite de diffraction, doit être de l'ordre de la longueur d'onde, c'est-à-dire 300 µm. Pour certains matériaux cependant, la génération d'ondes THz peut se produire directement à partir de l'interaction laser fs. En focalisant étroitement l'illumination pulsée, la réponse d'émission THz du matériau lui-même peut être sondée avec une résolution spatiale bien plus élevée, de l'ordre de quelques micromètres, déterminée plutôt par la longueur d'onde centrale de la source laser [140]. Cette technique, connue sous le nom de microscopie à émission THz excitée par laser (LTEM de l'anglais laser-excited THz emission microscopy), a été initialement proposée pour le contrôle non destructif et l'inspection de dispositifs électroniques tels que les circuits intégrés à semi-conducteurs [141–143]. Peu après l'émergence du LTEM, une généralisation de la technique, connue sous le nom de microscopie chimique THz (TCM de l'anglais THz chemical microscopy), a été proposée pour cibler l'imagerie diagnostique d'échantillons chimiques et biologiques [144, 145]. Cependant, les systèmes actuels de LTEM et de TCM présentent un défaut commun : leur dépendance à l'égard du balayage mécanique en un mono-pixel des échantillons, dont la nécessité a fortement limité la portée des phénomènes observables, la résolution d'échantillonnage et la richesse des données collectées, en raison du temps nécessaires pour l'acquisition d'images. La nécessité d'un balayage mono-pixel découle des limites de l'équipement de détection qui, en raison des exigences techniques de la détection THz cohérente, ne peut pas être construit dans différents formats. Malgré ces difficultés, le potentiel des approches d'imagerie computationnelle pour l'imagerie LTEM et TCM est jusqu'à présent resté inexploré.

Dans ce contexte, les travaux en cours qui sont présentés dans ce chapitre visent à améliorer les capacités techniques de ces technologies, en particulier l'imagerie de la microscopie chimique THz (TCM), en utilisant les principes de calcul de l'imagerie mono-pixel SPI pour éliminer le balayage de trame, et ainsi élargir les horizons de la technologie de la TCM en tant que plateforme d'imagerie diagnostique. Dans ce but, l'auteur propose une technique nouvelle et vérifiée expérimentalement pour moduler le processus d'émission THz en utilisant un éclairage laser à ondes continues (CW de l'anglais continuous wave). En introduisant une illumination CW structurée dans une région élargie de l'émission THz induite par le laser fs, l'imagerie mono-pixel à balayage SPI-ASAP peut être incorporée par des modifications minimales de l'architecture des systèmes TCM établis, tout en évitant de manière cruciale les interférences avec les phénomènes chimiques et physiques enregistrés par le système. Bien qu'il n'ait pas encore atteint le stade de la collecte de données, le travail de l'auteur en vue d'un prototype fonctionnel a produit à ce jour une conception effectivement achevée, dont les composants ont été entièrement fournis et assemblés en laboratoire. Une description des aspects de la conception de ce prototype, ainsi que la preuve expérimentale du potentiel de modulation de l'illumination laser CW, sont les sujets de ce chapitre.

Méthodes

Pour les semi-conducteurs sondés sous microscopie à émission THz excitée par laser LTEM ou la microscopie chimique THz (TCM), la réponse de l'émission THz reflète le mouvement dynamique des porteurs photoexcités qui, par le biais des lois de l'électrodynamique classique, entraîne la création d'un rayonnement THz résultant d'une densité de courant variant dans le temps,

$$E_{\mathrm{THz}} \propto \frac{\partial \boldsymbol{J}(t)}{\partial t} = e\,v(t)\frac{\partial n(t)}{\partial t} + e\,n(t)\frac{\partial v(t)}{\partial t} \tag{6.5}$$

où $\boldsymbol{J}(t) = e\,n(t)\,v(t)$ est la densité de courant instantané, e est la charge élémentaire, et $n(t)$ et $v(t)$ sont la densité de porteurs instantanée et la vitesse moyenne des porteurs, respectivement. Normalement, le temps de dérivée de la densité de porteurs $\partial n(t)/\partial t$ est liée aux caractéristiques de l'impulsion du laser fs utilisé pour l'excitation et, par conséquent, a une influence non variable dans des cas où le laser est stable [146]. En revanche, dans les situations où la partie photoexcitée du semi-conducteur est soumise à l'influence de champs électriques localisés, l'émission THz devient modulée en raison de l'impact proportionnel des champs électriques sur l'accélération des porteurs $\partial v(t)/\partial t$. Si l'on ajoute à cela le fait que de nombreux phénomènes chimiques et biologiques pertinents peuvent avoir un impact sensible sur les champs électriques microscopiques près des surfaces des semi-conducteurs [140, 146, 147], c'est par cette influence que les méthodes d'imagerie par microscopie à émission THz excitée par laser LTEM et la microscopie chimique THz TCM tirent leur principale valeur diagnostique.

Contrairement à l'imagerie LTEM qui repose uniquement sur la composition matérielle non modifiée de ses cibles pour la compatibilité à l'émission THz induite par le laser, la configuration expérimentale de l'imagerie TCM fournit un composant semi-conducteur particulier, appelé "plaque d'impact" (sensing plate), qui est utilisée pour fournir la source d'émission THz. La Fig. 6.10a présente un schéma de la plaque d'impact d'un système TCM. En pratique, des molécules chimiques ou biologiques placées en solution sont utilisées pour mouiller la surface de la plaque d'impact, qui est ensuite imagée par le biais d'un balayage à point unique du faisceau laser focalisé, ainsi que par la détection cohérente des formes d'onde THz. Bien qu'il soit parfois modifié par l'ajout d'autres molécules, le composant de la plaque d'impact traditionnellement choisie pour l'imagerie de la TCM est le silicium sur saphir (SOS), un matériau composite disponible sur le marché constitué d'un film mince de silicium (Si) déposé par croissance épitaxiale sur une tranche de saphir ($\mathrm{Al_2O_3}$). Il est important de noter que pour l'émission de rayonnement THz, l'exposition à l'air entraîne la présence d'une couche native d'oxyde de silicium ($\mathrm{SiO_2}$) sur le matériau SOS, ce qui produit une zone de déplétion statique du champ électrique près de la surface du semi-conducteur qui peut être modifiée par l'interaction de réactifs chimiques [140]. Le substrat en saphir servant

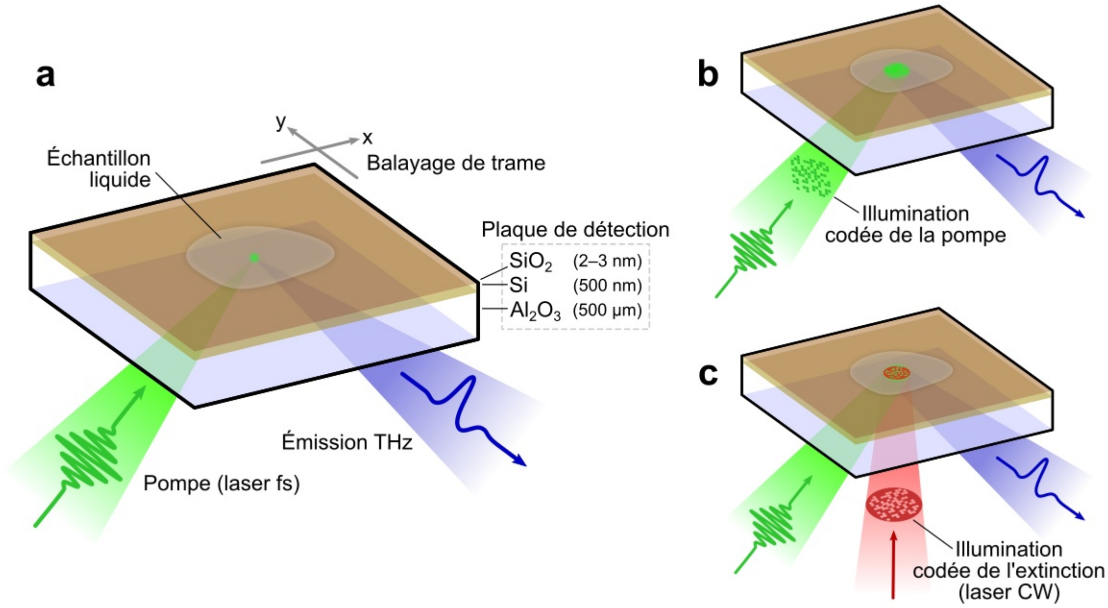

Figure 6.10 Principes de l'imagerie TCM conventionnelle et de l'imagerie computationnelle proposée. **(a)** Schéma de l'imagerie TCM conventionnelle montrant la composition d'une plaque de détection SOS. **(b)**–**(c)** Disposition de la TCM computationnelle utilisant la structuration spatiale de l'illumination pulsée (b), et la structuration spatiale de l'illumination CW séparée (c).

de structure transparente aux longueurs d'onde THz et optiques, une solution placée sur la surface supérieure de la plaque d'impact orientée horizontalement est éclairée par le laser fs focalisé depuis le côté inférieur, la détection THz ultérieure ayant également lieu depuis le côté inférieur orienté selon l'angle de réflexion de l'éclairage laser. De cette façon, un chemin pour les signaux optiques est fourni qui n'est pas influencé par les propriétés d'absorption de l'échantillon liquide.

Pour généraliser le fonctionnement du système de TCM afin d'utiliser l'imagerie mono-pixel SPI, il faut trouver un moyen de moduler spatialement la réponse THz. En revenant à l'expression de la réponse du champ électrique THz dans l'équation (6.5), on peut voir qu'en dehors de l'influence des champs électriques locaux sur le terme d'accélération des supports $\partial v(t)/\partial t$, la densité de photocourant elle-même $n(t)$ fournit un moyen indépendant pour le contrôle externe des signaux THz. Si l'on considère les options pour le réglage optique de $n(t)$, une approche évidente, représentée sur la Fig. 6.10b, est la modulation du laser fs lui-même, remplaçant l'éclairage focalisé à point unique par un champ élargi d'éclairage structuré qui modèle sélectivement la densité des photocourants, et donc les sites d'émission THz, dans le champ de vision. Cependant, comme l'ont montré les mesures d'efficacité optique effectuées en laboratoire, cette approche directe présente plusieurs inconvénients, notamment le fait que la puissance disponible pour l'éclairage actif est limitée, principalement en raison de l'efficacité optique intrinsèquement faible du matériel DMD. Par conséquent, afin de maximiser la puissance optique disponible pour l'illumination pulsée, la modulation de la densité de porteurs peut être assurée par une source optique séparée avec des énergies de photons suffisantes pour la photo-excitation. Avec l'utilisation d'un seul laser visible à ondes entretenues, l'arrangement décrit dans la Fig. 6.10c est proposé avec le codage spatial du faisceau incident fourni par SPI-ASAP.

Résultats

Afin de démontrer l'effet de la modulation CW pour le contrôle des signaux d'émission THz, un système TCM existant disponible à l'INRS a été utilisé [147]. L'expérience a consisté en une illumination par un laser pulsé (durée 250 fs) à 523 nm défocalisé à une taille de point d'environ 2 mm sur une plaque d'impact SOS sans échantillon liquide. À l'intérieur de ce point, un laser CW (671 nm) a été introduit avec une puissance optique variable. Les formes d'onde THz résultantes enregistrées en fonction de la puissance du laser de pompe et de la puissance du laser CW incident sont illustrées à la Fig. 6.11. Les résultats démontrent l'existence d'un effet d'extinction spectralement uniforme dont l'effet proportionnel est indépendant de la puissance du laser de pompage incident. Important pour la possibilité de calculer la TCM, ces résultats indiquent que des modèles contrôlés d'illumination CW sont capables de réduire l'amplitude crête à crête des signaux THz jusqu'à 35% à la limite de la puissance optique disponible dans l'expérience. Dans le cadre du SPI, cette force de modulation, bien que partielle, est néanmoins tout à fait suffisante pour réaliser l'imagerie computationnelle.

La Fig. 6.12 présente un plan de conception du système ainsi qu'une photographie du prototype de système de TCM computationnel actuellement construit. Suivant la conception des systèmes TCM établis, le système prototype incorpore une configuration pompe-sonde avec une ligne à retard pour la détection cohérente des formes d'onde THz à l'aide d'une antenne photoconductrice (PCA). En permettant le positionnement variable des lentilles, le système permet un champ élargi d'illumination laser fs dans un FOV conçu de 5 mm de diamètre. Pour faciliter l'installation, la plaque de détection est positionnée verticalement, les échantillons liquides étant contenus contre la plaque d'impact à l'aide d'une puce de fluide moulée dans un polydiméthylsiloxane élastomère (PDMS) [158]. L'utilisation facultative d'un cristal pour la génération de deuxième harmonique (SHG), bien qu'elle ne soit pas une exigence pour la TCM avec des plaques d'impact SOS, est fournie comme un moyen supplémentaire d'étudier les performances d'imagerie du système avec d'autres matériaux potentiels de plaque d'impact. Afin de minimiser l'encombrement du système, la source laser à ondes et le système SPI-ASAP sont installés à une hauteur de 9 pouces au-dessus de la table optique, les motifs de codage générés étant reproduits sur la plaque de détection par l'intermédiaire d'un périscope à miroir vertical et d'un relais optique. Tel qu'il est conçu, le système comprend un ordinateur pour l'automatisation du fonctionnement du système et la collecte des données, ainsi que plusieurs pièces d'équipement électronique de soutien, dont un amplificateur à verrouillage.

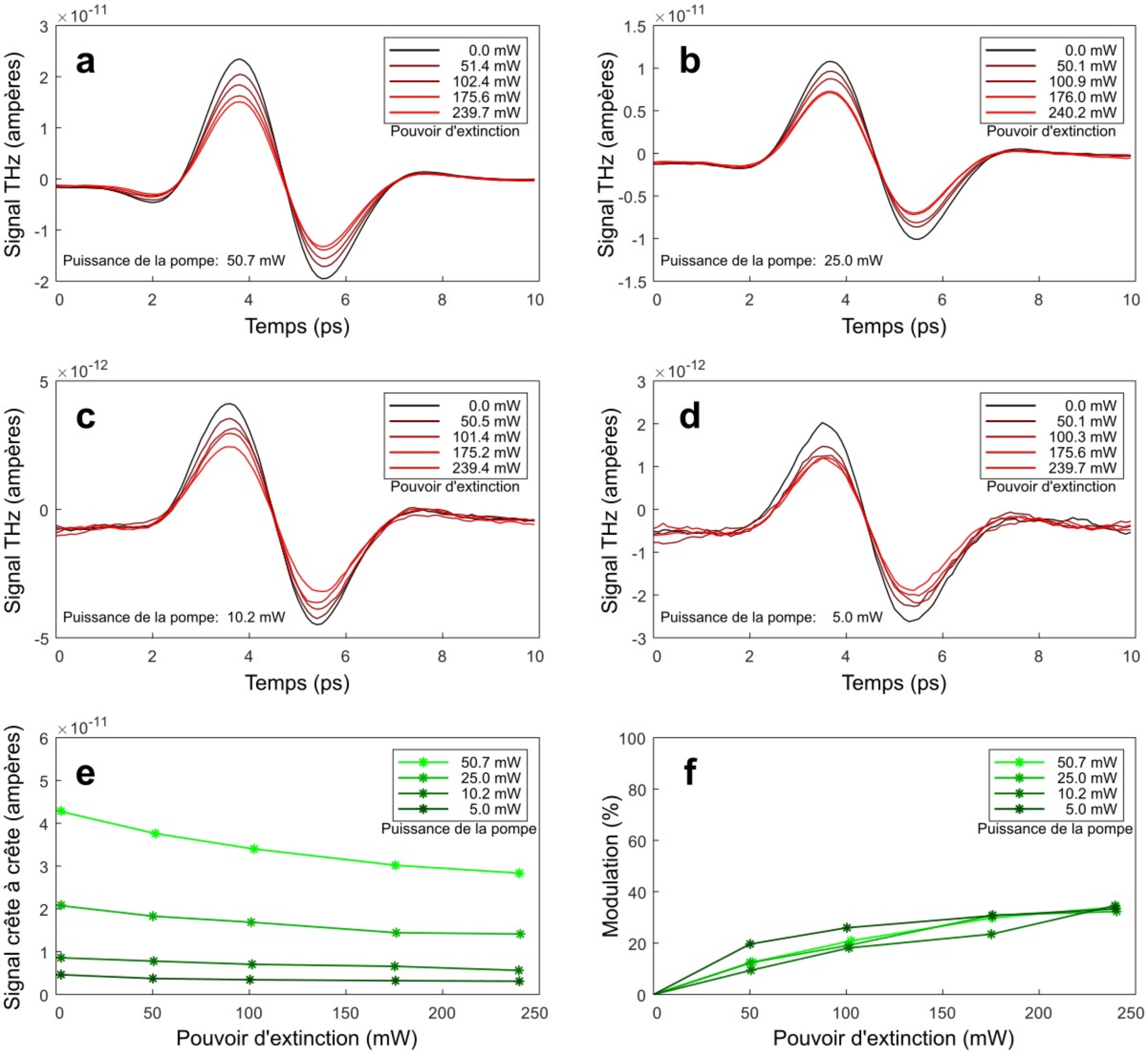

Figure 6.11 Preuve de l'extinction des émissions THz par le laser CW. **(a)**–**(d)** Formes d'onde THz dans le domaine temporel mesurées à partir de SOS avec des puissances de laser fs (pompe) variables, chaque graphique montrant les formes d'onde superposées d'une série de puissances de laser CW (extinction). **(e)** Tracés de l'amplitude du signal crête à crête en fonction de la puissance d'extinction pour différentes puissances de pompe. **(f)** Profondeur de modulation, définie comme la différence relative d'amplitude crête à crête, montrée pour les mêmes données présentées en (e).

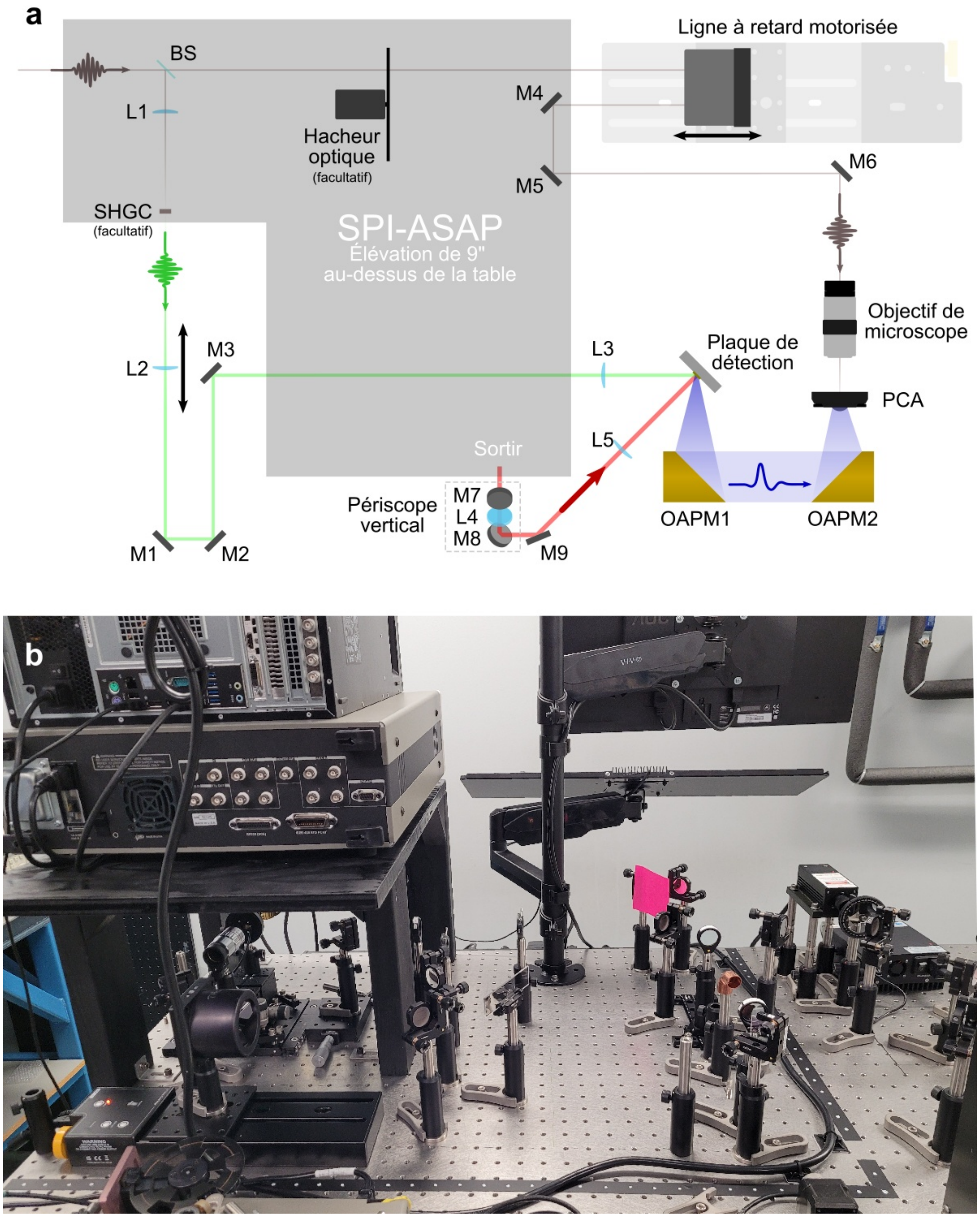

Figure 6.12 Conception et construction du prototype de système de TCM computationnel. **(a)** Diagramme à l'échelle de l'empreinte du système, montrant les composants pour la détection des formes d'onde cohérentes. L'éclairage structuré en ondes entretenues est fourni par le système SPI-ASAP qui est installé à une hauteur de 9 pouces au-dessus de la table et dont l'image est transmise à la plaque de détection à l'aide d'un périscope vertical et d'un relais optique. BS, diviseur de faisceau ; M1–M6, miroirs ; PCA, antenne photoconductrice ; L1–L4, lentilles ; OAPM1–OAPM2, miroirs paraboliques hors axe ; SHGC, cristal de génération de seconde harmonique. **(b)** Photographie du système actuellement construit (le module SPI-ASAP n'est pas représenté).

6.5 Conclusion

Le cadre diversifié de l'imagerie scientifique, bien qu'il soit dominé dans le spectre visible par des photodétecteurs au silicium de format de réseau, nécessite néanmoins une diversité de méthodes et de technologies pour combler les lacunes, tant spectrales que temporelles, là où les capteurs multi-pixels ne peuvent pas voir. En tant que stratégie visant à résoudre les contraintes techniques fondamentales qui affectent les technologies de photodétecteurs aux frontières du développement, l'imagerie à mono-pixel cherche à maximaliser l'utilisation des capteurs existants, en permettant aux vitesses d'acquisition d'images de dépasser les limitations mécaniques du balayage à point unique, et donc de se rapprocher de la pleine utilisation des bandes passantes des détecteurs disponibles.

Cette thèse a présenté l'imagerie à mono-pixel accélérée par balayage de motifs agrégés SPI-ASAP, une plateforme pour l'imagerie mono-pixel SPI conçue pour permettre des applications d'imagerie à grande vitesse et en temps réel. En augmentant les performances des dispositifs numériques à micromiroir DMD conventionnels avec du matériel de balayage laser disponible sur le marché, SPI-ASAP prend en charge l'imagerie à haute et ultra-haute vitesse grâce au déploiement par balayage de motifs de codage agrégés, permettant ainsi aux taux de modulation d'atteindre des largeurs de bande MHz supérieures de deux ordres de grandeur aux vitesses maximales réalisables avec le dispositif DMD seul. En outre, en étendant des approches distinctes et génériques de la modulation et de la reconstruction, SPI-ASAP prend en charge l'imagerie vidéo en temps réel en intégrant les étapes de modulation et de reconstruction étroitement couplé, basé sur les propriétés mathématiques optimales des matrices circulantes. Contrairement à d'autres méthodes concurrentes dans le domaine de l'imagerie mono-pixel SPI haute vitesse et en temps réel, SPI-ASAP conserve une flexibilité supérieure en ce qui concerne les paramètres d'imagerie tels que le nombre de pixels et la fréquence d'images, tout en restant compatible avec une grande variété de sources lumineuses spécialisées.

Les applications explorées dans cette thèse pour l'imagerie 3D, l'imagerie à ultra-haute vitesse, l'imagerie en temps réel et l'imagerie THz, bien que très variées, ne reflètent qu'une fraction des scénarios d'imagerie auxquels les techniques de SPI ont été appliquées jusqu'à présent. En effet, étant donné que l'imagerie mono-pixel SPI englobe un ensemble d'approches informatiques pour l'échantillonnage des données en général, on peut considérer que des applications potentielles de la SPI apparaissent chaque fois qu'un moyen de modulation déterministe de la lumière peut être mis en œuvre dans une méthodologie d'imagerie existante. Cependant, il reste encore beaucoup à faire dans le domaine de la recherche SPI pour trouver les méthodes d'imagerie qui ne disposent pas des outils des capteurs multi-pixels, et pour faire progresser leurs capacités. En ce sens, les capacités de fonctionnement à grande vitesse et en temps réel doivent être considérées comme des objectifs lucratifs de la technologie de l' imagerie mono-pixel SPI, dont la réalisation a le pouvoir de transformer radicalement la facilité d'utilisation, la maturité, le champ d'application et le potentiel commercial de toute modalité d'imagerie précédemment limitée au balayage à un seul point. C'est dans ce contexte ambitieux que s'inscrit le travail de réalisation de SPI-ASAP.

L'objectif le plus immédiat du travail futur de SPI-ASAP, déjà décrit, sera son application à un microscope chimique THz informatique. Au-delà de cet objectif, d'autres possibilités d'imagerie THz existent pour SPI-ASAP, en particulier pour les systèmes qui modulent le rayonnement THz en espace libre en utilisant la photoexcitation structurée dans des masques semi-conducteurs [19, 33, 46]. L'amélioration des composantes matérielles de base de SPI-ASAP par le biais du dispositif numérique à micromiroir DMD plus rapides et de miroirs polygonaux permettrait d'améliorer immédiatement la vitesse d'imagerie d'un facteur 10 [11]. Comme indiqué précédemment, SPI-ASAP pourrait être utilisé pour mettre en œuvre la profilométrie 3D mono-pixel à grande vitesse et/ou en temps réel en étendant le système STDP [10]. Bien qu'utilisé jusqu'à présent pour la SPI en mode actif, le matériel de SPI-ASAP pourrait être utilisé pour l'imagerie en mode passif pour des applications qui reposent sur des événements auto-luminescents, comme la caractérisation des propriétés optiques des nanomatériaux [120] et la surveillance des activités neuronales [121]. Comme l'a démontré avec succès l'imagerie de filaments incandescents, la SPI-ASAP pour l'imagerie dans des conditions de lumière ambiante forte pourrait être adoptée pour l'étude d'autres phénomènes de combustion [122]. L'extension de la gamme spectrale opérationnelle de SPI-ASAP à l'aide de sources lumineuses et de détecteurs adaptés pourrait permettre d'améliorer encore la détection rapide des gaz dangereux, une application déjà éprouvée au sein de SPI [18]. Enfin, le compromis entre la qualité de l'image et la vitesse de calcul pour la méthode de reconstruction de SPI-ASAP pourrait être approfondi par l'application de techniques d'apprentissage automatique [38–40].

BIBLIOGRAPHY

[1] Edgar, M. P., Gibson, G. M. & Padgett, M. J. Principles and prospects for single-pixel imaging. *Nat. Photonics* **13**(1), 13–20 (2019). doi:10.1038/s41566-018-0300-7.

[2] Zhang, S., Van Der Weide, D. & Oliver, J. Superfast phase-shifting method for 3-D shape measurement. *Opt. Express* **18**(9), 9684–9689 (2010). doi:10.1364/oe.18.009684.

[3] Takhar, D., Laska, J. N. et al. A new compressive imaging camera architecture using optical-domain compression. In *Computational Imaging IV*, 606509. SPIE (2006). doi:10.1117/12.659602.

[4] Duarte, M. F., Davenport, M. A. et al. Single-pixel imaging via compressive sampling. *IEEE Signal Proc. Mag.* **25**(2), 83–91 (2008). doi:10.1109/MSP.2007.914730.

[5] Bian, L., Suo, J., Dai, Q. & Chen, F. Experimental comparison of single-pixel imaging algorithms. *J. Opt. Soc. Am. A* **35**(1), 78–87 (2018). doi:10.1364/JOSAA.35.000078.

[6] Sun, M. J. & Zhang, J. M. Single-pixel imaging and its application in three-dimensional reconstruction: a brief review. *Sensors* **19**(3), 732 (2019). doi:10.3390/s19030732.

[7] Donoho, D. Compressed Sensing. *IEEE T. Inform. Theory* **52**(4), 1289–1306 (2006). doi:10.1109/TIT.2006.871582.

[8] Candès, E. & Wakin, M. An introduction to compressive sampling. *IEEE Signal Proc. Mag.* **25**(2), 21–30 (2008). doi:10.1109/MSP.2007.914731.

[9] Czajkowski, K. M., Pastuszczak, A. & Kotyński, R. Real-time single-pixel video imaging with Fourier domain regularization. *Opt. Express* **26**(16), 20009–20022 (2018). doi:10.1364/OE.26.020009.

[10] Kilcullen, P., Jiang, C., Ozaki, T. & Liang, J. Camera-free three-dimensional dual photography. *Opt. Express* **28**(20), 29377–29389 (2020). doi:10.1364/OE.402310.

[11] Kilcullen, P., Ozaki, T. & Liang, J. Compressed ultrahigh-speed single-pixel imaging by swept aggregate patterns. *Nat. Commun.* **13**, 7879 (2022). doi:10.1038/s41467-022-35585-8.

[12] Phillips, D. B., Sun, M.-J. et al. Adaptive foveated single-pixel imaging with dynamic supersampling. *Sci. Adv.* **3**(4), e1601782 (2017). doi:10.1126/sciadv.1601782.

[13] Hahamovich, E., Monin, S., Hazan, Y. & Rosenthal, A. Single pixel imaging at megahertz switching rates via cyclic Hadamard masks. *Nat. Commun.* **12**, 4516 (2021). doi:10.1038/s41467-021-24850-x.

[14] Harwit, M. & Sloane, N. J. A. *Hadamard Transform Optics*. Academic Press (1979). doi:10.1016/B978-0-12-330050-8.X5001-X.

[15] Sloane, N. J. A., Fine, T., Phillips, P. G. & Harwit, M. Codes for multislit spectrometry. *Appl. Opt.* **8**(10), 2103–2106 (1969). doi:10.1364/AO.8.002103.

[16] Sloane, N. J. A. & Harwit, M. Masks for Hadamard transform optics, and weighing designs. *Appl. Opt.* **15**(1), 107–114 (1976). doi:10.1364/AO.15.000107.

[17] Cohn, J. H. E. On the value of determinants. *P. Am. Math. Soc.* **14**(4), 581–588 (1963). doi:10.1090/s0002-9939-1963-0151479-1.

[18] Gibson, G. M., Sun, B. et al. Real-time imaging of methane gas leaks using a single-pixel camera. *Opt. Express* **25**(4), 2998–3005 (2017). doi:10.1364/OE.25.002998.

[19] Stantchev, R. I., Sun, B. et al. Noninvasive, near-field terahertz imaging of hidden objects using a single-pixel detector. *Sci. Adv.* **2**(6), e1600190 (2016). doi:10.1126/sciadv.1600190.

[20] Zhao, W., Chen, H. et al. Ultrahigh-speed color imaging with single-pixel detectors at low light level. *Phys. Rev. Appl.* **12**(3), 034049 (2019). doi:10.1103/PhysRevApplied.12.034049.

[21] Sun, M.-J., Edgar, M. et al. Single-pixel three-dimensional imaging with time-based depth resolution. *Nat. Commun.* **7**, 12010 (2016). doi:10.1038/ncomms12010.

[22] MacWilliams, F. J. & Sloane, N. J. A. *The Theory of Error-Correcting Codes*. North-Holland Mathematical Library. Elsevier B.V. (1977). doi:10.1016/s0924-6509(08)x7030-8.

[23] Golomb, S. W. Cyclic Hadamard Difference Sets - Constructions and Applications. In *Sequences and their Applications*, chapter 3, 39–48. Springer London (1999). doi:10.1007/978-1-4471-0551-0_3.

[24] Bromberg, Y., Katz, O. & Silberberg, Y. Ghost imaging with a single detector. *Phys. Rev. A* **79**(5), 053840 (2009). doi:10.1103/PhysRevA.79.053840.

[25] Yang, Z., Zhang, W. X., Liu, Y. P., Ruan, D. & Li, J. L. Instant ghost imaging: algorithm and on-chip implementation. *Opt. Express* **28**(3), 3607–3618 (2020). doi:10.1364/OE.379293.

[26] Gibson, G. M., Johnson, S. D. & Padgett, M. J. Single-pixel imaging 12 years on: a review. *Opt. Express* **28**(19), 28190–28208 (2020). doi:10.1364/OE.403195.

[27] Vaz, P. G., Amaral, D., Requicha Ferreira, L. F., Morgado, M. & Cardoso, J. Image quality of compressive single-pixel imaging using different Hadamard orderings. *Opt. Express* **28**(8), 11666–11681 (2020). doi:10.1364/OE.387612.

[28] Baraniuk, R., Davenport, M., DeVore, R. & Wakin, M. A simple proof of the restricted isometry property for random matrices. *Constr. Approx.* **28**(3), 253–263 (2008). doi:10.1007/s00365-007-9003-x.

[29] Becker, S., Bobin, J. & Candès, E. J. NESTA: A fast and accurate first-order method for sparse recovery. *SIAM J. Imaging Sci.* **4**(1), 1–39 (2011). doi:10.1137/090756855.

[30] Candès, E. J. & Romberg, J. K. L1-MAGIC (v1.0). California Institute of Technology (2005). https://candes.su.domains/software/l1magic/.

[31] Li, C., Yin, W., Jiang, H. & Zhang, Y. An efficient augmented Lagrangian method with applications to total variation minimization. *Comput. Optim. Appl.* **56**(3), 507–530 (2013). doi:10.1007/s10589-013-9576-1.

[32] Bioucas-Dias, J. M. & Figueiredo, M. A. T. A new TwIST: two-step iterative shrinkage/thresholding algorithms for image restoration. *IEEE Trans. Image Process.* **16**(12), 2992–3004 (2007). doi:10.1109/TIP.2007.909319.

[33] She, R., Liu, W., Lu, Y., Zhou, Z. & Li, G. Fourier single-pixel imaging in the terahertz regime. *Appl. Phys. Lett.* **115**(2) (2019). doi:10.1063/1.5094728.

[34] Zhang, Z., Ma, X. & Zhong, J. Single-pixel imaging by means of Fourier spectrum acquisition. *Nat. Commun.* **6**, 6225 (2015). doi:10.1038/ncomms7225.

[35] Sun, M.-J., Meng, L.-T., Edgar, M. P., Padgett, M. J. & Radwell, N. A russian dolls ordering of the Hadamard basis for compressive single-pixel imaging. *Sci. Rep.* **7**(1) (2017). doi:10.1038/s41598-017-03725-6.

[36] Radwell, N., Mitchell, K. J., Gibson, G. M., Edgar, M. P., Bowman, R. & Padgett, M. J. Single-pixel infrared and visible microscope. *Optica* **1**(5), 285–289 (2014). doi:10.1364/OPTICA.1.000285.

[37] Edgar, M. P., Gibson, G. M. et al. Simultaneous real-time visible and infrared video with single-pixel detectors. *Sci. Rep.* **5**, 10669 (2015). doi:10.1038/srep10669.

[38] Shimobaba, T., Endo, Y. et al. Computational ghost imaging using deep learning. *Opt. Commun.* **413**, 147–151 (2018). doi:10.1016/j.optcom.2017.12.041.

[39] Higham, C. F., Murray-Smith, R., Padgett, M. J. & Edgar, M. P. Deep learning for real-time single-pixel video. *Sci. Rep.* **8**, 2369 (2018). doi:10.1038/s41598-018-20521-y.

[40] Hoshi, I., Shimobaba, T., Kakue, T. & Ito, T. Single-pixel imaging using a recurrent neural network combined with convolutional layers. *Opt. Express* **28**(23), 34069–34078 (2020). doi:10.1364/OE.410191.

[41] Hornbeck, L. J. Digital light processing for high-brightness high-resolution applications. In *Projection Displays III*, 27–40 (1997). doi:10.1117/12.273880.

[42] Blanche, P.-A. & Ketchum, R. S. Texas Instruments phase light modulator for holography. In *OSA Imaging and Applied Optics Congress 2021*, DW4B.3 (2021). doi:10.1364/dh.2021.Dw4b.3.

[43] Xu, Z.-H., Chen, W., Penuelas, J., Padgett, M. & Sun, M.-J. 1000 fps computational ghost imaging using LED-based structured illumination. *Opt. Express* **26**(3), 2427–2434 (2018). doi:10.1364/OE.26.002427.

[44] Huang, H., Li, L., Ma, Y. & Sun, M. 25,000 fps computational ghost imaging with ultrafast structured illumination. *Electron. Mater.* **3**(1), 93–100 (2022). doi:10.3390/electronicmat3010009.

[45] Musarra, G., Lyons, A. et al. Non-line-of-sight three-dimensional imaging with a single-pixel camera. *Phys. Rev. Appl.* **12**(1), 011002 (2019). doi:10.1103/PhysRevApplied.12.011002.

[46] Stantchev, R. I., Yu, X., Blu, T. & Pickwell-MacPherson, E. Real-time terahertz imaging with a single-pixel detector. *Nat. Commun.* **11**, 2535 (2020). doi:10.1038/s41467-020-16370-x.

[47] Chan, W. L., Charan, K., Takhar, D., Kelly, K. F., Baraniuk, R. G. & Mittleman, D. M. A single-pixel terahertz imaging system based on compressed sensing. *Appl. Phys. Lett.* **93**(12), 121105 (2008). doi:10.1063/1.2989126.

[48] Chan, W. L., Moravec, M. L., Baraniuk, R. G. & Mittleman, D. M. Terahertz imaging with compressed sensing and phase retrieval. *Opt. Lett.* **33**(9), 974–976 (2008). doi:10.1364/OL.33.000974.

[49] Shen, H., Newman, N., Gan, L., Zhong, S. C., Huang, Y. & Shen, Y. C. Compressed terahertz imaging system using a spin disk. In *35th International Conference on Infrared, Millimeter, and Terahertz Waves*. IEEE (2010). doi:10.1109/ICIMW.2010.5612977.

[50] Shen, H., Gan, L. et al. Spinning disk for compressive imaging. *Opt. Lett.* **37**(1), 46–48 (2012). doi:10.1364/OL.37.000046.

[51] Ma, Y., Grant, J., Saha, S. & Cumming, D. R. S. Terahertz single pixel imaging based on a Nipkow disk. *Opt. Lett.* **37**(9), 1484–1486 (2012). doi:10.1364/OL.37.001484.

[52] Li, C., Grant, J., Wang, J. & Cumming, D. R. S. A Nipkow disk integrated with Fresnel lenses for terahertz single pixel imaging. *Opt. Express* **21**(21), 24452–24459 (2013). doi:10.1364/OE.21.024452.

[53] Jiang, W., Jiao, J., Guo, Y., Chen, B., Wang, Y. & Sun, B. Single-pixel camera based on a spinning mask. *Opt. Lett.* **46**(19), 4859–4862 (2021). doi:10.1364/OL.431848.

[54] Born, M. & Wolf, E. *Principles of Optics: Electromagnetic Theory of Propagation, Interference and Diffraction of Light*. Cambridge University Press, 7th edition (1999). doi:10.1017/CBO9781139644181.

[55] Sen, P., Horowitz, M. et al. Dual photography. In *SIGGRAPH '05*, 745–755 (2005). doi:10.1145/1186822.1073257.

[56] Sen, P. & Darabi, S. Compressive dual photography. *Comput. Graph. Forum* **28**(2), 609–618 (2009). doi:10.1111/j.1467-8659.2009.01401.x.

[57] Zhang, S. High-speed 3D shape measurement with structured light methods: a review. *Opt. Laser Eng.* **106**, 119–131 (2018). doi:10.1016/j.optlaseng.2018.02.017.

[58] Zhang, S., Royer, D. & Yau, S.-T. GPU-assisted high-resolution, real-time 3-D shape measurement. *Opt. Express* **14**(20), 9120–9129 (2006). doi:10.1364/OE.14.009120.

[59] Zhang, S. & Huang, P. S. Novel method for structured light system calibration. *Opt. Eng.* **45**(8), 083601 (2006). doi:10.1117/1.2336196.

[60] Jiang, C., Kilcullen, P. et al. Real-time high-speed three-dimensional surface imaging using band-limited illumination profilometry with a CoaXPress interface. *Opt. Lett.* **45**(4), 964–967 (2020). doi:10.1364/OL.378939.

[61] Jiang, C., Kilcullen, P., Lai, Y., Ozaki, T. & Liang, J. High-speed dual-view band-limited illumination profilometry using temporally interlaced acquisition. *Photonics Res.* **8**(11), 1808–1817 (2020). doi:10.1364/prj.399492.

[62] Jiang, C., Kilcullen, P., Lai, Y., Wang, S., Ozaki, T. & Liang, J. Multi-scale band-limited illumination profilometry for robust three-dimensional surface imaging at video rate. *Opt. Express* **30**(11), 19824–19838 (2022). doi:10.1364/oe.457502.

[63] Zuo, C., Feng, S., Huang, L., Tao, T., Yin, W. & Chen, Q. Phase shifting algorithms for fringe projection profilometry: a review. *Opt. Laser Eng.* **109**, 23–59 (2018). doi:10.1016/j.optlaseng.2018.04.019.

[64] Ghiglia, D. C. & Pritt, M. D. *Two-Dimensional Phase Unwrapping: Theory, Algorithms, and Software*. Wiley-Interscience (1998). ISBN: 978-0-471-24935-1.

[65] Ghiglia, D. C. & Romero, L. A. Robust two-dimensional weighted and unweighted phase unwrapping that uses fast transforms and iterative methods. *J. Opt. Soc. Am. A* **11**(1), 107–117 (1994). doi:10.1364/JOSAA.11.000107.

[66] Zhang, Z. Flexible camera calibration by viewing a plane from unknown orientations. In *Proceedings of the Seventh IEEE International Conference on Computer Vision*, 666–673. IEEE (1999). doi:10.1109/ICCV.1999.791289.

[67] Hartley, R. & Zisserman, A. *Multiple View Geometry in Computer Vision*. Cambridge University Press, 2nd edition (2004). doi:10.1017/CBO9780511811685.

[68] Bouguet, J.-Y. Camera Calibration Toolbox for Matlab (v1.0). California Institut of Technology (2015). doi:10.22002/D1.20164.

[69] Veach, E. *Robust Monte Carlo Methods for Light Transport Simulation*. Ph.D. dissertation, Stanford University (1998). ISBN: 978-0-591-90780-3.

[70] Koppal, S. & Narasimhan, S. G. Beyond perspective dual photography with illumination masks. *IEEE Trans. Image Process.* **24**(7), 2083–2097 (2015). doi:10.1109/tip.2015.2413291.

[71] Koppelhuber, A. & Bimber, O. Computational imaging, relighting and depth sensing using flexible thin-film sensors. *Opt. Express* **25**(3), 2694–2702 (2017). doi:10.1364/OE.25.002694.

[72] O'Toole, M., Lindell, D. B. & Wetzstein, G. Confocal non-line-of-sight imaging based on the light-cone transform. *Nature* **555**, 338–341 (2018). doi:10.1038/nature25489.

[73] Paniagua-Diaz, A. M., Starshynov, I. et al. Blind ghost imaging. *Optica* **6**(4), 460–464 (2019). doi:10.1364/optica.6.000460.

[74] Zhang, Z., Liu, S., Peng, J., Yao, M., Zheng, G. & Zhong, J. Simultaneous spatial, spectral, and 3D compressive imaging via efficient Fourier single-pixel measurements. *Optica* **5**(3), 315–319 (2018). doi:10.1364/optica.5.000315.

[75] Ralasic, I., Donlic, M. & Sersic, D. Dual imaging–can virtual be better than real? *IEEE Access* **8**, 40246–40260 (2020). doi:10.1109/access.2020.2976870.

[76] Chiba, N. & Hashimoto, K. Ultra-fast multi-scale shape estimation of light transport matrix for complex light reflection objects. In *2018 IEEE International Conference on Robotics and Automation (ICRA)*, 6147–6152 (2018). doi:10.1109/icra.2018.8460892.

[77] Wang, J., Sankaranarayanan, A. C., Gupta, M. & Narasimhan, S. G. Dual structured light 3D using a 1D sensor. In *European Conference on Computer Vision (EECV 2016)*, 383–398 (2016). doi:10.1007/978-3-319-46466-4_23.

[78] O'Toole, M., Mather, J. & Kutulakos, K. N. 3D shape and indirect appearance by structured light transport. In *2014 IEEE Conference on Computer Vision and Pattern Recognition*, 3246–3253 (2014). doi:10.1109/cvpr.2014.421.

[79] Xiao, Y.-L., Wen, Y., Li, S., Zhang, Q. & Zhong, J. Large-scale structured light 3D shape measurement with reverse photography. *Opt. Laser Eng.* **130**, 106086 (2020). doi:10.1016/j.optlaseng.2020.106086.

[80] Liang, C.-K. & Ramamoorthi, R. A light transport framework for lenslet light field cameras. *ACM Trans. Graph.* **34**(2), Article 16 (2015). doi:10.1145/2665075.

[81] Sen, P. & Darabi, S. A novel framework for imaging using compressed sensing. In *2009 16th IEEE International Conference on Image Processing (ICIP)*, 2133–2136 (2009). doi:10.1109/icip.2009.5414289.

[82] Sen, P. On the relationship between dual photography and classical ghost imaging. *arXiv preprint*, 1309.3007 (2013). doi:10.48550/arXiv.1309.3007.

[83] Liang, J., Gao, L., Li, C. & Wang, L. V. Spatially Fourier-encoded photoacoustic microscopy using a digital micromirror device. *Opt. Lett.* **39**(3), 430–433 (2014). doi:10.1364/ol.39.000430.

[84] Sun, B., Edgar, M. P. et al. 3D computational imaging with single-pixel detectors. *Science* **340**(6134), 844–847 (2013). doi:10.1126/science.1234454.

[85] Zhang, Y., Edgar, M. P., Sun, B., Radwell, N., Gibson, G. M. & Padgett, M. J. 3D single-pixel video. *J. Opt.* **18**(3), 035203 (2016). doi:10.1088/2040-8978/18/3/035203.

[86] Salvador-Balaguer, E., Latorre-Carmona, P., Chabert, C., Pla, F., Lancis, J. & Tajahuerce, E. Low-cost single-pixel 3D imaging by using an LED array. *Opt. Express* **26**(12), 15623–15631 (2018). doi:10.1364/OE.26.015623.

[87] Gorthi, S. S. & Rastogi, P. Fringe projection techniques: whither we are? *Opt. Laser Eng.* **48**(2), 133–140 (2010). doi:10.1016/j.optlaseng.2009.09.001.

[88] Seitz, S., Matsushita, Y. & Kutulakos, K. A theory of inverse light transport. In *Tenth IEEE International Conference on Computer Vision (ICCV'05)* **2**, 1440–1447 (2005). doi:10.1109/ICCV.2005.25.

[89] Chiba, N. & Hashimoto, K. 3D measurement by estimating homogeneous light transport (HLT) matrix. In *2017 IEEE International Conference on Mechatronics and Automation (ICMA)*, 1763–1768 (2017). doi:10.1109/icma.2017.8016084.

[90] Gopalsami, N., Liao, S. et al. Passive millimeter-wave imaging with compressive sensing. *Opt. Eng.* **51**(9), 091614 (2012). doi:10.1117/1.OE.51.9.091614.

[91] Ermeydan, E. Ş. & Çankaya, İ. Compressed sensing with cyclic-S Hadamard matrix for terahertz imaging applications. In *6th International Eurasian Conference on Mathematical Sciences and Applications (IECMSA-2017)* **1926**(1), 020040 (2017). doi:10.1063/1.5020489.

[92] Stanton, R. G. & Sprott, D. A. A family of difference sets. *Canadian J. Math.* **10**, 73–77 (1958). doi:10.4153/CJM-1958-008-5.

[93] Zhang, Z. & Zhong, J. Three-dimensional single-pixel imaging with far fewer measurements than effective image pixels. *Opt. Lett.* **41**(11), 2497–2500 (2016). doi:10.1364/OL.41.002497.

[94] Liang, J., Kohn, R. N., Becker, M. F. & Heinzen, D. J. Homogeneous one-dimensional optical lattice generation using a digital micromirror device-based high-precision beam shaper. *J. Micro/Nanolith. MEMS MOEMS* **11**(2), 023002 (2012). doi:10.1117/1.JMM.11.2.023002.

[95] Liang, J., Wu, S.-Y., Kohn, R. N., Becker, M. F. & Heinzen, D. J. Grayscale laser image formation using a programmable binary mask. *Opt. Eng.* **51**(10), 108201 (2012). doi:10.1117/1.OE.51.10.108201.

[96] Liang, J. Punching holes in light: recent progress in single-shot coded-aperture optical imaging. *Rep. Prog. Phys.* **83**(11), 116101 (2020). doi:10.1088/1361-6633/abaf43.

[97] Faccio, D., Velten, A. & Wetzstein, G. Non-line-of-sight imaging. *Nat. Rev. Phys.* **2**, 318–327 (2020). doi:10.1038/s42254-020-0174-8.

[98] Liu, X., Bauer, S. & Velten, A. Phasor field diffraction based reconstruction for fast non-line-of-sight imaging systems. *Nat. Commun.* **11**, 1645 (2020). doi:10.1038/s41467-020-15157-4.

[99] Kirmani, A., Venkatraman, D. et al. First-photon imaging. *Science* **343**(6166), 58–61 (2013). doi:10.1126/science.1246775.

[100] Peng, X., Zhao, X.-Y., Li, L.-J. & Sun, M.-J. First-photon imaging via a hybrid penalty. *Photonics Res.* **8**(3), 325–330 (2020). doi:10.1364/prj.381516.

[101] Jaffe, J., Moore, K., McLean, J. & Strand, M. Underwater optical imaging: status and prospects. *Oceanography* **14**(3), 64–75 (2001). doi:10.5670/oceanog.2001.24.

[102] Gong, W., Zhao, C., Yu, H., Chen, M., Xu, W. & Han, S. Three-dimensional ghost imaging lidar via sparsity constraint. *Sci. Rep.* **6**, 26133 (2016). doi:10.1038/srep26133.

[103] Chen, Q., Chamoli, S. K., Yin, P., Wang, X. & Xu, X. Imaging of hidden object using passive mode single pixel imaging with compressive sensing. *Laser Phys. Lett.* **15**(12), 126201 (2018). doi:10.1088/1612-202X/aae216.

[104] Stantchev, R. I., Phillips, D. B., Hobson, P., Hornett, S. M., Padgett, M. J. & Hendry, E. Compressed sensing with near-field THz radiation. *Optica* **4**(8), 989–992 (2017). doi:10.1364/OPTICA.4.000989.

[105] Guerboukha, H., Nallappan, K. & Skorobogatiy, M. Toward real-time terahertz imaging. *Adv. Opt. Photon.* **10**(4), 843–938 (2018). doi:10.1364/aop.10.000843.

[106] Zanotto, L., Piccoli, R., Dong, J., Caraffini, D., Morandotti, R. & Razzari, L. Time-domain terahertz compressive imaging. *Opt. Express* **28**(3), 3795–3802 (2020). doi:10.1364/OE.384134.

[107] Torke, P. R., Nuster, R. & Paltauf, G. Photoacoustic computational ghost imaging. *Opt. Lett.* **47**(6), 1462–1465 (2022). doi:10.1364/ol.452229.

[108] Jiang, W., Li, X., Peng, X. & Sun, B. Imaging high-speed moving targets with a single-pixel detector. *Opt. Express* **28**(6), 7889–7897 (2020). doi:10.1364/oe.387024.

[109] Kanno, H., Mikami, H. & Goda, K. High-speed single-pixel imaging by frequency-time-division multiplexing. *Opt. Lett.* **45**(8), 2339–2342 (2020). doi:10.1364/ol.390345.

[110] Futia, G., Schlup, P., Winters, D. G. & Bartels, R. A. Spatially-chirped modulation imaging of absorbtion and fluorescent objects on single-element optical detector. *Opt. Express* **19**(2), 1626–1640 (2011). doi:10.1364/oe.19.001626.

[111] Stockton, P., Murray, G., Field, J. J., Squier, J., Pezeshki, A. & Bartels, R. A. Tomographic single pixel spatial frequency projection imaging. *Opt. Commun.* **520**, 128401 (2022). doi:10.1016/j.optcom.2022.128401.

[112] Heidari, A. & Saeedkia, D. A 2D camera design with a single-pixel detector. In *34th International Conference on Infrared, Millimeter, and Terahertz Waves*. IEEE (2009). doi:10.1109/ICIMW.2009.5324725.

[113] Babacan, S. D., Luessi, M. et al. Compressive passive millimeter-wave imaging. In *18th IEEE International Conference on Image Processing*, 2705–2708. IEEE (2011). doi:10.1109/ICIP.2011.6116227.

[114] Spinoulas, L., Qi, J., Katsaggelos, A. K., Elmer, T. W., Gopalsami, N. & Raptis, A. C. Optimized compressive sampling for passive millimeter-wave imaging. *Appl. Opt.* **51**(26), 6335–6342 (2012). doi:10.1364/AO.51.006335.

[115] Vasile, T., Damian, V., Coltuc, D. & Petrovici, M. Single pixel sensing for THz laser beam profiler based on Hadamard transform. *Opt. Laser Technol.* **79**, 173–178 (2016). doi:10.1016/j.optlastec.2015.12.009.

[116] Tajahuerce, E., Durán, V. et al. Image transmission through dynamic scattering media by single-pixel photodetection. *Opt. Express* **22**(14), 16945–16955 (2014). doi:10.1364/OE.22.016945.

[117] Durán, V., Soldevila, F. et al. Compressive imaging in scattering media. *Opt. Express* **23**(11), 14424–14433 (2015). doi:10.1364/OE.23.014424.

[118] Chai, X., Gu, H., Li, F., Duan, H., Hu, X. & Lin, K. Deep learning for irregularly and regularly missing data reconstruction. *Sci. Rep.* **10**, 3302 (2020). doi:10.1038/s41598-020-59801-x.

[119] Burden, R. L. & Faires, J. D. *Numerical Analysis*. Brooks/Cole, Cengage Learning, 9th edition (2011). ISBN: 978-0-538-73351-9.

[120] Liu, X., Skripka, A. et al. Fast wide-field upconversion luminescence lifetime thermometry enabled by single-shot compressed ultrahigh-speed imaging. *Nat. Commun.* **12**, 6401 (2021). doi:10.1038/s41467-021-26701-1.

[121] Zhang, Y., Shen, B. et al. Ultrafast and hypersensitive phase imaging of propagating internodal current flows in myelinated axons and electromagnetic pulses in dielectrics. *Nat. Commun.* **13**, 5247 (2022). doi:10.1038/s41467-022-33002-8.

[122] Sick, V. High speed imaging in fundamental and applied combustion research. *P. Combust. Inst.* **34**(2), 3509–3530 (2013). doi:10.1016/j.proci.2012.08.012.

[123] Bouchard, M. B., Voleti, V. et al. Swept confocally-aligned planar excitation (SCAPE) microscopy for high speed volumetric imaging of behaving organisms. *Nat. Photonics* **9**, 113–119 (2015). doi:10.1038/nphoton.2014.323.

[124] Wang, Y., Liu, Y., Suo, J., Situ, G., Qiao, C. & Dai, Q. High speed computational ghost imaging via spatial sweeping. *Sci. Rep.* **7**, 45325 (2017). doi:10.1038/srep45325.

[125] Zhang, K., Hu, J. & Yang, W. Deep compressed imaging via optimized pattern scanning. *Photonics Res.* **9**(3), B57–B70 (2021). doi:10.1364/prj.410556.

[126] Wang, Z., Bovik, A. C., Sheikh, H. R. & Simoncelli, E. P. Image quality assessment: from error visibility to structural similarity. *IEEE Trans. Image Process.* **13**(4), 600–612 (2004). doi:10.1109/tip.2003.819861.

[127] Mittleman, D., Jacobsen, R. & Nuss, M. T-ray imaging. *IEEE J. Sel. Top. Quant.* **2**(3), 679–692 (1996). doi:10.1109/2944.571768.

[128] Chan, W. L., Deibel, J. & Mittleman, D. M. Imaging with terahertz radiation. *Rep. Prog. Phys.* **70**(8), 1325–1379 (2007). doi:10.1088/0034-4885/70/8/R02.

[129] Baxter, J. B. & Guglietta, G. W. Terahertz Spectroscopy. *Anal. Chem.* **83**(12), 4342–4368 (2011). doi:10.1021/ac200907z.

[130] Kilcullen, P., Hartley, I. D., Jensen, E. T. & Reid, M. Terahertz time domain gas-phase spectroscopy of carbon monoxide. *J. Infrared Millim. THz Waves* **36**(4), 380–389 (2015). doi:10.1007/s10762-014-0139-z.

[131] Karpowicz, N., Zhong, H. et al. Compact continuous-wave subterahertz system for inspection applications. *Appl. Phys. Lett.* **86**(5) (2005). doi:10.1063/1.1856701.

[132] Dong, J., Kim, B., Locquet, A., McKeon, P., Declercq, N. & Citrin, D. S. Nondestructive evaluation of forced delamination in glass fiber-reinforced composites by terahertz and ultrasonic waves. *Composites Part B* **79**, 667–675 (2015). doi:10.1016/j.compositesb.2015.05.028.

[133] Kilcullen, P., Shegelski, M., Na, M., Purschke, D., Hegmann, F. & Reid, M. Terahertz spectroscopy and Brewster angle reflection imaging of acoustic tiles. *J. Spectroscopy* **2017**, 2134868 (2017). doi:10.1155/2017/2134868.

[134] May, R. K., Evans, M. J. et al. Terahertz in-line sensor for direct coating thickness measurement of individual tablets during film coating in real-time. *J. Pharm. Sci.* **100**(4), 1535–1544 (2011). doi:10.1002/jps.22359.

[135] Inagaki, T., Ahmed, B., Hartley, I. D., Tsuchikawa, S. & Reid, M. Simultaneous prediction of density and moisture content of wood by terahertz time domain spectroscopy. *J. Infrared Millim. THz Waves* **35**(11), 949–961 (2014). doi:10.1007/s10762-014-0095-7.

[136] Fukunaga, K., Ogawa, Y., Hayashi, S. & Hosako, I. Application of terahertz spectroscopy for character recognition in a medieval manuscript. *IEICE Electronics Express* **5**(7), 223–228 (2008). doi:10.1587/elex.5.223.

[137] Jackson, J. B., Bowen, J. et al. A survey of terahertz applications in cultural heritage conservation science. *IEEE Trans. THz Sci. Techn.* **1**(1), 220–231 (2011). doi:10.1109/TTHZ.2011.2159538.

[138] Koch-Dandolo, C. L., Filtenborg, T., Fukunaga, K., Skou-Hansen, J. & Jepsen, P. U. Reflection terahertz time-domain imaging for analysis of an 18th century neoclassical easel painting. *Appl. Opt.* **54**(16), 5123–5129 (2015). doi:10.1364/AO.54.005123.

[139] Mittleman, D. M. Twenty years of terahertz imaging. *Opt. Express* **26**(8), 9417–9431 (2018). doi:10.1364/OE.26.009417.

[140] Wang, J., Sato, K., Yoshida, Y., Sakai, K. & Kiwa, T. A versatile terahertz chemical microscope and its application for the detection of histamine. *Photonics* **9**(1), 26 (2022). doi:10.3390/photonics9010026.

[141] Kiwa, T., Tonouchi, M., Yamashita, M. & Kawase, K. Laser terahertz-emission microscope for inspecting electrical faults in integrated circuits. *Opt. Lett.* **28**(21), 2058–2060 (2003). doi:10.1364/ol.28.002058.

[142] Yamashita, M., Kawase, K., Otani, C., Kiwa, T. & Tonouchi, M. Imaging of large-scale integrated circuits using laser-terahertz emission microscopy. *Opt. Express* **13**(1), 115–120 (2005). doi:10.1364/opex.13.000115.

[143] Murakami, H., Uchida, N., Inoue, R., Kim, S., Kiwa, T. & Tonouchi, M. Laser terahertz emission microscope. *Proceedings of the IEEE* **95**(8), 1646–1657 (2007). doi:10.1109/JPROC.2007.898829.

[144] Kiwa, T., Oka, S. et al. A terahertz chemical microscope to visualize chemical concentrations in microfluidic chips. *Jpn. J. Appl. Phys.* **46**(44), L1052–L1054 (2007). doi:10.1143/jjap.46.L1052.

[145] Kiwa, T., Kondo, J. et al. Chemical sensing plate with a laser-terahertz monitoring system. *Appl. Opt.* **47**(18), 3324–3327 (2008). doi:10.1364/ao.47.003324.

[146] Kiwa, T., Kamiya, T. et al. Imaging of chemical reactions using a terahertz chemical microscope. *Photonics* **6**(1), 10 (2019). doi:10.3390/photonics6010010.

[147] Mohamed, A., Walsh, R. et al. High-sensitivity small-molecule detection of microcystin-LR cyano-toxin using a terahertz-aptamer biosensor. *Analyst* **146**(24), 7583–7592 (2021). doi:10.1039/d1an01577j.

[148] van Exter, M. & Grischkowsky, D. R. Characterization of an optoelectronic terahertz beam system. *IEEE Transactions on Microwave Theory and Techniques* **38**(11), 1684–1691 (1990). doi:10.1109/22.60016.

[149] Harde, H. & Grischkowsky, D. Coherent transients excited by subpicosecond pulses of terahertz radiation. *Journal of the Optical Society of America B* **8**(8) (1991). doi:10.1364/josab.8.001642.

[150] Hebling, J. Derivation of the pulse front tilt caused by angular dispersion. *Opt. Quant. Electron.* **28**(12), 1759–1763 (1996). doi:10.1007/BF00698541.

[151] Geng, Q., Gu, C., Cheng, J. & Chen, S.-c. Digital micromirror device-based two-photon microscopy for three-dimensional and random-access imaging. *Optica* **4**(6), 674–677 (2017). doi:10.1364/OPTICA.4.000674.

[152] Murate, K., Roshtkhari, M. J., Ropagnol, X. & Blanchard, F. Adaptive spatiotemporal optical pulse front tilt using a digital micromirror deviceand its terahertz application. *Opt. Lett.* **43**(9), 2090–2093 (2018). doi:10.1364/OL.43.002090.

[153] Nahar, S., Mohamed, A. et al. Noninvasive, label-free, and quantitative monitoring of lipase kinetics using terahertz emission technology. *Biotechnol. Bioeng.* **118**(11), 4246–4254 (2021). doi:10.1002/bit.27893.

[154] Mouroulis, P. Z., Malone, R. M. et al. Design of a thermal imaging diagnostic using 90-degree off-axis parabolic mirrors. In *Current Developments in Lens Design and Optical Engineering VII* (2006). doi:10.1117/12.681080.

[155] Brückner, C., Notni, G. & Tünnermann, A. Optimal arrangement of 90° off-axis parabolic mirrors in THz setups. *Optik* **121**(1), 113–119 (2010). doi:10.1016/j.ijleo.2008.05.024.

[156] Hejduk, M. & Heazlewood, B. R. Off-axis parabolic mirror relay microscope for experiments with ultra-cold matter. *Rev. Sci. Instrum.* **90**, 123701 (2019). doi:10.1063/1.5123792.

[157] Kiwa, T., Oka, S., Minami, Y., Kawayama, I., Tonouchi, M. & Tsukada, K. Measurement of pH in fluidic chip using a terahertz chemical microscope. *IEEJ Trans. S. M.* **129**(7), 221–224 (2009). doi:10.1541/ieejsmas.129.221.

[158] Ahmed, F., Mahana, A., Taniizumi, K., Wang, J., Sakai, K. & Kiwa, T. Terahertz imaging technique for monitoring the flow of buffer solutions at different pH values through a microfluidic chip. *Jpn. J. Appl. Phys.* **60**(2), 027003 (2021). doi:10.35848/1347-4065/abd86e.

[159] Ahmed, F. *Visualization of the interaction of solutions through a microfluidic chip using Terahertz technology*. Ph.D. dissertation, Okayama University (2021). doi:10.18926/62159.

[160] Application Report: Wavelength Transmittance Considerations for DLP® DMD Window, DLPA031E. Texas Instruments (2019). https://www.ti.com/lit/an/dlpa031e/dlpa031e.pdf.